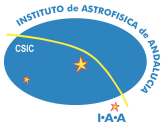

UNIVERSIDAD DE GRANADA

Tesis doctoral
Julio 2009

The nature of Dark Matter: γ-ray searches and the formation of CDM halos

[PhD THESIS]

Miguel Ángel Sánchez Conde
Instituto de Astrofísica de Andalucía (CSIC)

Memoria de Tesis
presentada en la Universidad de Granada
para optar al grado de Doctor en Astrofísica

Directores de tesis:
Dr. Francisco Prada Martínez
Prof. Mariano Moles Villamate

A ti, Raquel, por venir al mundo,
y a ti, María, por traerla.

Y a mis padres,
por su apoyo y confianza ciegos.

Lo que sabemos es una gota de agua;
lo que ignoramos es el océano.

- Isaac Newton -

Una vez sentí el ansia
de una sed infinita.

- en *Azul*, de Rubén Darío -

Una vez más percibí ese raro contraste
entre las estrellas y nosotros.
La incalculable potencia del Cosmos
acrecentaba misteriosamente la verdad
de nuestra breve chispa, y el breve
e incierto destino de los hombres.

- en *El hacedor de estrellas*, de Olaf Stapledon -

Agradecimientos

Siempre quise ser astrofísico. Pese a los años transcurridos, recuerdo con total nitidez aquella tarde de invierno del 91 en la que me compré mi primer telescopio, cuando aún no era más que un chiquillo de 11 años. Aún me es posible rememorar la emoción e ilusión que me embargaban cuando el Universo se iba desvelando ante mi tras aquel pequeño catalejo. He de reconocer que, afortunadamente, aún me llena el mismo sentimiento, ahora sin duda más maduro. Ha sido un largo camino hasta aquí y hay, por fortuna, mucho que agradecer y muchos a quienes agradecer.

En primer lugar, quisiera dar profundamente las gracias a mi director de tesis, Paco Prada. Ciertamente esta Tesis debe verse como producto de un trabajo compartido por ambos a lo largo de estos años. Su guía en estos mis primeros y temblorosos pasos en la investigación ha sido fundamental en la consecución de las metas impuestas así como en el verdadero conocimiento de mis propias posibilidades. Su ambición y motivación científicas han supuesto para mi un incentivo para llegar siempre más allá, a cuestionarme con curiosidad científica cada paso a dar y cada paso dado, a lograr alcanzar objetivos a priori inalcanzables y que luego han demostrado ser tangibles. Gracias también por tu esfuerzo, dedicación y preocupación en moldearme como un buen científico.

No puedo dejar de acordarme también de todos aquellos colegas de profesión que a lo largo de estos años han sido fuente inagotable de conversación científica y pasión compartida. Gracias especialmente a Mariano Moles por su apoyo y por creer en mi desde el principio, así como por compartir conmigo sus vastos conocimientos. Gracias también a mi asiduo colaborador en la distancia, Juan Betancort, por obligarme siempre a ser particularmente metódico y conciso. Es a a él a quien debo por entero mis incursiones en la Cosmología más teórica, pero también la confirmación de mi fe en el valor de los ideales. Mi agradecimiento también a todo mi grupo de trabajo en el IAA -Alberto, Antonio, Fabio, Hugo, Toño-, por ayudarme a respirar un ambiente de trabajo más científico todos los días, y en definitiva por compartir conmigo este duro aunque apasionante camino. No quiero pasar la oportunidad para agradecer igualmente a todos aquellos amigos y colegas astrofísicos que me han hecho sentirme como uno más del gremio siempre: Jürg Diemand, Mario Gómez, David Paneque, Carlos Delgado, Michele Doro, Radek Wojtak, Ewa Łokas, Elliott Bloom, Anatoly Klypin, Carlos Muñoz, Gustavo Yepes, Daniel Kranich, Abelardo Moralejo. También en el

IAA he contado con la simpatía y ayuda de varias personas que ya permanecerán en mi memoria como una página más de esta Tesis: Antxon Alberdi, Benigno Cantero, María Ángeles Cortés, Emilio García, Isabel Márquez, Paco Navarro, Rafael Parra, Miguel A. Pérez Torres.

Es cierto. Siempre quise ser astrofísico. Y sin duda lo soy gracias a mi familia, que con una confianza sin límites me alentó siempre a perseguir mis más alocados sueños. Esta Tesis no es sino la mejor muestra de ello. Mis padres, Antonio y Concha, siempre me apoyaron incondicionalmente a lo largo de todos estos años, pese a que esta pasión suponía alejarme cientos de kilómetros de ellos y además con destino incierto. Gracias por darme tanto y exigir tan poco, por moldearme como persona y esculpir en mi vuestra visión del mundo, por escuchar, por lanzaros al abismo conmigo sin siquiera preguntar cuando hizo falta... Mi hermano mayor, Alaly, a quien con toda seguridad debo el hecho de haberme dedicado a esto de por vida, y con quien me asomé por vez primera a los secretos de la Astronomía. Gracias por aquellas noches inolvidables al raso entre las viñas, a un paso de casa pero en realidad muy lejos, entre las estrellas. A mi hermano Jesús, que encontró sus propias estrellas en la música, y que siempre ha significado para mi un soplo sincero de cariño incondicional y un ejemplo maestro de tesón y valor ante lo que cada uno ansía. Gracias también a mis cuñadas María José y Txus, por brindar la felicidad a mis hermanos y formar parte de nosotros. Definitivamente, los valores y el amor de mi familia han impregnado siempre todo lo que he tocado y, por ende, esta Tesis necesariamente encierra una gran dosis del modo de hacer (y de ser) de los Sánchez Conde.

En el largo camino hasta aquí, no sólo los misterios del Cosmos han ido desfilando ante mis ojos, sino también los de mi propia vida. María, mi esposa y mejor confidente y amiga, supone para mi la mayor motivación que es posible imaginar para continuar adelante. Sin duda es ella la luz que ilumina mi camino en esta vasta y tenebrosa oscuridad que es la propia existencia. Ella mejor que nadie sabe de mis triunfos y alegrías, pero también de mis miedos y fracasos, derrotas y frecuentes tropiezos, pues ha sido ella quien ha compartido más de cerca conmigo cada subir y bajar de estos últimos nueve años. Ella ha sido el bálsamo necesario para recuperar la serenidad y las ansias de seguir adelante en los momentos difíciles a lo largo de esta tesis. Gracias, cariño, por estar siempre a mi lado. Y gracias también por darme a nuestra Raquel, que ya es la estrella más brillante de nuestro cielo particular. Mi agradecimiento también a mis suegros Miguel y Sole, y a mis cuñados Miguel, Ana y Alberto, por tratarme como uno más de la familia y comprender el camino al que me veía abocado por mi pasión por las estrellas.

También tengo mucho que agradecer a aquellos buenos amigos que, por fortuna, me han acompañado a lo largo de mi vida o en distintos momentos de ella. Mi ilusión ha permanecido intacta todo este tiempo en buena medida gracias a muchos de mis

amigos de Almendralejo, que con devoción ciega han seguido mi trayectoria y me han aportado seguridad y confianza en mi mismo, además de entregarme su amistad más profunda y sincera: Moi, Leandro, Julio, Paco, Jesus, Mario, Lucky, Martín, Zaca, los hermanos Jareño. También Agustín, Alex, Belén, Chovis, Diego, Jose, Juan, Marcos, Merchán, Paco Melado, Patricia, Velarde... ¡Cómo olvidar aquellas noches en el Puente de las Peras (que no de la Espera) trazando nuestros planes de comernos el mundo a la única luz de las estrellas! Bien sabéis muchos de vosotros que este era el más preciado para mi... También mis tres años de estudios en Badajoz me proporcionaron amigos que aún hoy siguen en mi vida y a los que agradezco enormemente su apoyo continuo y amistad: Pedro, Víctor, Juli, Merche, Vicente, Lidia, Miguel A y B, Noelia, Rosalía, Raquel, Luis, Juampe... En Badajoz también conocí a Antonio, con el que ya entonces compartía aficiones y conocimientos, y con el que luego compartiría día a día, y como uña y carne, todo sueño y todo anhelo. Fue con él con quien me embarqué en mi aventura canaria, en nuestra mutua determinación por llegar a ser lo que ahora somos (esto es, ni más ni menos que lo que siempre quisimos ser). Gracias por mantenerte siempre cerca. De esa etapa universitaria canaria, rodeado de mar y a tres meses de casa, debo agradecer que el destino pusiera en mi camino en especial a Luis, con su inagotable vitalidad, a Plácido, con sus férreos ideales, a Charly, Darío (en aquella época el Peludo), Omaira, Mar, Alicia, Manolo, los dos Jorge, Jairo, Rubén, Teo, Susi, David, Javi, Rebeca. Con ellos compartí aquellos años inolvidables al pie del Teide, y sobre él también, y muchos amaneceres sobre el mar. El destino burlón ha vuelto a juntarnos a varios de nosotros en Granada, donde nuestra amistad ha madurado y se ha estrechado aún más. El Triunvirato de Cuatro es buena prueba de ello: Charly, Dani, Darío han sido mis más leales amigos y compañeros de aventuras y desventuras durante todos los días de la Tesis. Gracias por aguantarme incluso en los peores días, por poner siempre un toque de humor a todo y por salir en mi auxilio cuando lo necesitaba. Gracias en Granada también a todos los doctorandos con los que he coincidido, en especial a Antonio (de Ugarte), Antonio (García), Diego, Gabriela, Geli, Marcos, Marta, Meme, Nieves, Paco, Silbia y Víctor. Hay luz al final del tunel, chicos. Y gracias a la peña de futbito, por esos momentos de relax y desconexión. Por último, no quisiera olvidarme de aquellos que, aun no siendo ni de Almendralejo, Badajoz, Tenerife o Granada, han jugado un papel esencial en esta afición mía primero y profesión después. Mil gracias especialmente a Paco Rica, al que (a pesar de ser de Mérida) me une ya una vieja y sólida amistad y una gran admiración mutua. Gracias por creer siempre en mi... Y gracias también a los colombianos Rafa y Esteban, con quienes compartí mi primera aventura americana y mi primer contacto real con la investigación en la NASA.

He de agradecer aquí también a aquellos lugares que han sido especialmente importantes para mi, cada uno por sus propios motivos, y cuya simple evocación siempre ha supuesto una motivación extra para conseguir aquello que me propusiera. Entre ellos destacaré a Extremadura, y en particular Almendralejo, con sus campos de viñas y olivos, su cielo azul inmenso y sus gentes, y que sin duda ha dejado su huella en mi

forma de ser; el Río Guadiana, en cuyas orillas encontré a la mujer de mi vida; La Palma y sus telescopios recortados sobre el fondo estrellado; ya más cercanos en el tiempo y el espacio, Granada y sus tapas, el Enano Rojo, el Rodri y el Romero, igualmente importantes en algunos momentos para conseguir acabar la Tesis. Y, desde luego, por encima de todo, gracias a la ventana por la que nos asomamos al Universo, y al Universo mismo, por ser tan absolutamente maravilloso y fascinante.

Aún conservo aquel pequeño telescopio con el que empecé a escrudiñar el cielo en mi infancia. Cada vez que vuelvo a casa (que por siempre será Almendralejo), su visión me reconforta y me ayuda a recordar, y no olvidar, de dónde vengo. Me reconforta igualmente sentir dentro de mi cómo mi vieja pasión por desvelar los misterios del Cosmos no ha disminuido en absoluto; al contrario, puedo sentirla más viva que nunca corriendo por mis venas y aguantando en pie mis huesos. Sirva de muestra esta Tesis. A día de hoy, tengo claro que esto también es así gracias a vosotros, a todos aquellos que habéis hecho que estas líneas de agradecimiento sean tan extensas, porque como ya dije al principio, hay mucho, mucho, de lo que agradecer y a quien agradecer. A buen seguro, no hubiera llegado tan lejos sin vuestro afecto y compañía. Por tanto, es mi deseo que penséis en esta Tesis también, al menos en parte, como algo genuinamente vuestro.

Resumen

En esta Tesis Doctoral, la principal línea de investigación se ha centrado en la comprensión de la naturaleza de la Materia Oscura. Con el objetivo de abordar de forma adecuada dicho problema científico y arrojar luz sobre el mismo, he usado differentes aproximaciones, tanto observacionales como teóricas. A lo largo de estas líneas resumiré las que han sido mis más notables contribuciones en el campo.

Desde el comienzo de mi Tesis, he dedicado un gran esfuerzo para entender como se forman y evolucionan los halos de Materia Oscura Fría (o CDM, de sus siglas en inglés) en el marco del modelo cosmológico estándar. En particular, en un primer trabajo me centré en la compresión y caracterización de las partes más externas de dichos halos de CDM, más allá del radio virial. Este trabajo se presenta en detalle en el Capítulo 2, y está basado en el uso del modelo de Colapso Esférico (o SIM, de sus siglas en inglés) sin cruce de capas. En el mismo Capítulo describo además el marco teórico que permite llevar a cabo la comparación entre las predicciones de dicho modelo con los resultados obtenidos mediante simulaciones cosmológicas de N-cuerpos. La conclusión principal de este trabajo es que SIM, a pesar de su simplicidad, es capaz de proporcionar predicciones detalladas que están en buen acuerdo con las simulaciones al menos a grandes distancias del centro del halo.

Todavía relacionado con lo anterior, comencé un ambicioso trabajo con el objetivo de estudiar la formación y evolución de halos de CDM haciendo uso de un modelo SIM mejorado, esta vez incluyendo el cruce de capas en el formalismo. En el Capítulo 3 presento el marco teórico necesario para manejar dicho efecto de forma apropiada, que además no involucra el uso de ningún invariante adiábatico y que está basado en el seguimiento numérico, en el tiempo, de una capa individual de materia de las que componen el halo. Este trabajo no incluye, por el momento, ni momento angular ni velocidades de dispersión.

Dentro de este marco teórico -que llamé *Spherical Shell Tracker (SST)*, y que podría ser traducido como *Rastreador de Capas Esféricas* - estudié en detalle la evolución del halo, obteniendo por ejemplo el momento exacto en el cual ocurre el primer cruce de capas, los valores exactos de tiempo y radio para los cuales se alcanza un cierto valor de contraste de densidad lineal y real, δ_l y δ respectivamente, el valor de ambos

contrastes de densidad en el momento en el cual se produce el colapso de acuerdo al modelo SIM sin cruce de capas, o la relación entre los contrastes de densidad lineal y real, esto es, la función $\delta_l(\delta)$. Asimismo, investigué la dependencia de la evolución del halo con su masa virial, con la fracción de masa considerada respecto a dicha masa virial, y con la cosmología para los casos de un Universo Einstein-deSitter y uno con Ω_m=0.3 y Ω_Λ=0.7. Lo que encontré es que los resultados obtenidos son muy sensibles a la variación de la masa virial o a la fracción de masa virial que se considere. Sin embargo, obtuve una dependencia totalmente despreciable con la cosmología. Por otro lado, en el mismo Capítulo muestro que el efecto del cruce de capas juega un papel fundamental en la forma en que el halo evoluciona y alcanza el equilibrio virial y su estabilización en radio. Además, discuto cómo los valores que se adoptan comúnmente en la literatura para los contrastes de densidad lineal y real podrían no ser del todo precisos. Este hecho tiene importantes implicaciones por ejemplo para una correcta definición de masa y radio viriales en el halo.

En esta Tesis, la mayor parte del trabajo realizado respecto a la detección de materia oscura, y en particular todo el trabajo que concierne a la búsqueda de aniquilación de dicha materia, se centra *únicamente* en el rango de los rayos gamma. Esto quiere decir que no se han explorado ni la antimateria ni los neutrinos como otros posibles productos de la aniquilación. Pero, ¿por qué rayos gamma y no otras longitudes de onda? El punto esencial es que la escala de energías de los productos de aniquilación viene determinada por la masa de la partículas que conforman la materia oscura, puesto que son estas las que típicamente se llevan una gran fracción de la energía de aniquilación disponible. Dado que las partículas que se barajan más seriamente como candidatas a formar la materia oscura, como el neutralino, se espera que tengan masas del orden de ∼GeV-TeV, esto explica que las búsquedas de materia oscura se lleven a cabo especialmente en la banda energética de los rayos gamma. Por otro lado, además de centrarme en dicha banda espectral, he invertido la mayor parte de mis esfuerzos de búsqueda de materia oscura en un escenario de aniquilación en el cual el neutralino es el largamente buscado WIMP (del inglés *Weakly Interacting Massive Particle*, o en español *partícula masiva débilmente interactuante*) y que además existe en suficientes cantidades como para dar cuenta de la totalidad de la materia oscura no bariónica en el Universo. Este trabajo se presenta en los Capítulos 4, 6, 8, 9. La excepción es el Capítulo 5, en el cual se abordan y estudian en detalle las perspectivas de detección para otro candidato posible (el axión), también en rayos gamma. En este caso, el método usado para la búsqueda de dicha partícula se basa en las oscilaciones entre fotones y axiones predichas por la física de partículas.

Siempre que fue posible, combiné tanto teoría como observaciones (esto último gracias a mi participación en la Colaboración MAGIC). Más en detalle, y primero en relación a mi aproximación teórica al problema, he llevado a cabo cálculos precisos del flujo de aniquilación de materia oscura para los candidatos astrofísicos más prometedores. En particular, en el Capítulo 4 se presentan las predicciones de flujo así

como las perspectivas de detección de la galaxia esferoidal Draco para un telescopio IACT típico y para el satélite Fermi. Los resultados de este trabajo han ayudado a comprender el verdadero potencial de Draco como buen candidato para las búsquedas de materia oscura así como las posibilidades reales de detección de aniquilación de materia oscura en dicha enana por parte de los IACTs actuales.

En la vertiente observacional, y como miembro activo de la Colaboración MAGIC y de su Grupo de Trabajo de Materia Oscura, he estado involucrado durante mi Tesis en las campañas observacionales llevadas a cabo con dicho telescopio para la detección de materia oscura en dos galaxias enanas: Draco (Capítulo 8) y Willman 1 (Capítulo 9). No se encontró señal gamma alguna en ninguna de estas observaciones, y los límites superiores impuestos a un posible flujo gamma no detectado parecen estar todavía lejos de una posible detección, al menos de acuerdo a las predicciones teóricas más realistas. Tampoco fue posible la exclusión de alguna porción de la región permitida del espacio de parámetros; sin embargo, estas observaciones han representado el primer intento serio de búsqueda de materia oscura en galaxias enanas satélites de la Vía Láctea con IACTs, y los límites superiores al flujo permitieron excluir al menos un alto flujo de aniquilación (propuesto por algunos trabajos en la literatura). Finalmente, ni que decir tiene que las incertidumbres en las predicciones de flujo son enormes, por lo que en cualquier caso estas observaciones con IACTs no son sólo adecuadas sino también totalmente necesarias.

Además de MAGIC, también he invertido un esfuerzo muy significativo en el experimento de I+D conocido como GAW (de las siglas en inglés de *Gamma Air Watch*) con el objetivo de llegar a hacerlo una realidad. GAW es un conjunto de 3 telescopios con tecnología IACT que estará situado en el Observatorio de Calar Alto, y que operará por encima de los $\sim$700 GeV en un futuro próximo. El principal objetivo de GAW es examinar la viabilidad de una nueva generación de IACTs que combinen una alta sensibilidad con un gran campo de visión. En particular, mi trabajo en GAW se ha centrado en la definición de los objetivos científicos del instrumento así como en la justificación de la necesidad de semejante experimento. El Capítulo 6 se dedica por entero a describir mis principales contribuciones científicas dentro de la Colaboración GAW.

En un intento de explorar otros escenarios posibles en los cuales la partícula que constituye la materia oscura es diferente del neutralino, he investigado también el papel que los axiones ultraligeros podrían desempeñar como buenos candidatos. Los resultados, que presento en el Capítulo 5, podrían ser cruciales para los experimentos actuales que operan en rayos gamma y en especial para una correcta interpretación de sus observaciones. Si dichas partículas existen y tienen masas $\sim 10^{-10}$ eV, podría ocurrir que se dieran oscilaciones fotón/axión en presencia de campos magnéticos, tales como los que se espera que existan en los Núcleos de Galaxias Activas (o AGNs, de sus siglas en inglés) o en el Medio Intergaláctico. Esto conllevaría una distorsión

significativa en el espectro de aquellas fuentes astrofísicas emisoras de rayos gamma. Por tanto, en dicho trabajo exploré de un lado las perspectivas de detección de tales distorsiones espectrales, y de otro propuse la que podría representar la mejor estrategia observacional. Dicha estrategia requeriría de un esfuerzo conjunto entre Fermi e IACTs, así como de la observación con dichos telescopios de AGNs distantes ($z > 0.1$). Además, en el mismo Capítulo también muestro cómo el papel de los axiones podría ser crítico para una correcta interpretación y modelaje de la Luz de Fondo Extragaláctica (más conocida como EBL, de sus siglas en inglés).

Finalmente, los Capítulos 10 y 11 se dedican, respectivamente, a presentar las principales conclusiones alcanzadas en la Tesis y a exponer brevemente el trabajo que se planea desarrollar en un futuro.

Para concluir, sería natural preguntarse el por qué de este enorme interés en la búsqueda indirecta de materia oscura en la banda gamma precisamente ahora, al comienzo del siglo XXI (y especialmente teniendo en cuenta que este tipo de búsquedas ya fueron propuestas hace 25 años). Hay buenas razones para ser particularmente optimistas en el presente: los experimentos actuales que operan en rayos gamma, tales como los nuevos IACTs y el satélite Fermi de la NASA, están por vez primera alcanzando sensibilidades suficientemente buenas como para ser capaces de poner a prueba algunos de los escenarios permitidos y preferidos por la comunidad astrofísica y de partículas (esto es, aquellos que obedecen las restricciones impuestas por las observaciones del satélite WMAP, aquellos que hacen uso de perfiles de densidad de materia oscura bien motivados físicamente, y aquellos que se centran en la Supersimetría). Se espera que la situación mejore aún más con la entrada en funcionamiento de la nueva generación de telescopios IACT en el futuro cercano (CTA, AGIS...). La ventana espectral de los rayos gamma acaba de abrirse a nuestros descubrimientos, y sin duda una revolución en el cielo GeV-TeV está en ciernes. Es definitivamente el momento idóneo para las búsquedas de materia oscura en rayos gamma.

Summary

In this Thesis, the main research activities are focused on the understanding of the nature of the Dark Matter (DM). In order to shed some light on this challenging topic, I used different both theoretical and observational approaches. Below I summarize my work contribution to this field.

Since the beginning of my Thesis, a large effort was devoted to understanding how Cold DM halos form and evolve within the cosmological standard model. Indeed, I focused my first work on the understanding and characterization of the outskirts of CDM halos, i.e. well beyond the virial radius. This work is presented in detail in Chapter 2, and is based in the spherical infall model (SIM) without shell crossing. In addition, I also describe in the same Chapter the framework that allows for a comparison of these predictions with the results obtained from N-body cosmological simulations. The main conclusion of this work is that SIM, despite its simplicity, is capable to provide detailed predictions that are in good agreement with simulations at least at those large radii.

An ambitious work was also started to study the formation and evolution of cold DM halos by means of an improved SIM with shell-crossing. In Chapter 3, I present a framework to tackle this effect properly, that does not involve to use any adiabatic invariant, and that is based on the numerical follow-up of an individual shell of matter with time. This work does not include, by the moment, neither angular momentum nor velocity dispersion.

Within this framework -which I named as the Spherical Shell Tracker (SST)- I studied in detail the evolution of a halo, e.g. obtaining the exact moment when the first shell-crossing occurs, the exact values of time and radius for a given value of the linear or actual density contrasts, δ_l and δ respectively, the value of both density contrasts when the collapse occurs according to the standard *SIM*, or the relation between the linear and actual density contrasts, i.e., the function $\delta_l(\delta)$. I investigated the dependence of the evolution with the virial mass, with the fraction considered respect to this virial mass, and with the cosmology for the cases of Einstein-deSitter and $\Omega_m = 0.3$, $\Omega_\Lambda = 0.7$ cosmologies. What I found is that the results are very sensible to a variation of the virial mass or the fraction of virial mass that we consider.

However, I obtain a negligible dependence with the cosmology. Furthermore, I show that the effect of shell-crossing plays a crucial role in the way that the halo evolves and reaches the virial equilibrium and the stabilization in radius. Indeed, the values currently adopted in the literature for the actual density contrast at the moment of virialization may not be accurate enough. This fact has important implications e.g. in the definition of a virial mass and a virial radius for the halo.

In this Thesis, most of the work related to DM detectability, and in particular all the work done concerning DM annihilations, is focused *only* on γ-ray searches. This means that neither antimatter nor neutrinos as other possible annihilation products were explored. But why γ-rays and not other wavelenghts? The keypoint is that the energy scale of the annihilation products is determined by the mass of the DM particles, as they typically carry a relatively large fraction of the available annihilation energy. Since the preferred DM candidates like the neutralino are expected to have masses of the order of $\sim$GeV-TeV, this explains that DM searches are specially performed in the γ-ray energy band. Furthermore, I centered most of my DM search efforts in a DM annihilation scenario where the neutralino is the long-searched for WIMP that exists in sufficient quantities to constitute the totality of the non-baryonic DM in the Universe. This work is presented in Chapters 4, 6, 8, 9. The exception is Chapter 5, in which the DM detection prospects for another plausible candidate (the axion) was studied in detail, also in γ-rays. In this case, predicted photon/axion mixings rather than self-annihilations are the vehicle used in the search of the DM particle.

Whenever possible, I combined both theory and observations, the latter being possible thanks to my participation in the MAGIC Collaboration. More in detail, and first regarding the theoretical approach, I carefully calculated the DM annihilation flux for the most promising candidates. In particular, flux predictions as well as detection prospects for a typical IACT and for the Fermi satellite for the Draco dwarf spheroidal galaxy are presented in Chapter 4. The results helped to understand the real potential of Draco as a good DM candidate and the real capabilities of the current IACTs in the search for DM in this dwarf. In the same Chapter, I also stress the crucial role of the angular resolution of the instrument in a correct interpretation of the observational data in the context of DM searches.

In the observational side, and as a member of the MAGIC Collaboration and active member of the MAGIC DM Working Group, I have been involved in the observational campaigns carried out for two dwarf galaxies: Draco (Chapter 8) and Willman 1 (Chapter 9). No gamma signal was found in any of these observations, and the derived upper limits seem to be still far from a successful detection according to theoretical predictions. An exclusion of some portion of the allowed region in the parameter space is not possible either; however, these observations represented the first serious attempt of DM searches in dwarf galaxy satellites carried out by an IACT, and the upper limits excluded a large annihilation signal at least (as claimed

by some works in the literature). Finally, needless to say that the uncertainties in the flux predictions are huge, so IACT observations are encouraged in any case.

In addition to MAGIC, I also invested a significant effort in order to launch the GAW R&D experiment. GAW is an array of 3 IACTs planned to be located at Calar Alto Observatory, that will operate above $\sim$700 GeV in the near future. The main objective of GAW is to test the feasibility of a new generation of IACTs, which combine high sensitivity with a large Field of View. I worked on the definition of the science objectives of the instrument as well as in the justification of such an experiment. Chapter 6 is devoted to GAW and to describe my main scientific contributions inside the GAW Collaboration.

In an attempt to find and explore other plausible DM scenarios where the DM particle could be different from the neutralino, I have also investigated the possible role of ultra-light axions as DM candidates. The results, presented in Chapter 5, could be crucial for current gamma-ray experiments and observations. If these particles exist and have masses $\sim 10^{-10}$ eV, photon/axion oscillations might occur in the presence of magnetic fields, such as those expected to be present in AGNs or in the Intergalactic Medium. This would lead to a distortion in the spectra of gamma-ray sources significantly, depending on source distance and the involved magnetic fields. Therefore, I did explore the detection prospects and propose the most appropriate observational strategy. This strategy would require a joint effort of Fermi and IACTs looking at distant AGNs ($z > 0.1$). Moreover, I show that axions might be critical in a correct interpretation and modeling of the Extragalactic Background Light as well.

Main conclusions of the work presented in this Thesis and future work is presented in Chapters 10 and 11 respectively.

To conclude, it would be natural to ask why this huge interest on indirect γ DM searches precisely now, at the beginning of the 21st Century (specially taking into account that these kind of searches were proposed at least 25 years ago). There are good reasons to be specially optimistic at present: current γ-ray experiments like IACTs and Fermi are reaching for the first time sensitivities good enough to be able to test some of the allowed and preferred scenarios (i.e. obeying WMAP constraints, taking well-motivated DM density profiles and using SUSY). The situation is expected to be even better when new generation telescopes enter in operation in the near future (CTA, AGIS...). The γ-ray energy window has just opened to our discoveries, and a revolution in the GeV-TeV sky is on the way. It is time for γ-ray DM searches.

Index

List of Tables

List of Figures

1

Introduction: the Dark Matter challenge

1.1 Observational evidences for Dark Matter

During the last century, a huge amount of detailed astrophysical observations of different objects at different scales seems to point to the same fact: that the luminous matter in the Universe is just a tiny fraction of its total content. Effectively, there exists a strong evidence to believe that most of the matter in our Universe is dark. While the dark matter (DM) has not been directly detected in laboratory experiments, their gravitational effects have been observed in the Universe on all spatial scales, ranging from the inner kiloparsecs of galaxies out to some Mpc and cosmological scales. The first steps in the DM paradigm were given by the astronomer F. Zwicky in the 1930s to explain the velocity dispersion in galaxy clusters. Today, the most conclusive observations in this sense come from the rotational speeds of galaxies, the orbital velocities of galaxies within clusters, gravitational lensing, the cosmic microwave background, the light element abundances and large scale structure. However, and despite these many observational indications of DM, we still do not know what is the DM made of, although it is clear that it does not consist of baryonic material. In the following we will briefly present and revisit the observational evidences for DM at all astronomical scales.

1. **Galactic scales:** the most convincing and direct evidence for DM on galactic scales comes from the observations of the rotation curves of galaxies, i.e. circular velocities of stars and gas as a function of their distance from their galactic centers. These rotation curves are usually obtained by combining observations of the 21cm line with optical surface photometry. In the 1970s, Ford and Rubin discovered that rotation curves of galaxies are flat. The velocities of objects (stars or gas) orbiting the centers of galaxies remain constant out to very large radii, rather than decreasing as a function of the distance from the galactic centers, as expected from Newtonian dynamics.

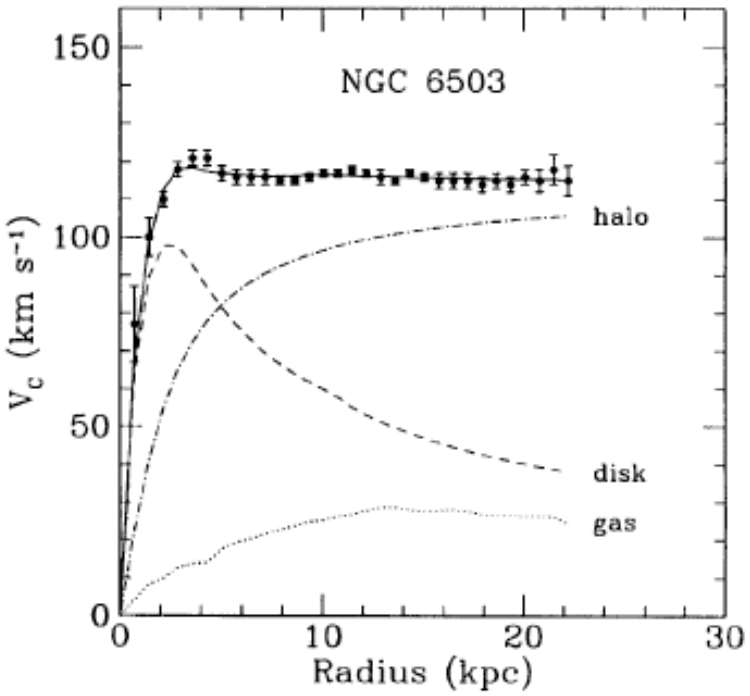

Figure 1.1 Galactic rotation curve for NGC 6503 showing disk and gas contribution plus the dark matter halo contribution needed to match the data. Figure taken from Begeman et al. (1991).

Similar flat rotation curves have been observed in all galaxies studied, including our Milky Way. The simplest explanation is that galaxies contain more mass than can be explained by the bright stellar objects residing in galactic disks. This mass provides the force to speed up the orbits. This means that the DM content in spiral galaxies seems to be independent of its luminosity: DM does not trace light. Furthermore, and in order to explain the data, galaxies must have enormous dark halos made of unknown DM. Indeed, according to recent calculations, more than 95% of the mass of galaxies consists of DM. This is illustrated in Fig. 1.1, where the velocity profile of the galaxy NGC 6503 is shown as a function of radial distance from its galactic center. The baryonic matter which accounts for the gas and disk cannot alone explain the galactic rotation curve. A good fit is obtained, however, by adding a large amount of DM. A common way to determine the amount of DM in an astrophysical object is through the *mass-to-light ratio*, M/L, typically expressed in solar units, $M_\odot/L_{odot}$. As clearly seen in Fig. 1.1, for galaxies this ratio depends on the distance to the galaxy center, with typical values for spirals galaxies $\sim M/L = 10$ at 10 kpc.

The limitations of rotations curves are that they can only be measured up to distances of some tens of kpc, since the observations are based on the distribution of light or neutral hydrogen (21 cm). Therefore, we are only obtaining information about the very inner parts of DM haloes, and nothing about those places where most of the DM is (lensing experiments or satellite dynamics can skip these limitations, as I will discuss below). Because of that, the total amount of DM present is difficult to quantify. However, despite the uncertainties of the slope in the innermost regions of galaxies, rotation curves of disk galaxies provide strong evidence for the existence of a spherical DM halo. Additional evidence for DM at galactic scales comes from mass modeling of the most detailed rotation curves available, such as spiral arm features. Other galaxies also show evidence for DM via strong gravitational lensing (Koopmans & Treu 2003). In addition, X-ray evidence reveals the presence of extended atmospheres of hot gas that fill the DM halos of isolated ellipticals and whose hydrostatic support provides evidence for DM as well (Fabian & Allen 2003). Lensing measurements also confirm the existence of enormous quantities of DM in galaxies. The Sloan Digital Sky Survey used weak lensing (statistical studies of lensed galaxies) to conclude that galaxies, including the Milky Way, are even larger and more massive than previously thought, and require even more DM out to great distances (Adelman-McCarthy et al. 2006). This technique can study the DM distribution to much larger distances than could be probed by rotation curves: the DM is seen in galaxies out to 200 kpc from their centers.

There are other observations both on subgalactic and intergalactic scales that point in the same direction, i.e. that a large amount of DM is needed in order to explain the observed properties. We can cite some of them, as compiled in Bertone (2005):

- Weak modulation of strong lensing around individual massive elliptical galaxies. This provides evidence for substructure on scales of $\sim 10^6\ M_\odot$ [Metcalf et al. 2004; Moustakas & Metcalf 2003).
- The so-called Oort discrepancy in the disk of the Milky Way (see e.g. Bahcall et al. 1992). The argument follows an early suggestion of Oort, inferring the existence of unobserved matter from the inconsistency between the amount of stars, or other tracers in the solar neighborhood, and the gravitational potential implied by their distribution.
- Weak gravitational lensing of distant galaxies by foreground structure (see e.g. Hoekstra et al. 2002).
- The velocity dispersions of dwarf spheroidal galaxies which imply mass-to-light ratios larger than those observed in our "local" neighborhood. While

the profiles of individual dwarfs show scatter, there is no doubt about the overall DM content (see Vogt et al. 1995; Mateo 1998; Strigari et al. 2008).

- The velocity dispersions of galaxy satellites which suggest the existence of DM halos around their host galaxies, similar to our own, extending at galactocentric radii larger than 200 kpc, i.e. well beyond the optical disc. This applies in particular to the Milky Way, where both dwarf galaxy satellites and globular clusters probe the outer DM halo (Zaritsky et al. 1997; Prada et al. 2003).

2. **Galaxy Clusters scales:** In 1933, F. Zwicky inferred, from measurements of the velocity dispersion of galaxies in the Coma cluster, a mass-to-light ratio of around 400 solar masses per solar luminosity (Zwicky 1933). This was the first modern hint of the presence of large amounts of DM in the Universe. At present, observations of galactic clusters continue to be of central importance in understanding the DM problem. Today, most dynamical estimates (Bahcall & Fan 1998; Kashlinsky 1998, Carlberg et al. 1999) are consistent with a value of $M/L \sim 200 - 300$ on cluster scales. Another piece of gravitational evidence for DM in clusters is the existence of huge amounts of hot gas in the intracluster medium. This can be clearly seen in the top panels of Fig. 1.2 for the Coma Cluster. The existence of this gas in the cluster can only be explained by a large DM component that provides the potential well to hold on to the gas. Similar findings were recently discovered in the famous Bullet cluster (see right bottom panel in Fig. 1.2).

   That individual galaxies and galaxy clusters are completely dominated by DM with the visible baryonic matter being subdominant is demonstrated without doubt also in analyses of strong lensing of background galaxies (Tyson et al. 1998) (see left bottom panel in Fig. 1.2 The gravitational lensing analysis of (Falco et al. 1998), based on the frequency of double images in large surveys of quasars, indicates that there is plenty of DM. Also observations of the Lyman-α forest (Weinberg et al. 1999), combined with the observed mass function of galaxy clusters, clearly need from a substantial amount of non-baryonic DM. Still on very large scales, analyses of the peculiar velocity "flow" of large clusters and other structures seem to need a lot of DM for its explanation (Sigal et al. 1998). It is interesting to note that cluster mass estimates based on gravitational lensing, X-ray emission, the SZ effect and galaxy motions all give similar mass estimates within about a factor of two.

3. **Cosmological scales:** Further evidence for DM comes from measurements on cosmological scales of anisotropies in the CMB (Spergel et al. 2007). Given the relevance of the CMB for the present status of Cosmology, this issue will be discussed in detail in Section 1.2.2). Also the Sunyayev-Zel'dovich (SZ) effect can be used to extract the amount on non-baryonic DM, by which the CMB

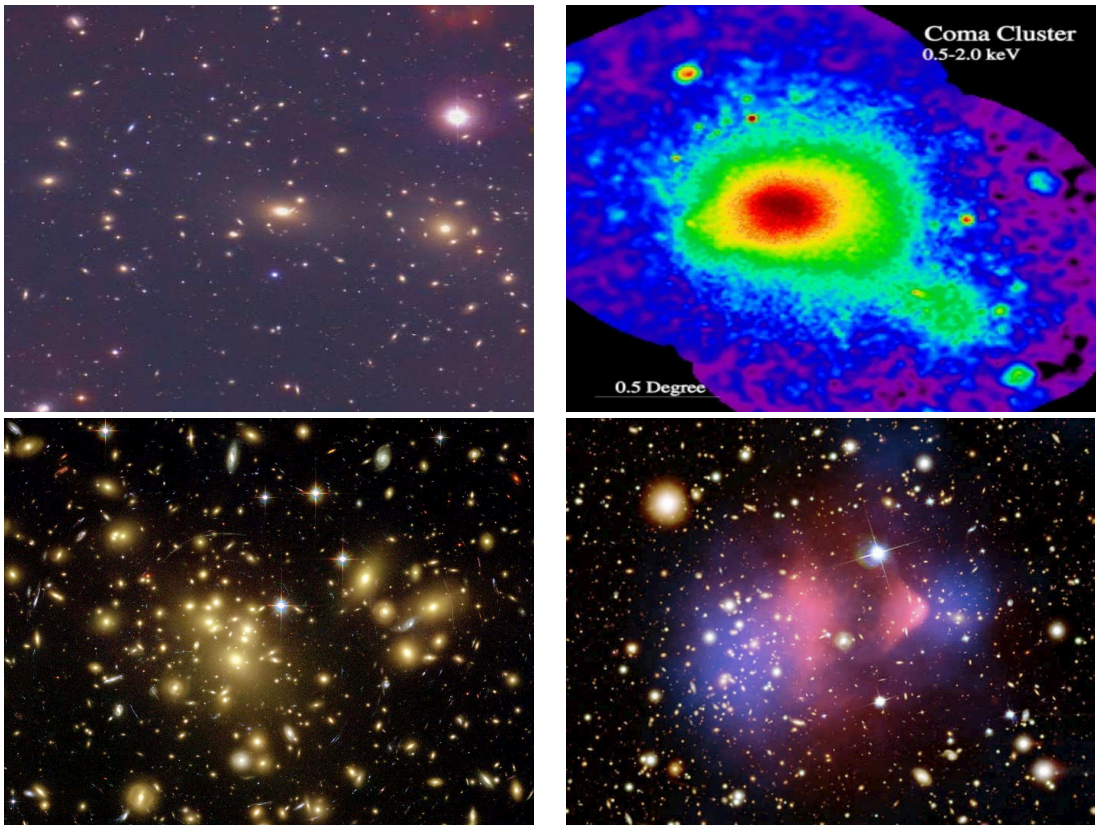

Figure 1.2 *Top panels:* Without dark matter, the hot gas in the Coma Cluster would evaporate. Optical image in the left; X-ray image from ROSAT satellite in the right (Briel & Henry 1997). *Left bottom panel:* A good example of strong gravitational lensing is the Abell 1689 galaxy cluster. *Right bottom panel:* A collision of galactic clusters (the Bullet cluster) shows baryonic matter (pink) as separate from dark matter (blue), whose distribution is deduced from gravitational lensing (Clowe et al. 2006).

gets spectrally distorted through Compton scattering on hot electrons in galaxy clusters. With present SZ data, it is estimated that ∼25% of the Universe is in the form of DM (Holder and Carlstrom 1999). In addition, recent predictions for the primordial nucleosynthesis exactly match the data as long as atoms are only 4% of the total constituents of the Universe.

1.2 The ΛCDM paradigm

Nowadays, most of the astrophysical community seems to agree in a standard cosmological picture of the Universe, the so-called ΛCDM paradigm (from Λ Cold Dark Matter). This general picture did not emerge suddenly; on the contrary, it has to be understood as the final result obtained after more than 80 years of continuous debate both in the observational and theoretical side. This scenario, based on General

Relativity, is now capable to explain in general terms the observations, as well as to reconcile them with a congruent theoretical picture of the Universe as a whole and of its evolution.

In the ΛCDM paradigm, the geometry of the Universe is flat (i.e. euclidean) and its energy-density is distributed in ∼4% baryonic matter, ∼23% of still unknown non-baryonic dark matter and roughly 73% of a even more mysterious dark energy. This paradigm is settled in the *Big Bang* scenario, in which the Universe had a beginning in time and is as a system evolving from a highly compressed state existing around 10^{10} years ago. The Big Bang has its roots in the important discoveries of E. Hubble in the 1920s, who realized that all galaxies seem to move away from us. The Big Bang theory, and more in general, the ΛCDM scenario, has survived to all kinds of tests and observations until now. Indeed, this huge theoretical and observational effort to refute the model has derived in a even stronger and extremely sophisticated cosmological scenario, that allows us to explain in a satisfactory way the thermal history, relic background radiation, abundance of elements, large scale structure (LSS) and many other properties of the Universe. Nevertheless, our knowledge is still partial, and there are indeed a lot of open questions that the model will have to face in the coming years.

1.2.1 A brief mathematical description of the model

The fundamental equation in the ΛCDM paradigm, that comprises the symmetry of the problem (metrics), specify the physical properties of matter and energy content (equation of state) and, more importantly, relates the geometry of the Universe with its matter and energy content (Einstein equations) can be written as (see e.g. Bertone 2005 or Bergström 2000):

$$R_{\mu\nu} - \frac{1}{2} g_{\mu\nu} R = -\frac{8\pi G_N}{c^4} T_{\mu\nu} + \Lambda g_{\mu\nu} \tag{1.1}$$

where $R_{\mu\nu}$ and R are, respectively, the Ricci tensor and scalar (obtained by contraction of the Riemann curvature tensor). $g_{\mu\nu}$ is the metric tensor, G_N is Newton's constant, $T_{\mu\nu}$ is the energy-momentum tensor, and Λ is the so-called cosmological constant. The key point of this equation, which is also the key concept of General Relativity, is to understand that the *the geometry of the Universe*, represented by the left-hand-side, *is determined by its energy content*, as given by the energy-momentum tensor that appears on the right-hand-side.

The cosmological constant Λ represents a "vacuum energy" associated with space-time itself, rather than its matter content, and is a source of gravitational field even in the absence of matter. The contribution of such "vacuum energy" to the total energy of the Universe seems to be crucial, attending to the analyses of type Ia supernovae and the estimations of the cosmological parameters from the CMB.

To solve the above equation it is necessary to introduce a symmetry for the problem. Cosmologists typically suppose *homogeneity* and *isotropy* for the whole Universe, as confirmed by the most recent observations. This simplifies a lot the mathematical analysis. High isotropy is supported for example by CMB data; homogeneity at scales $\gtrsim$100 Mpc seems to be very near reality according to recent galaxy surveys like SDSS (Tegmark et al. 2004) or 2dF-GRS (Cole et al. 2005). With isotropy and homogeneity, the line element can be expressed as:

$$ds^2 = -c^2\mathrm{d}t^2 + a(t)^2\left(\frac{\mathrm{d}r^2}{1-kr^2} + r^2\mathrm{d}\Omega^2\right), \tag{1.2}$$

where $a(t)$ is the so-called *scale factor* and the constant k, describing the spatial curvature, can take the values $k = -1,\ 0,\ +1$ (which means open, flat and closed universe respectively). Given this metric, it is possible to solve the Einstein equations and get the Friedmann equation:

$$H^2 \equiv \left(\frac{\dot{a}}{a}\right)^2 + \frac{k}{a^2} = \frac{8\pi G_N}{3}\rho_{tot} + \frac{\Lambda}{3} \tag{1.3}$$

where ρ_{tot} is the total average energy density of the universe, and H is the Hubble parameter. The most recent value achieved for the Hubble parameter at present time, also known as H_0 or Hubble constant, is $H_0 = 72 \pm 1$ km s^{-1} Mpc^{-1} (Hinshaw et al. 2009). In Eq. 1.3, the Universe is flat ($k = 0$) provided that the energy density equals the *critical density*, ρ_c, i.e.:

$$\rho_c \equiv \frac{3H^2}{8\pi G_N} \quad . \tag{1.4}$$

The abundance of a substance in the Universe (matter, radiation or vacuum energy) is usually expressed in units of ρ_c. Let us define the quantity Ω_i of a substance of species i and density ρ_i as $\Omega_i \equiv \frac{\rho_i}{\rho_c}$. At the present epoch, we have for the matter, cosmological constant, radiation and curvature respectively:

$$\Omega_m \equiv \frac{8\pi G_N \rho_m}{3H_0^2} \qquad \Omega_\Lambda \equiv \frac{\Lambda}{3H_0^2} \tag{1.5}$$

$$\Omega_r \equiv \frac{8\pi G_N \rho_r}{3H_0^2} \qquad \Omega_k \equiv \frac{-k}{a_0^2 H_0^2} \tag{1.6}$$

Following with these sort of definitions, it is also useful $\Omega = \sum_i \Omega_i$. Therefore, now we can rewrite the Friedmann equation for the present epoch simply as $1 = \Omega_m + \Omega_\Lambda + \Omega_r$, where the radiation contribution is typically neglected due to its tiny value today ($\sim 10^{-5}$).

By the other side, the expansion of the Universe means that the scale factor $a(t)$ has been increasing since the earliest times after the Big Bang. This affects the light

emitted by distant objects. In particular, for an emitted wavelength λ_{emit} and an observed wavelength λ_{obs}, the redshift z is given by:

$$1 + z \equiv \frac{\lambda_{obs}}{\lambda_{emit}}. \tag{1.7}$$

Finally, and as noted in Bergstrom (2000), the Ω_i evolve with time differently, depending on the equation of state of the component. A general expression for the expansion rate of the Universe is:

$$\frac{H^2(z)}{H_0^2} = \left[\Omega_\Lambda (1+z) + \Omega_K (1+z)^2 + \Omega_M (1+z)^3 + \Omega_R (1+z)^4\right] \tag{1.8}$$

z being the redshift.

1.2.2 Cosmological parameters

Although the observational evidence for the existence of DM is huge (as discussed in previous sections), it is not possible from those observations to determine the total amount of DM in the Universe. Fortunately, this information can be extracted from the Cosmic Microwave Background (CMB). Effectively, the analysis of CMB anisotropies allows us to derive the cosmological parameters with a high level of precision. The method consist on obtaining the best-fit parameters from a likelihood analysis starting with a cosmological model with a fixed number of (cosmological) parameters.

The existence of background radiation (the CMB) originating from the propagation of photons in the early Universe (once they decoupled from matter) was already predicted by G. Gamow in 1948, but it was not until 1965 when it was discovered by A. Penzias and R. Willson from Bell Laboratories in a kind of scientific *serendipity*[1]. The CMB is very isotropic, with tiny fluctuations in temperature of the order of 10^{-5} and follows with extraordinary precision the spectrum of a black body corresponding to a temperature T $\sim$ 2.726 K. These tiny fluctuations are of vital importance, however, since they reflect real initial matter density deviations from the mean density at that early epoch. Therefore, it is possible to extract crucial cosmological information from them. Fluctuations in the CMB were first observed by the COBE satellite in 1990 (see final COBE results in Fixsen et al. 1996). Later, in 2001, CMB anisotropies were measured with an unprecedent precision by the WMAP satellite (see Hinshaw et al. 2009 for the most recent release). In Fig. 1.3 the anisotropies maps as observed by both satellites are shown. I refer here to Lin & Wandelt (2006) for a good review on CMB measurements and analysis.

Not only WMAP but also other several instruments and groups are presently working in order to estimate the cosmological parameters by using different techniques, such as Baryonic Acoustic Oscillations (BAO), SDSS and 2dF-GRS surveys

[1] http://en.wikipedia.org/wiki/Serendipity

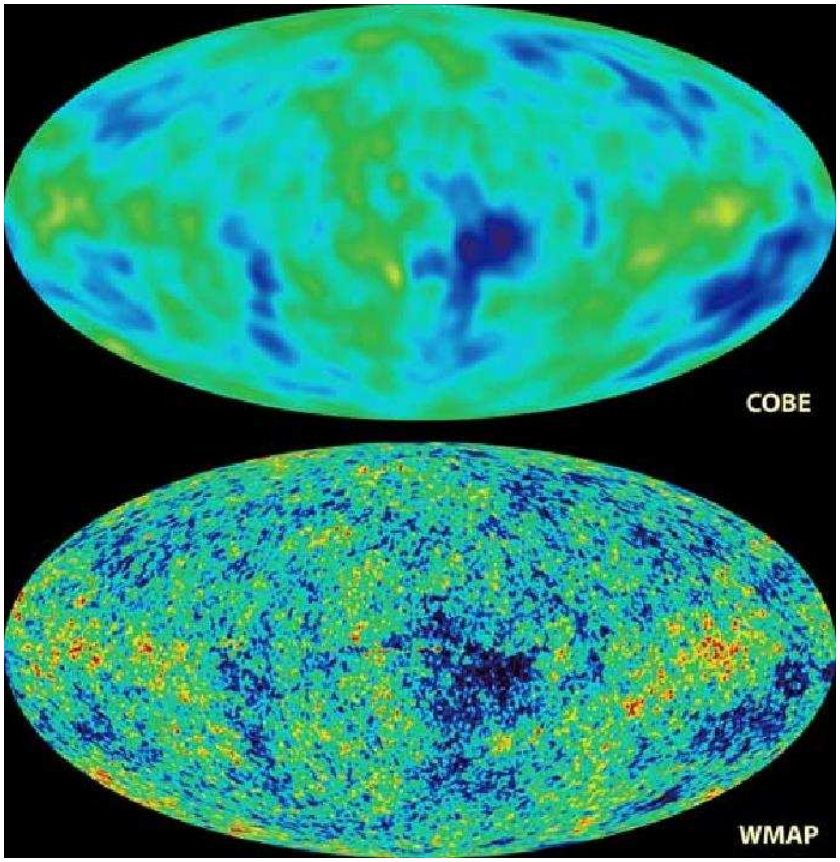

Figure 1.3 CMB anisotropy maps (i.e. maps of temperature fluctuations), as obtained by the COBE satellite (top) and by the more recent WMAP (bottom). Credit: NASA.

data, detailed observations of distant Supernova type Ia, etc. Indeed, observations carried out by the Supernova Cosmology Project and the High-z Supernova Search Team in the last 1990s represented the first solid evidence of the (now almost undoubted and well established and accepted) fact that the Universe is accelerating (Riess et al. 1998; Perlmutter et al. 1999), which was interpreted as due to a cosmological constant Λ or, more generically, to a "dark energy" dominant component in the Universe. Figure 1.4 (actually a table) summarizes the cosmological parameters as deduced for the WMAP team after the analysis of 5-years CMB data obtained with this satellite (Hinshaw et al. 2009). Also shown are the cosmological parameters deduced when crossing WMAP results with those obtained from BAO and supernovae. This Table represents the most refined ΛCDM cosmological model available at present, i.e. the 21st century state-of-the-art Cosmology. Nevertheless, it is expected that the Planck satellite, which was successfully launched last May, 14th 2009 and which represents the natural WMAP successor, improves these records even more[2].

[2]http://sci.esa.int/science-e/www/area/index.cfm?fareaid=17

Description	Symbol	*WMAP*-only	*WMAP*+BAO+SN
Parameters for Standard ΛCDM Model [a]			
Age of universe	t_0	13.69 ± 0.13 Gyr	13.73 ± 0.12 Gyr
Hubble constant	H_0	$71.9^{+2.6}_{-2.7}$ km/s/Mpc	70.1 ± 1.3 km/s/Mpc
Baryon density	Ω_b	0.0441 ± 0.0030	0.0462 ± 0.0015
Physical baryon density	$\Omega_b h^2$	0.02273 ± 0.00062	0.02265 ± 0.00059
Dark matter density	Ω_c	0.214 ± 0.027	0.233 ± 0.013
Physical dark matter density	$\Omega_c h^2$	0.1099 ± 0.0062	0.1143 ± 0.0034
Dark energy density	Ω_Λ	0.742 ± 0.030	0.721 ± 0.015
Curvature fluctuation amplitude, $k_0 = 0.002$ Mpc^{-1} [b]	$\Delta^2_{\mathcal{R}}$	$(2.41 \pm 0.11) \times 10^{-9}$	$(2.457^{+0.092}_{-0.093}) \times 10^{-9}$
Fluctuation amplitude at $8h^{-1}$ Mpc	σ_8	0.796 ± 0.036	0.817 ± 0.026
$l(l+1)C^{TT}_{220}/2\pi$	C_{220}	5756 ± 42 μK^2	5748 ± 41 μK^2
Scalar spectral index	n_s	$0.963^{+0.014}_{-0.015}$	$0.960^{+0.014}_{-0.013}$
Redshift of matter-radiation equality	$z_{\rm eq}$	3176^{+151}_{-150}	3280^{+88}_{-89}
Angular diameter distance to matter-radiation eq.[c]	$d_A(z_{\rm eq})$	14279^{+186}_{-189} Mpc	14172^{+141}_{-139} Mpc
Redshift of decoupling	z_*	1090.51 ± 0.95	$1091.00^{+0.72}_{-0.73}$
Age at decoupling	t_*	380081^{+5843}_{-5841} yr	375938^{+3148}_{-3115} yr
Angular diameter distance to decoupling [c,d]	$d_A(z_*)$	14115^{+188}_{-191} Mpc	14006^{+142}_{-141} Mpc
Sound horizon at decoupling [d]	$r_s(z_*)$	146.8 ± 1.8 Mpc	145.6 ± 1.2 Mpc
Acoustic scale at decoupling [d]	$l_A(z_*)$	$302.08^{+0.83}_{-0.84}$	$302.11^{+0.84}_{-0.82}$
Reionization optical depth	τ	0.087 ± 0.017	0.084 ± 0.016
Redshift of reionization	$z_{\rm reion}$	11.0 ± 1.4	10.8 ± 1.4
Age at reionization	$t_{\rm reion}$	427^{+88}_{-65} Myr	432^{+90}_{-67} Myr
Parameters for Extended Models [e]			
Total density [f]	$\Omega_{\rm tot}$	$1.099^{+0.100}_{-0.085}$	1.0052 ± 0.0064
Equation of state [g]	w	$-1.06^{+0.41}_{-0.42}$	$-0.972^{+0.061}_{-0.060}$
Tensor to scalar ratio, $k_0 = 0.002$ Mpc^{-1} [b,h]	r	< 0.43 (95% CL)	< 0.20 (95% CL)
Running of spectral index, $k_0 = 0.002$ Mpc^{-1} [b,i]	$dn_s/d\ln k$	-0.037 ± 0.028	$-0.032^{+0.021}_{-0.020}$
Neutrino density [j]	$\Omega_\nu h^2$	< 0.014 (95% CL)	< 0.0065 (95% CL)
Neutrino mass [j]	$\sum m_\nu$	< 1.3 eV (95% CL)	< 0.61 eV (95% CL)
Number of light neutrino families [k]	$N_{\rm eff}$	> 2.3 (95% CL)	4.4 ± 1.5

Figure 1.4 Cosmological parameters obtained after 5 years of WMAP observations (third column) and after crossing the 5-years WMAP results with other techniques (Barionic Acoustic Oscillations and Supernovae; fourth column), as presented in Hinshaw et al. (2009). See this same work for more details.

1.2.3 Structure formation

In the hierarchical scenario for structure formation in the Universe, the small primordial density fluctuations grow due to non-linear gravitational evolution and finally become the first virialized structures (halos). In this picture, larger Cold Dark Matter (CDM) halos will be formed by the accretion and merger of those first smaller halos, forming in this way massive structures, and so on. This bottom-up scenario, that constitutes the actual paradigm of hierarchical structure formation, is able to explain in general terms the Large Scale Structure (LSS) in the Universe that we see today.

In the previous section, it was discussed that values of $\Omega_m \sim 0.26$ and $\Omega_\Lambda \sim 0.74$ give the best fits to cosmological data coming from several observations. It is notorious that also the observed LSS, as mapped by large sky surveys like the Sloan Digital Sky Survey (SDSS; Tegmark et al. 2004) or 2dF-GRS (Cole et al. 2005), point to the same direction (Sánchez et al. 2006). Furthermore, there is an important question related to LSS that can help to clarify why the ΛCDM scenario needs from non-baryonic dark matter, and why this has to be cold. Indeed, LSS can be seen as one of the strongest arguments in favour of CDM. As discussed e.g. in Bergström (2000), it becomes very difficult to bridge the epoch of the emission the CMB (∼300000 years after the Big Bang) and that of formation of LSS in the Universe without the help of non-baryonic matter: the measured anisotropy of the CMB, at the level of a few times 10^{-5}, represents the imprint of the density perturbations in the Universe at that epoch (z∼1100). The gravitational instability caused the (linear with the scale factor, at that time) growth of these primordial and tiny fluctuations with time. But this growth is only possible in a matter-dominated Universe, which for baryons only (i.e. without non-baryonic DM) happened roughly at the time when the CMB was emitted. Since many structures that we can see today are highly non-linear and are much evolved than the factor 1100 that the linear growth could yield, it is difficult to understand how they can exist. Non-baryonic DM helps since, if it exists, matter domination occurred earlier, causing also the perturbations to start to grow earlier. In this way, once the baryons decoupled from photons after the CMB epoch, they could fall into the gravitational wells already formed by the non-baryonic DM.

Moreover, in structure formation not only the amount of DM is important, but also the type of DM particle. If the particle is very light (e.g. neutrinos), it will be relativistic at the time structure starts to form and will free-stream out of galaxy-sized overdense regions, so that only very large structures can form early. This kind of DM is known as Hot Dark Matter (HDM), and leads to an up-bottom hierarchical structure formation scenario in which large structures form early and smaller structures (such as galaxies) form some time later by fragmentation. However, this scenario is strongly disfavored by the observed distribution of galaxies at different redshifts as measured by the largest surveys (SDSS, 2dF; see Fig. 1.5). Nevertheless, this does not mean that a HDM contribution to Ω_m up to ∼10% can be excluded.

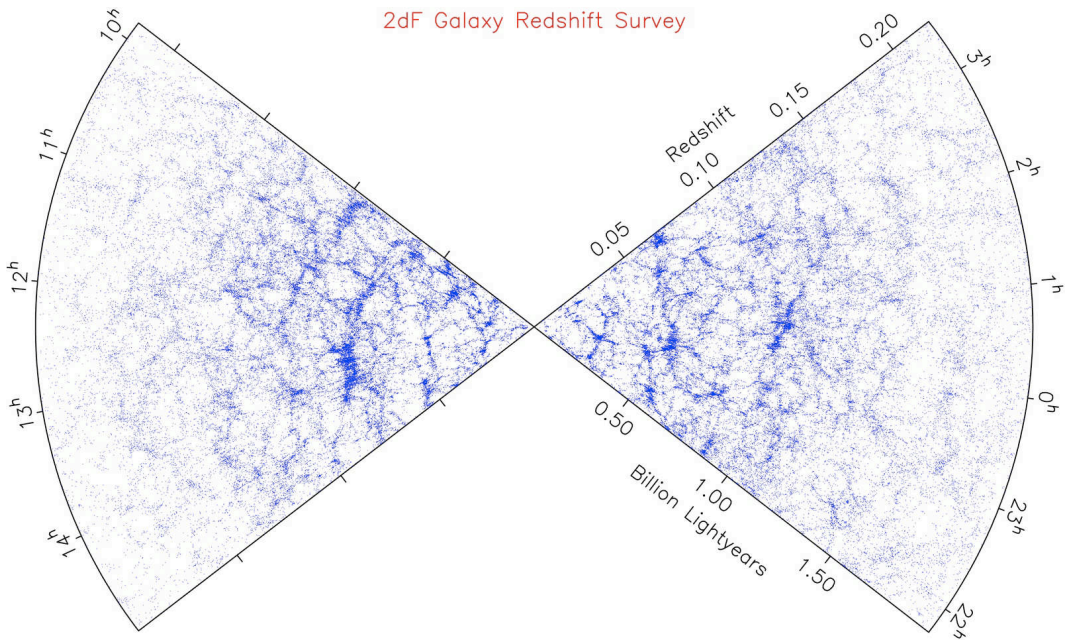

Figure 1.5 The Large Scale Structure of the Universe, as observed by the 2dF Galaxy Redshift Survey. Each of the blue points represents a galaxy. Earth is at the center.

In the case of massive particles (∼GeV or more), they are expected to move with non-relativistic velocities when they decoupled from radiation in the early Universe, and can therefore clump also on smaller scales[3]. This is Cold Dark Matter (CDM) and provides the kind of structure formation scenario preferred by observations, i.e. small clumps merging in larger ones, forming galaxy halos and successively larger structures (see Fig. 1.6). Finally, also Warm Dark Matter (WDM), made of ∼keV particles, could exist. However, WDM is not very favored at the moment, both for particle physics and structure formation reasons.

1.2.4 Problems to be solved. Any alternative scenario?

There is no doubt that the ΛCDM cosmological model is a well defined, simple and predictive model which is consistent with most of current cosmological observations. Effectively, observations seem to point to a Universe that has entered a phase of accelerating expansion, i.e. a Universe where the role of dark energy is crucial to understand its evolution. As discussed, we have direct geometrical probes: standard candles like SN Ia (e.g. Riess et al. 1998, Perlmutter et al. 1999b, Wood-Vasey et al. 2007, Kowalsky et al. 2008), gamma-ray bursts (Amati 2006) and standard rulers like the CMB sound horizon (Wang & Mukherjee 2006); and dynamical probes:

[3]There are particles, like the axion, which can behave like CDM although they are indeed very light, due to the non-thermal way they were produced.

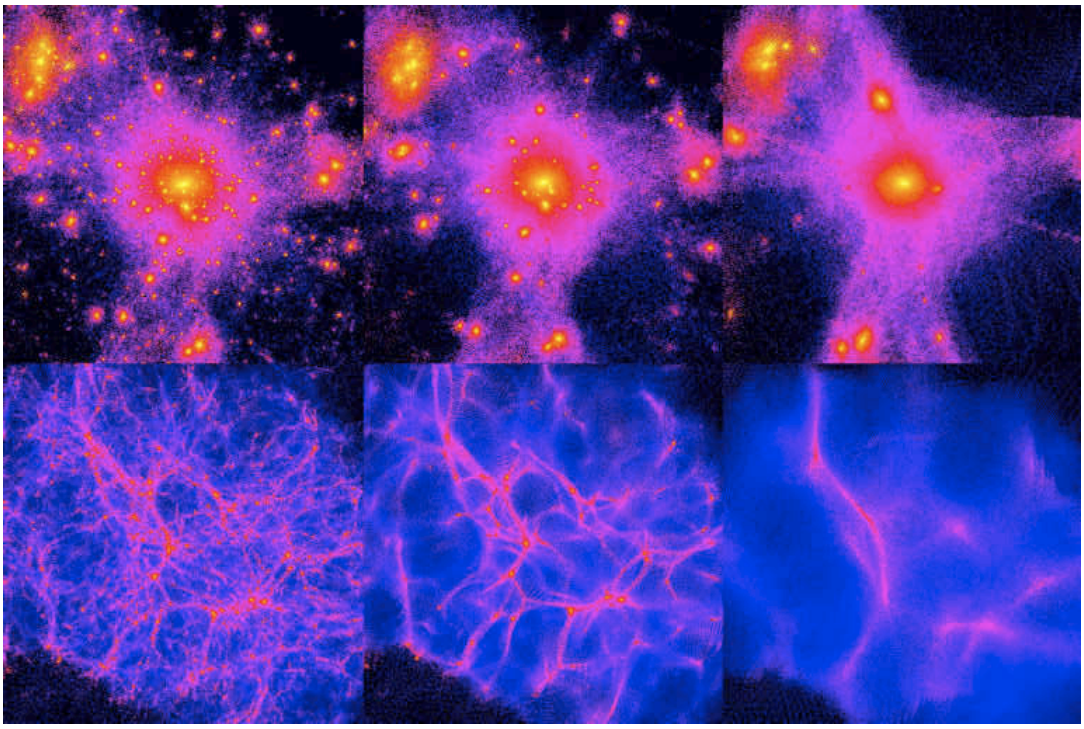

Figure 1.6 CDM is needed in order to obtain the kind of bottom-up hierarchical structure formation favored by present observations (see Fig. 1.5), as well as to explain the abundances of substructure in the Universe. *From left to right*: LSS with CDM, WDM and HDM, see text for details. Credit: B. Moore.

growth rate of cosmological perturbations (Polarski & Gannouji 2008) probed by the redshift distortion factor or by weak lensing (Munshi et al. 2008). However, there are some specific observations which differ from the predictions of the ΛCDM scenario (with those cosmological parameters given by 5-years WMAP data) at a level of 2σ or higher, such as (Perivolaropoulos 2008):

- *Large Scale Velocity Flows*: ΛCDM predicts significantly smaller amplitude and scale of flows than what observations indicate (e.g. Watkins et al. 2008, Kashlinsky et al. 2008).
- *Brightness of Type Ia Supernovae (SNIa) at High Redshift*: ΛCDM predicts fainter SNIa at high z (Perivolaropoulos & Shafieloo 2008).
- *Emptiness of Voids*: ΛCDM predicts more dwarf or irregular galaxies in voids than observed (e.g. Tikhonov & Klypin).
- *Profiles of Cluster Haloes*: ΛCDM predicts shallow low concentration and density profiles in contrast to observations which indicate denser high concentration cluster haloes (Broadhurst et al. 2008).

- *Profiles of Galaxy Haloes*: ΛCDM predicts halo mass profiles with cuspy cores and low outer density while lensing and dynamical observations indicate a central core of constant density and a flattish high dark mass density outer profile (de Blok 2005; Gentile et al. 2005).

- *"Missing satellites problem"*: N-body ΛCDM cosmological simulations seem to give much more substructure of DM within clusters and galactic halos than what is observed (e.g. Klypin et al. 1999). It is not clear, however, how serious these problems are in view of the large uncertainties and different results obtained by different groups working in the field. Moreover, the recent discoveries of ultrafaint dwarfs in the Milky Way halo may alleviate this problem considerably (see Kravtsov 2009 for a recent review on this issue).

- *Sizable Population of Disk Galaxies*: ΛCDM predicts a smaller fraction of disk galaxies due to recent mergers expected to disrupt cold rotationally supported disks (Bullock et al. 2008).

Not all the above mentioned problems have probably similar importance. Perhaps the most difficult ones are those related with the rotation in the inner parts of spiral galaxies, where the theory predicts too much DM inside the central ~ 1 kpc (Moore 1994, Flores & Primack 1994, de Blok et al. 2001). Some solutions have been proposed to this problem (see e.g. Valenzuela et al. 2007), but still the description of what happens at small scales is the strongest challenge the ΛCDM cosmological model has encountered.

There are also some weak points from the theoretical point of view concerning the ΛCDM model (e.g. Copeland et al. 2006):

- *The Fine Tuning Problem*: What is the physical mechanism that sets the value of Λ to its observed value which is 120 orders of magnitude smaller than the physically anticipated value, i.e. the natural energy scale of Quantum Gravity?

- *The Coincidence Problem*: Why is the energy density corresponding to the cosmological constant just starting to dominate the Universe at the present cosmological time?

Even though some of the above given puzzles may be resolved by more complete observations or with conventional astrophysics still inside the standard model, more fundamental modifications of the ΛCDM model should not be excluded at present. A significant effort has been made for several people in order to build alternative cosmological models. That is the case of Modified Newtonian Dynamics (MOND), initially proposed by Milgrom (1983) to explain the rotation of galaxies without DM. According to MOND, the rotation curves in the outer regions of galaxies do not decline because the force of gravity is significantly stronger than for Newtonian gravity.

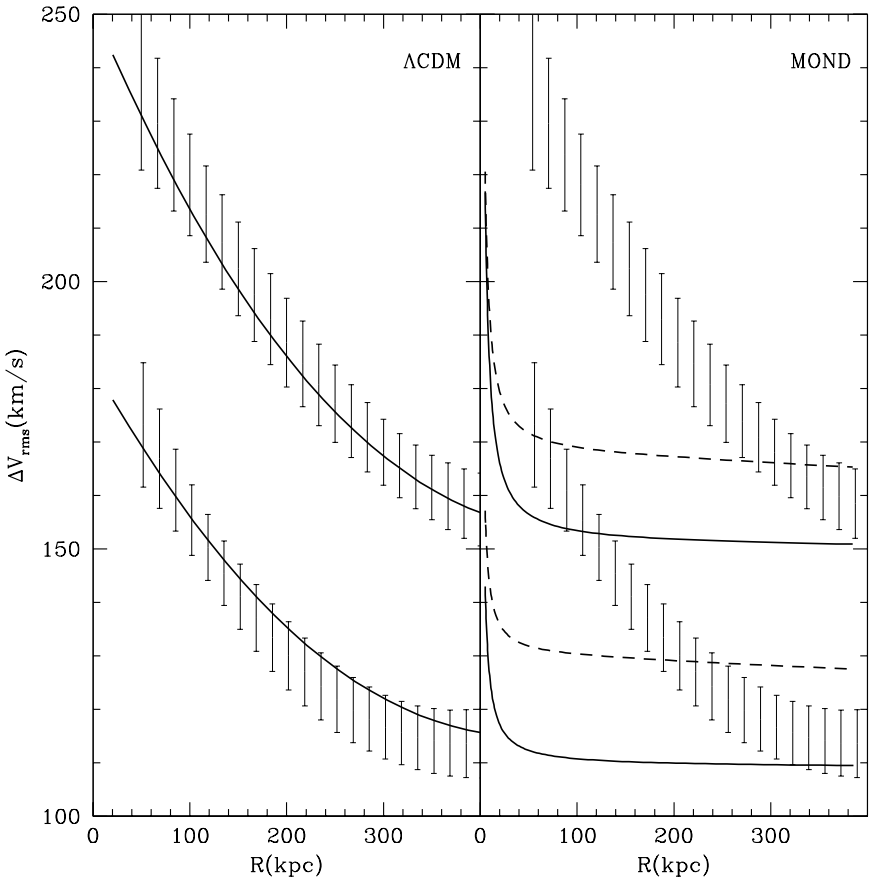

Figure 1.7 The line-of-sight velocities of 5000 galaxies. The vertical lines indicate 68% confidence levels. *Left panel*: predictions (full curves) of the ΛCDM model for galaxies hosted by DM halos with maximum circular velocities of $\sim$ 340 km/s (top curve) and $\sim$ 270 km/s (bottom curve). *Right panel*: MOND predictions (see Klypin & Prada 2009 for a detailed description of this particular analysis). As clearly seen, MOND has big problems to fit the data, while the ΛCDM model makes quite reasonable predictions. Figure taken from Klypin & Prada (2009).

As pointed out in Baltz (2004), because present gravitational lensing mass estimates agree with dynamical estimates, the MOND acceleration scale must apply to photons as well. This means that a relativistic theory is needed in any case to build a consistent cosmological model. There were several attempts in the past for MOND, each with fatal inconsistencies (Bekenstein & Milgrom 1984, Bekenstein 1988, Soussa & Woodard 2003). Only recently, Bekenstein proposed a relativistic version called *TeVeS* (Bekenstein 2004), capable to make predictions of crucial observational phenomena. However, in this new framework, rotation curves of some galaxies cannot be explained by MOND and also other incongruences appeared, such as the RMS ve-

locities of stars in some dwarf spheroidal galaxies (Lokas et al. 2006). Still, the most important problems for MOND are those related to clusters of galaxies. Dynamics of galaxies in clusters cannot be explained by MOND and requires introduction of DM, possibly in the form of a massive ($\sim$ 2eV) neutrino (Sanders et al. 2002). In Fig. 1.7 a comparison between those predictions coming from the ΛCDM model and those coming from MOND for a specific astrophysical case is shown.

Despite the problems of MOND (which is only the most famous among all the possible alternative proposed scenarios to ΛCDM), the key point of this subsection, however, remains completely valid: there is no simple cosmological model which does not have problem with at least some sets of data. Therefore, it is worth keeping several possibilities open, while awaiting data of even higher precision that helps to refine even more the ΛCDM model or to build new and testable theoretical frameworks to be explored.

1.3 Dark Matter and N-body cosmological simulations

Although we are confident to have reached a general picture of large scale structure (LSS), our understanding is still far from to be completed. The description of the evolution of structures from primordial density fluctuations, is complicated by the action of many physical processes like gas dynamics, radiative cooling, photoionization, recombination and radiative transfer. The most widely adopted approach to the problem of LSS formation involves the use of N-body cosmological simulations (see Bagla 2005 for a review). The first simulation was performed by Holmberg (1941) on interacting galaxies. He used an analog optical computer. At present, high resolution simulations make full use of the tremendous computational power available.

In Cosmology, the evolution of structure is often approximated with non-linear gravitational clustering from specified initial conditions of DM particles and can be refined by introducing the effects of gas dynamics, chemistry, radiative transfer and other astrophysical processes. In principle, N-body simulations are simple, since they just involve integrating the 6N ordinary differential equations defining the particle motions in Newtonian gravity. In practice, the problem is the huge number N of particles (the highest resolution simulations at present include many millions, see Fig. 1.8). Since the number of interactions needing to be computed is proportional to N^2, ordinary methods of integrating numerical differential equations are inadequate. Therefore, a number of refinements are commonly used. By the other side, many simulations simulate only CDM ($\sim$5/6 of the total matter content of the Universe), and therefore include only the gravitational force. Incorporating baryons in the simulations dramatically increases their complexity. A large effort is being carried out at present by several groups in order to successfully implement them in the simulations, since they are expected to be crucial in the understanding of astrophysical processes such as galaxy formation.

The reliability of an N-body simulation is measured by its mass and length resolu-

tion. The mass resolution is specified by the mass of the smallest ("elementary") particle considered, being the scale below which fluctuations become negligible. Length resolution is limited by the so-called softening scale, introduced to avoid infinities in the gravitational force when elementary particles collide.

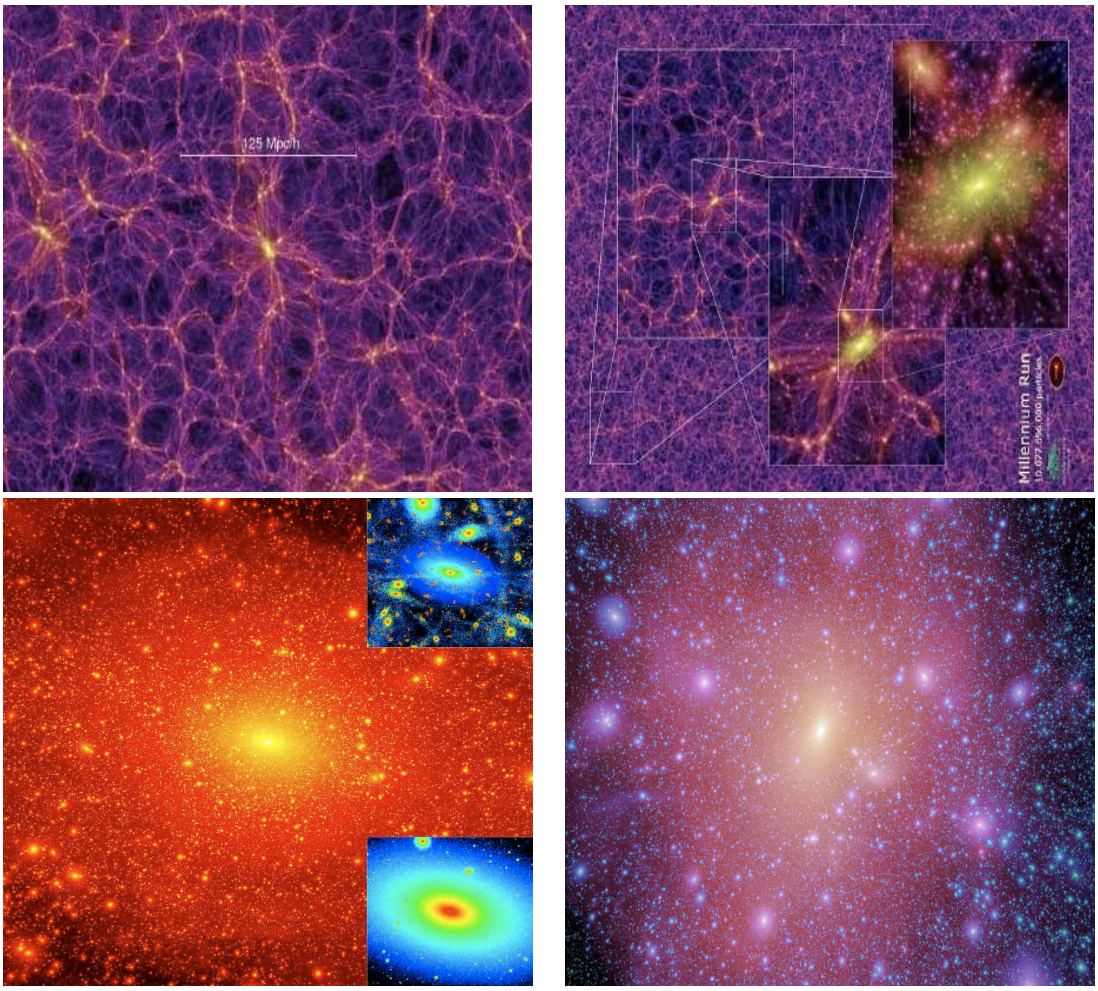

Figure 1.8 N-body cosmological simulations are a powerful tool to understand the LSS of the Universe as well as smaller structures like our own Milky Way. *Top panels*: the result of one of the largest simulations ever done -the Millenium Run, with 2160^3 particles-, which tries to reproduce the LSS and the Universe we observe today (Springel et al. 2005). *Bottom panels*: The highest Milky Way sized halo simulations to date, with more than 200 million particles: the Via Lactea II simulation in the left (Diemand et al. 2008) and the Aquarius project (Springel et al. 2008).

Current N-body simulations suggest the existence of a universal DM density profile, with the same shape for all masses, epochs and input power spectra (Navarro, Frenk & White 1996). Kravtsov et al. (1998) proposed a general parametrization for

the DM halo density in order to agglutinate most of the fitting formulae that can be found in the literature:

$$\rho(r) = \rho_s/[(r/r_s)^{\gamma}\ (1+(r/r_s)^{\alpha})^{(\beta-\gamma)/\alpha}], \tag{1.9}$$

where ρ_s and r_s represent a characteristic density and a scale radius respectively. Effectively, these density profiles are well motivated by high-resolution N-body cosmological simulations. The Navarro-Frenk-White (Navarro, Frenk & White 1997; hereafter NFW), with (α,β,γ) = (1,3,1), and Moore profiles (Moore et al. 1998), with (α,β,γ) = (1.5,3,1.5), are some examples of the most widely DM density profiles used in the literature so far (see Fig. 1.9). As it can be seen from these values, various groups have ended up with different results for the spectral shape in the innermost regions of galaxies and galaxy clusters, which are by far the most conflictive regions to be simulated, given the short dynamical time-scales and strong gravitational forces (which also means a more expensive computational cost). For this Thesis, the DM density profile inner slope will become crucial in the estimations of the DM annihilation flux, as we will see later in more detail. Also related to this issue, the effects of the adiabatic baryonic compression of the DM near the center of haloes, typically discarded in N-body simulations, may enhance the DM density considerably (up to one order of magnitude according to Prada et al. 2004), as well as the possible effect of central black holes (see Gnedin & Primack 2004 or Diemand et al. 2005 for discussion on this particular issue).

N-body cosmological simulations based on the ΛCDM paradigm are in good agreement with a wide range of observations, such as the abundance of clusters at $z \leq 1$ and the galaxy-galaxy correlation functions (see e.g. Primack 2001 for a review of CDM). However, as pointed out e.g. in Taoso et al. (2008), there are important discrepancies, some of them already discussed in subsection 1.2.4. For example, the number of satellite halos in Milky Way-sized galaxies, as predicted by simulations, exceeds the number of observed dwarf galaxies (Moore et al. 1999, Klypin et al. 1999). The rotation curves of low surface brightness (LSB) disk galaxies point to DM distributions with constant density cores rather than the cuspy profiles preferred by N-body simulations (Flores & Primack 1994; McGaugh & de Blok 1998). As for the angular momentum of DM halos, in simulations gas cools at early time into small mass halos, leading to massive low-angular momentum cores in conflict with the observed exponential disks (Bullock et al. 2001). However, astrophysical processes such as major mergers and astrophysical feedback might help to solve these problems (Vitvitska et al. 2002). The low efficiency of gas cooling and star formation may decrease the number of satellites in Milky Way-sized galaxies (e.g. Moore et al. 2006) as well as tidal stripping (e.g. Kravtsov et al. 2004). Furthermore, new ultra-faint dwarf galaxies recently detected with SDSS data seems to importantly alleviate the discrepancy between CDM predictions and observations, as also discussed in previous sections (Simon & Geha 2007). The measurements of the LSB galaxies rotation curves may suffer of observational biases, for example due to the fact that DM halos are triaxials

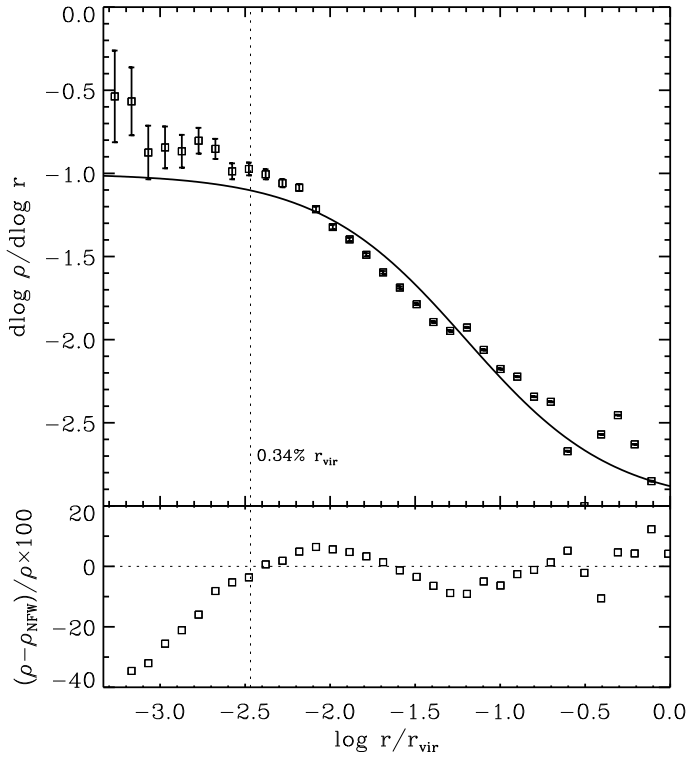

Figure 1.9 Top: Logarithmic slope of the density profile of the Via Lactea simulation as a function of radius. The thin line shows the slope of the best-fit NFW profile. Bottom: Residuals in percent between the density profile and the best-fit NFW profile. Figure taken from Diemand et al. (2007).

rather than spherically symmetric (Hayashi et al. 2007). Moreover, small deviations of the primordial power spectrum from scale invariance, the presence of neutrinos (Hofmann et al. 2001) or astrophysical processes (e.g. Weinberg & Katz 2002) can sensibly affect the halo profiles.

1.4 What is Dark Matter made of?

We have already discussed in previous sections that there is a lot of observational evidence of the existence of Dark Matter. The natural question now is which kind of particles can account for the huge fraction of the total content of the Universe predicted to be in the form of DM. Up to now, a plethora of DM candidates have been proposed. For example, MACHOs, or Massive Compact Halo Objects, which

are still baryonic DM in the form of faint stars or stellar remnants. However, we know that they do not exist in sufficient quantity to completely resolve the DM challenge. It seems necessary to make use of physics beyond the Standard Model of Particle Physics, where good non-baryonic DM candidates arise that fulfill all the cosmological requirements. The most popular are probably the neutralinos and the axions, both of them proposed for other reasons in extensions of the Standard Model of particle physics. Ordinary massive neutrinos are too light to be cosmologically significant, though sterile neutrinos remain a possibility. Other candidates include primordial black holes, non-thermal WIMPzillas, and Kaluza-Klein particles. In this section I will briefly review only those candidates with a larger acceptance in the community at present. For a detailed picture, see e.g. Bergström (2000), Bertone (2005) or Steffen (2009).

1.4.1 Barionic Dark Matter

It is possible to estimate the baryon density of the Universe from the fraction of observed light elements (H, D and He). The found value, however, $\Omega_{baryons} \sim 0.02$, is too low to account for the total DM content needed to explain cosmological data, like the CMB (which gives a total matter content $\Omega_m \sim$0.27), and to explain the observed LSS. Nevertheless, it seems also clear that even the minimum value of $\Omega_{baryons}$ allowed by Big Bang nucleosynthesis (BBN) ($\Omega_{baryons} \sim 0.044$) is higher than the contribution from luminous baryons. This means that there exists also a DM problem for baryons, i.e. that a high fraction of them will be hidden.

Effectively, it is possible to think about ordinary matter difficult to be observed with the present technology and current telescopes. For example, apart from the relatively large amounts of hot X-ray emitting gas in clusters, the main baryonic component of the Universe may be diffusively distributed gas in-between galaxies and clusters difficult to be detected. In addition, it cannot be excluded that a large amount of baryonic mass may be hidden in galactic halos in the form of sub-solar mass objects, known as **MACHOs** (from MAssive Compact Halo Objects), that include faint stars, planetary objects (brown dwarfs and Jupiter-like planets), and stellar remnants (white dwarfs, neutron stars, and black holes). In order to detect them, astrophysicists have used the microlensing technique very specially. The idea is to monitor 1 to 10 million stars in a satellite galaxy, e.g. the Large Magellanic Cloud (LMC) or Small Magellanic Cloud (SMC). The intensity of one of these background stars will rise in a typical, time-symmetric and achromatic fashion during a few days, weeks, or months (depending on the mass and transverse velocity of the intervening object) if an object such as a non-luminous star passes the line-of-sight to the star (Paczynski 1986) and if such stars make up a sizeable fraction of the Galactic halo. Microlensing experiments, like MACHO (Alcock et al. 2000) and EROS (Ansari et al. 2004), as well as a combination of other observational (HST) and theoretical results (Graff & Freese 1996) have shown that MACHOs less massive than 0.1 $M_\odot$

make an insignificant contribution to the energy density of the Galaxy. Alcock et al. (2000) and Freese et al. (2000) claim that roughly 20% halo fraction could be made at most of $\sim$0.5 $M_{\odot}$ objects which might be made of stellar remnants such as white dwarfs, although this fraction could be probably even smaller according to other works (Zaritsky et al. 1999; Salati et al. 1999). Therefore, the conclusion is that such experiments evidence that most of the DM in the Galaxy is not in the form of baryons, which is consistent with what it is inferred from CMB-combined cosmological measurements: most of the DM in the Universe should be non-baryonic matter.

Finally, and even though there is not much room at present for a major component of DM in the Universe being of baryonic form, one cannot entirely rule out some exotic but still baryonic scenarios. However, since many of these invoke "conventional" matter, such as difficult to detect (and exclude) cold molecular clouds or very low mass stars with an extremely fine-tuned mass function, a major yet unsolved problem for these models is to circumvent the BBN bound. A form of baryonic DM which could avoid the BBN bound, for example, is primordial black holes (Ivanov et al. 1994).

1.4.2 Non-baryonic Dark Matter particle candidates

A good DM particle candidate should fulfill a series of important properties (Baltz 2004; Taoso et al. 2008) in order to provide a convincing explanation to all the observed phenomenology:

1. It should be weakly interacting to ordinary matter and electrically neutral, i.e. with neither electromagnetic nor strong interactions.

2. It should be long-lived enough for having been present since the early Universe, when they were created.

3. It has to be cold (see Section 1.2.3 to remember the reasons).

4. It must be massive enough to account for the measured Ω_m.

5. It must be consistent with observations (BBN, relic density, stellar evolution, LSS...) and present constraints (direct and indirect detections; see Section 1.5).

These particles are known as *Weakly Interacting Massive Particles* or, simply, WIMPs.

As also discussed in Baltz (2004), the mass range of the proposed non-baryonic DM candidates covers at least $\sim$90 orders of magnitude in mass (from e.g. "fuzzy" CDM to WIMPzillas); unfortunately astrophysical observations do not help in constraining this huge mass range. However, the energy scale $\sim$100 GeV is of special interesting for the DM problem, as we will describe in next sections. In the following,

I will briefly present some of the preferred DM candidates at present. Again, I refer to Bergström (2000), Bertone (2005), Buckley et al. (2008b), Steffen (2009) for detailed reviews on each of the candidates presented below as well as on other plausible scenarios.

- **Neutrinos**: Until very recently, neutrinos were considered excellent DM candidates for their "undisputed virtue of being known to exist" (Bergström 2000). However, neutrinos are simply not abundant enough to be the dominant DM component: from the analysis of CMB anisotropies, combined with LSS data, we know that $\Omega_\nu h^2 < 0.0065$ (95% confidence limit; see Table 1.4). Furthermore, they are *hot* (HDM), which as discussed in subsection 1.2.3 is disfavored by current observations. Effectively, being relativistic collisionless particles, neutrinos erase fluctuations below a scale of ~ 40 Mpc $(m_\nu/30$ eV) (Bond et al. 1980), which would imply a *top-down* hierarchical scenario for the formation of structures in the Universe, contrary to present trends.

  Also *sterile neutrinos* have been proposed as CDM; they are similar to standard neutrinos, but without Standard Model weak interactions apart from mixing and can be much heavier. Proposed as DM candidates by Dodelson & Widrow (1993), stringent cosmological and astrophysical constraints on sterile neutrinos come from the analysis of their cosmological abundance and the study of their decay products (Abazajian et al. 2001).

- **Axions**: the existence of axions requires physics beyond the Standard Model of particle physics, since they were introduced in an attempt to solve the problem of CP violation. Laboratory searches, stellar cooling and the dynamics of supernova 1987A constrain axions to be very light ($\lesssim 0.01$ eV). Because of axions couple so weakly to the rest of matter, they were not produced in thermal equilibrium in the early Universe; therefore, despite their light masses, they can behave as CDM. Their relic abundance matches the DM cosmological density for masses around 10 μeV (although this value is quite uncertain due to the uncertainties in the production mechanisms).

- **SUSY candidates**: as discussed above, and despite the fact that neutrinos are thought to be massive, they are essentially ruled out as DM candidates. Consequently, the Standard Model does not provide a viable DM candidate. Supersymmetry (SUSY) is capable to provide good DM candidates with all the needed characteristics enumerated above. Before presenting the SUSY candidates, a brief introduction to SUSY seems to be not only convenient but also necessary. Further details can be found in a huge number of SUSY reviews (e.g. Wess & Bagger 1992; Jungman et al. 1996; Binetruy et al. 2001).

  In particle physics, a solution to the so-called hierarchy problem (why the expected mass of the Higgs particle is so low) requires new physics. An example is

provided by SUSY, a symmetry in nature between fermions and bosons, where the supersymmetric partners of standard model particles lead to cancellations in the radiative corrections to the Higgs mass. SUSY seems to be a necessary ingredient in superstring theory, which unites all the fundamental forces of nature, including gravity. SUSY is designed to keep particle masses at the right value. As a consequence, each particle has a partner: photino for the photon, squark for quark, selectron for the electron, and so on. The hierarchy problem in particle physics motivates the existence of new particle degrees of freedom in the mass range of 100 GeV to TeV scale. It is a remarkable coincidence that if DM is composed of a WIMP with an approximate mass of this order, one could naturally produce the required cosmological density through thermal decoupling of the DM component (this is the so-called WIMP miracle). Note, however, that supersymmetric DM should be seen just as one particular realization of a generic WIMP. Here weakly interacting, electrically neutral massive (GeV to TeV range) particles are assumed to carry a conserved quantum number (R-parity in the case of supersymmetry) which suppresses or forbids the decay into lighter particles. Such particles should have been copiously produced in the early universe through their weak interactions with other forms of matter and radiation. As the universe expanded and cooled, the number density of the WIMPs successively became too low for the annihilation processes to keep up with the Hubble expansion rate. A relic population of WIMPs should thus exist, and it is very suggestive that the canonical weak interaction strength is, according to detailed calculations, just right to make the relic density fall in the required range to contribute substantially to the total content of energy-density of the Universe.

The most preferred DM candidates that arises in the context of SUSY are:

Neutralinos: probably the best WIMP candidate, and the preferred and most widely studied as well. In SUSY, if one postulates a conserved quantity arising from some new symmetry (R-parity), the lightest supersymmetric particle (LSP) is stable and would provide a natural candidate for DM. In fact, as pointed out e.g. in Buckley et al. (2008b), R-parity conservation is introduced into SUSY not to solve the DM problem, but rather to ensure the stability of the proton. In many regions of supersymmetric parameter space, the LSP is the neutralino, a Majorana particle (its own antiparticle) that is the lightest supersymmetric partner to the electroweak and Higgs bosons.

The attractiveness of this candidate, besides its particle physics convenience, is that it fulfill all the WIMP requirements with excellent marks. Furthermore, it has gauge couplings and a mass which for a large range of parameters in the supersymmetric sector imply a relic density in the

required range to explain the observed $\Omega_m \sim 0.3$.

Axinos: if the axions proposed to solve the strong CP problem exist and in addition SUSY is valid, the axion will naturally have as a partner the axino. Their mass ranges between the eV and the GeV scale, and they can be efficiently produced through thermal and non-thermal processes in the early Universe under the form of cold, warm or even hot DM (see e.g. Choi & Roszkowski 2006; Covi et al. 2004). In particular, axinos CDM is achieved for masses $\geq$ 100 keV.

Gravitinos: they are the superpartner of the graviton. It was the first SUSY particle considered for the DM problem (Pagels & Primack 1982). In models where the gravitino is the LSP, it is often quite light (keV), and would thus be warm (WDM). In Cosmology, the overproduction of gravitinos can be problematic, though the difficulties can be circumvented (Kawasaky et al. 1995). Gravitinos at the weak scale, whose relic density would be obtained through the decays of the next lightest superpartner, are also an interesting possibility (Feng et al. 2003).

- **Kaluza-Klein particles**: if our four-dimensional space-time is embedded in a higher dimensional space, accessible only at very small length or very high energy scales, excitations of Standard Model states along the orthogonal dimensions (called Kaluza-Klein excitations) may be viable DM candidates as well and act therefore as WIMPs (e.g. Servant & Tait 2003). Masses around 1 TeV provide reasonable relic densities from thermal freeze-out.

As a final remark, it is important to note here that the total amount of DM in the Universe could be constituted by several particle species of those given above. Indeed, we already know that standard neutrinos contribute to DM, but cannot account for all of it. A detailed discussion on the detection prospects of a subdominant density component of DM can be found in Duda et al. (2003).

From the list of DM candidates given above, I focused my efforts and my work very specially in two scenarios (probably the most promising and popular): the neutralino (for which most of the work on DM searches presented in this Thesis was done), and the axion (Chapter 5).

1.5 Dark Matter searches

There is a huge effort and an enormous array of experiments trying to detect CDM at present. The detection techniques are typically divided in direct and indirect. Direct DM searches are based on the elastic scattering of DM particles on target nuclei, for which nuclei recoil are expected. By the other side, indirect DM searches try to detect self-annihilation products of DM particles in high DM density environments.

An additional strategy for DM searches is the **direct production of DM particles** in laboratory experiments (typically at accelerators). In SUSY, as superparticles (sparticles) are expected to be very massive, they can only be tested at powerful particle accelerators, like the Large Hadron Collider (LHC), which it is expected to enter in operation again during next Fall 2009. There is the hope that some of these spartners can be definitely discovered by these experiments. providing also in this way evidence for grand unification and string theory.

In the following I will briefly describe the direct and indirect detection techniques.

1.5.1 Direct detection

Direct DM searches try to detect DM particles by measuring nuclear recoils produced by DM scattering. This should be possible if our own Milky Way is filled with WIMPs as expected, since many of them should pass through the Earth and should weakly interact with ordinary matter. The key ingredients for the calculation of the signal in direct detection experiments are the density and the velocity distribution of WIMPs in the solar neighborhood as well as the WIMP-nucleon scattering cross section. From this information we can evaluate the rate of events expected in an experiment (i.e. WIMP-nucleon scattering events) per unit time and per unit detector material mass. Assuming a local neutralino density $\sim$0.3 GeV/cm^3 in the Solar System and a typical velocity v/c$\sim 10^{-3}$, the flux of particles of mass 100 GeV should be $\sim 10^9$ m^{-2}s^{-1}. Despite this large DM flux expected at Earth, the weakness of WIMP interactions with nuclei makes direct detection challenging (see e.g. Muñoz 2004 and Ellis et al. 2005 for recent reviews on direct searches).

As already commented, the signature of DM elastic scattering off nuclei are nuclear recoils, with typical energies of a few keV or less for WIMP masses 1-100 GeV (see e.g. Jungman et al. 1996). The real challenge lies in discriminating such processes from the natural radioactivity background, and this the reason why direct detection experiments are normally placed in low background radiation environments. Current experiments exploit a variety of detection techniques, focusing on signals such as scintillation, phonons, ionization or a combination of them, as well as a variety of targets, e.g. NaI, Ge, Si and Xe. As for present bounds and current experiments, most of them based on the detection of DM particles through their elastic scattering with nuclei, such as CDMS (Ahmed et al. 2008), XENON (Angle et al. 2008), ZEPLIN (Alner et al. 2007), EDELWEISS (Sanglard et al. 2005), CRESST (Angloher et al. 2005), CoGeNT (Aalseth et al. 2008), DAMA/LIBRA (Bernabei et al. 2008), COUPP (Behnke et al. 2008), WARP (Benetti et al. 2008), and KIMS (Lee et al. 2007). Current constraints on the WIMP-nucleon spin-independent elastic scattering cross section, as a function of the WIMP mass are shown in Fig. 1.10. The most stringent constraints currently come from the CDMS and XENON-10 collaborations. Although difficult to assess, it might be expected that future experiments can reach sensitivities near 10^{-9}-10^{-10} pb within the next few to several years.

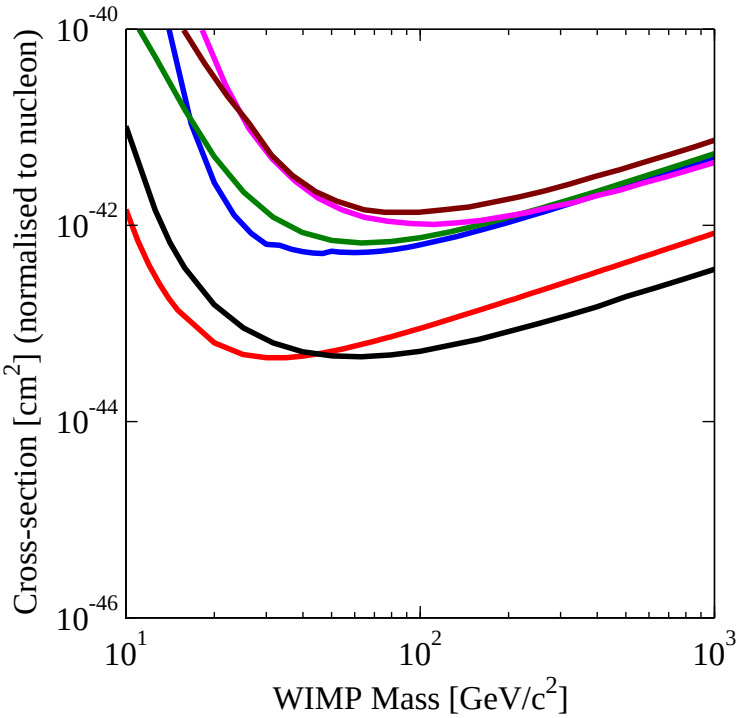

Figure 1.10 Current constraints on the WIMP-nucleon (as of January 2009), spin-independent elastic scattering cross section. From bottom-to-top on the right side of the figure, the lines correspond to the limits from the CDMS, XENON-10, WARP, CRESST, ZEPLIN, and EDELWEISS experiments. Figure taken from Hooper (2009).

There are also other experiments that try to discriminate the expected DM signal against the natural background by means of an annual modulation of the measured event rate, based on the fact that the Earth rotation around the Sun should produce a modulation in the velocity of DM particles (Drunkier et al. 1988). This is indeed the kind of search carried out by the DAMA Collaboration, who in 1998 claimed an evidence for a modulation of the event rate at a 6.3σ level, and repeated the claim in 2008 at more than 8σ. Their results are compatible with a $\sim$50 GeV DM particle mass and WIMP-nucleons scattering cross section of $\sim 10^{-41}$-10^{-42} cm^2. The claim that this signal is the result of DM interactions has been controversial, mostly because a number of other experiments appear to be in direct conflict with the DAMA result. Effectively, other experiments that could explore the same region of the parameter space than DAMA found null results (Benoit et al. 2002; Akerib et al. 2003). This comparison, however, is model-dependent, so it should be taken carefully.

1.5.2 Indirect detection and the γ-ray connection

Indirect DM searches consist on detecting the radiation produced in DM annihilations, i.e. the products of WIMP annihilations, such us gamma-rays, neutrinos, positrons, electrons and antiprotons. The flux of this radiation is proportional to the annihilation rate, which in turn is proportional to the squared DM density; this means that the best places to look for DM in the Universe will be those with the highest DM concentrations. Distance is also very important, since high DM dominated systems that are located too far from us will yield too low DM annihilation fluxes at Earth. Having both considerations in mind, it is clear that the Galactic Center should be a very good candidate, but dwarf spheroidal galaxies satellites of the Milky Way, and nearby galaxy clusters arise as very good candidates for DM searches as well. A complete review on indirect DM detection is given in Bergström et al. (1998).

It is possible to get photons from DM annihilations by three processes (Buckley et al. 2008): (1) direct annihilation into a two-photon final state, giving monoenergetic spectral lines (which, if discovered, would represent a unique "smoking gun" in favour of the DM interpretation); (2) through the annihilation into an intermediate state that subsequently decays and hadronizes, yielding photons through the decay of neutral pions and giving rise to a broad featureless continuum spectrum; (3) through internal-bremsstrahlung into a three-particle state, yielding gamma-rays with a very hard spectrum and sharp cutoff. DM searches based on gamma-rays have some advantages with respect to other indirect detection techniques (see e.g. Hooper 2009): they travel essentially unimpeded (at least in the Milky Way "cosmological" neighborhood), since they are not deflected by astrophysical magnetic fields, contrary to what happens for charged particles (electrons, positrons...). In addition, they are not attenuated (again true at least for the Milky Way "cosmological" neighborhood), and thus retain their spectral information, i.e. the observed spectrum will be identical to the DM annihilation spectrum (which only depends on the details of the WIMP considered).

But why γ-rays and not other wavelengths? The keypoint is that the energy scale of the annihilation products is determined by the mass of the DM particles, as they typically carry a relatively large fraction of the available annihilation energy. Since the preferred DM candidates like the neutralino are expected to have masses of the order of $\sim$GeV-TeV (see Section 1.4.2), this explains that DM searches are specially performed in the γ-ray energy band (see e.g. Bertone (2007) for a recent summary of the field of γ-ray DM searches).

WIMP annihilations, and in particular neutralino annihilations, could also be observed through the search of other products of the annihilation different from γ-rays, such as positrons, low-energy antiprotons and high-energy neutrinos. However, unlike γ-rays, which travel along straight lines, positrons and antiprotons will propagate suffering the effects of the Galactic magnetic field (diffusing and losing energy), since

they are charged particles. As a result, a diffuse spectrum is expected at Earth and the origin of the particles will be unknown, but still a DM detection would be possible by carefully studying the spectrum of such particles to identify signatures of DM annihilations. Neutrinos would not suffer these difficulties and, like gamma photons, would point back to their sources. However, given their very low detection cross section compared to gamma-rays, it will be very difficult for neutrino experiments to detect them from discrete sources like the Galactic Center. The alternative is to look for neutrinos in the local halo, e.g. the Sun or the Earth itself, where they can be captured by interactions and where they could exist in sufficient quantities to yield an observable signal.

In this Thesis, most of the work related to DM detectability, and in particular all the work done concerning DM annihilations, is focused *only* on γ-ray searches. This means that neither antimatter nor neutrinos as other possible annihilation products were explored. Furthermore, I centered my efforts in a DM annihilation scenario where the neutralino is the long-awaited WIMP that exists in sufficient quantities to constitute the totality of the non-baryonic DM in the Universe. The exception is Chapter 5, in which the DM detection prospects for another plausible candidate (the axion) was studied in detail, but also in γ-rays. In this case, predicted photon/axion mixings rather than self-annihilations are the vehicle used in the search of the particle.

To conclude, it would be natural to ask why this huge interest on indirect γ-DM searches precisely now, at the beginning of the 21st Century (specially taking into account that these kind of searches were proposed at least 25 years ago, see e.g. Gunn et al. 1978; Stecker 1978; Bergström & Snellman 1988). There are good reasons to be specially optimistic at present: current γ-ray experiments like IACTs and Fermi (that will be presented in the next section) are reaching for the first time sensitivities good enough to be able to test some of the allowed and preferred scenarios (i.e. obeying WMAP constraints, using well-motivated DM density profiles and SUSY as the particle physics model). The situation is expected to be even better when new generation telescopes enter in operation in the near future (CTA, AGIS...; see also next section). Indeed, we are just now starting to really unveil the γ-ray energy window, and almost every month new sources are been discovered in the GeV-TeV sky. It is time for γ-ray DM searches.

1.5.3 The importance of γ-ray DM searches

As pointed out also in Buckley et al. (2008), while it is possible that the LHC will provide evidence for SUSY, or that future direct detection experiments will detect a clear signature of nuclear-recoil events produced by DM, gamma-ray observations provide the only way to measure the DM halo profiles and to elucidate the exact role of DM in structure formation. Effectively, among all the above cited detection techniques (direct and indirect), γ-ray DM searches are unique in going beyond a

detection of the local halo to providing a measurement of the actual distribution of DM in the Universe.

The general picture is that the LHC will be able to scan neutralino masses up to ∼300 GeV, well below the upper end of the allowed mass range. As for direct detection, WIMP-nucleon recoil experiments are most sensitive in the 60 to 600 GeV regime. Indirect DM searches below 100 GeV can be accomplished by the Fermi satellite and probably by MAGIC as well (see Section 1.6), while IACTs like MAGIC itself or HESS should play a critical role for neutralino masses above 100 GeV. Therefore, and although direct detection and accelerator searches have an exciting discovery potential, there is a large region of parameter space for which gamma-ray instruments could provide the only detection (e.g. in case of nuclear recoil cross-section lies below the threshold of any planned direct detection experiment, or the mass is out of range of the LHC).

It seems clear that a combination of laboratory detection not only with direct but also with indirect γ-ray DM searches will be required in order to successfully scan the whole allowed SUSY parameter space, and to truly assess that a new particle detected by any of these methods really constitutes the enigmatic and long-awaited to be discovered DM.

1.6 The γ-ray energy window: IACTs, Fermi and future instruments

1.6.1 Gamma-ray astrophysics in a nutshell

The cosmos and its evolution are studied using all radiation, in particular electromagnetic waves. The observable spectrum extends from radio waves (at wavelengths of several tens of meters, or energies of some 10^{-5} eV) to ultra-high energy gamma quanta (wavelengths of picometers or energies of 100 TeV). Observations at visible wavelengths (0.5 to 1 micrometer) have a history of centuries, gamma astronomy by satellites (keV to few GeV) and ground-based telescopes (above 300 GeV) are end-of-20th century newcomers. Having no electric charge, gammas are not affected by magnetic fields, and can, therefore, act as messengers of distant cosmic events, allowing straight extrapolation to the source. Indeed, high energy γ-rays combine three characteristics that make these energetic photons ideal carriers of information about non-thermal relativistic processes in astrophysical settings (Aharonian 2004): (i) copious production in many galactic and extragalactic objects due to effective acceleration of charged particles and their subsequent interactions with the ambient gas, low frequency radiation, and magnetic fields; (ii) free propagation in space without deflection in the interstellar and intergalactic magnetic fields; (iii) effective detection by space-borne and ground based instruments. Therefore it is commonly believed that very high energy gamma-ray astronomy is destined to play a crucial role in exploration of non-thermal phenomena in the Universe in their most extreme

and violent forms.

Most generally, the observation of gamma rays (electromagnetic radiation of high energy) is one aspect of astroparticle physics. Astroparticle physics is a new field developing as an intersection of Particle Physics, Nuclear Physics, Astrophysics, Gravitation and Cosmology. One of its cornerstones is Cosmic Ray Physics, which has its origins many decades in the past; then scientists observed in balloons and in mountain top laboratories the many charged particles impinging upon the Earth. Today, the field has substantially widened, and includes all particles. Particularly in recent years, activities (and funding) have accelerated, with fundamental discoveries being made at an astonishing frequency. Using the understanding of particle interactions at very high energies, as derived from experiments in accelerator laboratories, the picture of how the Universe developed since its earliest beginnings, some ten billion years ago, is changing fast. Theoretical models fuel multiple experiments, using different particles coming to Earth from space.

The energy domain of gamma-ray astronomy spans from approximately E= $mc^2 \simeq 0.5 \times 10^6$ eV to $\geq 10^{20}$ eV. Given this enormous energy band of cosmic electromagnetic radiation, it is convenient to introduce several sub-divisions, taking into account the specific astrophysical objectives and detection methods relevant to different energy bands. Following Aharonian (2004), I will divide the observational gamma-ray astronomy in 6 areas: low (LE: below 30 MeV), high (HE: 30 MeV - 30 GeV), very high energy (VHE: 30 GeV - 30 TeV), ultra high (UHE: 30 TeV - 30 PeV), and finally extremely high (EHE: above 30 PeV) energies. While observations in the first two energy bands are covered by satellite- or balloon-borne detectors, the last three energy intervals can be best addressed with ground-based instruments.

VHE γ-ray astronomy using ground-based telescopes is a recent addition to the panoply of astroparticle physics instruments, and the number of established sources is small, so far. Some examples of what can be expected to be the most interesting subjects of observation during the coming years are:

1. **Active galactic nuclei (AGNs)**: recent results indicate that most if not all galaxies (including our own Milky Way) have an active center, in which a supermassive black hole is building up. Some of them (Mrk 421, Mrk 501) have been observed to be active in the VHE gamma region, with occasional outbreaks and even with quasi-periodic fluctuations. The preferred theory explains the VHE gammas as products of high acceleration fields (shock waves) in the jet that bundles charged particles along two directions at 180 degrees to each other. We currently believe that the VHE gamma rays are produced within the jets, close to the black hole. The origin of the jets is not yet understood. Models relate the jet directions (seemingly constant over millions of years) to the spin axis (axis of rotation) of the black hole. Understanding more about these objects and the acceleration mechanisms both in the vicinity of the black holes and in intergalactic space is a task in which Imaging Atmospheric Cherenkov Telescopes (IACTs; see next subsection) have an important role to play.

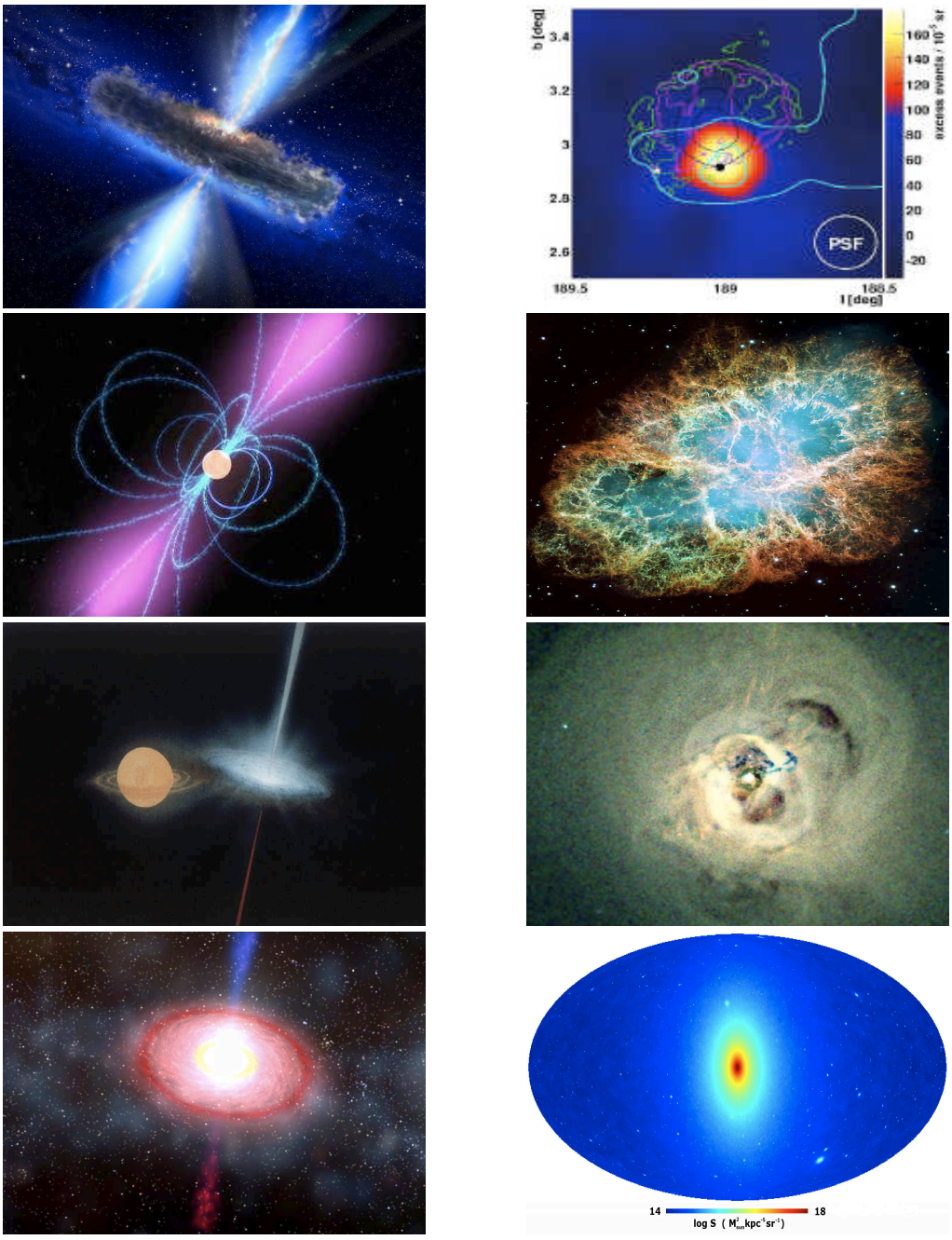

Figure 1.11 Some examples of scientific targets for γ-ray astronomy in the coming years. *From left to right and top to bottom*: artistic view of an AGN; the IC-443 SNR discovered by MAGIC (Albert et al. 2007); an artistic impression of a pulsar; the Crab Nebula, the most famous PWN; an artistic picture of a microquasar; the Perseus galaxy cluster as seen by the Chandra satellite in X-rays (Fabian et al. 2006); an artistic view of a GRB; the simulated DM annihilation signal from our own galaxy (Springel et al. 2008b).

2. **Supernova remnants**: in the wake of a certain class of supernova explosions, the so-called SN of types II and Ia, gas clouds expand and a very dense core develops; the core may be a spinning neutron star or a black hole. Supernova remnants may be VHE gamma sources of different types. According to the standard model of cosmic ray origin, the shell type supernova remnants (radiating from the expanding cloud) are sites of acceleration of nuclei to very high energies: if so, they not only are the main accelerators of charged cosmic rays, but should also copiously produce gamma rays. SN remnants of the plerion type, instead, are expected to radiate from the core. A systematic high-sensitivity scan of candidates, most of them lying in our own galaxy, has still to be done.

3. **Sources found at lower energies but not yet identified**: all-sky surveys of wide-angle searching experiments in satellites have discovered a large number of lower energy gamma-ray emitters. The angular resolution of these detectors is limited, so that for more than half of these sources, it was not yet possible to relate them to known sources observed at different wavelengths. The (third) 1999 catalogue of sources established by the (no longer operating) EGRET detector is a well-known book of astrophysics riddles: it lists 170 unidentified sources, along with 101 whose origin is thought to be understood. IACTs will collect many more gamma rays from these sources, and thus pinpoint their positions and contribute to their identification. The situation is now even more challenging, since it is expected that the recently launched Fermi satellite discover a lot of new unidentified sources in gamma-rays that it will be necessary to study as well.

4. **Gamma Ray Bursts (GRBs)**: every day, a few powerful stellar explosions illuminate the sky from all directions. Usually, they do not get recorded at visible wavelengths, or only a very weak optical signal is seen. GRBs last for seconds to minutes only. Sometimes, an afterglow in the optical or X-ray domain is observed after much longer delays. The energy observed makes them the beacons of most likely the most energetic events known in the universe. Discovered 30 years ago, these GRBs have been objects for research and speculation ever since. Today, a few thousand GRBs have been carefully charted, mostly by the BATSE satellite experiment. These objects cover the entire sky, seem spatially uncorrelated, many of them have large redshifts, i.e. we observe them at billions of years in the past, in the period of active star formation. Observations in the VHE gamma domain are not available, so far, but are expected to help clarifying these mysterious phenomena.

5. **Other contributions to cosmology and fundamental physics**: observations of VHE gammas, if done systematically, will also allow to formulate constraints on stellar formation in the early Universe, by measuring the extragalactic infrared radiation field. They will further allow searches for the

stable lightest supersymmetric particle, expected to annihilate with its own self-conjugate antiparticle into gamma photons in areas of high gravitational field. Quantum gravity effects might become apparent if subtle time differences can be detected in the arrival of gammas from a given source, at different wavelengths.

Gamma-ray astronomy is currently under an extraordinary revolution, mainly due to a battery of new instruments that has entered in operation in the last few years. From the ground, new generation Imaging Atmospheric Cherenkov Telescopes (IACTs) like MAGIC (Lorentz et al. 2004), HESS (Hinton et al. 2004), VERITAS (Weekes et al. 2002) or CANGAROO-III (Enomoto et al. 2002) have crucially contributed to revolutionize the field exploring the Universe above 50 GeV up to few TeV, making possible the discovery of new gamma-ray sources, checking theoretical scenarios on gamma-ray emission mechanisms in AGNs, imposing strong constraints to cosmological models through observations of high redshift quasars, unveiling the nature of pulsars, etc. In space we have the small Italian satellite AGILE (Tavani et al. 2008) and very specially Fermi (Gehrels & Michelson 1999; previously called GLAST), in operation since Summer 2008 and covering energies in the range 0.02-300 GeV. In the next subsections I will briefly review the present status of the field as well as present gamma-ray experiments, both on the ground and out in space.

1.6.2 The imaging atmospheric Cherenkov technique. Present IACTs

IACTs are detectors for high-energy gamma quanta, installed on the surface of the Earth. The name Imaging Atmospheric Cherenkov Telescope (IACT) contains most of the characteristics of this type of instrument:

1. The detectors have a light collection mirror and a camera, so they resemble optical telescopes at least superficially.

2. These telescopes detect light produced by the Cherenkov effect, a radiation emitted by relativistic particles when being slowed down; the slowing down is in the atmosphere, where the high-energy gamma quanta get absorbed.

3. IACTs record many Cherenkov photons for a single original gamma; they are seen by the camera as an image whose characteristics allow to identify the recorded particle as a gamma, and to specify its direction and energy.

Because tha atmosphere has only narrow windows for wavelengths to pass, high-energy gamma rays do not reach the earth. They get absorbed in the atmosphere, transparent essentially only for visible and infrared light, and for long radio waves, as shown in Fig. 1.12. The absorption of the primary gamma leaves behind an avalanche, called an electromagnetic shower. The numerous secondary charged particles in such a shower (for an incident gamma rather exclusively electrons and positrons) all radiate

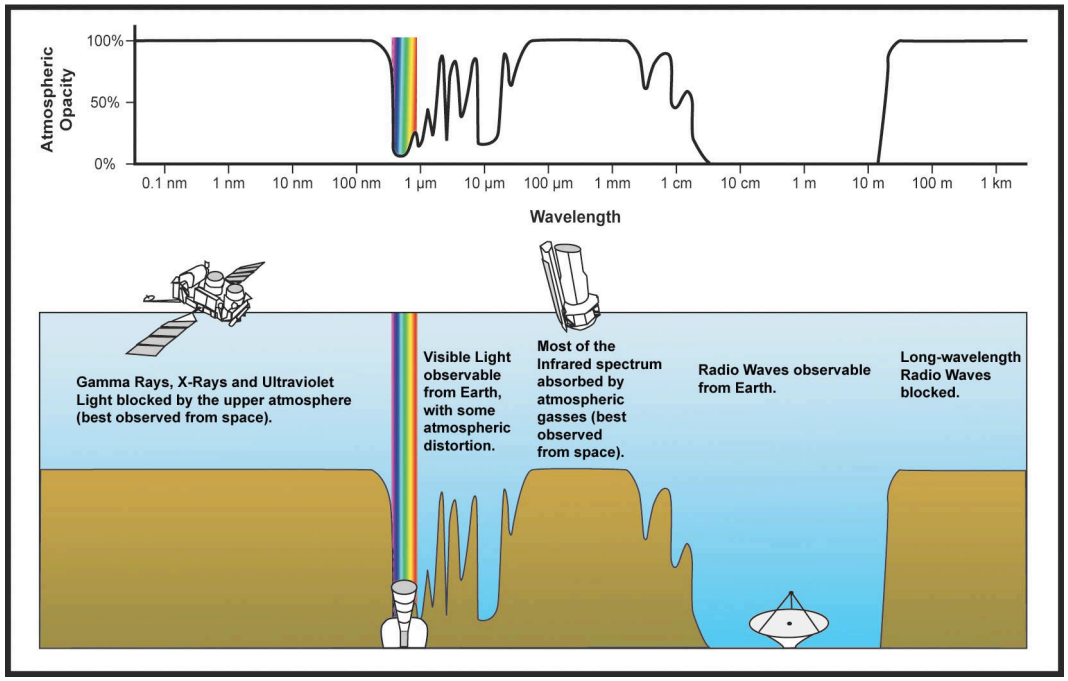

Figure 1.12 The atmosphere is essentially only transparent for visible and infrared light, as well as for a portion of radio waves. The rest gets absorbed at different altitudes. Gamma-rays, for example, do not reach the ground and are absorbed typically at an altitude from 20 to 10 km, depending on the energy of the incident particle.

low-energy (visible to ultraviolet) photons, the Cherenkov radiation. This radiation is emitted at a characteristic angle with the radiating particle, an angle which widens as the atmosphere thickens. Most of the shower development happens at an altitude above sea level from 20 to below 10 km. The radiated photons have an energy corresponding to a window of penetration, and arrive in large enough numbers on the surface of the earth to become an indirect image of the shower, allowing identification against backgrounds and reconstruction of the original particle's direction and energy.

The showering process and the generation of Cherenkov light in a foreward cone have two immediate experimental consequences: the light is spread over a large area, typically a circle with a diameter of 250 m, and hence the light intensity per unit area on ground is low. This allows detection of a gamma impinging anywhere inside this disk, i.e. an effective area of 30 to 10^5 m^2, as long as the initial energy is high enough to produce enough Cherenkov light. Conversely, the signals are weak, marginally detectable; hence, the instrumental sensitivity must be pushed as far as possible: the collection area (mirror surface) must be maximized, and the camera elements (photomultipliers) must respond to single photons with high efficiency. To further improve sensitivity, experiments are installed on mountain tops far from background light and with as little observation time lost due to clouds as possible. In Figs. 1.13

and 1.14 a sketch of the Imaging Atmospheric Cherenkov Technique is shown.

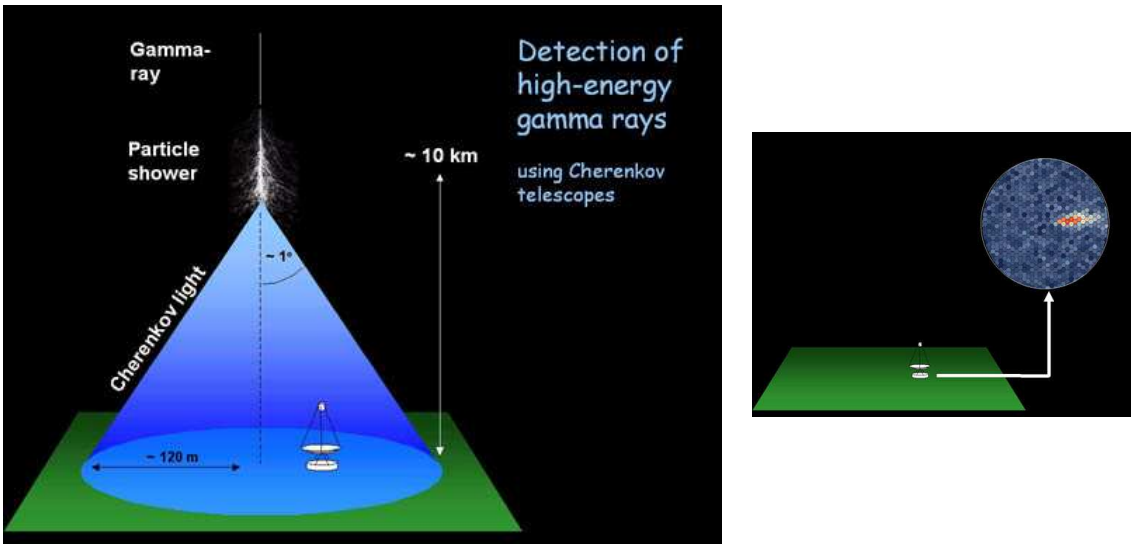

Figure 1.13 *Left*: An incident high-energy gamma ray interacts high up in the atmosphere and generates an air shower of secondary particles. The Cherenkov light is beamed around the direction of the incident primary particle and illuminates on the ground an area of about 250 m diameter. A telescope located somewhere within the light pool will "see" the air shower. *Right*: The image obtained with the telescope shows the track of the air shower, which points back to the celestial object where there incident gamma ray originated. The intensity of the image is related to the energy of the gamma ray. The shape of the image can be used to reject unwanted background, such as showers induced by cosmic ray particles.

Gammas of the high energies that can be recorded by IACTs are relatively rare events. They have to be discriminated against a cosmic ray background several orders of magnitude more abundant. These are mostly protons or light ionized atoms, producing (more dissipated) hadronic showers, in which the charged particles also radiate Cherenkov photons. Hadronic showers do not typically come from the direction in which the telescope is trying to observe a gamma source. Also, hadronic showers are much less concentrated (see Fig. 1.15); the hadrons interact via the strong interaction, producing hadrons and leptons as secondary particles; multiple electromagnetic and hadronic secondary showers appear, with large fluctuations in relative energy, spread over a volume much larger than for an electromagnetic shower. Hadronic showers frequently contain long-lived high-energy muons, whose radiation shows typical patterns and in some cases may also be mistaken for gammas. The image hadrons produce in the detector, therefore, has characteristics different from gamma shower images; using suitable discrimination algorithms, fairly clean gamma signals can be obtained.

With a single telescope providing a single view of a shower, it is difficult to reconstruct the exact geometry of the air shower in space. Multiple telescopes are used which view the shower from different points and allow a stereoscopic reconstruction

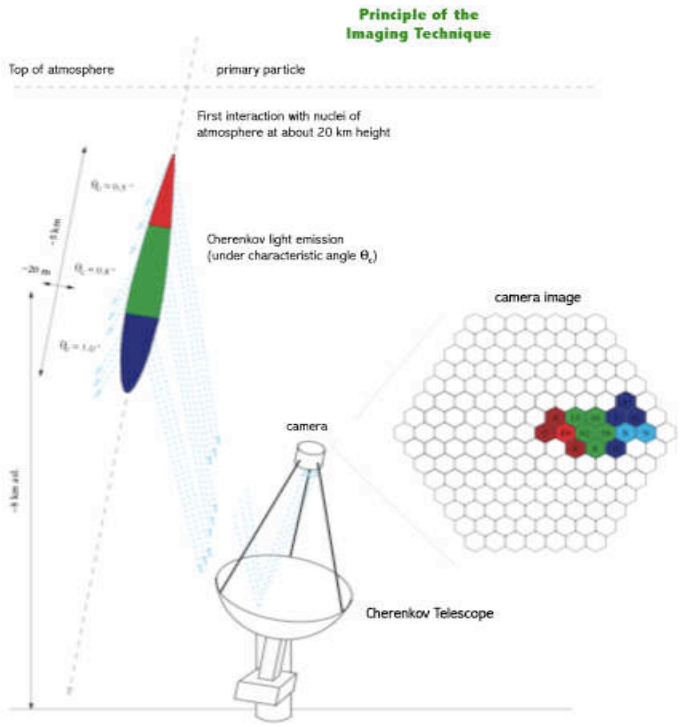

Figure 1.14 Sketch of the Imaging Atmospheric Cherenkov Technique. The pixelated camera is represented by the hexagonal honeycomb-like structure. The given numbers are for a typical 1 TeV incident γ-ray. See text for details.

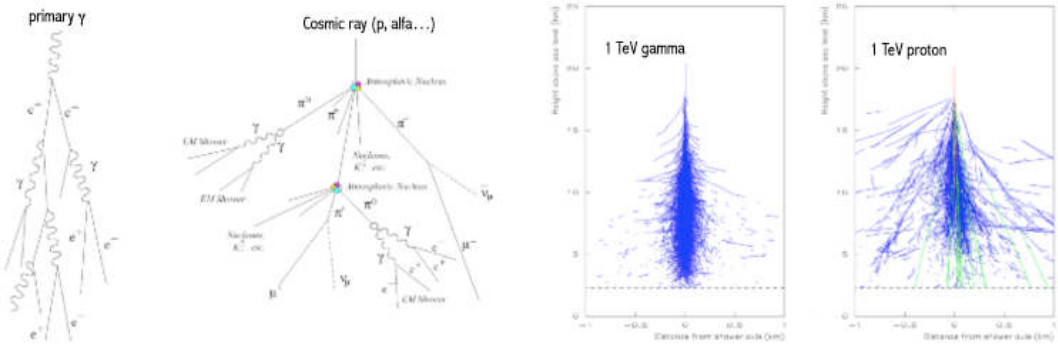

Figure 1.15 *Left*: Scheme of electromagnetic and hadronic showers. *Right*: Montecarlo simulations of the induced showers by a 1 TeV gamma photon and a 1 TeV proton impinging the high atmosphere. The shape of each image in the detector can be used to discriminate between both showers.

of the shower geometry. Because of that, stereoscopic observations lead to a more precise reconstruction of the shower parameters as well as a stronger suppression of the background, as schematically shown in Fig. 1.16.

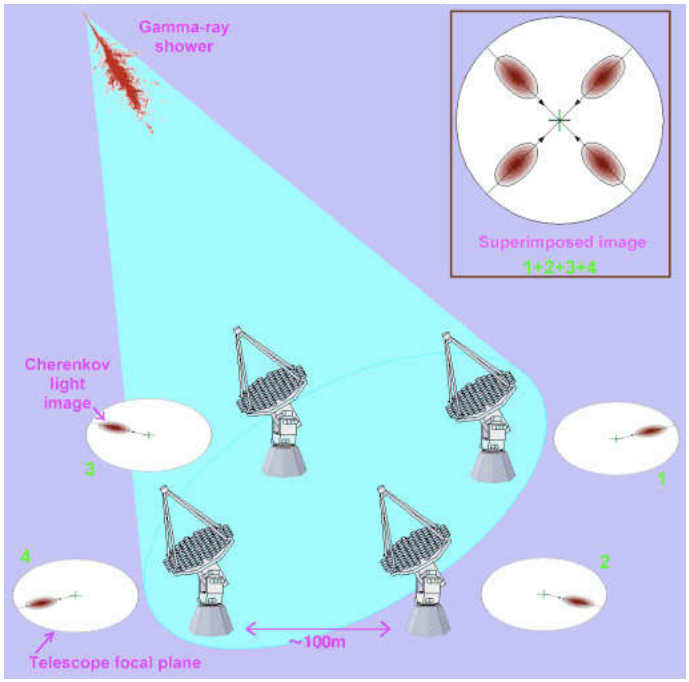

Figure 1.16 Multiple telescopes are used to record the shower from different points and allow a stereoscopic reconstruction of the shower geometry. This kind of stereoscopic observations provides a more precise reconstruction of the shower parameters as well as a stronger suppression of the background.

The IACT was pioneered by the Whipple collaboration and led to the discovery of TeV emission from the Crab Nebula in 1989. The Whipple 10m telescope also discovered the first extra-galactic source of TeV emission with the detection of very high energy gamma-ray emission from the active galaxy Markarian 421. The HEGRA telescope array was the first system to use multiple telescopes, i.e. the stereoscopic technique. Nowadays, the largest IACT telescope is the 17 m MAGIC telescope at the Roque de los Muchachos Observatory in La Palma, which will be presented in detail is Section 7. However, as mentioned at the beginning of this section, there are at least other three IACTs which, together with MAGIC, lead the field above 100 GeV at present: CANGAROO-III, HESS and VERITAS (see Figs. 1.17 and 1.18).

1.6.3 The Fermi satellite

The Fermi Gamma-ray Space Telescope (Fermi) satellite is a next generation high-energy gamma-ray observatory designed for making observations of celestial gamma-ray sources in the energy band extending from 10 MeV to more than 100 GeV. It follows in the footsteps of the CGRO-EGRET experiment, which was operational between 1991 and 1999. Effectively, the Fermi Large Area Telescope (LAT), one of the two instruments on board in the satellite (the other main instrument is the

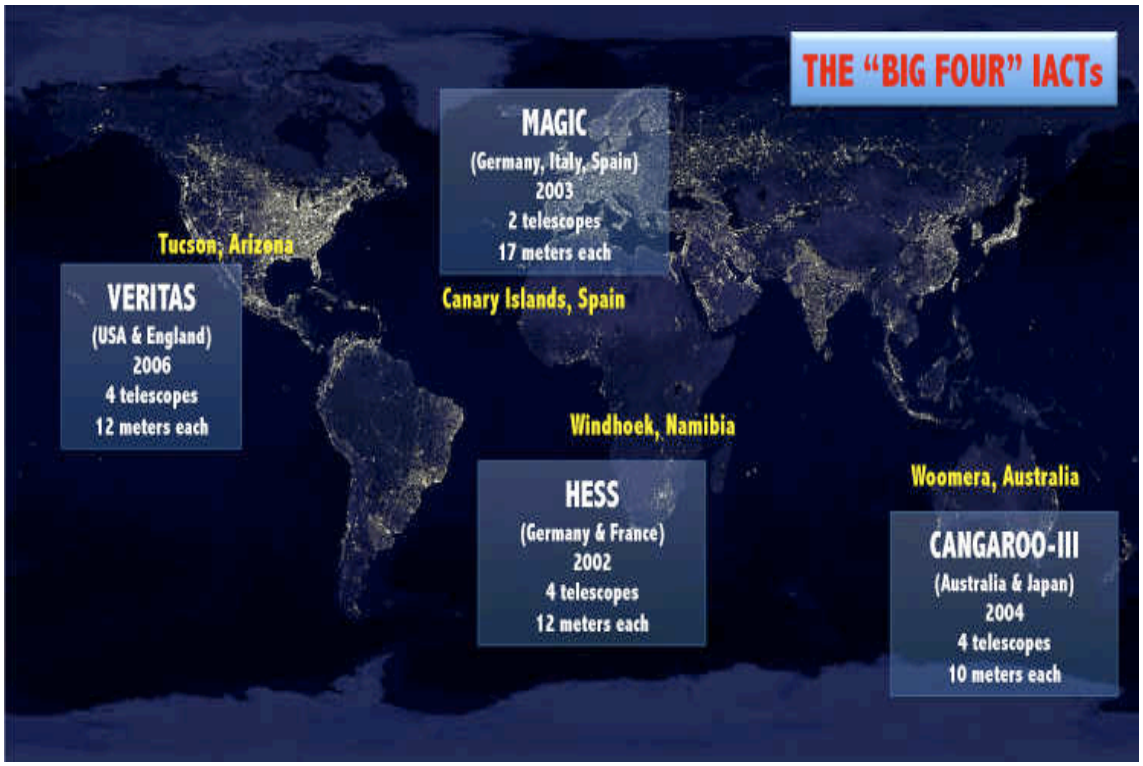

Figure 1.17 The commonly called "Big Four": the new generation of IACTs leading the field at present and exploring the Universe from a few dozens of GeV to a few TeV.

Gamma Burst Monitor), can be considered as the successor to EGRET, with greatly improved sensitivity, resolution, and energy range.

The key scientific objectives of the Fermi mission are:

1. To understand the mechanisms of particle acceleration in AGNs, pulsars, and SNRs.

2. Resolve the gamma-ray sky: unidentified sources and diffuse emission.

3. Determine the high-energy behavior of gamma-ray bursts and transients.

4. Probe dark matter and early Universe.

More in particular, the Large Area Telescope (Fermi/LAT, hereafter LAT), the primary instrument on the Fermi Gamma-ray Space Telescope (Fermi) mission, is an imaging, wide field-of-view, high-energy gamma-ray telescope, covering the energy range from below 20 MeV to more than 300 GeV. A full description can be found in (Atwood et al. 2009). Here I will only briefly summarize the main characteristics of the instrument. The LAT is a pair-conversion telescope with a precision tracker

Figure 1.18 The "Big Four" again. *From left to right and top to bottom*: MAGIC, HESS, VERITAS and CANGAROO-III, the leading IACTs in the world at present.

and calorimeter. The tracking section has 36 layers of silicon microstrip detectors to measure the tracks of charged particles, interleaved with 16 layers of tungsten foil to promote γ-ray pair conversion. The tracker is followed by an array of CsI crystals to determine the γ-ray energy and is surrounded by segmented charged-particle detectors (plastic scintillators with photomultiplier tubes) to reject cosmic-ray backgrounds. The LAT's improved sensitivity compared to EGRET stems from a large peak effective area ($\sim$8000 cm^2, or $\sim$6 times greater than EGRET's), large field of view ($\sim$2.4 sr, or nearly 5 times greater than EGRET's), good background rejection, superior angular resolution (68% containment angle $\sim$0.6° at 1 GeV for the front section and about a factor of 2 larger for the back section), and improved observing efficiency (keeping the sky in the field of view with scanning observations). Pre-launch predictions of the instrument performance are described in Atwood et al. (2009). Verification of the on-orbit response is in progress but the indications are that it is close to expectations. The sensitivity is about 50 times that of EGRET at 100 MeV and even more at higher energies. Its two year limit for source detection in an all-sky survey is 1.6×10^{-9} photons cm^{-2} s^{-1} (at energies $>$ 100 MeV). It can locate sources to positional accuracies of 30 arc seconds to 5 arc minutes, depending

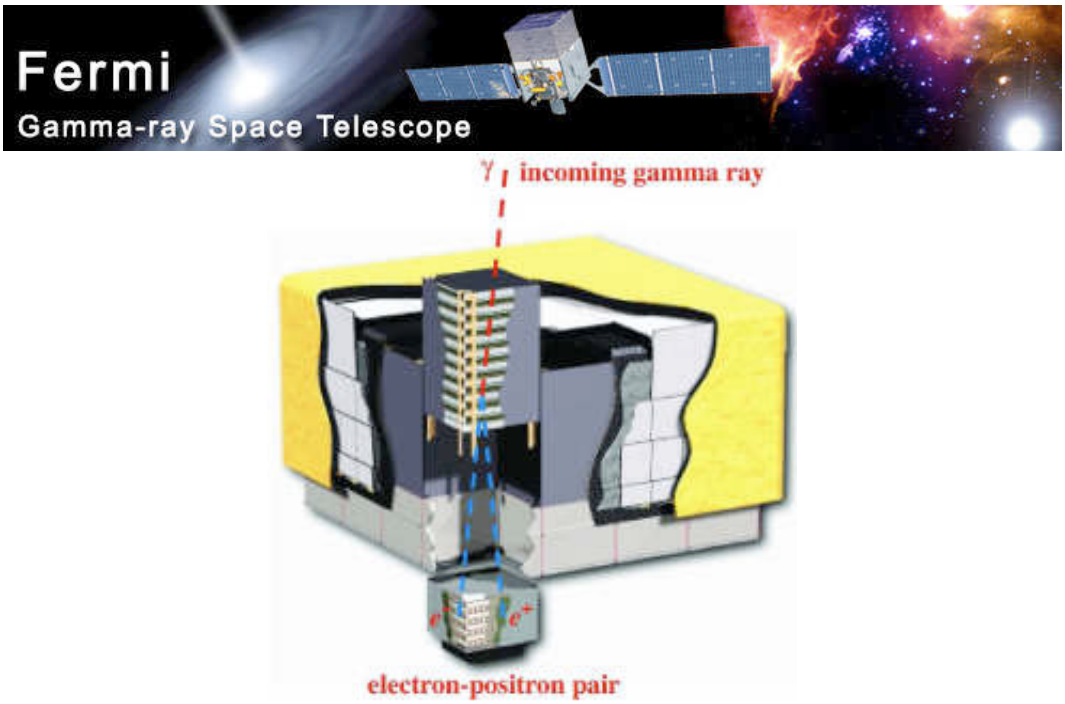

Figure 1.19 *Top:* The recently launched Fermi satellite will revolutionize our knowledge of the gamma-ray sky (credit: NASA). *Bottom:* schematic diagram of the Fermi Large Area Telescope (Fermi/LAT). The telescope's dimensions are 1.8 m × 1.8 m × 0.72 m. The power required and the mass are 650 W and 2.789 kg respectively. Figure taken from Atwood et al. (2009).

on energy.

Data obtained with the LAT are intended to (i) permit rapid notification of high-energy gamma-ray bursts (GRBs) and transients and facilitate monitoring of variable sources, (ii) yield an extensive catalog of several thousand high-energy sources obtained from an all-sky survey, (iii) measure spectra from 20 MeV to more than 50 GeV for several hundred sources, (iv) localize point sources to 0.3-2 arc minutes, (v) map and obtain spectra of extended sources such as SNRs, molecular clouds, and nearby galaxies, (vi) measure the diffuse isotropic gamma-ray background up to TeV energies, and (vii) explore the discovery space for dark matter (see Baltz et al. 2008 for a detailed roadmap on this last issue).

As for the present status, following its launch in June 2008, Fermi began a sky survey in August 2008. The Fermi/LAT instrument in 3 months produced a deeper and better-resolved map of the γ-ray sky than any previous space mission. The Fermi Collaboration has already presented initial results for energies above 100 MeV for the 205 most significant (statistical significance greater than 10σ) γ-ray sources in these data, which are the best-characterized and best-localized γ-ray sources in the early-mission data (Abdo et al. 2009). This catalog is the so-called Bright Source

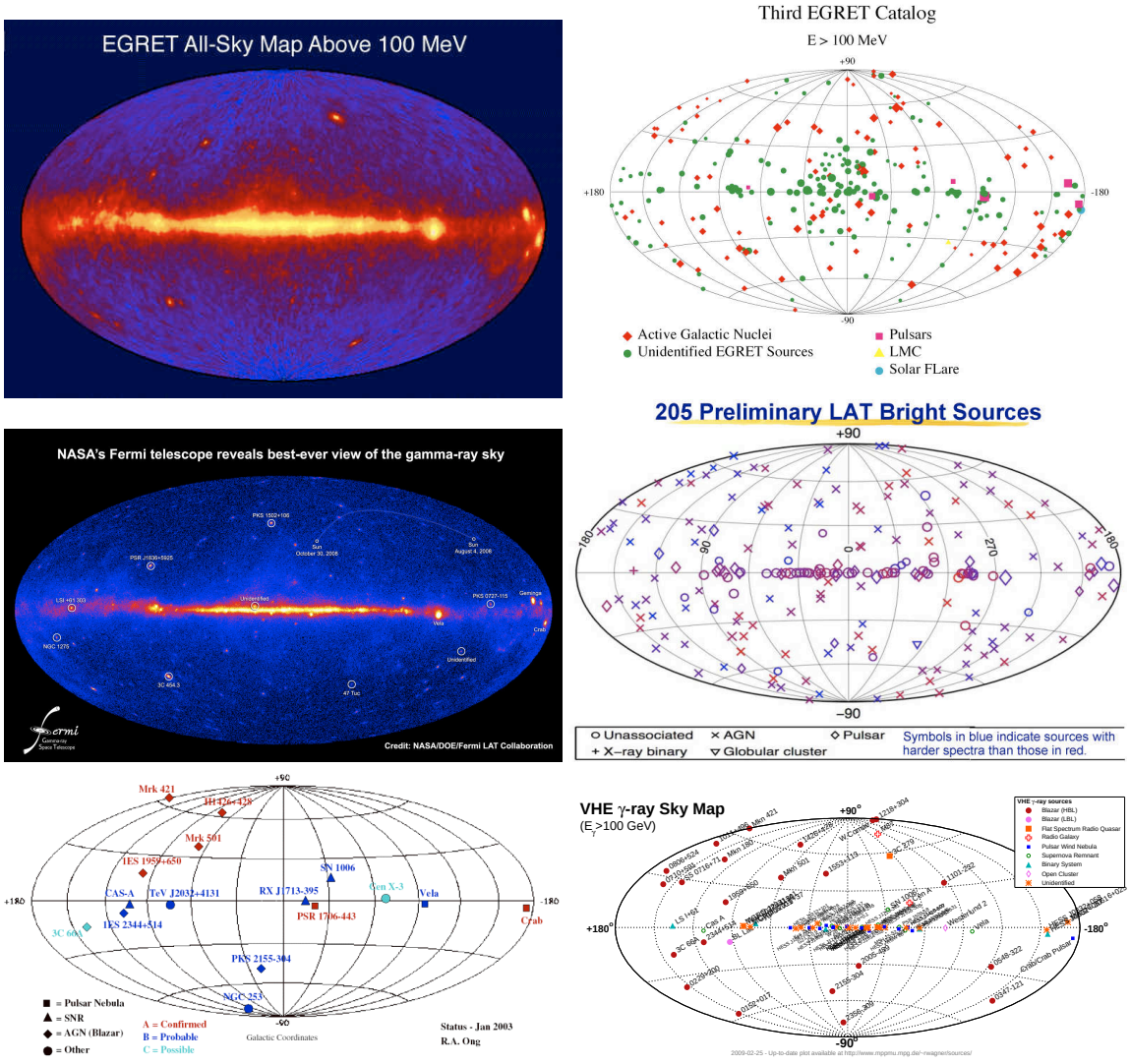

Figure 1.20 *Top*: The EGRET all-sky map above 100 MeV (left) and the Third (and final) EGRET Catalog of detected sources (right) (Credit: EGRET team). *Middle*: The Fermi all-sky map after 3 months of operation (left) and the corresponding 205 Fermi Bright Source Catalog (right) (Credit: Fermi team). *Bottom*: The TeV sky as of early 2003 (left), with only 17 sources known; since then, a lot of new sources have been discovered with the new generation IACTs, as can be clearly seen in the updated version of this map above 100 GeV (right).

Catalog (BSC), although the first official LAT catalog is planned for release after the first year of operations. In FIg. 1.20 the sources of the BSC are shown in an all-sky map. The Third EGRET Catalog is also shown as comparison in the same Figure, as well as an all-sky map of detected sources at even higher energies (>100 GeV). In addition to this important new γ-ray catalog, there are other Fermi highlights, like

the measurement of the Cosmic Ray $e^+ + e^-$ spectrum from 20 GeV to 1 TeV (Abdo et al. 2009b) or the discovery of new pulsars and AGNs (see e.g. Abdo et al. 2008 and Abdo et al. 2009c respectively).

1.6.4 Planned instruments for the near future

There are essentially two enormous efforts under way to improve the IACT capabilities for the next decade: the Cherenkov Telescope Array, or CTA, which is essentially an European effort, and the Advanced Gamma-ray Imaging System (AGIS), which is the analogous in the U.S.

The Cherenkov Telescope Array (CTA) is an European project to build a new generation ground-based γ-ray instrument that operates in the energy range extending from some tens of GeV to above 100 TeV. It is conceived as an open observatory and will consist of two arrays of IACTs: a first one at the Northern Hemisphere which will preferentially study extragalactic objects at the lowest possible energies; a second array at the Southern Hemisphere to cover the full energy range and specially concentrate on galactic sources. The CTA scientific objectives go beyond high energy astrophysics into Cosmology and Fundamental Physics. A more detailed description of the project can be found in Martínez (2008)[4].

CTA intends to improve the flux sensitivity of the current generation of IACTs such as MAGIC, HESS and VERITAS by an order of magnitude. Although the exact design of CTA is being studied and not precisely defined as of now, a possible design could be a combination of arrays of 2-3 different telescope sizes. A large number (several tens) of mid-size telescopes will provide for the millicrab sensitivity and high angular resolution (up to a factor $\sim$5 than present IACTs) in the core energy range from about 100 GeV up to 10 TeV. An extension of a few (4-9) very large diameter telescopes and many (up to 100) very small telescopes distributed over a large area enlarge the energy range from several 10 GeV up to 100 TeV. A sketch of the design is shown in Fig. 1.21. The project could be running as early as 2015, although this date is very dependent on funding.

The Advanced Gamma-ray Imaging System (AGIS) is a next-generation ground-based γ-ray observatory being planned in the U.S. The AGIS project mirrors the CTA project being discussed in Europe. As CTA, it is expected that AGIS will improve the sensitivity of current IACTs by one order of magnitude. AGIS will also have substantially improved angular resolution, which will constrain the origin of detected gamma-rays more tightly, enabling astronomers to better model the mechanisms responsible for emission. The energy range

[4]or you can also visit the CTA website: http://www.cta-observatory.org

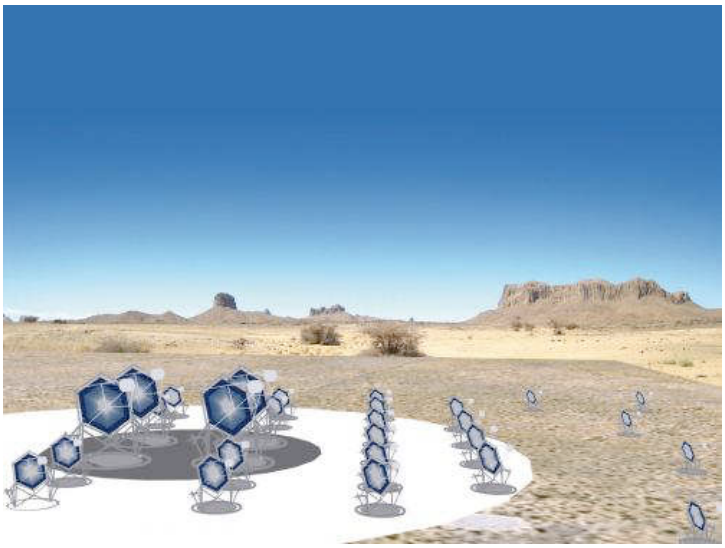

Figure 1.21 *Left*: A possible design of CTA, the Cherenkov Telescope Array project. Large mirrors in the centre collect enough light to catch dim showers from low-energy gamma rays. To collect large statistics at high energies smaller mirrors cover an area of a few square kilometers (ASPERA/D.Rouable). *Right*: A telescope prototype for AGIS.

over which AGIS is sensitive will also be larger than available in the present day (few GeV to ∼100 TeV). This will allow detection of more distant sources, from which higher energy γ-rays are absorbed. Although the exact configuration of the AGIS observatory has not been specified yet, it will probably consist of a large array of moderate sized IACTs covering an area of 1 km^2 on the ground. A more detailed description of the project can be found in Buckley et al. (2008)[5].

1.7 Present status of γ-ray Dark Matter searches and hints of detection

As already discussed, there is an increasing hope that the new generation of IACTs would detect in the very near future the gamma-rays coming from the annihilation products of the SUSY Dark Matter (DM) in galaxy haloes, thus helping to solve the problem of the nature of the DM. The lightest supersymmetric particle (LSP) has been proposed to be a suitable candidate for the non-baryonic Cold Dark Matter (CDM). The LSP is stable in SUSY models where R-parity is conserved and its annihilation cross section and mass leads appropriate relic densities in the range allowed by WMAP, i.e. $0.095 < \Omega_{DM}\ \mathrm{h}^2 < 0.129$. Most of SUSY symmetry breaking scenarios yields the lightest neutralino as the leading candidate for the cold DM.

[5]or you can also visit the AGIS website: http://www.agis-observatory.org

In the Lambda Cold Dark Matter (ΛCDM) paradigm, which represents the most accepted cosmological scenario at present (see Section 1.2), around 23% of the Universe consists of non-barionic Dark Matter (DM). This kind of DM is needed in order to explain a large amount of astrophysical processes at all scales, such as the formation of structures in the early Universe, their evolution with time so that they can form the structures observable today, the results from gravitational lensing, the rotation curves of individual galaxies, etc (Section 1.1). To be able to explain these astrophysical puzzles, the DM particles should interact very weakly with the ordinary matter and should have low thermal velocities (Section 1.4.2). A very good candidate is the neutralino, that fulfill the above mentioned characteristics and arises in the context of SUSY (SuperSymmetry, the most preferred Particle Physics scenario beyond the Standard Model, briefly presented in Section 1.4.2 as well). An interesting property of the neutralino is that it is predicted to be its own antiparticle, which means that it will annihilate when interacting with other neutralinos. This fact is crucial for detectability purposes and represents indeed the main vehicle used at present in DM searches. One of the products of these annihilations are predicted to be gamma-rays (Section 1.5.2), whose specific energy will vary according to the chosen particle physics model, but that is expected to lie in the energy range covered by the current Imaging Atmospheric Cherenkov Telescopes (IACTs) like CANGAROO, HESS, MAGIC and VERITAS (Section 1.6.2). The DM annihilation flux is proportional to the square DM density, which means that the best places to search for DM in the Universe are those with the highest expected DM densities. Distance is also very important, since high DM dominated systems that are located too far from us will yield too low DM annihilation fluxes at Earth. Having both considerations in mind, it is clear that the Galactic Center should be a very good candidate, but also dwarf spheroidal galaxies satellites of the Milky Way, and nearby galaxy clusters arise as very good candidates for DM searches.

At present, different astrophysical objects (the Galactic Center, galaxy clusters, dwarf galaxies) have been observed in γ-rays and studied in the context of DM searches. These observations were mainly carried out by current IACTs from the ground, like MAGIC or HESS. As known, no clear signal from DM annihilation has been found yet (at least unequivocal). Here I will briefly review the present status of DM searches, although some of them will be discussed more in detail in other Chapters of this Thesis (in particular MAGIC observations of dwarfs).

- **Galactic Center**: In principle, the best option for DM searches seems to be the Galactic Centre (GC), since a high DM concentration is expected there and it is also very near compared to other potential targets. However, the GC is a very crowded region, which makes it difficult to discriminate between a possible γ-ray signal due to neutralino annihilation and other astrophysical sources. Whipple (Kosack et al. 2004), CANGAROO (Tsuchiya et al. 2004),

and specially HESS (Aharonian et al. 2004) and MAGIC (Albert et al. 2006) have already carried out detailed observations of the GC and all of them reported a gamma point-like source at the Sag A* location. However, if this signal was interpreted as fully due to DM annihilation, it would correspond to a very massive neutralino very difficult to fit within the WMAP cosmology in the preferred SUSY framework (Bergström 2005) (although an alternative scenario with multi-TeV neutralinos compatible with WMAP is still possible, see Profumo 2006). Furthermore, an extended emission was also discovered in the GC area (see Fig. 1.22), but it correlates very well with already known dense molecular clouds (Aharonian et al. 2006). Recently, new HESS data on the GC have been published and a reanalysis has been carried out by the HESS collaboration (Aharonian et al. 2006b). In this work, they especially explore the possibility that some portion of the detected signal is due to neutralino annihilation. According to their results, at the moment it is not possible to exclude a DM component hidden under a non-DM power-law spectrum due to an astrophysical source.

- **Dwarf spheroidal galaxies**: they represent a very good option, since they are not plagued by the problems of the GC, some of them are the most DM dominated systems known in the Universe, with very high mass to light ratios up to $\sim$1000 according to recent works (Strigari et al. 2007), and several are located nearer than 100 kpc from us. Draco is probably the dwarf with more observational constraints and represents a very good DM candidate. The MAGIC telescope observed Draco for a total observation time of 7.8 hours during May 2007 (Albert et al. 2008), but found no gamma signal above an Energy threshold of 140 GeV. It was possible to derive, however, an upper limit for the flux (2σ level) to be around 1.1 x 10^{-11} ph cm^{-2} s^{-1}, assuming a power-law with spectral index -1.5 (probably quite appropriate for neutralino annihilations) and a point-like source. Following Sánchez-Conde et al. (2007) to assume a DM distribution model for Draco and Battaglia et al. (2004) to choose some benchmark mSUGRA models, they estimate how far they could be from a successful DM signal detection in Draco. Doing so, the obtained upper limits from MAGIC observations are $\sim 10^3$-10^9 above the predicted values. Although still very far, these results exclude at least a very high DM annihilation flux. Furthermore, it has to be noted that first-order radiative corrections (Bringmann et al. 2008) and the role of substructure (Kuhlen et al. 2008), which may boost the signal, were not yet included in the calculations.

  Some time later (Spring 2008) also the Willman 1 dSph was observed for a total of 15.5 hours with MAGIC. Again, no significant γ-ray emission was found above 100 GeV, although the derived upper limits for the flux were more stringent in this case (Aliu et al. 2009), of the order of 10^{-12} ph cm^{-2} s^{-1}. A comparison with predictions from several of the established neutralino benchmark models

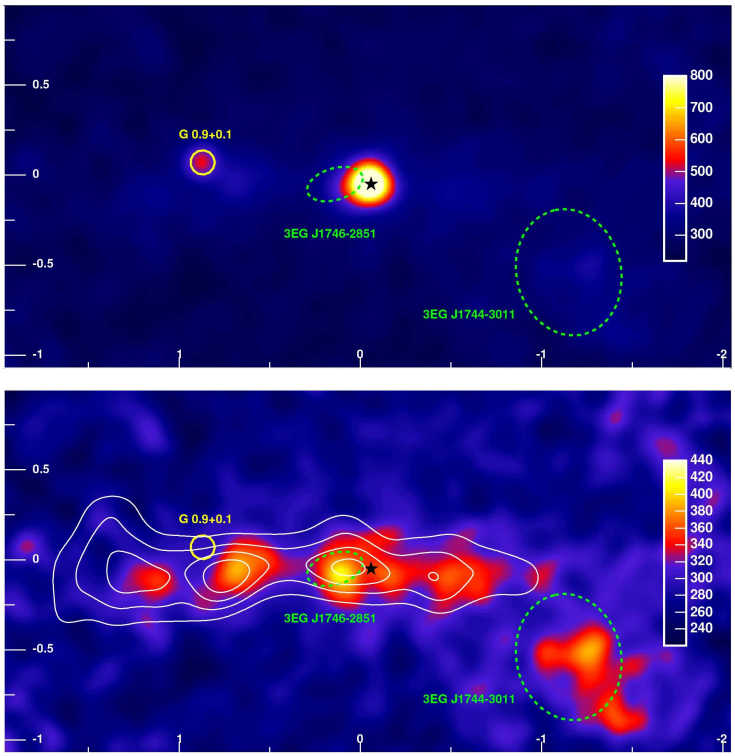

Figure 1.22 HESS γ-ray images of the GC region. *Top*: γ-ray count map. *Bottom*: same map after subtraction of the two dominant point sources, showing an extended band of gamma-ray emission. White contour lines indicate the density of molecular gas, traced by its CS emission. The excess observed along the Galactic plane consists of $\sim$3500 gamma photons, with a significance of 14.6σ. The energy threshold of the maps is 380 GeV due to the tight γ-ray selection cuts applied here to improve signal/noise and angular resolution (Aharonian et al. 2006). See text for DM-related discussion.

in the mSUGRA parameter space was made, this time including the recently discovered contribution of internal bremsstrahlung from the virtual sparticles that mediate the annihilation (Bringmann et al. 2008), but not possible substructure in the dwarf. The conclusion is that flux boost factors of three orders of magnitude are required even in the most optimistic scenario to match the obtained upper limits.

In addition to MAGIC, there are also other IACTs that have already carried out observations of some of the Milky Way satellite galaxies in the context of DM searches. This is the case of HESS, which observed Canis Major for 9.6 hours observation time in November 2006 (Aharonian et al. 2009). No significant excess was found above an energy threshold around 100 GeV. Unlikely, from this data they cannot exclude any of the pMSSM or KK models compatible

with WMAP+SDSS constraints. They derived, however, an upper limit for the mass of this dwarf to be around 10^9 $M_\odot$. HESS also observed Sagittarius for 11 hours exposure time in June 2006 (Aharonian et al. 2008). No significant excess was found above E_{th} >250 GeV, although they claimed the exclusion of some pMSSM models from the data assuming a core DM density profile for this galaxy. The Whipple IACT also observed two galaxy satellites during 2003: Draco (14.3 h) and UMi (17.2 h). Again, no significant excess was found above 400 GeV, and it was not possible to rule out any of the MSSM allowed models from these observations (Wood et al. 2008).

The MAGIC observational campaigns carried out in the context of DM searches for Draco and Willman 1 constitute an essential part of this Thesis, since I was involved both in the data acquisition and in the theoretical interpretation of the data. Therefore, they will be presented in detail in Chapters 8 (Draco) and 9 (Willman 1).

- **Galaxy clusters**: Clusters of galaxies are the largest and most massive gravitationally bound systems in the Universe, with masses of 10^{14}-10^{15} $M_\odot$, of which galaxies, gas and DM contribute roughly 5, 15 and 80 %, respectively (see e.g. Sarazin (1988) for a review). This makes them very attractive also in DM searches, despite the fact that they are not as near as other potential DM candidates. While no cluster has been firmly detected as a gamma-ray source so far, they are expected to be significant gamma-ray emitters for conventional physical processes. For DM purposes, it will be necessary to understand and to model this non-exotic emission in order to discriminate it from a possible DM annihilation signal. Some galaxy cluster observations have been performed by some of the IACTs currently in operation, but only poor upper limits have been obtained. For example, those coming from the HESS Collaboration for Coma, Abell 496 (Domainko et al. 2008), and Abel 85 (Aharonian et al. 2009b); from VERITAS for Coma (Perkins 2008) and from Whipple for Perseus and Abell 2029 (Krawczynski et al. 2005). All of them were preceded by EGRET upper limits at lower energies (Reimer et al. 2003).

There are also other proposed DM scenarios in the literature that still lack gamma observations, like Milky Way substructure (for which Fermi could be specially relevant), nearby microhalos (again more readily accessible to Fermi), Intermediate Mass Black Holes (IMBHs), etc.

In conclusion, there is no conclusive evidence of DM annihilation at present, but there have been several claims of discovery in the last few years, or at least **hints of DM detection**, coming from different DM search strategies rather than those based on γ-rays (note that, in γ-rays, certainly the **Galactic Center** observations may be considered as a hint, although as discussed above a DM interpretation of the data

is strongly disfavored by the most preferred theoretical models). Below I will briefly discuss some of them (I refer to Hooper 2009 for an excellent and updated review on each of them):

1. *The PAMELA and ATIC Excesses*: The PAMELA experiment recently reported an unexpected anomaly in the positron to positron-plus-electron ratio above 10 GeV (Adriani et al. 2009), in this way confirming previous claims from HEAT (Coutu et al. 2001) and AMS-01 (Olzem et al. 2006). Also recently, the ATIC balloon experiment has published a feature between ∼300-800 GeV in the cosmic ray electron (plus positron) spectrum, with a maximum ∼600 GeV. In addition to both excesses, WMAP data from the central region of our galaxy seems to point to an excess of microwave emission that can be interpreted as due synchrotron emission coming from a population of electron and positrons with a hard spectral index (e.g. Hooper et al. 2007). All these observations taken together seemed to point to essentially one of the following interpretations: (1) emission from pulsars (e.g. Profumo 2008) or DM annihilations (e.g. Bergström et al. 2009). Certainly, although the data could be explained by the latter possibility, the an annihilation rate should be many hundred times larger than typically expected, and should need a rather special DM distribution as well. Therefore, at present, the most plausible explanation of this excess is an scenario where its origin is a nearby pulsar or pulsars. It is important to note here, however, that very recently Fermi also published relevant data in this discussion: Fermi does not confirm the ATIC excess (Abdo et al. 2009b). Also the HESS collaboration reported data above 340 GeV in the cosmic ray electron spectrum (Aharonian et al. 2009c). The H.E.S.S. data with their lower statistical errors show no indication of a structure in the electron spectrum, but rather a power-law spectrum. This makes the situation even more difficult to clarify (see Fig. 1.23).

2. *The WMAP Haze*: In addition to detailed CMB maps, data from WMAP has also provided critical information on the standard interstellar medium mechanisms. These observations have revealed an excess of microwave emission 20° around the Galactic Center, more or less with radial symmetry, known as "the WMAP haze" (Dobler & Finkbeiner 2008). One of the possible explanations is DM annihilation (Hooper et al. 2007; Cáceres 2009). Again, Fermi should play a crucial role to dilucidate the real origin of this excess, specially taking into account that, according to recent works, the annihilation cross section as well as the DM density profile needed to reproduce the WMAP haze imply a gamma-ray flux that should be observed by this satellite (Hooper et al. 2008).

3. *DAMA Annual Modulation*: recently, this DM direct detection experiment reported evidence for an annual modulation (at 8σ level) in its rate of nuclear recoils that could be interpreted as due to WIMP interactions with ordinary

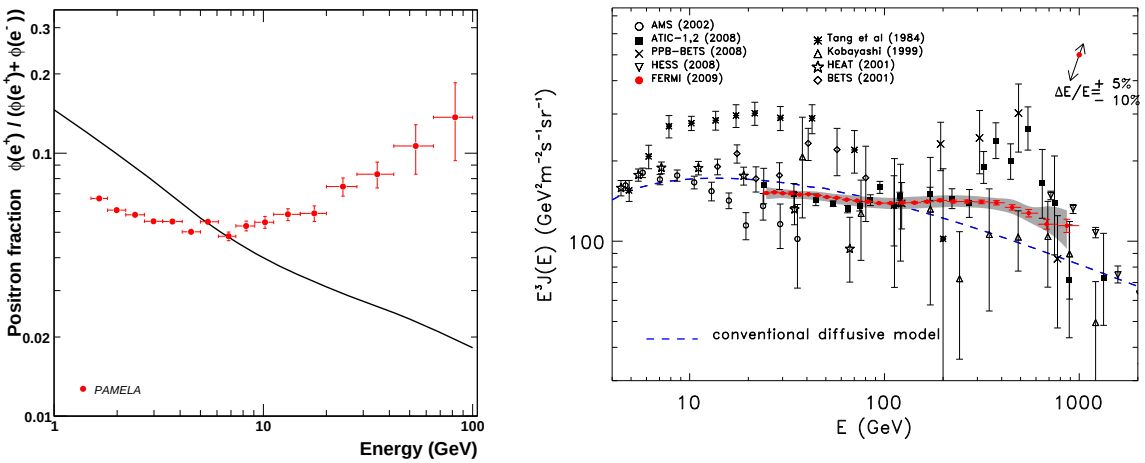

Figure 1.23 *Left*: The PAMELA positron fraction compared with the theoretical model (Adriani et al. 2009). *Right*: The Fermi LAT cosmic ray electron spectrum (red filled circles). Systematic errors are shown by the gray band. Other high-energy measurements and a conventional diffusive model are shown (Abdo et al. 2009b).

matter (Bernabei et al. 2008). The DAMA Collaboration excluded any systematics that could be producing the measured signal. However, this DM detection claim is very controversial, since other experiments that are currently scanning the same region of the DAMA parameter space could not find the same evidence. This point was already previously discussed in Section 1.5.1.

4. *The INTEGRAL 511 keV Line*: in 2003, the INTEGRAL satellite confirmed a bright emission of 511 keV photons from the region of the Galactic Bulge approximately spherically symmetric ($\sim$6° diameter). This signal is some orders of magnitude larger than expected from pair creation via cosmic ray interactions with the interstellar medium (Jean et al. 2003). Therefore, given the difficulties to explain this emission with conventional astrophysical sources, some works appeared that proposed a DM annihilation origin (Boehm et al. 2004). If this was the case, the DM particle should have a mass in the range 1-3 MeV, i.e. the so-called Light DM.

5. *EGRET Diffuse Galactic Spectrum*: an excess of gamma-rays seems to be present also in EGRET data collected from the whole sky above approximately 1 GeV, which has been interpreted as an evidence of DM annihilations in the Milky Way halo (e.g. de Boer et al. 2005). The data would imply a WIMP mass $\sim$50-100 GeV, although this interpretation is not exempt of several difficulties. Preliminary data from the Fermi satellite, however, does not support this excess. More Fermi observations are needed in order to definitely clarify the situation.

6. *EGRET Diffuse Extragalactic Spectrum*: it exists the possibility that a portion of the measured EGRET extragalactic diffuse gamma-ray flux could be due to DM annihilations taking place throughout the Universe (e.g. Elsaesser & Mannheim 2005). Indeed, EGRET data fits quite well with WIMP masses around 500 GeV. The DM annihilation rate, however, seems to be quite high if compared to what it is expected from the most preferred particle physics and astrophysical models. More data is also needed, specially from Fermi.

Bibliography

Aalseth C. E., et al., 2008, Phys. Rev. Lett., 101, 251301

Abazajian K., Fuller G. M. and Patel M., 2001, Phys. Rev. D, 64, 023501

Abdo A. A., et al. [Fermi collaboration], 2008, Science, 322, 1218

Abdo, A. A., et al., 2009, ApJS, 183, 46

Abdo A. A., et al. [Fermi collaboration], 2009b, Phys. Rev. Lett., 102, 181101

Abdo A. A., et al. [Fermi collaboration], 2009c, ApJ, 697, 934

Adelman-McCarthy, J. K., et al. 2006, ApJS, 162, 38

Adriani O., et al., 2009, Nature, 458, 607

Aharonian F. A., 2004, *Very High Energy Cosmic Gamma radiation*, World Scientific Publishing Co., Singapore

Aharonian F. et al., [HESS Collaboration], 2004, A&A, 425, L13

Aharonian F. et al., [HESS Collaboration], 2006, Nature, 439, 695

Aharonian F. et al., [HESS Collaboration], 2006b, Phys. Rev. Lett., 97, 221102

Aharonian, F., et al., [HESS Collaboration], 2008, Astroparticle Physics, 29, 55

Aharonian F. et al., [HESS Collaboration], 2009, ApJ, 691, 175

Aharonian, F. et al., [HESS Collaboration], 2009b, A&A, 495, 27

Aharonian, F. et al., [HESS Collaboration], 2009c, arXiv:0905.0105

Ahmed, Z., et al. 2009, Phys. Rev. Lett., 102, 011301

Akerib D. S., et al., 2003, Phys. Rev. D, 68, 082002

Albert J., et al. [MAGIC collaboration], 2006, ApJ, 638, L101

Albert J., et al. [MAGIC collaboration], 2008, ApJ, 679, 428

Aliu J., et al. [MAGIC collaboration], 2009, ApJ, 695, 1

Alcock C., et al. 2000, ApJ, 542, 281

Alner G. J., et al., 2007, Astropart. Phys. 28, 287

Amati L., 2006, Mon. Not. Roy. Astron. Soc. 372, 233

Angle J., et al., [XENON Collaboration], 2008, Phys. Rev. Lett. 100, 021303

Angloher G., et al., Astropart. Phys. 2005, 23, 325

Ansari R., et al., 2004, arXiv:astro-ph/0407583

Atwood W. B., et al. [Fermi collaboration], 2009, ApJ, 697, 1071

J. Bagla, 2005, Curr. Sci. 88, 1088

Bahcall, J. N., Flynn, C., and Gould, A. 1992, ApJ, 389, 234

Bahcall N. and Fan X., 1998, ApJ, 504, 1

Baltz E. A. et al., 2004, arXiv:astro-ph/0412170

Baltz E. A. et al., 2008, JCAP, 7, 013

Battaglia, M., et al., 2004, European Phys. J. C, 33, 273

Begeman K. G., Broeils A. H. and Sanders R. H., 1991, MNRAS, 249, 523

Behnke E., et al. [COUPP Collaboration], Science, 319, 933

Bekenstein J. and Milgrom M., 1984, ApJ, 286, 7

Bekenstein J.D., 1988, Phys. Lett. B, 202, 497

Bekenstein, J. D., 2004, Phys.Rev. D, 70, 083509

Benetti et al. [Warp Collaboration], et al. 2008, Astroparticle Physics, 28, 495

Benoit A. et al., 2002, Phys. Lett. B, 545, 43

Bergström L. and Snellman H., Phys. Rev. D, 1988, 37, 3737

Bergström, L., Ullio, P., & Buckley, J. H., 1998, Astroparticle Physics, 9, 137

Bergström, L. 2000, Reports on Progress in Physics, 63, 793

Bergstrom L. et al., 2005, Phys. Rev. Lett., 95, 241301

Bergstrom, L., Edsjo, J., & Zaharijas, G. 2009, arXiv:0905.0333

Bernabei R., et al. [DAMA Collaboration], 2008, Eur.Phys.J., C56, 333

Bertone, G., Hooper, D., & Silk, J. 2005, Phys. Reports, 405, 279

Bertone, G., 2007, Astrophys. Space Sci., 309, 505

Binetruy P., Gaillard M.K. and Nelson B.D., 2001, Nucl. Phys. B, 604, 32

Boehm C., Hooper D., Silk J., Casse M. and Paul J., Phys. Rev. Lett., 2004, 92, 101301

Bond J.R., Efstathiou G. and Silk J., 1980, Phys. Rev. Lett., 45, 1980

Briel, U.G. and Henry, J.P., 2007, arXiv:astro-ph/9711237

Bringmann, T., Bergström, L., & Edsjö, J. 2008, *JHEP*, 1, 49

Broadhurst T., Umetsu K., Medezinski E., Oguri M. and Rephaeli Y., 2008, ApJ, 685, L9

Buckley J. et al., 2008, *Procs. of the 4th International Meeting on High Energy Gamma-Ray Astronomy*, AIP Conf. Procs., 1085, 902-905

Buckley J. et al., 2008, *Report from the Dark Matter Science Working group of the APS commissioned White paper on ground-based TeV gamma ray astronomy*, arXiv:astro-ph/0812.0795

Bullock, J. S., Dekel, A., Kolatt, T. S., Kravtsov, A. V., Klypin, A. A., Porciani, C., & Primack, J. R. 2001, ApJ, 555, 240

J. S. Bullock, K. R. Stewart and C. W. Purcell, 2008, *IAU Symposium 254, The Galaxy Disk in Cosmological Context*, arXiv:0811.0861

Cáceres, G., 2009, *SnowPAC 2009 conference proceeding*, to appear in ASP Conference Series, arXiv:0906.4306

Carlberg R.G. et al., 1999, ApJ, 516, 552

Choi K.Y. and Roszkowski L., 2006, AIP Conf.Proc., 805, 30

Clowe, D., et al., 2006, ApJ, 648, L109

Cole, S., et al. 2005, Mon. Not. Roy. Astron. Soc., 362, 505

Copeland E.J., Sami M. and Tsujikawa S., 2006, Int. J. Mod. Phys. D 15, 1753

Coutu S., et al. [HEAT-pbar Collaboration], 2001, *in Proceedings of 27th ICRC*

Covi L., Roszkowski L., Ruiz de Austri R. and Small M., 2004, J. High Energy Phys., 0406, 003

de Blok, W. J. G., McGaugh, S. S., Rubin, V. C., 2001, Astron. J., 122, 2396

de Blok W. J. G., 2005, ApJ, 634, 227

de Boer W., Sander C., Zhukov V., Gladyshev A. V. and Kazakov D. I., 2005, Phys. Rev. Lett. 95, 209001

Diemand, J., Zemp, M., Moore, B., Stadel, J., & Carollo, C. M. 2005, Mon. Not. Roy. Astron. Soc., 364, 665

Diemand, J., Kuhlen, M., & Madau, P. 2007, ApJ, 657, 262

Diemand J., Kuhlen M., Madau P., Zemp M., Moore B., Potter D., Stadel J., 2008, Nature, 454, 735

Dobler G. and Finkbeiner D. P., ApJ, 2008, 680, 1222

Dodelson S. and Widrow L. M., 1994, Phys. Rev. Lett., 72, 17

Domainko, W., Benbow, W., Hinton, J. A., & et al. 2008, *in International Cosmic Ray Conference, Vol. 3, International Cosmic Ray Conference*, 953

Drukier A. K., Freese K. and Spergel D. N., 1988, Phys. Rev. D 37, 3388

Duda G., Gelmini G., Gondolo P., Edsjo J. and Silk J., 2003, Phys. Rev. D, 67, 023505

Ellis, J., Olive, K. A., Santoso, Y., & Spanos, V. C. 2005, Phys. Rev. D, 71, 095007

Elsaesser D. and Mannheim K., 2005, Phys. Rev. Lett., 94, 171302

Enomoto R. et al., 2002, Astropart. Phys., 16, 235

Fabian A. and Allen S., 2003, *Procs. of the XXI Texas Symposium on Relativistic Astrophysics*, World Scientific Publishing, 197

Fabian et al., 2006, MNRAS, 366, 417

Falco E.E., Kochanek C.S. and Munoz J.A., 1998, ApJ, 494, 47

Feng J. L., Rajaraman A. and Takayama F., 2003, Phys. Rev. D, 68, 063504

Fixsen, D. et al. [COBE Collaboration], 2006, ApJ, 473, 576

Flores, R. A., & Primack, J. R., 1994, ApJ, 427, L1

Freese, K., Fields, B., & Graff, D. 2000, *Marina del Rey 2000, Sources and detection of Dark Matter and Dark Energy in the Universe*, astro-ph/0007444

Gehrels N. and Michelson P., 1999, Astropart. Phys., 11, 277

Gentile G., Tonini C. and Salucci P., 2007, Astron. Astrophys. 467, 925

Gnedin O. and Primack J., 2004, Phys. Rev. Lett. 93, 061302

Graff D.S. and Freese, K. 1996, ApJ, 467, L65

Gunn J. E., Lee B. W., Lerche I., Schramm D. N. and Steigman G., 1978, ApJ, 223, 1015

Hayashi, E., Navarroberg, J. F., & Springel, V. 2007, MNRAS, 377, 50

G. Hinshaw, et al. [WMAP collaboration], 2009, ApJS, 180, 225-245

Hofmann, S., Schwarz, D. J., & Stöcker, H. 2001, Phys. Rev. D, 64, 083507

Holder, G. P., & Carlstrom, J. E. 1999, Microwave Foregrounds, 181, 199

Holmberg E., 1941, ApJ, 94, 385

Hooper D., Finkbeiner D.P. and Dobler G., 2007, Phys. Rev. D, 083012

Hooper D., Zaharijas G., Finkbeiner D. P. and Dobler G., 2008, Phys. Rev. D, 77, 043511

Hooper D., 2009, *Based on lectures given at the 2008 Theoretical Advanced Study Institute (TASI)*, astro-ph/0901.4090

Ivanov P., Naselsky P. and Novikov I., 1994, Phys. Rev. D, 50, 7173

Kashlinsky A., 1998, Phys. Rep., 307, 67

Kashlinsky, A., Atrio-Barandela, F., Kocevski, D., & Ebeling, H. 2008, ApJL, 686, L49

Koopmans L. V. and Treu T., ApJ, 2003, 583, 606

Hinton J. A., 2004, New Astron. Rev., 48, 331

Hoekstra H., Yee H. and Gladders M., 2002, New Astron. Rev., 46, 767

Jean P. et al., 2003, Astron. Astrophys. 407, L55

Jungman G., Kamionkowski M. and Griest K., 1996, Phys. Rept., 267, 195

Kawasaki M. and Moroi T., 1995, Prog. Theor. Phys. 93, 879

Klypin, A.A. et al., 1999, ApJ, 522, 82

Klypin A.A. and Prada F., 2009, ApJ, 690, 1488

Kosack K. et al., 2004, ApJ, 608, L97

Kowalski, M., et al. 2008, ApJ, 686, 749

Kravtsov, A. V., Klypin, A. A., Bullock, J. S., & Primack, J. R. 1998, ApJ, 502, 48

Kravtsov, A. V., Gnedin, O. Y., & Klypin, A. A. 2004, ApJ, 609, 482

Kravtsov A., 2009, Advances in Astronomy, submitted, astro-ph/0906.3295

Krawczynski, H., Perkins, J., and VERITAS Collaboration. 2005, *in Bulletin of the American Astronomical Society*, Vol. 37, Bulletin of the American Astronomical Society, 1421

Kuhlen, M., Diemand, J., & Madau, P. 2008, ApJ, 686, 262

Lee H. S. et al. [KIMS Collaboration], 2007, Phys. Rev. Lett. 99, 091301

Lin Y. and Wandelt B.D. , 2006, Astropart. Phys., 25, 151

Łokas, E., Mamon, G., Prada, F., 2006, EAS Publications Series, 20, 113

Lorentz E. et al., 2004, New Astron. Rev., 48, 339

Martínez M., 2008, *Proceedings of the 4th International Meeting on High Energy Gamma-Ray Astronomy*, AIP Conf. Procs., 1085, 824

Mateo M., 1998, Ann. Rev. Astron. Astrophys., 36, 435

McGaugh, S. S., & de Blok, W. J. G. 1998, ApJ, 499, 41

Metcalf, R. B., Moustakas, L. A., Bunker, A. J., & Parry, I. R. 2004, ApJ, 607, 43

Milgom, M., 1983, Astrophys. J., 270, 365

Moore, B., 1994, Nature, 370, 629

Moore B., Governato F., Quinn T., Stadel J. and Lake G., 1998, MNRAS, 499, L5

Moore, B., Ghigna, S., Governato, F., Lake, G., Quinn, T., Stadel, J., & Tozzi, P. 1999, ApJ, 524, L19

Moore, B., Diemand, J., Madau, P., Zemp, M., & Stadel, J. 2006, MNRAS, 368, 563

Moustakas L.A. and Metcalf R. B., 2003, MNRAS, 339, 607

Munshi D., Valageas P., Van Waerbeke L. and Heavens A., 2008, Phys. Rept. 462, 67

Muñoz C., 2004, Int. J. Mod. Phys. A, 19, 3093

Navarro J. F., Frenk C. S. and White S. D., 1996, ApJ, 462

Navarro J. F., Frenk C. S. and White S. D. M., 1997, ApJ, 490, 493

Olzem, Jan [AMS Collaboration], 2006, *Talk given at the 7th UCLA Symposium on Sources and Detection of Dark Matter and Dark Energy in the Universe, Marina del Ray, CA, Feb 22-24, 2006*

Paczynski B., 1986, ApJ, 304, 1

Pagels H. and Primack J. R., 1982, Phys. Rev. Lett. 48, 223

Perivolaropoulos, L., & Shafieloo, A. 2009, Phys. Rev. D, 79, 123502

Perivolaropoulos L., 2008, *Invited article to the TSPU anniversary volume "The Problems of Modern Cosmology" on the occasion of the 50th birthday of Prof. S. D. Odintsov*, astro-ph/0811.4684

Perkins, J. S. 2008, *in American Institute of Physics Conference Series*, Vol. 1085, American Institute of Physics Conference Series, ed. F. A. Aharonian, W. Hofmann, & F. Rieger, 569â€“572

Perlmutter, S., 1999, Phys. Rev. Lett., 83, 670

Perlmutter S. et al., 1999b, ApJ, 517, 565

Polarski D. and Gannouji R., 2008, Phys. Lett. B, 660, 439

Prada, F., et al. 2003, ApJ, 598, 260

Prada, F., Klypin, A., Flix, J., Martínez, M., & Simonneau, E. 2004, Phys. Rev. Lett., 93, 241301

Primack J.R., 2001, *Proceedings of International School of Space Science 2001*, ed. Aldo Morselli (Frascati Physics Series), astro-ph/0112255

Profumo S., 2006, Phys. Rev. D, 72, 103521

Profumo S., 2008, preprint, arXiv:0812.4457

Reimer, O., Pohl, M., Sreekumar, P., and Mattox, J. R. 2003, ApJ, 588, 155

Riess, A. G. et al., 1998, Astron. J., 116, 1009

Salati P. et al., 1999, Astron. and Astrophys., 350, 57

Sánchez A.G. et al., 2006, MNRAS, 366, 189

Sánchez-Conde M. A., Prada F., Lokas E. L., Gomez M. E., Wojtak, R. & Moles, M., 2007, Phys. Rev. D, 76, 123509

Sanders, R. H. & McGaugh, S. S., 2002, Ann.Rev.Astron. & Astrophys, 40, 263

Sanglard V. et al. [The EDELWEISS Collaboration], 2005, Phys. Rev. D, 71, 122002

Sarazin, C. L. 1988, *X-ray emission from clusters of galaxies* (Cambridge Astrophysics Series, Cambridge: Cambridge University Press

Servant G. and Tait T. M. P., 2003, Nucl. Phys. B, 650, 391

Sigad Y., Eldar A., Dekel A., Strauss M.A. and Yahil A., ApJ, 495, 516

Simon, J. D., & Geha, M. 2007, ApJ, 670, 313

Soussa M. E. and Woodard R. P., 2003, Class. Quant. Grav. 20, 2737

Spergel D. N. et al. [WMAP Collaboration], 2007, Astrophys. J. Suppl. 170, 377

Springel, V. et al., 2005, Nature, 435, 629

Springel, V. et al., 2008, MNRAS, 391, 1685

Springel V. et al., 2008b, Nature, 456, 73

Stecker F. W., 1978, ApJ, 223, 1032

Steffen F.D., 2009, Eur. Phys. J., C59, 557

Strigari L. E., Koushiappas S. M., Bullock J. S and Kaplinghat M., 2007, Phys. Rev. D, 75, 083526

Strigari L E, Koushiappas S M, Bullock J S, Kaplinghat M, Simon J D, Geha M and Willman B, 2008, ApJ, 678, 614

Taoso M, Bertone G. and Masiero A., 2008, JCAP 0803, 022

Tavani M. et al., 2008, Nuclear Instruments and Methods in Physics Research Sec. A, 588, 52

Tegmark M. et al. [SDSS Collaboration], 2004, ApJ, 606, 702

Tikhonov, A. V., & Klypin, A. 2009, MNRAS, 395, 1915

Tsuchiya K. et al., 2004, ApJ, 606, L115

Tyson J.A., Kochanski G.P. and Dellâ€™Antonio I.P., 1998, ApJ, 498, 107

Valenzuela, O., Rhee, G., Klypin, A., Governato, F., Stinson, G., Quinn, T., & Wadsley, J., 2007, ApJ, 657, 773

Vitvitska, M., Klypin, A. A., Kravtsov, A. V., Wechsler, R. H., Primack, J. R., & Bullock, J. S. 2002, ApJ, 581, 799

Vogt S. S., Mateo M., Olszewski E. W. and Keane M. J., 1995, Astron. Journal, 109, 151

Weekes T. C. et al., 2002, Astropart. Phys., 17, 221

Wang Y. and Mukherjee P., 2006, ApJ, 650, 1

Watkins, R., Feldman, H. A., & Hudson, M. J. 2009, MNRAS, 392, 743

Weinberg D.H. et al., 1999, ApJ, 522, 563

Weinberg, M. D., & Katz, N. 2002, ApJ, 580, 627

J. Wess and J. Bagger, 1992, *Supersymmetry And Supergravity*, Princeton, USA. Univ. Pr.

Wood-Vasey W. M. et al. [ESSENCE Collaboration], 2007, ApJ, 666, 694

Wood, M., et al., [Whipple Collaboration], 2008, ApJ, 678, 594

Zaritsky D., Smith R., Frenk C. and White S.D.M., 1997, ApJ, 478, 39

Zaritsky D., Shectman S.A., Thompson I., Harris J. and Lin D.N.C., 1999, Astronom. J., 117, 2268

Zwicky F., 1933, Helv. Phys. Acta 6, 110

Part I

A semi-analytical approach to the formation and evolution of CDM halos

2

Theoretical predictions for the outskirts of DM halos and comparison with N-body simulations[1]

In the present work we describe the formalism necessary to derive the properties of dark matter halos beyond two virial radius using the spherical collapse model (without shell crossing), and provide the framework for the theoretical prediction presented in Prada et al. (2006). We show in detail how to obtain within this model the probability distribution for the spherically-averaged enclosed density at any radii $P(\delta, r)$. Using this probability distribution, we compute the most probable and mean density profiles, which turns out to differ considerably from each other. We also show how to obtain the typical profile. Three probability distributions are obtained: a first one is derived using a simple assumption. Then we introduce an additional constraint to obtain a more accurate $P(\delta, r)$ which reproduces to a higher degree of precision the distribution of the spherically averaged enclosed density found in the simulations. A third probability distribution, the most accurate, is obtained imposing a strongest constraint. Finally, we compare our theoretical predictions for the mean and most probable density profiles with the results found in the simulations.

2.1 Introduction

The study of the density profile of cold dark matter halos beyond the virial radius is a subject of considerable relevance. From an observational point of view, knowledge of the shape of the density profile far beyond the virial radius is essential for an appropriate interpretation of gravitational lensing phenomena (e.g. Smith et al. 2001; Guzik & Seljak 2002; Hoekstra et al. 2004; Sheldon et al. 2004), the pattern of Lyman

[1]Based on the work by Betancort-Rijo et al. (2006) and Prada et al. (2006) (both including M. A. Sánchez-Conde).

alpha absorption around virialized systems (e.g. Barkana 2004; Bajtlik, Duncan & Ostriker 1988) as well as the motion of satellite galaxies as a test for dark matter distribution at large radii (Zaritsky & White 1994, Zaritsky et al. 1997; Prada et al. 2003, Brainerd 2004; Conroy et al. 2004). From the theoretical point of view, the study of the properties of dark matter halos at several virial radius in cosmological simulations provides an excellent benchmark for developing and testing the basic theoretical framework which will be decisive for a full understanding of the physical origin and formation of the ΛCDM halos.

Understanding halo properties involves a set of theoretical considerations. First, we have the issue of choosing the correct initial density profile. Also, there is the question of which processes are relevant to the gravitational evolution of the initial profile: is only the spherical collapse what matters or is triaxiality important? up to which radius can we use the standard spherical collapse model without shell crossing? are highly asymmetrical processes, like merging, relevant? In order to answer these questions it is very convenient to focus first on those properties of the halos which involve the fewest theoretical uncertainties.

The dark matter density profiles at several virial radius are particularly suitable to check whether the spherical collapse model can provide accurate predictions (see Prada et al. 2006). In fact, it has been shown that the spherical collapse model reproduces very well the relationship between the small values of the spherically-averaged enclosed density at those large distances and the radial velocity (Lilje et al. 1986).

We define the spherically-averaged enclosed density as:

$$\frac{\rho(< r)}{< \rho_m >} = 1 + \delta$$

where δ is the enclosed density contrast and $< \rho_m >$ the average matter density in the Universe. We can also define the spherically-averaged local density as:

$$\frac{\rho(r)}{< \rho_m >} = 1 + \delta'$$

where δ' is the density contrast in a narrow shell of radius r. We can then obtain the density contrast δ' from the enclosed density contrast δ using the relation:

$$\delta'(r) = \frac{1}{3r^2}\ \frac{d}{dr}(r^3\delta(r)). \tag{2.1}$$

Despite to all the effort done to understand the central dense regions of the dark matter halos in cosmological simulations, not much attention has been devoted to the study of the regions beyond the formal virial radius, i.e. the radius within which the spherically-averaged enclosed density is equal to some specific value. The main goal of the work presented in this Chapter is focused on the outskirts of the dark matter halos, where the correct evolution of the spherically-averaged enclosed density

profiles can essentially be obtained using the standard (without shell crossing) spherical collapse model. This model, first developed by Gunn & Gott (1972) and Gunn (1977), describes the collision-less collapse of a spherical perturbation in an expanding background. They introduced for the first time the cosmological expansion and the role of adiabatic invariance in the formation of individual objects. Later, Fillmore & Goldreich (1984) found analytical predictions for the density of collapsed objects seeded by scale-free primordial perturbations in a flat universe. Hoffman & Shaham (1985) generalized these solutions to realistic initial conditions in flat and open Friedmann models. Some studies have been done to include more realistic dynamics of the growth process (e.g. Padmanabhan 1996; Avila-Reese, Firmani & Hernández 1998; Lokas 2000; Subramanian, Cen & Ostriker 2000).

There are plenty of works in the literature using the spherical collapse model to predict the density profiles of dark matter halos mainly focused on explaining their central regions. For example Bertschinger (1985) used the spherical collapse with shell crossing to obtain the density profiles resulting from initial power law density profiles. Lokas & Hoffman (2000) considered more general initial profiles. The effect of non-radial motions has also been widely treated (see Ryden & Gunn 1987; Gurevich & Zybin 1988; Avila-Reese et al. 1998; White & Zaritsky 1992; Sikivie et al. 1997; Nusser 2001; Hiotelis 2001). Some of these authors have used arbitrary initial profiles, while others have assumed the mean initial profile around density maxima (Bardeen et al. 1986, BBKS). In all these works angular momentum is introduced by hand, although more recently it has been done in a more natural way (Nusser 2001; Ascasibar et al. 2004). Concerning to the outer parts of the dark matter halos, only Barkana (2004) has adopted an appropriate initial profile, but only for a restricted type of density profile (the typical profile). The more recent work by Prada et al. (2006) have obtained predictions for the mean and most probable density profiles and have provided a detailed comparison with cosmological simulations.

A proper understanding of the physics of dark matter halos involves predicting correctly not only the mean halo density profile for any given mass but also the whole probability distribution for the enclosed density contrast at any given radii, $P(\delta, r)$. A first attempt to determine it can be found in Prada et al. (2006), where it has been shown to be generally in good agreement with the cosmological simulations. Nevertheless, this probability distribution shows, at any radius, a longer tail for large values of δ, as compared to that from simulations at any radius. In this Chapter we present a more accurate prediction for the probability distribution $P(\delta, r)$ that constitutes the main new result of this work. We also give in detail the theoretical background of the predictions presented in Prada et al. (2006). The agreement of our new predictions with the simulations is excellent even in the tail of the distribution.

The work is organized as follows. In section 2.2 we present our theoretical framework and obtain the typical density profile of dark matter halos. In section 2.3 we show in detail how to obtain the probability distribution for the spherically-averaged enclosed density contrast at a given radii, $P(\delta, r)$, presented in Prada et al. (2006).

The most probable and mean profiles are derived. Then, in section 2.4, we compare our theoretical results with the results found in high resolution N-body cosmological simulations. In section 2.5, we obtain more accurate probability distributions than that used in the previous sections, and compare again with that found in the simulations. Final remarks are given in section 2.6.

2.2 The typical density profile of Dark Matter Halos

The present spherically-averaged enclosed density profiles attains a density contrast value of Δ_{vir} at certain radius, the so called virial radius. At larger radii the density contrast must be, by definition, smaller than Δ_{vir}, otherwise the virial radius would be larger than its nominal value.

We shall now make some comments on the values of Δ_{vir} and δ_{vir} that we use: although at several virial radius the spherically-averaged enclosed linear and actual densities are related by the spherical collapse model, the same does not apply within the virial radius. The spherically-averaged enclosed density contrast within one virial radius, Δ_{vir}, and the corresponding enclosed linear density contrast, δ_{vir}, are not related as homologous quantities at larger radii, because at one virial radius shell crossing has already becomes important. Consequently, the value of δ_{vir} corresponding to Δ_{vir}=340 (the value we adopted to define the virial radius) is somewhat uncertain. As a result of work still in progress (whose first steps have been already given in Sánchez-Conde et al. 2007) we will be able to provide the precise values for δ_{vir} and determine its possible small dependence on mass. Here we use for all masses δ_{vir}=1.9, a value that leads to very good results and that may be inferred from the fact that when Δ_{vir}=180, δ_{vir} seems to be close to 1.68 for all cosmologies (Jenkins et al. 2001).

It must be noted that for all our predictions it is irrelevant whether the value of Δ_{vir} that we use actually corresponds to the virial density contrast or not. By virial density contrast is usually meant the enclosed density contrast within the largest radii so that we have statistical equilibrium. The precise value of Δ_{vir} corresponding to this definition is still problematic but, to our purposes, it can be chosen freely to define a conventional "virial radius". Since we have used numerical simulations with Δ_{vir} equal to 340, we will take the same value by default in all the calculations.

Let $\delta_l(q, i)$ be a realization of the spherically-averaged initial enclosed density profile around a protohalo (with a given present virial radius, R_{vir}) linearly extrapolated to the present, where q is the lagrangian distance from the center of the halo to the given point and i is an index running over realizations. Any realization of the initial profile may be transformed using the standard spherical collapse model (without shell-crossing). We can use the relationship between the linear value of the density contrast within a sphere, δ_l, and the actual density contrast within that sphere, δ, for the concordant cosmology (Sheth and Tormen (2002)):

$$\delta_l(\delta) = \frac{1.676}{1.68647}\left[1.68647 - \frac{1.35}{(1+\delta)^{2/3}} - \frac{1.12431}{(1+\delta)^{1/2}} + \frac{0.78785}{(1+\delta)^{0.58661}}\right] \tag{2.2}$$

or, rather its inverse function $\delta(\delta_l)$ (Patiri et al.(2006) expression (4)):

$$\begin{aligned}\delta(\delta_l) = 0.993[(1 - 0.607(\delta_l - 6.5 \times 10^{-3}(1 - \theta(\delta_l)+ \\ +\theta(\delta_l - 1.55))\delta_l^2))^{-1.66} - 1]\end{aligned} \tag{2.3}$$

being θ the step function:

$$\theta(x) = \begin{cases} 1 & \text{if x} > 0 \\ 0 & \text{if x} \leq 0 \end{cases}$$

Transforming for every shell δ_l and q into δ and r (the Eulerian radius of the shell) we may obtain, in parametric form, the initial profile $\delta_l(q,i)$ spherically evolved, $\delta(r,i)$.

$$\delta(r,i) = \delta(\delta_l(q,i)); \qquad r = [1 + \delta(\delta_l(q,i))]^{-1/3} q \tag{2.4}$$

Consider now the ensemble of all halos, $\delta(r,j)$, attaining a δ value equal to Δ_{vir} at a virial radius and smaller values for larger radii. If we transform back these profile to their linear counterpart, we obtain the ensemble $\delta_l(q,j)$. Let us now take the average over this ensemble (now for a fixed value of q):

$$\bar{\delta}(q) \equiv < \delta(q,j) >_j$$

Evolving this profile by means of the spherical collapse model we obtain a profile which we call typical profile and represent by $\delta_t(r)$, that is, this profile is simply the mean profile in the initial conditions spherically evolved.

To obtain the mean linear density profile $\overline{\delta}_l(q)$, in our approach we first obtain the probability for $\delta_l(q)$ only with the condition $\delta_l(Q) = \delta_{vir}$:

$$P(\delta_l, q) \equiv P(\delta_l(q)|\delta_l(Q) = \delta_{vir}) = \frac{\exp\left(-\frac{1}{2}\frac{\left(\delta_l(q) - \frac{\sigma_{12}}{\sigma_1^2}\delta_{vir}\right)^2}{g}\right)}{\sqrt{2\pi}\ g^{\frac{1}{2}}} \tag{2.5}$$

where

$$g(q) \equiv \left(\sigma_2^2 - \frac{\sigma_{12}^2(q)}{\sigma_1^2}\right)$$

$$\sigma_1 \equiv \sigma(Q); \qquad \sigma_2 \equiv \sigma(q)$$

$$(\sigma(x))^2 = \frac{1}{2\pi^2}\int_0^\infty \mid \delta_k \mid^2 W_T^2(xk)\ k^2\ dk$$

$$\sigma_{12} = \sigma_{12}(q) = \frac{1}{2\pi^2} \int_0^\infty \mid \delta_k \mid^2 W_T(qk)\ W_T(Qk)\ k^2\ dk$$

$$W_T(x) = \frac{3(sin\ x\ - x\ cos\ x\ )}{x^3}$$

where $|\delta_k|^2$ stands for the power spectra of the density fluctuations linearly extrapolated to the present.

It is convenient to use a simple and accurate approximation for $\sigma_{12}(q)$:

$$\frac{\sigma_{12}(q)}{(\sigma(Q))^2} \simeq e^{-b(Q)\left((\frac{q}{Q})^2-1\right)} \tag{2.6}$$

where $b(Q)$ is a coefficient depending on the the size of the halo, Q:

$$b(Q) = -\frac{1}{2}\ \frac{d\ln\sigma(x)}{d\ln x}\bigg|_{x=Q}$$

If no restriction other than $\delta_l(Q) = \delta_{vir}$ were imposed on $\delta_l(q)$ the mean linear profile would be:

$$\overline{\delta}_l(q) = \int_{-\infty}^{\infty} P(\delta_l(q)/\delta_l(Q) = \delta_{vir})\ \delta_l(q)\ d(\delta_l(q)) = \delta_{vir}\frac{\sigma_{12}(q)}{\sigma(Q)} \equiv \delta_0(q) \tag{2.7}$$

However, we are interested on the mean profiles satisfying also $\delta_l(q) < \delta_{vir}$ **for** $q > Q$. So, we must use as mean profile:

$$\overline{\delta}_l(q) = \frac{\int_{-\infty}^{\delta_{vir}} P(\delta_l(q)/\delta_l(Q) = \delta_{vir})\ \delta_l(q)\ d(\delta_l(q))}{\int_{-\infty}^{\delta_{vir}} P(\delta_l(q)/\delta_l(Q) = \delta_{vir})\ d(\delta_l(q))} \tag{2.8}$$

$$= \delta_0(q) - \frac{\overline{\sigma}(q)\ e^{-\frac{1}{2}\ \frac{\left(\delta_{vir}-\delta_0(q)\right)^2}{(\overline{\sigma}(q))^2}}}{1 - \frac{1}{2}erfc\left(\frac{\delta_{vir}-\delta_0(q)}{\sqrt{2}\ \overline{\sigma}(q)}\right)}$$

$$\overline{\sigma}(q) \equiv (g(q))^{1/2}$$

Once we have $\bar{\delta}_l(q)$ all we need to do is to evolve it with the spherical collapse model. Using equations (2.4) we may write (Patiri et al.(2006) expression (20)):

$$\delta(r) = \delta(\overline{\delta}_l(q)); \qquad q \equiv r\ [1+\delta(r)]^{\frac{1}{3}} \tag{2.9}$$

where the right hand side of this equation is simply the function defined in expression (2.3) evaluated at $\overline{\delta}_l(q)$ (given by expression (2.9)). For each value of r we must solve this equation for the variable $\delta(r)$. One may obtain all couples of values of $\delta(r)$, r using (2.9) and running over all values of q. The profile obtained in this way is the typical enclosed density contrast profile, $\delta_t(r)$.

2.3 The Probability Distribution, $P(\delta, r)$. Most Probable and Mean Profiles

At a given value of r, δ takes different values, $\delta(r, j)$, over the assemble of halos. The question now is which is the probability distribution of δ over this ensemble, P(δ,r). As we saw in the previous section, this can be done, in principle, by making realizations of the initial profile, $\delta_l(q, i)$, and evolving them accordingly with equations (2.4). Let's assume, as a first approximation, that the realizations of the initial profile may be carried out by generating for each value of q a value of δ_l accordingly with distribution (2.5). That is, we assume that the distribution of δ_l is only conditioned by the fact that $\delta_l(Q) = \delta_{vir}$. We shall latter consider initial profiles with an additional constraint. With these realizations we can elaborate for each value of r a histogram for $P(\delta, r)$. There is, however, a direct analytical procedure to obtain $P(\delta, r)$ from the probability distribution for δ_l (expression (2.5) in the present approximation).

Fortunately, there is a simple expression relating $P(\delta, r)$ and $P(\delta_l, q)$ probability distributions, which is valid as long as shell-crossing is not important:

$$P(\delta, r) = -\frac{d}{d\delta} \frac{\int_{\delta_l(\delta)}^{\delta_{vir}} P(\delta_l, q)\ d\delta_l}{\int_{-\infty}^{\delta_{vir}} P(\delta_l, q)\ d\delta_l} \tag{2.10}$$

$$q \equiv r\ (1+\delta)^{\frac{1}{3}}$$

where $\delta_l(\delta)$ is given by expression (2.2) and $P(\delta_l, q)$ is the linear profile. Note that δ enters not only in the integration limit but also in the integrand through q. The derivation of this relationship can be found in Betancort-Rijo et al. (2006), Appendix B.

Using expression (2.5) for P(δ_l,q) we find:

$$\frac{\int_{\delta_l(\delta)}^{\delta_{vir}} P(\delta_l, q)\ d\delta_l}{\int_{-\infty}^{\delta_{vir}} P(\delta_l, q)\ d\delta_l} = \frac{1}{2}\ \frac{erfc(F(x=\delta_l(\delta))) - erfc(F(x=\delta_{vir}))}{1 - \frac{1}{2} erfc(F(x=\delta_{vir}))} \tag{2.11}$$

$$F(x) \equiv \frac{x - \frac{\sigma_{12}(q)}{\sigma(Q)}\ \delta_{vir}}{\sqrt{2\ g(q)}}$$

$$q \equiv (r\ (1+\delta))^{\frac{1}{3}}$$

with $\sigma_{12}(q)$, $\sigma(Q)$, $g(q)$ as defined in (2.5).

For the purposes of this section we may neglect the term $erfc(F(x=\delta_{vir}))$. The full expression shall be used in section 2.5 along with a more refined one. We then have:

$$P(\delta, r) = \frac{1}{\sqrt{\pi}}\ e^{-F^2(x=\delta_l(\delta))} \frac{d}{d\delta} F(x=\delta_l(\delta)) \tag{2.12}$$

By construction, δ at r must be smaller than Δ_{vir} and larger than certain value, $\delta_{min}(r)$:

$$\delta_{min}(r) = 341\ (R_{vir}/r)^3 - 1 \tag{2.13}$$

This minimum value corresponds to a situation where there is no matter in between R_{vir} and r. So, for δ values outside the interval $(\delta_{min}(r), \Delta_{vir})$, $P(\delta, r)$ is zero.

We may obtain an analytical expression for P(δ,r) using approximation (2.6) for $\frac{\sigma_{12}(q)}{\sigma_1^2}$ and the following approximation for $\sigma(q)$ (which enters $g(q)$, defined below expression (2.5)):

$$\sigma(q) \simeq (1.65\ 10^{-2} + 0.105(q\ h\ Mpc^{-1}))^{-\frac{1}{2}} \qquad \text{for } q < 3\ h^{-1}Mpc$$

Expression (2.10) is valid as long as shell-crossing is not important. In Prada et al. (2006) we have found by mean of comparison with numerical simulations that, beyond three virial radius, the relevance of shell-crossing diminishes quickly. This relevance can be estimated a priori (i.e. without comparison with simulations) obtaining P(δ,r) directly through realizations of the initial profile accordingly with expression (2.5) and evolving them accordingly with equations (2.4). If shell-crossing were irrelevant, the P(δ,r) obtained in this way should be equal to that given by expression (2.12). The presence of certain amount of shell-crossing will cause the P(δ,r) obtained with realization to have a somewhat smaller maxima and a more extended tail than that given by (2.12) (note that it is this expression that corresponds to realizations elaborated with expression (2.5). In this case none of the procedures gives the correct P(δ,r) because both assume that δ is related to δ_l by means of expression (2.2), which is inconsistent when shell-crossing is important. However, the difference between the results obtained with both procedures is of the same order of the difference between any of them and the profile obtained with a proper treatment of shell-crossing. Note that even this last P(δ,r) is not the real one, since, as we said before, we are generating the initial profile using only a two point distribution (expression (2.5)).

In Figure 2.1 we compare the P(δ,r) obtained by the two procedures mentioned above for several values of r expressed in unit of the virial radius (that we denote by s). We also show the corresponding histograms obtained from the numerical simulations described in Prada et al. (2006), which were done using the Adaptive Refinement Tree (ART) code (Kravtsov et al. 1997) for the standard ΛCDM cosmological model with $\Omega_0 = 0.3$, $\Omega_\Lambda = 0.7$, $h = 0.7$, and cover a wide range of scales with different mass and force resolutions (see Prada et al. 2006 for a detailed description). In particular, the histograms in Figure 2.1 were obtained for a total of 654 halos in a mass range of $3 \pm 1 \cdot 10^{12} h^{-1}\ M_\odot$ selected without any kind of isolation criteria.

We can see that, for $s = 2.5$, where shell-crossing is already important, there is substantial difference between the results of both procedures. A considerable amount of probability is transfered from the most probable value to much larger values ($\delta \approx$

100) causing the distribution obtained through the realizations to be bimodal. For $s = 3.5$ there is still a small amount of shell-crossing causing the maxima obtained with both procedures to differ by roughly a 20%. For larger values of s this difference steadily diminishes.

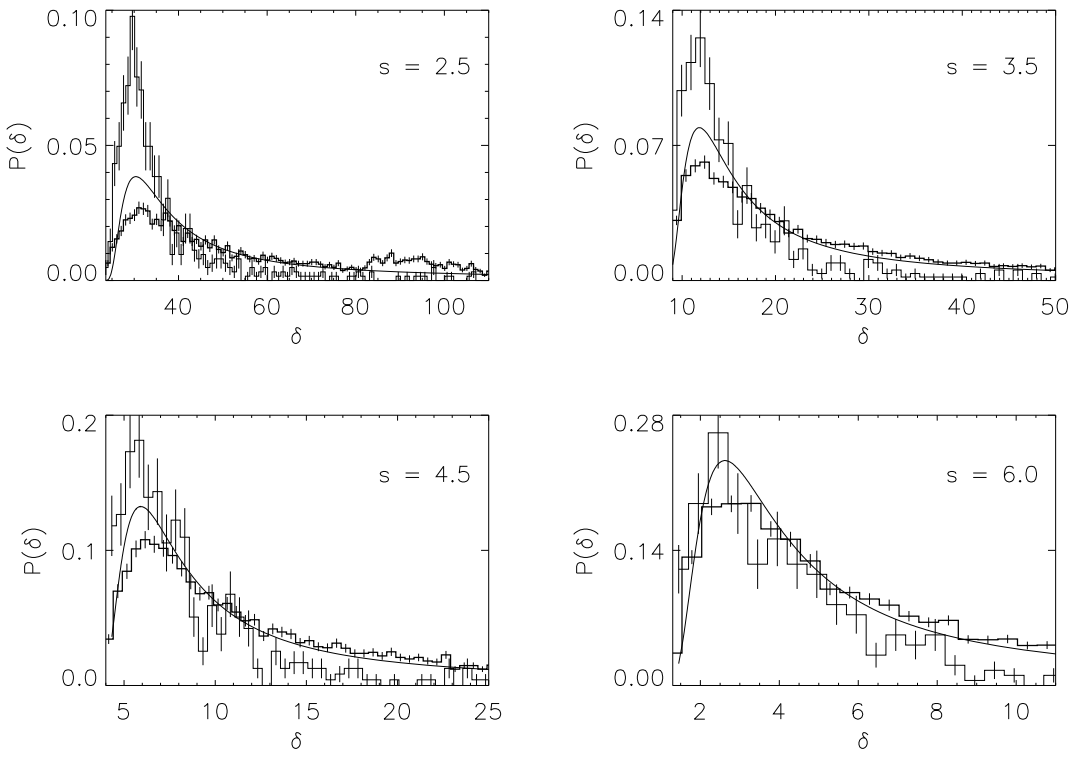

Figure 2.1 $P(\delta, r)$ as given by expression (2.12) compared with the corresponding histogram obtained through realizations (histogram with small error bars) and that found in the simulations (histogram with large error bars) for four values of s ($\equiv r/R_{vir}$) and a mass of $3 \times 10^{12} h^{-1}\ M_{\odot}$ ($\Delta_{vir} = 340$ and $\delta_{vir} = 1.9$).

Furthermore, as s increases the difference between the distribution given by expression (2.12) and the histogram obtained with the numerical simulations reduces. In fact, even for $s = 3.5$ the relative values of P(δ,r) at different values of δ to the left of the maxima are very well given by (2.12). The difference in the absolute values with respect to those in the histogram is due to the normalization. For δ values to the right of the maxima, expression (2.12) gives a considerably more extended tail than in the actual distribution. Therefore the normalization constant is larger in the latter case.

Note that, although the maxima of expression (2.12) and that of the histogram corresponding to the numerical simulations approach as s increases, due to the increasing irrelevance of the tail, this tail is still substantially more extended even for

$s = 6$. Now, since the relevance of shell-crossing is small for s larger than 3, the most likely explanation for the excess in the tail given by expression (2.12) lies on the fact that we are using expression (2.5) for P(δ_l,q). In the last section we shall consider a better P(δ,r) and discuss the resulting improvement of the behaviour of its tail.

Using P(δ,r) (as given by (2.12)) we may immediately obtain the most probable and the mean profiles. For the first one we have:

$$\delta_{prob}(r) \equiv \delta_{max}; \qquad \left.\frac{d}{d\delta}P(\delta, r)\right|_{\delta=\delta_{max}} = 0 \tag{2.14}$$

And for the mean profile, in principle:

$$\overline{\delta}(r) \equiv \int_{\delta_{min}}^{\Delta_{vir}} P(\delta, r)\delta \; d\delta \tag{2.15}$$

However, due to the fact that the mean is rather sensitive to the form of the tail, we must artificially cut off the tail. From the simulations we know that the real tail practically ends at $\delta \sim \delta_0(r)$ with δ_0 given by:

$$P(\delta_0, r) = \frac{P(\delta_{max}, r)}{25}$$

So, instead of (2.15) we use (Prada et al. 2006):

$$\overline{\delta}(r) \equiv \frac{\int_{\delta_{min}}^{\delta_0(r)} P(\delta, r)\delta \; d\delta}{\int_{\delta_{min}}^{\delta_0(r)} P(\delta, r) \; d\delta} \tag{2.16}$$

In Table 2.1 we give the values of δ_0 and δ_{max} for several values of s ($\equiv r/R_{vir}$).

Table 2.1 Artificial cut-off for $P(\delta, r)$

s	δ_{max}	δ_0
1.5	115.2	495.4
2.5	28.6	135.3
3.5	11.3	67.9
4.5	5.8	42.2
5.5	3.3	29.3
6.5	2.0	19.6
7.5	1.3	12.8
8.5	0.82	8.1

2.4 Comparison with N-body simulations

In this section we combine the statistics of the initial density fluctuations with the spherical collapse model to obtain predictions for the mean and most probable density profiles of collapsed galaxy-size dark matter halos with masses $10^{11} - 5 \times 10^{12} \mathrm{M}_{\odot}$. We then compare our results with those obtained by means of high resolution N-body cosmological simulations presented in Prada et al. (2006) for same halo masses and radii. The model gives excellent results beyond 2-3 formal virial radii.

In Figure 2.2 we have computed, both for δ and for δ', the most probable (squares) and mean (crosses) density profiles found in our simulations for two mass intervals with the mean values equal to the masses used in the theoretical derivation. We have taken 277 halos in the mass range $(6.5 \pm 1.5) \times 10^{10} h^{-1}\ M_{\odot}$ and 654 halos in the mass range $(3 \pm 1) \times 10^{12} h^{-1}\ M_{\odot}$ (from $Box80S$ and $Box80G$ simulations, with parameters given in Table 2 of Prada et al. 2006). No isolation criteria was used. In Table 2.4 we list for the mean halo with mass $< M >= 3 \times 10^{12} h^{-1}\ M_{\odot}$ the estimations of the most probable and mean value of the density at different radii compare with that from the spherical collapse model for the most probable, the mean and the typical profiles.

In Figure 2.2 one can see that beyond 2 virial radius the mean and the most probable profiles, both for δ and for δ', differ considerably. This is due to the fact that for this radii the probability distribution for δ, $P(\delta, r)$, is rather wide, with a long upper tail. This can be seen in Figure 2.3 were this distribution is shown inside 3.5 ± 0.05 virial radius for the mass $< M >= 3 \times 10^{12} h^{-1}\ M_{\odot}$. We show for comparison the theoretical prediction for $P(\delta, r)$ as well as we give the most probable $\delta_{\max}$ and mean value $< \delta >$ of the distribution.

It is apparent from Figure 2.2 that the δ' profiles are steeper for smaller masses, so that they go below the background at smaller r/R_{vir} and reach larger underdensities. The δ profiles are also steeper for smaller masses although the difference is, obviously, much smaller. We have found that the theoretical prediction for the typical and the most probable profile are, in general, almost indistinguishable (see Table 2.4). They are both found to be in very good agreement with the most probable δ profile found in the numerical simulations beyond two virial radii. There is also qualitative agreement between the predictions of the most probable δ' profiles and those found in the numerical simulations. It must be noted, however, that by predicted δ' profile we understand simply the one obtained from the corresponding δ profile by means of relationship given in Eq.(2.1). Note that this is not the same as the most probable profile for δ' (see Figure 2.2). This is due to the fact that the most probable δ' value at a given $s(\equiv r/R_{vir})$ corresponds to a different halo than the most probable δ value at the same s. This explains that, while the prediction for δ_{prob} agrees very well with the simulations, the agreement is not so good for δ'_{prob}. The δ'_{prob} obtained from δ_{prob} by means of expression Eq.(2.1) is not a proper prediction but an indicative value, since we can not envisage a feasible procedure to obtain a proper prediction. On

the contrary, the mean profiles $< \delta >$ are exactly related to $< \delta' >$ by means of expression Eq.(2.1). The predictions for both profiles are in good agreement with the numerical simulations, showing a much flatter profile beyond 2 virial radius than those corresponding to $\delta_{\rm prob}$ and $\delta'_{\rm prob}$. This agreement is remarkable given the fact that the expression used for $P(\delta, r)$ is only a first approximation (see next section).

Table 2.2 Comparison between the simulated *mean* halo density profile and the theoretical predictions from the spherical collapse model for the mass $< M >= 3 \times 10^{12} h^{-1}\ M_{\odot}$.

	Numerical Simulations				Spherical Collapse					
$r/R_{\rm vir}$	$< \delta >$	$\delta_{\rm prob}$	$< \delta' >$	$\delta'_{\rm prob}$	$< \delta >$	$\delta_{\rm prob}$	$\delta_{\rm t}$	$< \delta' >$	$\delta'_{\rm prob}$	$\delta'_{\rm t}$
1.0	337	323	69.1	52.4	531	398	385	40.4	2.5	7.8
1.5	129	116	30.8	15.1	184	115	118	22.6	1.9	4.3
2.0	67.7	54.6	19.5	3.73	84.8	53.7	51.7	14.7	1.5	2.8
2.5	43.2	31.1	15.4	1.6	49.3	28.6	27.6	10.3	1.2	1.9
3.0	30.8	17.4	11.2	0.78	32.2	17.3	16.6	7.6	1.0	1.4
3.5	22.1	12.6	8.5	0.58	22.6	11.3	10.9	5.8	0.79	0.97
4.0	18.4	9.0	5.9	0.18	16.8	7.9	7.6	4.5	0.61	0.70
4.5	14.1	5.8	5.5	0.09	13.0	5.8	5.5	3.5	0.46	0.50
5.0	12.2	4.4	4.3	-0.08	10.4	4.3	4.1	2.7	0.32	0.34
5.5	9.4	3.5	3.3	-0.16	8.5	3.3	3.2	2.1	0.20	0.22
6.0	7.9	2.8	3.1	-0.17	7.1	2.5	2.5	1.6	0.09	0.12
6.5	6.8	2.1	2.5	-0.22	5.7	2.0	2.0	1.2	-0.008	0.03
7.0	6.2	1.6	1.9	-0.33	4.6	1.6	1.6	0.9	-0.10	-0.04

Note. — The symbols $< \delta >$, δ_{prob}, δ_t stand, respectively, for mean, most probable, and typical averaged enclosed fractional overdensity. The corresponding primed simbols are for the local fractional overdensities at given radius.

It is interesting to note, as we have previously pointed out, that larger masses have somewhat shallower profiles. In order to predict this trend correctly we must use the initial profile given by Eq.(2.9). If we dropped the second constraint used to derive this Eq.(2.9) and use in Eq.(2.9) the initial profile given by Eq.(2.7), which corresponds to high mass objects, the prediction would be the opposite. The reason for this being that, in this limit, the initial profile depend on mass only through c (the concentration parameter, defined as $c \equiv R_{vir}/r_s$, where r_s is a characteristic scale radius) which increases with increasing mass, thereby leading to steeper profiles

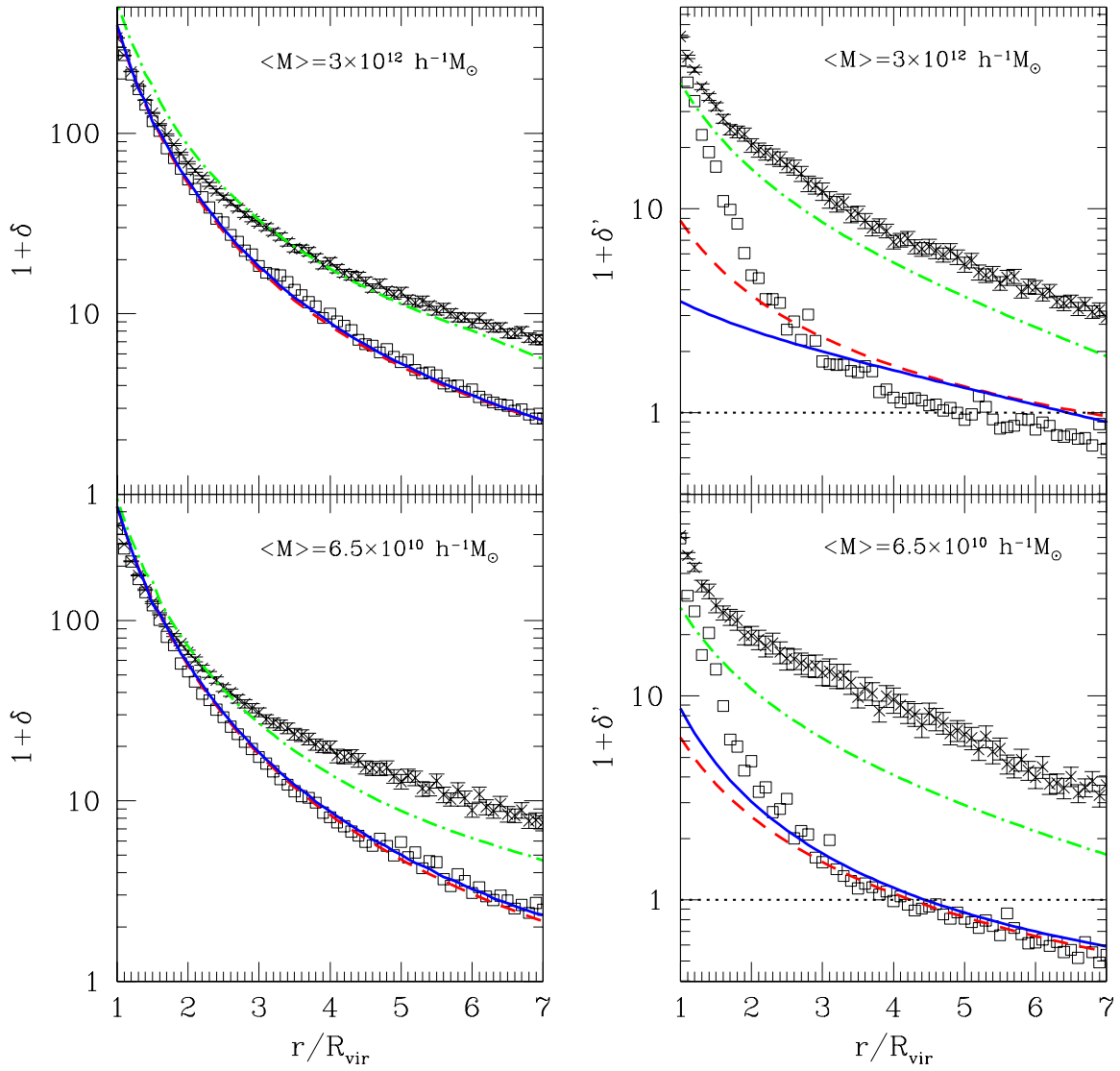

Figure 2.2 The most probable (squares) and the mean (crosses) halo density profiles up to $7R_{\rm vir}$ for the two masses ($< M >= 3 \times 10^{12} h^{-1}\ M_\odot$ and $< M >= 6.5 \times 10^{10} h^{-1}\ M_\odot$ in our simulations. We compare the simulated data with the predictions from the spherical collapse model for the most probable (solid line) and typical profiles (dashed line) which are almost indistinguishable and the mean profiles (dot-short dashed line). We have estimated that the errors in the most probable values of δ and δ' are about 25% larger than the error showed in the plots for their mean values.

for larger masses.

The computations of the *mean* profiles (in fact, the typical profile) around halos has independently been made by Barkana (2004). He used the spherical model and, in principle, imposed on the initial profile the same constraint as we do. The computing procedure he followed was somewhat different involving some approximations. He do not give explicitly the equation defining the profile, so that accurate comparison with our results are not possible. Furthermore he used different values of δ_{vir}, Δ_{vir}. However, his results are in good qualitative agreement with our predictions for the typical profile.

Table 2.3 The isolated *mean* halo density profile for the mass $< M >= 3 \times 10^{12} h^{-1}\ M_{\odot}$. The symbols are the same as Table 2.4.

$r/R_{\rm vir}$	$< \delta >$	$\delta_{\rm prob}$	$< \delta' >$	$\delta'_{\rm prob}$
1.0	336	323	56.1	52.4
1.5	119	119	15.1	14.4
2.0	55.4	65.6	5.5	4.2
2.5	30.1	29.4	3.1	1.4
3.0	18.5	18.2	1.8	0.36
3.5	12.3	11.0	1.4	0.14
4.0	8.5	7.0	1.7	-0.04
4.5	6.4	6.0	1.6	0.03
5.0	5.2	4.6	2.5	-0.14
5.5	4.5	2.9	1.8	0.12
6.0	3.9	2.7	1.4	-0.20
6.5	3.4	2.0	1.3	-0.34
7.0	3.0	1.5	1.3	-0.30

We have so far considered randomly chosen halos, i.e. without isolation criteria. When halos are chosen according with an isolation criteria (e.g. no massive companion within $2R_{\rm vir}$) they differ from the randomly chosen ones in two respects. On the one hand, the probability distribution for δ at a given value of s is narrower, so that most profiles cluster around the most probable one. Therefore, the difference between the mean and the most probable density profile becomes smaller. On the other hand, isolated profiles lay, on average, on somewhat more underdense environment than non-isolated ones, so that their most probable profiles are slightly steeper. Both effects may be seen by comparing Table 2.4 and Table 2.4 or the upper right pannel in Figure 2.2 with Figure 2.4 where we show the local density profile for the isolated mean halo density profile for the mass range $3 \pm 1 \times 10^{12} h^{-1}\ M_{\odot}$. In this mass range we have selected halos that do not have a companion with mass larger

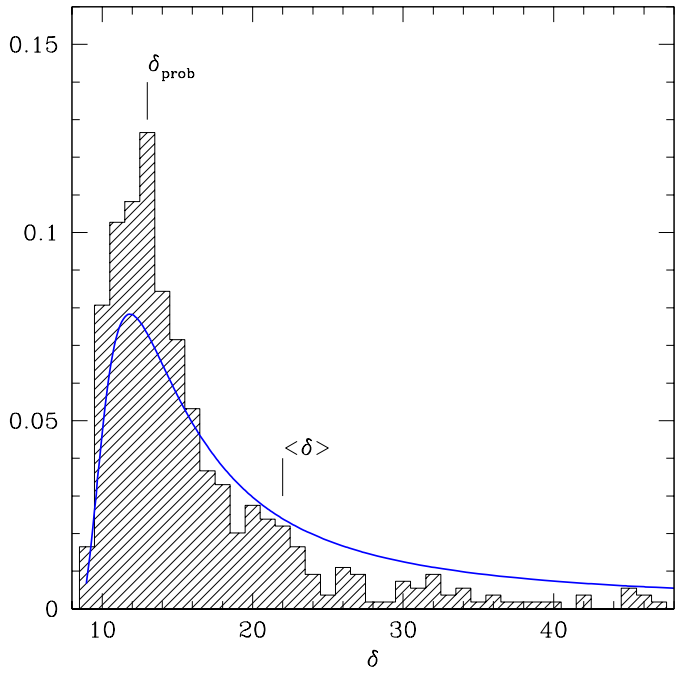

Figure 2.3 Distribution of the fractional cumulative density δ inside $3.5 \pm 0.05 R_{vir}$ for the mean halo of mass $< M >= 3 \times 10^{12} h^{-1}\ M_{\odot}$. We show for comparison the theoretical prediction of $P(\delta, s)$ as well as we give the most probable δ_{max} and mean value $< \delta >$ of the distribution. We display the density distribution from its minimum value up to 1σ from its mean $< \delta >$ (8% of the values of the distribution are beyond 1σ).

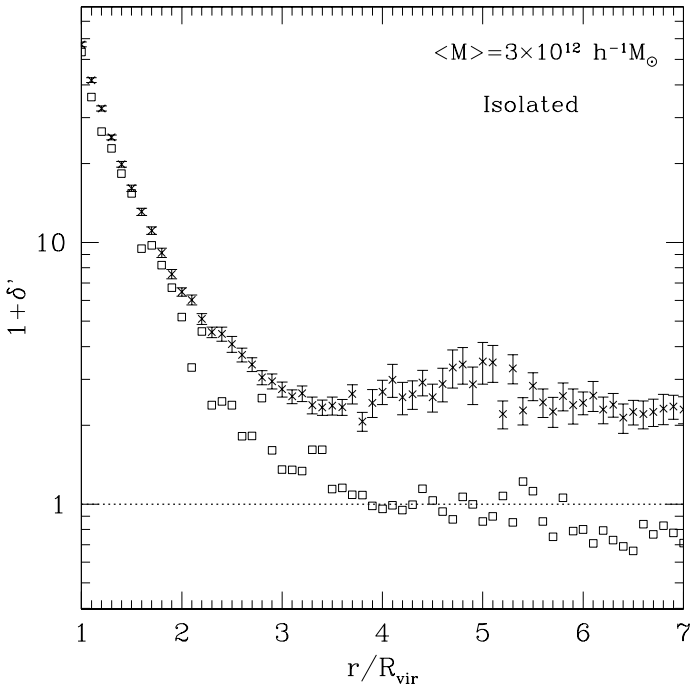

Figure 2.4 The mean (crosses) and most probable values (squares) of the local density profile for the mean isolated dark matter halo with mass $< M >= 3 \times 10^{12} h^{-1}\ M_{\odot}$.

than 10% of the halo mass within $4R_{vir}$. In total there are 156 halos, i.e. one quarter of all halos in this mass range.

In conclusion, for larger radii beyond 2-3 formal virial radius we have combined the statistics of the initial fluctuations with the spherical collapse model to obtain predictions of the mean halo density profiles for halos with different masses. We have considered two possibilities: the most probable and the mean density profiles. We find that the most probable profile obtained from the simulations presented in Prada et al. (2006) is in excellent agreement with the predictions from the spherical collapse model beyond 2-3 virial radius. For the mean density profile the predictions are not so accurate. This is due to the fact that the approximation, which we are using for the distribution of δ at a given radius, has an artificially long tail (this fact is improved in next section). Even so, the predictions are qualitatively good and quantitatively quite acceptable. We think that the discrepancies between the data and the predictions at radii smaller than 2-3 virial radii are due to the fact that these inner shells are affected by the shell-crossing (Sánchez-Conde et al. 2007; see Chapter 3). An appropiate treatment of this circunstance should lead to accurate predictions for all radii, so that the mean spherically averaged profiles may be understood in terms of the spherical collapse.

2.5 Improving $P(\delta, r)$

We have seen that for s ($= r/R_{vir}$) larger than 3 the realization of initial profiles and their subsequent evolution lead to values of $P(\delta, r)$ very close to those obtained using expression (2.12). This means that shell crossing is not important at these radii. So, the difference between the actual value of $P(\delta, r)$ (the histogram obtained from the simulations) and that given by expression (2.12) lies on the fact that this expression is only an approximation, or in the possible relevance of triaxiality, non-radial motions and pressure (velocity dispersions). To determine the amount of the discrepancy due to inaccuracies in the statistical description of the initial conditions as opposed to the discrepancy due to neglected dynamical factors, we must consider better approximation than that provided by expression (2.12). We shall use now two improved approximations. The first one is that obtained by using expression (2.11) in expression (2.10), which we represent by $P_1(\delta, r)$. Note that, to derive this approximation we have used the fact that at a given q larger than Q, δ_l must be smaller than δ_{vir}, but we have used expression (2.5) for $P(\delta_l, q)$. This distribution does not account for the fact that for all values of q larger than Q, $\delta_l < \delta_{vir}$. Consequently, $P(\delta_l, q)$ falls off with δ_l more slowly than it should and the same applies to $P(\delta, r)$. In the second approximation, which we represent by $P_2(\delta, r)$, we consider a $P(\delta_l, q)$ which takes into account this additional constraint. By comparing the predictions obtained with $P_2(\delta, r)$, $P_1(\delta, r)$ with those obtained with $P(\delta, r)$ (expression (2.12)) we may check whether $P_1(\delta, r)$ is accurate enough, so that the remaining discrepancy of the prediction with the results shown in the simulations may be ascribed to unaccounted dynamical factors.

To obtain $P_2(\delta_l, q)$ we must first obtain the joint probability distribution for the value of δ_l at Q, q and at the middle point $q' = \frac{1}{2}(q + Q)$. We represent by x_1, x_2, x_3 respectively the value of δ_l at these three points.

The joint distribution for these three variables is a Gaussian trivariate distribution $P(x_1, x_2, x_3)$, which can be obtained for a given power spectra. With this distribution we may immediately obtain the distribution of x_3 conditioned to $x_1 = \delta_{vir}$, $x_2 < \delta_{vir}$, namely: $\overline{P_2}(\delta_l, q)$. So, we have:

$$\overline{P_2}(\delta_l, q) = \frac{\int_{-\infty}^{\delta_{vir}} P(x_2|x_1)\ P(x_3|x_1, x_2)\ dx_2}{\int_{-\infty}^{\delta_{vir}} P(x_2|x_1)\ dx_2} \tag{2.17}$$

where $P(\delta_{vir}, x_2)$ is the joint probability distribution for x_1, x_2 with $x_1 = \delta_{vir}$. $\overline{P_2}(\delta_l, q)$ is the probability distribution of δ_l at q conditioned to $\delta_l(Q) = \delta_{vir}$ and $\delta_l(q') < \delta_{vir}$. We have not imposed yet the almost redundant condition (since $\overline{P_2}(\delta_l, q)$ is very small for $\delta_l > \delta_{vir}$) that δ_l at q must be smaller than δ_{vir}. The probability distribution for δ_l with this condition, $P_2(\delta_l, q)$, is simply obtained through normalization. Here we have just discussed the main lines of the derivation of $P_2(\delta_l, q)$. A full description can be found in Betancort-Rijo et al. (2006).

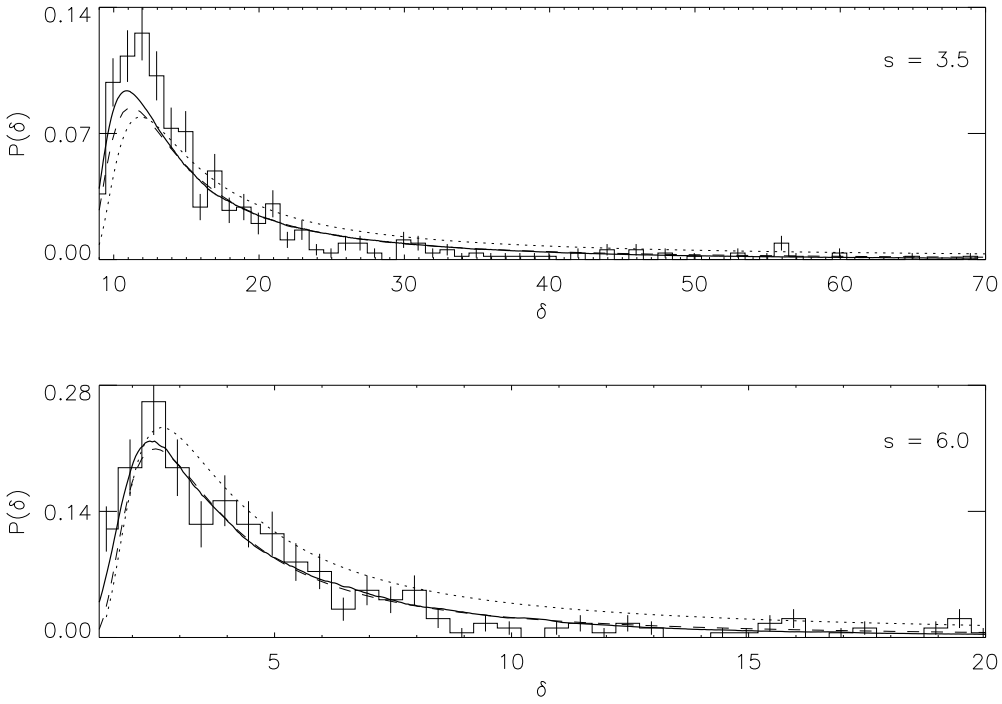

Figure 2.5 Probability distribution for δ at 3.5 and 6 virial radius for $3 \times 10^{12}\ h^{-1}M_{\odot}$. The filled curve corresponds to the approximation given by expression (2.18), the dashed curve to that given by full expression (2.10), and the dotted curve to expression (2.12). The histogram corresponds to the same simulations as in Fig. 2.1.

The distribution for δ at fixed r within this formalism, which we represent by $P_2(\delta, r)$, may be obtained from $P_2(\delta_l, r)$ by means of expression (2.10), which is valid when shell-crossing is not important ($s \gtrsim 3$):

$$P_2(\delta, r) = -\frac{d}{d\delta} \int_{\delta_l(\delta)}^{\delta_{vir}} P_2(\delta_l, q)\ d\delta_l \tag{2.18}$$

$$q \equiv r(1+\delta)^{\frac{1}{3}}$$

In Figure 2.5 we show the probability distributions for a mass of $3 \times 10^{12}\ h^{-1}M_{\odot}$ at 3.5 and 6.0 virial radius. As expected, $P_2(\delta, r)$ falls off much faster than $P(\delta, r)$ being in excellent agreement with the simulations. The tail of $P_1(\delta, r)$ falls off sufficiently fast to give sensible results for the density and velocity profiles averaged over all possible halos (δ between δ_{min} and Δ_{vir}). However, we know that for $\delta \gtrsim 70$ the standard spherical collapse model is not a good approximation, so we can not learn much by comparing simulations with predictions for averages over all halos. It is more instructive to compare the predictions for the averages corresponding to δ values

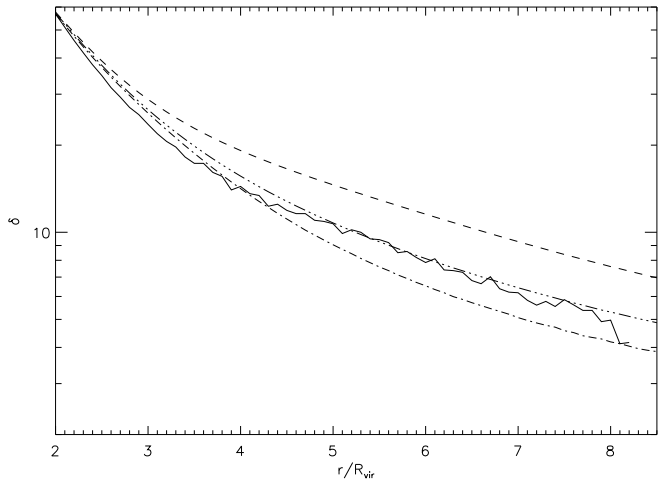

Figure 2.6 Mean δ profile for $3 \times 10^{12}\ h^{-1}M_{\odot}$ using the probability distribution given by expression (2.12) (dashed line), by full expression (2.10) (3dots-dashed line) and by expression (2.18) (dot-dashed line). Mean δ obtained from simulations is given for comparison (filled line). In all the cases, a maximum value of $\delta = 70$ was used.

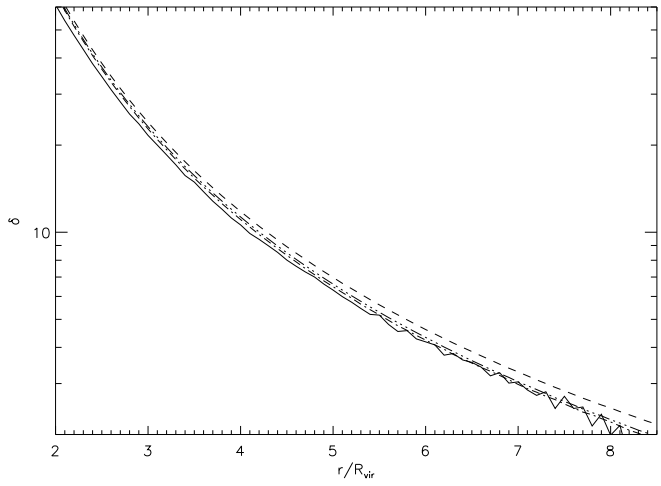

Figure 2.7 Mean δ profile for $3 \times 10^{12}\ h^{-1}M_{\odot}$ using the probability distribution given by expression (2.12) (dashed line), by full expression (2.10) (3dots-dashed line) and by expression (2.18) (dot-dashed line). Mean δ obtained from simulations is given for comparison (filled line). For all radius, the average was calculated excluding the 20% of the halos with the largest δ values.

between δ_{min} (expression (2.13)) and 70 with those found in the simulations for the same range of δ values.

In Figure 2.6 we show the predictions given by $P(\delta, r)$, $P_1(\delta, r)$, $P_2(\delta, r)$ for the

δ profile averaged between δ_{min} and 70 and the averaged found in the simulations. Only the relevance of triaxiality can explain the results shown in Figure 2.6. The effect is not large in this Figure, since only a small fraction of the halos are affected, but it is quite meaningful.

Knowing that for some halos the spherical collapse model can not be a good approximation, the relevant question now is to determine precisely how good is it for most halos. To this end, at each radial bin we search for the value, $\delta_1(r)$, such that the upper cumulative probability, as given by $P_2(\delta, r)$, is 0.2, and eliminate, both in the simulations and in the predictions, halos with larger δ values at that bin. By doing so, we eliminate many halos which simply have flatter profiles than average, but are otherwise sufficiently spherical for the model to apply. But, we are sure of having eliminated all halos with highly triaxial outskirts, most of them corresponding to situations where a couple of halos lie within a few virial radius from each other, so that each of them will show up in the outskirt of the other halo; a situation that, by no mean, can be described by the spherical model. The resulting profiles, as given by the different approximations to $P(\delta, r)$ and the simulations are given in Figure 2.7. The difference between the various approximations is now smaller, since the main difference occurs at the far tail (of $P(\delta, r)$), which has now been eliminated, but this difference increases for smaller masses. The profile obtained from the simulations lies now slightly below the best prediction, as it should be if the spherical model is a good approximation.

In summary, the distribution $P_2(\delta, r)$ is very close to the exact. To most purposes the simpler distribution $P_1(\delta, r)$ may be used, their difference being small, although it increases for smaller values. The density profiles obtained with $P_2(\delta, r)$ are in excellent agreement with those found in simulations beyond ~ 3 virial radius. The density dispersion and the radial velocity show some discrepancy below ~ 5 virial radius, which clearly indicate the relevance of unaccounted dynamical factors, specially velocity dispersions.

2.6 Final remarks

The spherical collapse model describes very well the properties of dark matter halos beyond three virial radius. This could seem surprising given the fact that the density contours around halos may be considerably aspherical and the presence of tidal fields.

Nevertheless, the assumption that the spherically averaged density profiles at several virial radius evolves according with the spherical collapse model is not just a simplification introduced to make the problem tractable. The mean evolution is given by the spherical collapse model with some dispersion (for a given δ_l) due to triaxiality. This have been shown by mean of simulations (Lilje et al. 1986) and analytical works (Bernardeau 1994). At sufficiently large radii where δ is sufficiently small ($\delta \lesssim 10$) the fractional dispersion becomes small. At small radii, not only the dispersion becomes larger, causing the mean value of δ for a given δ_l to be somewhat

different from $\delta(\delta_l)$ (expression (2.2)), but also the effect of non-radial motions and velocity dispersions starts to dominate. So studying the dark matter profile where the uncertainty of the evolution is small, we may check that the initial conditions we use are correct to a high degree of accuracy. With these conditions, as described by the most accurate probability distribution, $P_2(\delta_l, q)$, we should be able to obtain very accurate predictions for all possible definitions (typical, mean...) of density and velocity profile. Any residual discrepancy should be explained by triaxiality, non-radial motions and velocity dispersions, as we shall show in a future work, although, from the results shown in this work, the last two effects dominate at least up to roughly 5 virial radius. Going a step further, if we adequately take into account the neglected dynamical factors, the same initial conditions should explain the profile at any radii. In this way, we could be able to explain the dark matter profiles at least down to a virial radii understanding the role played by the initial conditions and by the different processes relevant to the evolution.

Bibliography

Avila-Reese, V., Firmani, C. & Hernandez, X. 1998, ApJ, 505, 37

Ascasibar, Y., Yepes, G., Gottloeber, S. & Mueller, V. 2004, MNRAS, 352, 1109

Bajtlik S., Duncan R. C., Ostriker J. P., 1988, ApJ, 327, 570

Bardeen, J. M., Bond, J. R., Kaiser, N. & Szalay, A. S. 1986, ApJ, 304, 15 (BBKS)

Barkana R., 2004, MNRAS, 347, 59

Bernardeau, F. 1994, ApJ, 427, 51

Bertschinger, E. 1985, ApJS, 58,39

Betancort-Rijo J., Sánchez-Conde M. A., Prada F. & Patiri, S., 2006, ApJ, 649, 579

Brainerd, T.G., 2004, astro-ph/0409381

Conroy, C., Newman, J. A., Davis, M., Coil, A. L., Yan, R., Cooper, M. C., Gerke, B. F., Faber, S. M., & Koo, D. C., 2004, ApJ, 635, 982

Fillmore, J. A. & Goldreich, P. 1984, ApJ, 281, 1

Gunn, J. E. & Gott, J. R. 1972, ApJ, 176, 1

Gunn J. E., 1977, ApJ, 218, 592

Gurevich, A. V. & Zybin, K. P. 1988, ZHETF, 94, 3

Guzik, J., & Seljak, U., 2002, MNRAS, 335, 311

Hoekstra, H., Yee, H. K. C., Gladders, M. D., 2004, ApJ, 606, 67

Hiotelis, N. 2002, å, 382, 84

Hoffman Y., Shaham J., 1985, ApJ, 297, 16

Jenkins A., Frenk C. S., White S. D. M., Colberg J. M., Cole S., Evrard A. E., Couchman H. M. P., Yoshida N., 2001, MNRAS, 321, 372

Kravtsov, A.V., Klypin, A.A., & Khokhlov, A.M., 1997, ApJS, 111, 73

Lilje, P.B., Yahil, A. & Jones, B.J.T. 1986, ApJ, 307, L91

Lokas E. L., 2000, MNRAS, 311, 423

Lokas, E. L. & Hoffman, Y. 2000, ApJ, 542, L139

Nusser, A. 2001, MNRAS, 325, 1397

Padmanabhan T., 1996, MNRAS, 278, L29

Patiri S., Betancort-Rijo J. E. & Prada F. 2006, MNRAS, 368, 1132

Prada, F., Vitvitska, M., Klypin, A., Holtzman, J. A., Schlegel, D. J., Grebel, E. K., Rix, H.-W., Brinkmann, J., McKay, T. A., & Csabai, I., 2003, ApJ, 598, 260

Prada F., Klypin A. A., Simmoneau E., Betancort-Rijo J., Patiri S. G., Gottlöber S., Sánchez-Conde M. A., 2006, ApJ, 645, 1001

Ryden, B. S. & Gunn, J. E. 1987, ApJ, 318, 15

Sánchez-Conde M. A., Betancort-Rijo J.E. and Prada F., 2007, MNRAS, 378, 339

Sheldon, E. S., et al., 2004, AJ, 127, 2544

Sheth, R. K. & Tormen, G. 2002, MNRAS, 329, 61

Sikivie, P., Tkachev, I. I. & Wang Y. 1997, *Phys. Rev. D*, 56(4), 1863 .

Smith, D. R., Bernstein, G. M., Fischer, P., & Jarvis, M., 2001, ApJ, 551, 643

Subramanian K., Cen R., Ostriker J. P., 2000, ApJ, 538, 528

White, S. D. M. & Zaritsky, D. 1992, ApJ, 394, 1

Zaritsky, D. & White, S. D. M. 1994, ApJ, 435, 599

Zaritsky, D., Smith, R., Frenk, C., & White, S. D. M. 1997, ApJ, 478, 39

3

The spherical collapse model with shell-crossing[1]

In this work, we study the formation and evolution of dark matter halos by means of the spherical infall model with shell-crossing. We present a framework to tackle this effect properly based on the numerical follow-up, with time, of that individual shell of matter that contains always the same fraction of mass with respect to the total mass. In this first step, we do not include angular momentum, velocity dispersion or triaxiality. Within this framework - named as the Spherical Shell Tracker (SST) - we investigate the dependence of the evolution of the halo with virial mass, with the adopted mass fraction of the shell, and for different cosmologies. We find that our results are very sensitive to a variation of the halo virial mass or the mass fraction of the shell that we consider. However, we obtain a negligible dependence on cosmology. Furthermore, we show that the effect of shell-crossing plays a crucial role in the way that the halo reaches the stabilization in radius and the virial equilibrium. We find that the values currently adopted in the literature for the actual density contrast at the moment of virialization, δ_{vir}, may not be accurate enough. In this context, we stress the problems related to the definition of a virial mass and a virial radius for the halo. The question of whether the results found here may be obtained by tracking the shells with an analytic approximation remains to be explored.

3.1 Introduction

In the hierarchical scenario for structure formation in the Universe, the small primordial density fluctuations grow due to non-linear gravitational evolution and finally become the first virialized structures (halos). In this picture, larger Cold Dark Matter (CDM) halos will be formed by the accretion and merger of those first smaller

[1]M. A. Sánchez-Conde, J. Betancort-Rijo and F. Prada, 2007, MNRAS, 378, 339

halos, forming in this way massive structures, and so on. This scenario, that constitutes the actual paradigm of hierarchical structure formation, is able to explain in general terms the universe that we see today. Yet, we do not have a framework or theory capable of reproducing this picture accurately. In this context, N-body cosmological simulations are a powerful tool to try to understand the formation and subsequent evolution of CDM halos. They constitute a very important help to build any theoretical model and their predictions explain many of different observations.

Basically, there are two analytical approaches that make the problem tractable, although some simplifications have to be made and, as it was said, comparison between these analytical studies and simulations are crucial to make progress: the Press-Schechter formalism (Press & Schechter 1974), based on the role of mergers (Nusser & Sheth 1999; Manrique et al. 2003), and the spherical infall model (*SIM*) focused on the understanding of the collapse of individual objects. We must note that in the Press & Schechter formalism, the *SIM* has also been widely used, but from a statistical point of view, to treat problems related to mass accretion histories, mass function, etc. The *SIM*, first developed by Gunn & Gott (1972) and Gunn (1977), describes the collision-less collapse of a spherical perturbation in an expanding background. In those two articles, they introduced for the first time the cosmological expansion and the role of adiabatic invariance in the formation of individual objects. Fillmore & Goldreich (1984) and Bertschinger (1985) found analytical predictions for the density profiles of collapsed objects seeded by scale-free primordial perturbations in a flat universe. Hoffman & Shaham (1985) generalized these solutions to realistic initial profiles in flat and open Friedmann models, and Baarden et al. (1986) (hereafter BBKS) improved this work introducing the peak formalism. Later, some studies have been done to include more realistic dynamics of the growth process of dark matter halos (e.g. Padmanabhan 1996; Avila-Reese, Firmani & Hernández 1998; Lokas 2000; Subramanian, Cen & Ostriker 2000).

In parallel, a large amount of numerical work have been done. Quinn, Salmon & Zurek (1986) and Frenk et al. (1988) obtained isothermal density profiles ($\rho \propto r^{-2}$) of CDM haloes, and Dubinski & Carlberg (1991) and Crone, Evrard & Richstone (1994) basically reproduced the predictions of Hoffman & Shaham (1985) and found some evidence for no pure power-law density profiles. Later, it was stablished that the density profiles of CDM halos have an universal form (Navarro, Frenk & White (1996, 1997, hereafter NFW), with $\rho \propto r^{-1}$ in the inner regions and $\rho \propto r^{-3}$ in the outskirts, although there is still controversy about the shape of the profile near the center and recently it has been found that the pfoiles flatten out close to $\rho \propto r^{-2}$ beyond ~ 2 virial radius. Moore et al. (1998,1999), amongst others, find $\rho \propto r^{-1.5}$ in the very center and other authors (Jing & Suto 2000; Klypin et al. 2001; Ricotti 2003) find an inner slope ranging from -1 to -1.5 depending on halo mass, merger history and substructure. Concerning to the outskirts of dark matter halos, Prada et al. (2006) carried out a detailed study and concluded that a 3D Sérsic three parameter approximation provides excelent density fits up to ~ 2 times the virial radius,

although these profiles differ considerably from the NFW ones beyond 2 virial radius.

There are also plenty of works in the literature using the *SIM* to predict the density profiles of dark matter halos mainly focused on explaining their central regions. Moreover, the *SIM* has been widely used to obtain some quantities specially relevant and directly related to crucial stages in the formation and evolution of CDM haloes for different cosmologies, redshifts, etc. A particularly relevant quantity is the value of the overdensity at the moment of virialization δ_{vir} (Δ_{vir} usually in the literature), where overdensity is defined here as a number of times the background density, and its linear counterpart $\delta_{l,vir}$. The values of $\delta_{l,vir}$ and δ_{vir} were obtained introducing the virial theorem into the *SIM* formalism. This has important implications in the way we define the virial radius (the radius that attains an overdensity δ_{vir} inside) of dark matter halos in N-body cosmological simulations. δ_{vir} is conventionally chosen to be near 180 for an Einstein-deSitter cosmology (e.g. Peebles 1980), or 340 for the $\Omega_\Lambda = 0.7$ cosmology (e.g. Bryan & Norman 1998; Lokas & Hoffman 2000).

In the standard derivation of $\delta_{l,vir}$ and δ_{vir}, the typical way to proceed is to assume that a shell of matter stabilizes at an epoch twice the time of turn-around (i.e. the time predicted by the standard *SIM* to collapse into a point), and in average with a radius that is 1/2 the turn-around radius (e.g. Peebles 1980; Lacey & Cole 1994; Eke, Cole & Frenk 1996). This 1/2 factor (in the Einstein-deSitter cosmology; for other cosmologies we need to use the Lahav equation, Lahav et al. 1991) is called the *collapse factor*. However, the justification to introduce this collapse factor and to suppose the time of virialization as twice the time of turn-around, is poor and lack a solid theoretical background. In contrast, in this work we will study the spherical collapse without supposing any collapse factor, only taking into account the shell-crossing as the dominant effect. The angular momentum and velocity dispersion may also play an important role. The question is that if these effects were included in the model, would we obtain the same values for δ_{vir} and $\delta_{l,vir}$ that those found in the most simplistic scenario described by the standard *SIM*? This issue is one of the aims of the present work.

The main goal of this line of work is to develop a theoretical framework that help us to understand the dynamical elements that determine the process of formation of structures (collapsed objects) using spherical simmetry to explain main properties of dark matter halos. In this first work we will tackle these questions by means of a "cold" collapse, that is, without including the effects of the velocity dispersion and angular momentum. The point is to ascertain if the non-uniformity of the density profiles generated via shell-crossing is able to provide the radial motions necessary to produce the virialization and stabilization in an appropiate time scale. In a future work, we will include the angular momentum and velocity dispersion to go a step further.

There are some issues that it is worth to mention and that make this work different from previous works that also included the shell-crossing in their formalism (e.g. Lokas & Hoffman 2000; Nusser 2001; Hiotelis 2002; Ascasibar et al. 2004). The way to proceed in these works is to handle the effect of shell-crossing by means of an adiabatic invariant, once the standard *SIM* becomes incorrect for late stages of the evolution. This adiabatic invariant, also known as *radial action*, makes the problem analitically tractable, and is based on the fact that the potential evolves in a time larger than the orbital period of the most inner shells. In contrast, we will study the shell-crossing effect doing a follow-up of the radius that contains inside always the same fraction of the virial mass. This way to tackle the problem is only one of the possible options, but is essential, for example, in order to build and study the relationship between the actual enclosed density contrast δ, defined as $\delta = \frac{\rho(<r)-<\rho_m>}{<\rho_m>}$, with $<\rho_m>$ the mean matter density of the Universe, and the linear density contrast, δ_l, obtained from the linear theory. Only Gehard Lemson did something similar, although using N-body simulations and mainly focused on showing how accurate are the predictions of the standard *SIM* compared to his simulations (Lemson 1995). Despite the fact that he showed that the *SIM* is a powerful tool to understand the evolution of halos, he never provided detailed quantites and relations for the actual and linear density contrasts. The function $\delta_l(\delta)$ is very important to obtain the density profiles of dark matter halos, as we discussed in previous works (Prada et al. 2006; Betancort-Rijo et al. 2006). Sheth & Tormen (2002) parametrized this function for the standard *SIM*. The framework presented here will allow us in the near future to provide also a simple parametrization for $\delta_l(\delta)$, but taking into account the important effect of shell-crossing, together with others relevant effects such as the angular momentum and velocity dispersion. This will lead us, for example, to obtain $\delta_{l,vir}$ and its corresponding δ_{vir}, to explain the shape of the dark matter density profiles or to shed light on the mass functions. All of this without supposing any collapse factor, as pointed before, or other vague assumptions. Nevertheless, it will not be possible to obtain useful applications by the moment, since in this first work we will include in our study only the shell-crossing, which is the dominant effect. The full treatment will be done and presented in an upcoming work. Here we will provide the first results of our theoretical framework related to the role played by the shell-crossing.

This work is organized as follows. In Section 3.2 we briefly describe the *SIM* and explain the formalism and units that we will use in the rest of the work. In Section 3.5 we will study in detail the dependence of the way that the evolution occurs varying some parameters, in particular, the virial mass of the halo, the fraction of mass for a given virial mass, and the cosmology. Section 3.6 will be specially dedicated to the moments of virialization and stabilization according to a given criterion, and their dependence with the same parameters described above. We will also emphasize here the difference between these two concepts. Finally, in Section 3.10, we address the

main results and ideas of the work, and point the lines for a future work.

3.2 The Spherical Shell Tracker Framework

In this section, we first describe the standard *SIM* and its equations, and then we present the formalism that we will use in the rest of the work, which will imply to describe the density profile and define our own unities. This will allow us to handle easily the equations involved. Later, the algorithm that we used to obtain the results will be described carefully step by step. All together will be known as the Spherical Shell Tracker Framework (*SST*). The main objetive of this section is to make easier a possible reproduction and implementation of the *SST* framework.

3.3 The formalism

In a flat Universe with $\Omega_\Lambda = 0$, the evolution of a homogeneous spherical (positive) density perturbation (the simplest way to tackle the problem of structure formation) with a mass M and radius R, is given by Newtonian dynamics (as shown by Tolman 1934 and Bondi 1947), provided that R be much smaller than the Hubble radius:

$$\frac{d^2R}{dt^2} = \frac{-G\ M}{R^2} \tag{3.1}$$

Integrating, since M is constant by definition, we obtain:

$$\frac{1}{2}\frac{dR}{dt^2} - \frac{G\ M}{R} = E \tag{3.2}$$

where E determines whether the sphere expands forever ($E > 0$) or it finally contracts ($E < 0$).

We can describe this spherical perturbation with a large number of mass particles, and even it is possible and more useful to imagine these particles as concentric shells (thanks to spherical simmetry) that do not cross each other, and each of them with a radius $r(j,t)$, where j denotes the shell, which satisfies equation (3.1):

$$\frac{d^2r(j,t)}{dt^2} = \frac{-G\ M(j,t)}{r(j,t)^2} \tag{3.3}$$

where $M(j,t)$ is the enclosed mass for each shell j at time t:

$$M(j,t) = \rho_{crit}\left(\frac{4\pi}{3}r(j,t)^3\right)[1 + \delta(r(j,t))] \tag{3.4}$$

being ρ_{crit} the critical density of the Universe, and $\delta(r)$ the actual density contrast whithin $r(j,t)$:

$$\rho_{crit} = \frac{3\ H^2}{8\pi\ G}; \qquad \delta(r) = \frac{\rho(<r) - <\rho_m>}{<\rho_m>} \tag{3.5}$$

with H the Hubble constant, and $<\rho_m>$ the mean matter density of the Universe.

As long as shell-crossing does not occurs, the actual density contrast is related to the linear one (given by the linear theory, see e.g. Padmanabhan 1993) in the Einstein-deSitter cosmology by the formula (Sheth & Tormen 2002):

$$\delta_l(\delta) = \left[1.68647 - \frac{1.35}{(1+\delta)^{2/3}} - \frac{1.12431}{(1+\delta)^{1/2}} + \frac{0.78785}{(1+\delta)^{0.58661}}\right] \tag{3.6}$$

The inverse function, $\delta(\delta_l)$, is given by (Patiri et al. 2004):

$$\begin{aligned}\delta(\delta_l) = 0.993\big[&(1 - 0.607(\delta_l - 6.5\times10^{-3}(1-\theta(\delta_l)+\\ &+\theta(\delta_l - 1.55))\delta_l^2))^{-1.66} - 1\big]\end{aligned} \tag{3.7}$$

being θ the step function:

$$\theta(x) = \begin{cases} 1 & \text{if x} > 0 \\ 0 & \text{if x} \leq 0 \end{cases}$$

It is possible to make some simplifications in the equations, choosing in an appropiate manner the value of some parameters. In particular, we choose:

$$\begin{gathered}\text{time unit} = \text{initial time} \\ \text{length unit} = \text{initial radius of the protohalo, } R_i \\ \text{mass unit} = [1 + \delta(R_i)]\end{gathered}$$

According to these units, and taking into account equations (3.4) and (3.5), and an Einstein-deSitter cosmology (where $H = \frac{2}{3}t^{-1}$), we have:

$$H_i = \frac{2}{3}; \qquad \rho_{crit,i} = \frac{3}{4\pi}; \qquad G = \frac{2}{9} \tag{3.8}$$

where i refers to the initial time.

The Lagrangian radius q for each shell j (i.e. the comoving radius at $t \to 0$) is related to the Eulerian one r by:

$$q(j) = r_i(j)\ [1 + \delta(r_i(j))]^{\frac{1}{3}} \tag{3.9}$$

So, for the initial enclosed mass of a shell j, we now have simply (using eq.(3.4)):

$$M(j, t_i) = M(j) = q(j)^3 \tag{3.10}$$

We must note that this enclosed mass of a shell j, $M(j)$, is different from the mass of each shell, $M_{shell}(j)$:

$$M_{shell}(j) = M(j) - M(j-1)$$

$$M(j,t) = \sum_{i=1}^{n} M_{shell}(i) \qquad \text{always than } r(i) \leq r(j) \tag{3.11}$$

To obtain $q(j)$ using Eq.(3.9) we need $\delta^i(r_i(j))$, that is, the actual density contrast at initial time, and to this end we need the linear profile at initial time, $\delta_l^i(q(j))$. In this work we will use the linear profile presented in Prada et al. (2006) and Betancort-Rijo et al. (2006):

$$\delta_0 = \delta_{l,vir} \frac{\sigma_{12}(q)}{\sigma(Q)} \tag{3.12}$$

where $\delta_{l,vir}$ is the linear density contrast at the moment of virialization, q and Q are the Lagrangian radii related to r and R_{vir} respectively, that can be obtained using equation (3.9), and:

$$(\sigma(x))^2 = \frac{1}{2\pi^2} \int_0^\infty \mid \delta_k \mid^2 W_T^2(xk)\ k^2\ dk$$

$$\sigma_{12} = \sigma_{12}(q) = \frac{1}{2\pi^2} \int_0^\infty \mid \delta_k \mid^2 W_T(qk)\ W_T(Qk)\ k^2\ dk$$

$$W_T(x) = \frac{3(sin\ x\ - x\ cos\ x\ )}{x^3} \tag{3.13}$$

where $|\delta_k|^2$ stands for the power spectra of the density fluctuations linearly extrapolated to the present.

There is a good approximation for δ_0:

$$\delta_0 = \delta_{l,vir}\ exp\left[-b\ \left(\left(\frac{q}{Q}\right)^2 - 1\right)\right]$$

$$b(Q) = -\frac{1}{2}\ \frac{d\ln\sigma(x)}{d\ln x}\bigg|_{x=Q} \tag{3.14}$$

with b a constant depending on the mass. In Table 3.1 we present the values of b and Q that we use for each mass. Moreover, it is necessary to assign a value to $\delta_{l,vir}$ so we can use the density profile, although one of our final objetives is to obtain a precise value for it. In this work we used a $\delta_{l,vir} = 1.9$, a value which led to good results in previous works (Prada et al. 2006; Betancort-Rijo et al. 2006).

Essentially, the profile given in Eq.(3.12) and its approximation in Eq.(3.14) takes into account only the restriction $\delta_l(Q) = \delta_{l,vir}$. In Hiotelis (2002) and Ascasibar et al. (2004), a very similar density profile was also used, but using the BBKS peak formalism to compute the initial conditions. In a future work we will use a more sophisticated density profile that includes also the restriction $\delta_l(q) < \delta_{l,vir}$ for $q > Q$ (see Betancort-Rijo et al. (2006) for a more detailed description), resulting in steeper actual density profiles for smaller masses (as confirmed by numerical simulations, see

Prada et al. 2006). This fact will probably change slightly the results. For a solce of simplicity we have preferred to use now a simple profile, although the major results of this work will not depend on the assumed profile.

Table 3.1 Values of b and Q neccesary to use the approximation for δ_0 given by (3.14).

M ($h^{-1}\ M_\odot$)	Q (h^{-1}Mpc)	b
6.5×10^{10}	0.57	0.1889
5×10^{11}	1.1252	0.2202
3×10^{12}	2.0445	0.2544
2×10^{13}	3.848	0.301
5×10^{14}	11.125	0.41

For the Einstein-deSitter cosmology, the $\delta_l^i(q(j))$ profile can be obtained from equation (3.12) simply rescaling by:

$$\delta_l^i(q(j)) = \frac{1}{1+z_i}\ \delta_l(q(j)) \tag{3.15}$$

where z_i is the redshift at initial time. We can obtain $\delta^i(r_i(j))$ from $\delta_l^i(q(j))$ using the function given in (3.7). Inserting this $\delta(\delta_l^i(q(j)))$ in Eq.(3.9) we obtain the Lagrangian radius for each shell j, $q(j)$, and also using Eq.(3.10 its enclosed mass $M(j)$.

Once we have the expressions related to the initial conditions and we have presented the density profile, we need the equations of evolution. If the shells do not cross each other, then there is an analytical solution for (3.2) (e.g. Martínez & Saar 2002) that can be written in the parametric form:

$$r = r_c(1 - cos\eta); \quad t = t_c(\eta - sin\eta) \tag{3.16}$$

where:

$$r_c = \frac{GM}{c^2}; \quad t_c = \frac{r_c}{c}; \qquad \frac{dt}{d\eta} = \frac{R}{c} \tag{3.17}$$

Here c is the velocity of light and we did a change to a nondimensional variable η. This solution means that the shell expands until it reaches a maximum radius r_{ta}, the turn-around radius, at a given time t_{ta}, which is different for each shell, and after that point the shell starts to contract. We can integrate analitically equation (3.3) to study the evolution of the spherical density perturbation, at least until the turn-around, thanks to the fact that the enclosed mass of the shells do not change with time. Nevertheless, after the turn-around, the recollapse begins and the shell-crossing also starts, so we can not proceed in the same way. At that point, it is common to use a prescription based on an adiabatic invariant, to account for this secondary infall and shell-crossing (e.g. Lokas & Hoffman 2000; Nusser 2001; Hiotelis 2002; Ascasibar

et al. 2004). On the other hand, one can also integrate numerically the equation (3.3), computing at each time step the new radius, velocity and enclosed mass for each shell. This is the method that we use in our work. Our purpose is to study and to include the shell-crossing in our treatment in a natural way, i.e. without making any assumption about the collapse factor, the time at which virialization occurs, or any other simplification.

We first divide our spherical density perturbation in n equal spherical shells (equivalent to particles), all of them with the same thickness, and later we choose the shell j that contain a given fraction of mass of the total protohalo. We do so for every time step, from the start of the evolution to the end: we recompute the new enclosed mass for each shell at each time step, and we always select that one that contains the fraction of mass we are interested in (in that sense, n must be big enough to choose with high precission and without problems at each step a shell that contains exactly the required fraction of mass; in our case, $n = 3000$ was enough). If we follow for a long time the shell related to this fraction of mass, at the end its radius will be almost constant (although the corresponding physical shell will change with time), that is, we will reach stabilization (see section 4). Lu et al. (2006) used a similar algorithm, but they divided the halo in equal mass shells, instead of shells with the same thickness, as we do. Moreover, their motivations were different, mainly focused on explain the inner shape of the density profiles, and they did not carried out a follow-up of any shell in particular.

3.4 The algorithm

We now describe the algorithm we used to compute the relevant quantities (radius, velocity and enclosed mass) for each shell at each time step.

First, we need to obtain the *initial conditions*:

1. We divide the protohalo in n equal shells to calculate our array of initial radii, $r_i(j)$, that contains the radius r for all the shells. Remember that, in our units, the radius of the total cloud is the unity; moreover, j increases decreasing the radius, so $r(j = 1) = R_i$ (the radius of the whole halo), and $r(j = 3000)$ is the radius of the deepest shell.

2. In a first approximation, we make $q(j) = r_i(j)$. This will allow us to compute a second and better estimation for $q(j)$ using in an appropiate way the relation given by equation (3.9), that is:

$$q(j) = r_i(j)[1 + \delta(\delta_l^i(q(j)))]^{\frac{1}{3}} \tag{3.18}$$

   where we introduce in the right side the $q(j)$ as given by the first approximation. The function $\delta(\delta_l)$ is given by eq.(3.7) and $\delta_l^i(q(j))$ is given by (3.15).

3. Now, we will use the $q(j)$ obtained in the last step as a new approximation to compute again a better estimation for $q(j)$, according to eq.(3.18).

4. Step (iii) must be repeated until there is no difference between the $q(j)$ that we obtain after each iteration.

5. With $r_i(j)$ and the last and best estimations for the initial Lagrangian radii of the shells, $q(j)$, we can calculate the initial enclosed mass array, $M(j)$, using equation (3.10), and the mass of each shell, $M_{shell}(j)$, knowing that $M_{shell}(j) = M(j) - M(j-1)$. We will need $M_{shell}(j)$ later to compute the enclosed mass array at each time step, since the mass of each shell will be always the same, although the order of the shells will be modified.

6. We also need the initial velocity for each shell, $v_i(j)$, as given by the *SIM* (Betancort-Rijo et al. 2006):

$$v_i(j) = H_i\ r_i(j)\ \left[1 - \frac{1}{3}\frac{1}{1+\delta(\delta_l^i(q(j)))} \times \frac{1}{\frac{d\delta_l(\delta)}{d\delta}|_{\delta=\delta(\delta_l^i(q(j)))}}\ \delta_l^i(q(j))\right] \quad (3.19)$$

where $\delta_l(\delta)$ and $\delta(\delta_l)$ are given by Eq.(3.6) and Eq.(3.7), and $\delta_l^i(q(j))$ is given by Eq.(3.15). H_i is the Hubble constant at initial time, which in our units is $H_i = 2/3$.

7. Now it is possible to select the shell that contains the fraction of mass that we are interested in. Our studies will be focused on the follow-up of this shell in particular.

   Once we have calculated the initial conditions, we now need to obtain the *equations of evolution*:

8. In our units, equation (3.3) can be written as:

$$\frac{d^2r(j,t)}{dt^2} = -\frac{2}{9}\frac{M(j,t)}{r(j,t)^2} \quad (3.20)$$

   so the equations of the evolution for $r(j)$ and $v(j)$ are:

$$r(j,t+\Delta t) = r(j,t) + v(j,t)\ \Delta t \quad (3.21)$$

$$v(j,t+\Delta t) = v(j,t) - \frac{2}{9}\frac{M(j,t)\ \Delta t}{r(j,t)^2} \quad (3.22)$$

9. We also need to compute how the linear and actual density contrasts evolve with time:

$$\delta_l(j,t) = \delta_l^i(q(j))\ t^{\frac{2}{3}} \tag{3.23}$$

$$\delta(j,t) = \left[[1+\delta(\delta_l^i(q(j)))]\left(\frac{r_i(j)}{r(j)}\right)^3\right] t^2 - 1 \tag{3.24}$$

10. At each time step, we need to recalculate the new enclosed mass array, $M(j)$, using the shell mass array $M_{shell}(j)$, since the enclosed mass for a given shell j is equal to:

$$M(j,t) = \sum_{i=1}^{n} M_{shell}(i) \qquad \text{always than } r(i) \leq r(j) \tag{3.25}$$

11. At this point, we can select again the shell that contains that fraction of mass we want to study, to see what happens with its radius, velocity, and linear and actual density contrasts.

12. For each step, we will have to repeat (ix) to (xii).

    It is worth to mention, for possible reproductions of the results, that the beginning was set to an initial redshift $z_i = 15$, to make sure that we are still well inside the linear regime, i.e. the initial value of δ_l is small enough. Moreover, we used an optimized temporal step of 0.003 in our units, which is good enough to give us robust results of δ_l and δ (we checked these values using well known moments of the evolution like the turn around, where there is no shell-crossing yet).

    Furthermore, there is another important question that it is necessary to take into account to implement without problems the described algorithm. This is the fact that we have not included yet the effect of the velocity dispersion and angular momentum. Therefore, we are in a totally radial (*cold*) collapse and we will have problems in the very center of the halo if we simply integrate numerically the equations following this framework. When we compute, according to equations (3.21) and (3.22), the new radius and velocity of a shell which is located very near to the center, we can obtain at the following time step a negative radius and a positive velocity, which means that actually this shell has crossed through the center and now it goes from the inner regions of the halo to the outer ones. Nevertheless, it will be very hard that the total energy will be conserved in this process due to numerical reasons. The distance that the shell covers in only one time step is comparable to its radius, which gives a considerable "leak" of energy. There are different ways to solve this problem; one of them, the solution we chose, is to define a parameter m to measure properly

this effect and to help us to prevent this lost of energy. If we define for each shell the parameter m as $m = dr/r(j,t)$ (where $dr = r(j,t+\Delta t) - r(j,t)$ is the distance that the shell has covered along this time step), then there is no problem while m is small enough, but when m reaches a larger value, the way to minimize the lost of energy in the process is to change the velocity for its absolute value, and keeping intact the value that we have for the radius. Doing so, we *skip* the very center and the loss of energy will be minimum. After many attemps, we saw that a value of $m = 0.02$ leads to very good results.

In the ΛCDM cosmology, the formalism and the algorithm are the same, but we must introduce some changes in the initial conditions and in the equations of the evolution the spherical to take into account the different cosmology with $\Lambda \neq 0$. The equations, modified adequately, are presented in Appendix A.1.

3.5 The evolution of the halo: effect of shell-crossing

At the beginning of the evolution, we will not obtain any difference using our formalism or using the standard *SIM*, because there is no shell-crossing yet. However, when this effect starts it is clear that this will become false. However, the expected deviation with respect to that given by the standard *SIM* may be different if one uses different values for the virial mass of the halo, or study different fractions of mass respect to this virial mass, or if we move to a different cosmology. To this end, that is, to quantify in detail how big are the dependences on these kind of factors, we carried out a study with varying the virial mass of the halo, M_{vir}, the fraction of mass related to this virial mass, what we call M_{frac}, and the cosmology through the value of Ω_Λ.

To illustrate the way that shell-crossing occurs and affects to the evolution of the halo, in Figure 3.1 we show the evolution with time of the radius related to different M_{frac} for the particular case of an Einstein-deSitter cosmology and a virial mass of $M_{vir} = 3 \times 10^{12} h^{-1}\ M_\odot$. It was been done in units of the turnaround radius and time (so we can compare between different M_{frac} in the same scale). It is worth to mention that Lemson (1995) presented in the same way data from his simulations and he obtained essentially the same results as shown here for the evolution of individual shells.

Before the first shell-crossing happens, the behaviour of the radii of different M_{frac} is essentially the same. This first shell-crossing occurs just before twice the time of turn-around (the time of virialization for the usual models), and what we can see is that this first shell-crossing means the beginning of the stabilization in radius, which finally occurs some time after that (in next section, we will carry out a detailed study of this process together with the virialization). The larger radius oscillations for each curve beyond $\sim 4\ t/t_a$ (see Figure 3.1) are only noise due to the growth of numerical

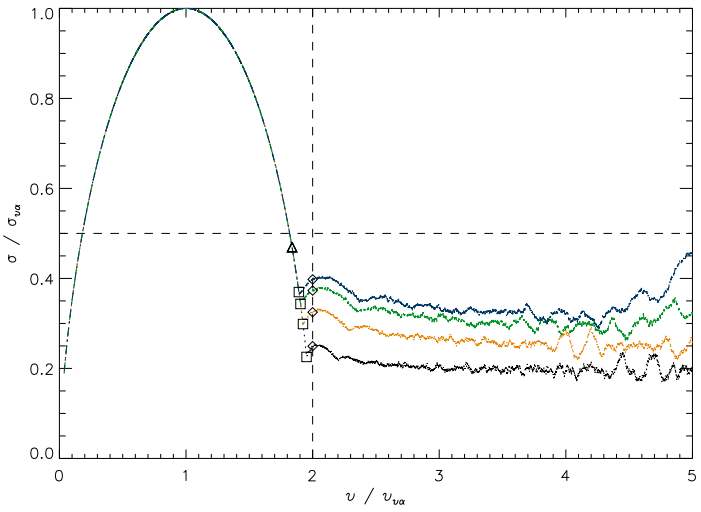

Figure 3.1 Evolution with time of the radius for different M_{frac}, for a halo with a virial mass $M_{vir} = 3 \times 10^{12} h^{-1}\ M_{\odot}$ and an Einstein-deSitter cosmology. Both radius and time are in units of the turnaround radius and time respectively. From down to top, the curves are for $M_{frac} = 0.2;\ 0.5;\ 0.8;\ 1.0$. Triangle means $\delta = 180$, squares the first shell-crossing, and circles indicate the time of collapse according to the standard *SIM*. The horizontal dashed-line corresponds to half the turnaround radius, and the vertical one the time of collapse, i.e. twice the turnaround time.

errors with time, although in the case of $M_{frac} = 1$ the larger deviations at larger times are partially and probably due to border effects, i.e. the shell that contains the required fraction of mass is near the border of the halo at that time, so there are no enough shells above to obtain a good behaviour using our algorithm.

In Table 3.2 we summarize the results for the linear and actual density contrasts for a halo with virial mass $M_{vir} = 3 \times 10^{12} h^{-1}\ M_{\odot}$ and four values of M_{frac} for two different cosmologies: the Eintein-deSitter and a model with $\Omega_m = 0.3$, $\Omega_\Lambda = 0.7$. In each case, the corresponding values of δ_l and δ are given for critical or interesting moments of the evolution, in particular when the first shell-crossing occurs (FSC), when $\delta = 180$ ($VIR1$), $\delta = 340$ ($VIR2$) and when the collapse occurs (COL) according to the standard *SIM*, that is, twice the time of turn-around. The selection of $VIR1$ and $VIR2$ was done because they are the preferred values of δ_{vir} in the literature for a flat universe with $\Omega_\Lambda = 0$ and $\Omega_\Lambda = 0.7$ respectively. They would be also useful to show a possible dependence (or not) of the function $\delta(\delta_l)$ on the cosmology. It must be noted here that for the $\Omega_\Lambda = 0.7$ cosmology, this value of Ω_Λ is always referred to redshift zero, so the given values of δ_l and δ in this case are actually related to other values of the cosmological constant, i.e. the value of this constant at that time FSC, $VIR1$, $VIR2$ or COL. This fact is common to the rest of tables of the work.

Table 3.2 Linear (δ_l) and actual (δ) density contrast values related to some important moments in the evolution of a halo with a virial mass $M_{vir} = 3 \times 10^{12} h^{-1}\ M_\odot$ and for the Einstein-deSitter and $\Omega_m = 0.3$, $\Omega_\Lambda = 0.7$ cosmologies. See text for details.

Einstein-deSitter ($\Omega_m = 1$, $\Omega_\Lambda = 0$)

	$M_{frac} = 0.2$		$M_{frac} = 0.5$		$M_{frac} = 0.8$		$M_{frac} = 1.0$	
Moment	δ_l	δ	δ_l	δ	δ_l	δ	δ_l	δ
FSC	1.667	1840	1.652	770	1.641	500	1.634	398
VIR1	1.601	180	1.602	180	1.602	180	1.602	180
VIR2	1.628	340	1.628	340	1.629	340	1.628	340
COL	1.695	1426	1.695	653	1.696	424	1.696	350

$\Omega_m = 0.3$, $\Omega_\Lambda = 0.7$

	$M_{frac} = 0.2$		$M_{frac} = 0.5$		$M_{frac} = 0.8$		$M_{frac} = 1.0$	
Moment	δ_l	δ	δ_l	δ	δ_l	δ	δ_l	δ
FSC	1.670	1728	1.655	761	1.644	516	1.639	427
VIR1	1.608	180	1.606	180	1.605	180	1.605	180
VIR2	1.632	340	1.632	340	1.631	340	1.631	340
COL	1.698	1364	1.698	338	1.697	445	1.696	380

It is important to note here that, although Table 3.2 is only for a given virial mass, the same kind of study was done for the evolution of halos with virial masses $M_{vir} = 6.5 \times 10^{10} h^{-1}\ M_\odot$ and $M_{vir} = 5 \times 10^{14} h^{-1}\ M_\odot$. We observed the same tendencies in the data and achieved the same conclusions. In Table 3.3 we show the values of δ_l and δ that we obtained for the three mentioned virial masses and for the Eintein-deSitter and the $\Omega_m = 0.3$, $\Omega_\Lambda = 0.7$ cosmologies, for the particular case in which we fixed M_{frac}=0.5.

Some interesting conclusions can be inferred from Figure 3.1 and Tables 3.2 and 3.3. The most important ones can be summarized as follows:

1. FSC, the first shell-crossing, occurs earlier as M_{frac} increases.
2. FSC occurs also earlier for larger masses.
3. FSC sets the beginning of the stabilization in radius.
4. FSC always occurs after $VIR1$ and $VIR2$ but always before COL, independently of M_{vir} and M_{frac}.
5. $VIR1$ and $VIR2$ have essentially the same associated linear density contrasts, no matter the value of M_{frac} or M_{vir}. This is because in all the cases, there

has not been any shell-crossing before $VIR1$ and $VIR2$, so the standard *SIM* is still valid.

6. Concerning to the linear and actual density contrasts for a given $M_{frac}$and M_{vir}, there is no substantial difference between the values obtained for different cosmologies.

   Specially relevant is the last conclusion, which means that there is no dependence with the cosmology in the values of δ_l and δ, or this dependence is really small and negligible.

Furthermore, we must note here the very high values found for the actual density contrast δ at the moment of the first shell-crossing (FSC) and collapse (COL). The reason for that is that there are other important effects, together with shell-crossing, involved in the formation and evolution of dark matter halos and that we have not included yet in our model. In particular, angular momentum and velocity dispersion will become very relevant and by sure will reduce the values that we obtain for δ. In fact, Avila-Reese, Firmani & Hernández (1998), Hiotelis (2002), Ascasibar et al. (2004) and Shapiro et al. (2004), amongs others, introduce and study the angular momentum and find shallower density profiles in the inner regions, as expected.

Table 3.3 Linear (δ_l) and actual (δ) density contrast values related to some important moments in the evolution of a halo for three different virial masses ($M_{vir} = 6.5 \times 10^{10} h^{-1}\ M_\odot$, $M_{vir} = 3 \times 10^{12} h^{-1}\ M_\odot$ and $M_{vir} = 5 \times 10^{14} h^{-1}\ M_\odot$) and two different cosmologies (Einstein-deSitter and $\Omega_m = 0.3$, $\Omega_\Lambda = 0.7$). A value of $M_{frac} = 0.5$ was set in all the cases. Virial masses in units of $h^{-1}\ M_\odot$.

Einstein-deSitter ($\Omega_m = 1$, $\Omega_\Lambda = 0$)

	$M_{vir} = 6.5 \times 10^{10}$		$M_{vir} = 3 \times 10^{12}$		$M_{vir} = 5 \times 10^{14}$	
Moment	δ_l	δ	δ_l	δ	δ_l	δ
FSC	1.660	1203	1.652	770	1.631	377
VIR1	1.602	180	1.602	180	1.601	180
VIR2	1.628	340	1.629	340	1.628	340
COL	1.695	986	1.695	653	1.694	335

$\Omega_m = 0.3$, $\Omega_\Lambda = 0.7$

	$M_{vir} = 6.5 \times 10^{10}$		$M_{vir} = 3 \times 10^{12}$		$M_{vir} = 5 \times 10^{14}$	
Moment	δ_l	δ	δ_l	δ	δ_l	δ
FSC	1.663	1170	1.655	761	1.637	392
VIR1	1.606	180	1.606	180	1.606	180
VIR2	1.632	340	1.632	340	1.632	340
COL	1.697	978	.698	632	1.698	338

Hence, it will be absolutely necessary to take into account at least these two effects if we want to go a step further in our analysis and if we want to obtain a good and accurate parametrization for the function $\delta_l(\delta)$. Nevertheless, the framework and algorithm we are using, as well as the conclusions and tendences we can obtain only including the shell-crossing, are totally valid although we can not reach, by now, exact values. Including other effects in our framework, specially those ones mentioned above, will be part of a future work.

Then, by the moment, we will not be able to provide an exact relation between the linear and actual density contrasts, neither a parametric form for the function $\delta_l(\delta)$. However, we can have a look to the relation that we obtain at this moment between both density contrasts, and try to extract some conclusions. In Figure 3.2, the function $\delta_l(\delta)$ is represented for the three virial masses under study and for the Einstein-deSitter cosmology. Figure 3.3 represents the same function but for different cosmologies, in particular for the Einstein-deSitter case and $\Omega_m = 0.3$, $\Omega_\Lambda = 0.7$. The linear region is clearly visible in both figures below $\delta_l \sim 1$. In this regime there is no still any difference between the different curves and the value of δ grows very slowly with δ_l, as expected. Then, there is a phase where δ increases very fast for small differences in δ_l, starting from $\delta_l \sim 1.6$ in all the cases. From this moment, the dependence with virial mass becomes clearly visible in figure 3.2, where we observe that the smaller the mass, the larger values of δ have reached for the same value of δ_l. Respect to the dependence on different cosmologies, it seems clear (see Figure 3.3) that this dependence is really small, as already mentioned.

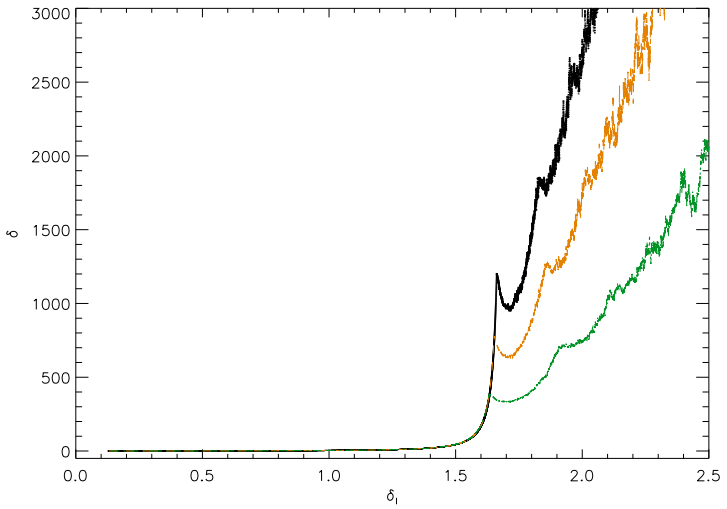

Figure 3.2 The relation $\delta_l - \delta$ for three virial masses. From down to top, the curves correspond to $M_{vir} = 5 \times 10^{14} h^{-1}\ M_\odot$, $M_{vir} = 3 \times 10^{12} h^{-1}\ M_\odot$ and $M_{vir} = 6.5 \times 10^{10} h^{-1}\ M_\odot$ (an Einstein-deSitter universe and M_{frac}=0.5 was used in all the cases).

3.6 Stabilization and Virialization

In the standard *SIM* and an Einstein-deSitter cosmology, the value of δ_l corresponding to the final stage of evolution, to the so-called *virialization*, is usually taken as $\delta_{l,vir} = 1.686$, that corresponds to an actual density contrast $\delta_{vir} \approx 180$ (e.g. Peebles 1980). For the $\Omega_m = 0.3$, $\Omega_\Lambda = 0.7$ cosmology, $\delta_{l,vir} = 1.676$ and $\delta_{vir} \approx 340$ (e.g. Lacey & Cole 1993; Eke, Cole & Frenk 1996; Bryan & Norman 1998). As pointed in previous sections, those calculations are based mainly on the following assumptions:

1. The halo virializes within a radius that is, on average, a given fraction of its maximum radius (the turnaround radius). This fraction is the collapse factor, and is equal to 1/2 in the Einstein-deSitter cosmology, and in other cosmologies it can be inferred from the Lahav equation (Lahav et al. 1991).

2. The time at which virialization occurs is twice the time of turn-around, that is, the time at which the collapse happens according to the standard *SIM*.

Although the values inferred for $\delta_{l,vir}$ and δ_{vir} in this way are commonly accepted as the correct ones and are widely used in the entire literature, the reasons to make the assumptions given above lack a solid theoretical base (see section 3.5). In fact, there are some works that point to another direction and estimate other values of $\delta_{l,vir}$ and δ_{vir}. Jenkins et al. (2001), for example, find a better agreement with the simulations if δ_{vir} is taken constant for all the cosmologies and near the value that it takes in the Einstein deSitter cosmology ($\delta_{vir} \sim 180$). Also Avila-Reese, Firmani

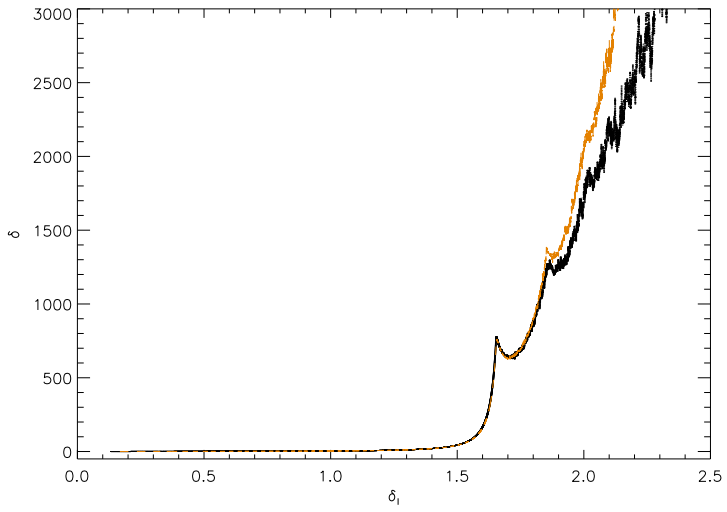

Figure 3.3 The relation $\delta_l - \delta$ for two different cosmologies. From down to top, the curves correspond to the Einstein-deSitter case and to the $\Omega_m = 0.3$, $\Omega_\Lambda = 0.7$ cosmology (a virial mass of $M_{vir} = 3 \times 10^{12} h^{-1}\ M_\odot$ and M_{frac}=0.5 was used in all the cases).

& Hernández (1998) find that a diferent value of $\delta_{l,vir}$ respect to that deduced using the above assumptions makes better the comparison between the analytical Prech-Schechter mass distribution and the results of N-body simulations.

Moreover, there is another important question related to the virialization that should be considered here. In the framework of the standard *SIM*, it is possible to apply the virial theorem if we suppose the halo to be an isolated system. However, real halos are non-isolated systems, since they are immersed in large filamentary structures, with surrounding material continously falling or scaping from the system, since they feel the tidal fields of their neighbours, etc. Hence, the virial theorem should not be applied in this case. Despite of this fact, the standard *SIM* together with the virial theorem have been used to obtain the values of $\delta_{l,vir}$ and δ_{vir}, and these values have been taken as the references to define the virial radius and the virial mass of the halos, which is specially adopted in N-body simulations. Furthermore, this fact has been traditionally supported for radial velocity early studies of massive dark matter halos from simulations (Crone et al. 1994; Cole & Lacey 1996). These studies apparently showed that the virial radius in this way defined (using $\delta_{l,vir} = 1.69$ and $\delta_{vir} \sim 180$ in the Einstein-deSitter) constitutes an adequate boundary to separate the inner region of the halo in dynamical equilibrium, i.e. that region where the radial velocities are zero, from the external region showing infall velocities. The popularization of these ideas came contemporarily with works that defined the virial mass and virial radius in simulations according to these preliminary results (specially the NFW papers). But the fact is that, as recently shown in Prada et al. (2006), this may not be totally correct. Concerning to galaxy-size halos, for example, they display all the properties of relaxed objects up to ~ 3 virial radius and there is no indication of infall of material beyond. Therefore, there is no reason to believe that only inside the virial radius, as currently defined, the halo is in equlibrium. In this context, it is important to understand the process of virialization more in depth.

In our work, no assumption is done related to the virialization. No collapse factor, no time for virialization *a priori* is adopted. Including shell-crossing in the way we do will allow us to obtain $\delta_{l,vir}$ and its corresponding δ_{vir} in a natural way, i.e. studying the evolution of different shells of the halo according to the *SST* framework, presented in section 2. It must be noted, however, that these values are still preliminary, since it will be necessary to include the effects of angular momentum and velocity dispersion to obtain precise and useful values. Nevertheless, this study will be suitable to isolate the role of shell-crossing and will be able to extract important conclusions related to the stabilization and virialization. We believe that these conclusions will no change when we introduce other physical considerations into the framework.

It is important to note here the difference between these two concepts: stabilization and virialization. The first one can be inferred studying the behaviour of the

radius of a given shell that contains a given fraction of the virial mass with time, as was shown in Figure 3.1. A criterion must be imposed to say if a given shell reaches stabilization or not, and when. The second concept, the virialization, will have to be inferred according to the virial theorem. There is no reason why stabilization and virialization should coincide, although instinctively one expect that they should be near in time at least.

3.7 Stabilization

In first place, we define the time of stabilization as the time at which the radius of the shell that we are studying varies less than a given percent, and during -at least- an interval of time equal to once the time of turnaround. In practice, what we do is to choose the moment inmediately after the time of first shell-crossing, and we see if there is no a variation in radius larger than the maximum variation that we want to impose as our criterion. It must be in this way during, at least, a time of turnaround from this moment to forward. The value of reference that we take to measure the variations in radius is the value of the radius at the initial moment of this interval. If the percentage of variation of the radius is exceeded in any time within this interval, then we choose the moment inmediately after the previouly chosen, and so on until we find an interval of time where the criterion is satisfied. The first moment at which this occurs is our time of stabilization, and the value of the radius at the time of stabilization is taken as our radius of stabilization.

This is illustrated in Figure 3.4, where the moments of stabilization are shown for a 5% and 10% of allowed variation of radius, for a particular cosmology ($\Omega_m = 0.3$, $\Omega_\Lambda = 0.7$), a value of M_{frac}, and for different virial masses. As one can see, in the case of 10% the stabilization is reached inmediately after the first shell-crossing, but the stabilization according to only 5% of allowed variation of the radius is not reached until roughly half of a time of turnaround later. Moreover, this stabilization remains during more than once the time of turnaround from that moment to forward (which is the minimum required by our criterion). Only at late times, where the evolution is dominated by numerical noise, the stabilization becomes worse than 5%. However, the most important conclusion is that the stabilization is not reached in any case for a radius that is 1/2 the radius of turnaround, value that corresponds to the collapse factor assumed in the standard derivation of $\delta_{l,vir}$ and δ_{vir}. This fact constitutes another proof that tell us how inappropiate are the current assumptions done about the virialization.

A detailed study was done for different values of M_{vir}, M_{frac} and cosmologies. A summary of this study can be found in Appendix A.2, Tables A.1 and A.2. In these tables we present the values for the density contrasts that we obtain for two different degrees of stabilization (5% and 10%), with varying M_{vir}, M_{frac} and for the

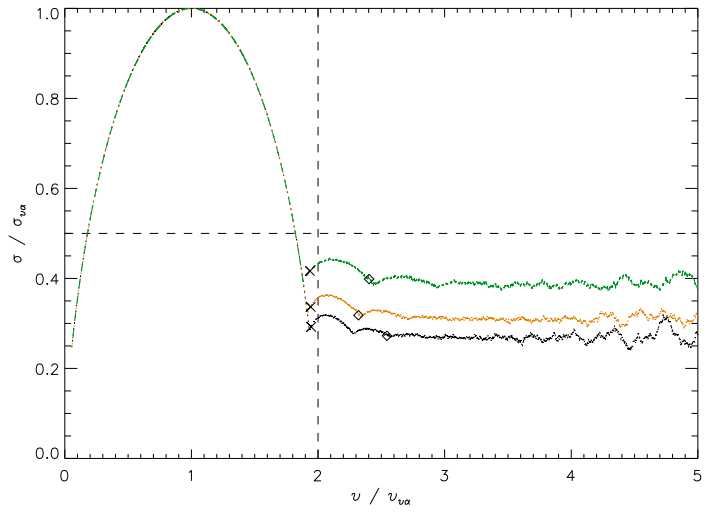

Figure 3.4 Stabilization at 5% (circles) and 10% (crosses) for the particular case of $\Omega_\Lambda = 0.7$ and $M_{frac} = 0.5$ for three different virial masses. From down to top, the curves correspond to $M_{vir} = 6.5 \times 10^{10} h^{-1}\ M_\odot$ $M_{vir} = 3 \times 10^{12} h^{-1}\ M_\odot$ $M_{vir} = 5 \times 10^{14} h^{-1}\ M_\odot$. Again, the horizontal dashed-line corresponds to half the turnaround radius, and the vertical one the time of collapse, i.e. twice the turnaround time.

Einstein-deSitter and $\Omega_m = 0.3$, $\Omega_\Lambda = 0.7$ cosmologies.

3.8 Virialization

Concerning to the virialization, what we did was to calculate the kinetic and potential energies related to the shell that we want to study. Then, we estimate the degree of agreement respect to that given by the virial theorem (i.e. $U + 2K = 0$, where U and K are the potential and kinetic energies related to the shell under study) by means of the quantity $|2K - U|/2K$. It must be noted that, if the virial theorem was exactly satisfied by the shell at some moment of its evolution, this quantity should be at that time equal to zero.

The algoritm to define the moment and radius of virialization is the same as already described for the stabilization. When we find an interval where the degree of virialization that we want to impose is satisfied in every moment inside this interval, then we define our time and radius of virialization as those ones corresponding to the beginning of the interval considered. Again, as in the case of the stabilization, a detailed study was done for different values of M_{vir}, M_{frac} and cosmologies. We summarize the results found in Tables A.3 and A.4 of Appendix A.2. In these tables we present the values for the density contrasts that we obtain for two different degrees of virialization (25% and 35%), with varying M_{vir}, M_{frac} and for the Einstein-deSitter

and $\Omega_m = 0.3$, $\Omega_\Lambda = 0.7$ cosmologies.

There is one issue related to Tables A.3 and A.4 that it is worth to mention. In those tables, a percent of 25% and 35% was set to look for virialization. This was done in this way because we noticed that below these percents it is impossible to reach virialization in most cases according to our criterion. A smaller percent means a degree of virialization too strong to be satisfied. Nevertheless, it seems that, when the virialization is reached using these high percents, the halo has *actually* reached the virialization. This may be inferred from the fact that the individual percents that we measure in every moment within the interval considered does not decrease monotonically from the beginning of the interval to its end. In fact, what one obtains is a small fluctuation around (and near) the high percent that was imposed to find the virialization. That is, the degree of virialization does not vary substantially within the whole interval, only small fluctuations are found. There is a possible explanation to the fact that we have actually reached virialization but the degree of virialization that we find according to our definition is still above 20% or more. Until now, we have used the standard virial theorem, that only involves the kinetic and potential energies. However, because of we are treating with a non-isolated system, with shells of matter continously going in and going out from the system that we are considering as our halo, we should include in the theorem another extra term. This term would be related to the pressures involved in the system, and surely may be the explanation and the cause of this "residual" percent that we obtain in all the cases.

3.9 Comparison between stabilization and virialization: general considerations

A summary of our results concerning to the degree of both stabilization and virialization for a given shell can be found in Tables 3.4 and 3.5. In these tables, we show the degree of stabilization and virialization reached for two known moments of evolution, $VIR1$ and $VIR2$ (see section 3), for different values of M_{vir}, M_{frac} and cosmologies. It must be noted that the numbers given for the stabilization are calculated taking as reference the moment of evolution where we have stabilization in radius better than 10%.

Both tables provide useful results to extract important conclusions. In first place, one can see that the points $VIR1$ and $VIR2$ are really far from the stabilization and also from the virialization, although these points are the preferred values for the moment of virialization in most of the works. In fact, in all the cases the first shell-crossing occurs even after $VIR1$ and $VIR2$, as pointed in section 3.5, so it is not possible that the shell has reached virial equilibrium or simply stabilization in radius at that moment. Also Lemson (1995) found similar results using N-body

Table 3.4 Degree of agreement with the virial theorem (VIR) and the moment of stabilization (STA) for two moments of evolution, VIR1 and VIR2, and for different values of M_{frac} and two cosmologies. A virial mass of $M_{vir} = 3 \times 10^{12}\ h^{-1}\ M_{\odot}$ was used in all the cases. See text for details.

Einstein-deSitter ($\Omega_m = 1$, $\Omega_\Lambda = 0$)

	$M_{frac} = 0.2$		$M_{frac} = 0.5$		$M_{frac} = 0.8$		$M_{frac} = 1.0$	
Moment	VIR	STA	VIR	STA	VIR	STA	VIR	STA
VIR1	4.64	0.57	2.98	0.43	2.58	0.33	1.01	0.25
VIR2	4.12	0.47	2.80	0.31	1.01	0.19	1.01	0.09

$\Omega_m = 0.3$, $\Omega_\Lambda = 0.7$

	$M_{frac} = 0.2$		$M_{frac} = 0.5$		$M_{frac} = 0.8$		$M_{frac} = 1.0$	
Moment	VIR	STA	VIR	STA	VIR	STA	VIR	STA
VIR1	4.32	0.49	2.75	0.35	1.80	0.23	1.42	0.19
VIR2	3.88	0.39	2.40	0.21	1.65	0.07	1.31	0.05

simulations, i.e. the equilibrium is reached in a longer time respect to that predicted by the standard *SIM*. This fact was one of the reasons to carry out the study in the way already described in the subsections dedicated to the stabilization and the virialization (with the results summarize in Tables A.1 to A.4). This alternative way is based on looking for the moment where we really have reached stabilization and virialization. In the first case according to a percent that we impose for the allowed variation of the radius during a significative interval of time; in the second case for the degree of agreement with the virial theorem during a similar interval. In most of the cases, both stabilization and virialization were obtained far from the value $\delta_l = 1.686$ or $\delta_l = 1.676$, the preferred values of $\delta_{l,vir}$ for the Einstein-deSitter and the $\Omega_m = 0.3$, $\Omega_\Lambda = 0.7$ cosmology respectively.

Concerning to the associated values of the actual density contrast, δ, we find very high values in most cases. It should be noted, however, that it is expected that these values decrease substantially when we include angular momentum and velocity dispersion in the formalism. So, the values showed in these tables are totally related to the isolated effect of shell-crossing.

There are also other issues that could be interesting to stress, and that should be explored more in detail in a future work:

1. Concerning to $VIR1$ and $VIR2$, the degree of both virialization and stabilization is better for longer values of M_{vir}.

2. Concerning to $VIR1$ and $VIR2$, the degree of both virialization and stabilization is also better for longer values of M_{frac}.

Table 3.5 Degree of agreement with the virial theorem (VIR) and the moment of stabilization (STA) for two moments of evolution, VIR1 and VIR2, and for three different virial masses and two cosmologies. A value of $M_{frac} = 0.5$ was used in all the cases. Virial masses in units of $h^{-1}\ M_{\odot}$. See text for details.

Einstein-deSitter ($\Omega_m = 1$, $\Omega_\Lambda = 0$)

	$M_{vir} = 6.5 \times 10^{10}$		$M_{vir} = 3 \times 10^{12}$		$M_{vir} = 5 \times 10^{14}$	
Moment	VIR	STA	VIR	STA	VIR	STA
VIR1	2.62	0.51	2.98	0.43	2.14	0.23
VIR2	2.36	0.41	2.80	0.31	2.21	0.05

$\Omega_m = 0.3$, $\Omega_\Lambda = 0.7$

	$M_{vir} = 6.5 \times 10^{10}$		$M_{vir} = 3 \times 10^{12}$		$M_{vir} = 5 \times 10^{14}$	
Moment	VIR	STA	VIR	STA	VIR	STA
VIR1	3.50	0.43	2.75	0.35	1.18	0.17
VIR2	2.86	0.31	2.40	0.21	1.14	0.05

3. Concerning to $VIR1$ and $VIR2$, the degree of both virialization and stabilization is worse in the $\Omega_m = 0.3$, $\Omega_\Lambda = 0.7$ cosmology.

4. The moment of stabilization is reached earlier in the $\Omega_m = 0.3$, $\Omega_\Lambda = 0.7$ cosmology.

5. The moment of virialization is reached earlier for smaller values of M_{vir}.

6. The moment of virialization is reached earlier for longer values of M_{frac}. It is worth to mention that Lemson (1995) found the same from his simulations, i.e. the inner shells reach equilibrium later.

7. The moment of virialization is reached later in the $\Omega_m = 0.3$, $\Omega_\Lambda = 0.7$ cosmology.

8. By the moment, it seems that there is no coincidence in time between virialization and stabilization, although it should substantially depend on the percent that we impose to define both concepts.

9. From Figure 3.1 one can see that the stabilization in radius occurs at a fraction of the turnaround radius that is different from that given by the collapse factor, 1/2 in the Einstein-deSitter case, independently of the value of M_{frac} and M_{vir}. The same is valid for the $\Omega_m = 0.3$, $\Omega_\Lambda = 0.7$ cosmology (see Figure 3.4).

3.10 Summary and future work

In this work we have studied the effect of shell-crossing in the formation and subsequent evolution of dark matter halos. To do that, we have used the spherical collapse model, which has been widely used in the literature for more than thirty years to manage and solve questions related to these processes. Nevertheless, despite of the large amount of works that have used this model or many others that have tried to improve it by introducing in the formalism more and more complex considerations, any of them have included the effect of shell-crossing accurately. It is expected that this effect of shell-crossing will play a crucial role in the subsequent evolution of the object. However, until now the shell-crossing has been always treated analytically, usually by means of an adiabatic invariant. This fact has paradoxically implied to manage this effect in a very generic way, not capable to provide exact results and predictions of relevant quantities or properties of dark matter halos.

Here we first use the exact expressions of the standard *SIM*, together with a realistic density profile, to compute the initial conditions. Then, we handle the effect of shell-crossing numerically. This allows us to study individually any shell of matter involved in the process of formation of the halo. Doing so, we can extract multiple conclusions about the way that this process occurs, like the relation between the linear and actual density contrasts, the process of stabilization of a shell of matter, the virialization, etc. Most of these issues have been treated in the present work to a greater or lesser extent, although the main objetive have been always the developing of an adequate framework -the *SST* framework- in which we can study in depth the shell crossing and also other secondary effects.

It is possible to summarize the main conclusions of this work as follows:

1. The *SST* framework is adequate to tackle the effect of shell-crossing in a way so we can extract exact results for different issues related to the evolution of the halo: the way that the radius of a given shell evolves with time, the relation between the linear and actual density contrasts, the stabilization, the virialization, etc.

2. The shell-crossing by itself is able to produce stabilization and virialization. Nevertheless, by the moment, it is not possible to obtain the exact values of the linear and actual density contrasts related to both moments of evolution. It is neccesary to take into account also other important effects.

3. Concerning to the relation between the linear and actual density contrasts, the dependence of this relation with the cosmology is very small and practically negligible. This conclusion is contrary to most of previous works, which find in general a large dependence with cosmology. However, the dependence with the virial mass or the fraction of virial mass that we consider, is large.

4. Neither stabilization nor virialization are reached in a time according to that given by the common assumptions related to the collapse factor and the time of virialization. In all the cases, we find that both stabilization and virialization occur at larger times.

5. The values tipically used in the literature for $\delta_{l,vir}$ and δ_{vir} seem to be clearly inadequate and incorrect, and are based on not very solid assumptions. In this work, new values of $\delta_{l,vir}$ and δ_{vir} are presented, but only taking into account the effect of shell-crossing. It will be neccesary to include in our framework other effects also relevant to be able to provide useful and final values for $\delta_{l,vir}$ and δ_{vir}.

It is worth to emphasize that this work constitutes only a first step in our attempt to obtain exact and precise predictions related to the formation and evolution of dark matter halos. In the future we plan to include in our framework other important effects that it will be absolutely neccesary to take into account if we really want to provide more useful results. In particular, including the angular momentum and velocity dispersion will be the next. Furthermore, in parallel we will implement a more sophisticated density profile than that used in this work, which fixes better that found in the simulations and could change the results presented here slightly. One of the final aims of this future work will be to provide a simple parametrization for the relation $\delta_l - \delta$, which takes into account the effects of shell-crossing, angular momentum and velocity dispersion, and include also the dependences observed with the virial mass and the fraction of virial mass.

It is also in our mind to explore most of these questions using the cosmological N-body simulations together with theSST framework. Comparison between both analytical and simulation studies will be, by sure, crucial to reach a better and deeper understanding of the processes involved in the formation and evolution of dark matter halos.

Bibliography

Avila-Reese, V., Firmani, C. & Hernandez, X. 1998, ApJ, 505, 37

Ascasibar, Y., Yepes, G., Gottloeber, S. & Mueller, V. 2004, MNRAS, 352, 1109

Bardeen, J. M., Bond, J. R., Kaiser, N. & Szalay, A. S. 1986, ApJ, 304, 15 (BBKS)

Barkana R., 2004, MNRAS, 347, 59

Bertschinger, E. 1985, ApJS, 58,39

Betancort-Rijo J., Sánchez-Conde M.A., Prada F., Patiri S.G., 2006, ApJ, in press, astro-ph/0509897

Bondi H., 1947, MNRAS, 107, 410

Bryan G., Norman M., 1998, ApJ, 495, 80

Cole S., Lacey C., 1996, MNRAS, 281, 716

Crone M.M., Evrard A.E., Richstone D.O., 1994, ApJ, 432, 402

Dubinski J., Carlsberg R.G., 1991, ApJ, 378, 496

Eke V.R., Cole S., Frenk C.S., 1996, MNRAS, 282, 263

Fillmore, J. A. & Goldreich, P. 1984, ApJ, 281, 1

Frenk C.S., White S.D.M., Davis M., Efstathiou G., 1988, ApJ, 327, 507

Gunn, J. E. & Gott, J. R. 1972, ApJ, 176, 1

Gunn J. E., 1977, ApJ, 218, 592

Hiotelis, N. 2002, å, 382, 84

Hoffman Y., Shaham J., 1985, ApJ, 297, 16

Jenkins A., Frenk C. S., White S. D. M., Colberg J. M., Cole S., Evrard A. E., Couchman H. M. P., Yoshida N., 2001, MNRAS, 321, 372

Jing Y.P., Suto Y., 2000, ApJ, 529, L69

Klypin A., Kravtsov A.V., Bullock J.S., Primack J.R., 2001, ApJ, 554, 903

Lacey C., Cole S., 1994, MNRAS, 271, 676

Lahav O., Lilje P.B., Primack J.R., Rees M.J., 1991, MNRAS, 251, 128

Lemson G., 1995, PhD: Statistics and dynamics of the perturbed universe, Groningen University

Lokas E. L., 2000, MNRAS, 311, 423

Lokas, E. L. & Hoffman, Y. 2000, ApJ, 542, L139

Lu Y., Mo H.J., Katz N., Weinberg D., 2006, MNRAS, 368, 1931

Manrique A., Raig A., Salvador-Solé E., Sanchis T., Solanes J.M., 2003, ApJ, 593, 26

Martínez V.J., Saar E., 2002, Statistics of galaxy distribution, Chapman & Hall/CRC

Moore B., Governato F., Quinn T., Stadel J., Lake G., 1998, ApJ, 499, L5

Moore B., Quinn T., Governato F., Stadel J., Lake G., 1999, MNRAS, 310, 1147

Navarro, J.F., Frenk C.S., White S.D.M., 1996, ApJ, 462, 563

Navarro, J.F., Frenk C.S., White S.D.M., 1997, ApJ, 490, 493

Nusser A., Sheth R.K., 1999, MNRAS, 303, 685

Nusser, A. 2001, MNRAS, 325, 1397

Padmanabhan T., 1993, Structure formation in the Universe, Cambridge University Press, Cambridge

Padmanabhan T., 1996, MNRAS, 278, L29

Patiri S., Betancort-Rijo J. E. & Prada F., 2004, MNRAS, 368, 1132

Peebles P.J.E., 1980, The large-scale structure of the universe, Princeton University Press, Princeton, N.J.

Prada F., Klypin A. A., Simmoneau E., Betancort-Rijo J., Patiri S. G., Gottlöber S., Sánchez-Conde M. A., 2006 ApJ, 645, 1001

Press W.H., Schechter P., 1974, ApJ, 187, 425

Ricotti M., 2003, MNRAS, 344, 1237

Quinn P.J., Salmon J.K., Zurek W.H., 1986, Nat, 322, 329

Shapiro P.R., Illiev I.T., Martel H., Alvarez M.A., 2004, astro-ph/0409173

Sheth, R. K. & Tormen, G. 2002, MNRAS, 329, 61

Subramanian K., Cen R., Ostriker J. P., 2000, ApJ, 538, 528

Tolman R.C., 1934, Relativity, Thermodynamics, and Cosmology. Clarendon Press, Oxford

Part II

γ-ray Dark Matter searches: detection prospects

4

Dark matter annihilation in Draco and detection prospects[1]

A new revision of the gamma flux that we expect to detect in Imaging Atmospheric Cherenkov Telescopes (IACTs) from neutralino annihilation in the Draco dSph is presented in the context of the minimal supersymmetric standard models (MSSM) compatible with the present phenomenological and cosmological constraints, and using the dark matter (DM) density profiles compatible with the latest observations. This revision takes also into account the important effect of the Point Spread Function (PSF) of the telescope, and is valid not only for Draco but also for any other DM target. We show that this effect is crucial in the way we will observe and interpret a possible signal detection. Finally, we discuss the prospects to detect a possible gamma signal from Draco for current or planned γ-ray experiments, i.e. MAGIC, Fermi and GAW. Even with the large astrophysical and particle physics uncertainties we find that the chances to detect a neutralino annihilation signal in Draco seem to be very scarce for current experiments. However, the prospects for future IACTs with upgraded performances (especially lower threshold energies and higher sensitivities) such as those offered by the CTA project, might be substantially better.

4.1 Introduction

Nowadays, it is generally believed that only a small fraction of the matter in the Universe is luminous. In the Cold Dark Matter (CDM) cosmological scenario around one third of the "dark" side of the Universe is supposed to be composed of weakly interacting massive particles (WIMPs). although other possible candidates like axinos or gravitinos are not excluded (see Bertone et al. 2005 for a recent review). The Standard Model can not provide a suitable explanation to the dark matter (DM) problem.

[1]M. A. Sánchez-Conde, F. Prada, E. L. Łokas, M. E. Gómez, R. Wojtak and M. Moles, 2007, Phys. Rev. D, 76, 123509

However, its supersymmetric extension (SUSY) provides a natural candidate for DM in the form of a stable uncharged Majorana fermion, called neutralino, which constitutes also one of the most suitable candidates according to the current cosmological constraints. At present, large effort is being carried out to detect this SUSY DM by different methods (Muñoz 2004). In the case of the new Imaging Atmospheric Cherenkov Telescopes (IACTs), the searches are based on the detectability of gamma rays coming from the annihilation of the SUSY DM particles. IACTs in operation like MAGIC (Lorentz et al. 2004) or HESS (Hinton et al. 2004), or satellites-based experiments like the Fermi satellite (previously known as GLAST) (Gehrels & Michelson 1999), will play a very important role in these DM searches.

A relevant question concerning the search of SUSY DM is where to search for the annihilation gamma ray signal. Due to the fact that the gamma flux is proportional to the square of the DM density, we will need to point the telescope to places where we expect to find a high concentration of dark matter. In principle, the best option seems to be the Galactic Centre (GC), since it satisfies this condition and it is also very near compared to other potential targets. However, the GC is a very crowded region, which makes it difficult to discriminate between a possible γ-ray signal due to neutralino annihilation and other astrophysical sources. Whipple (Kosack et al. 2004), Cangaroo (Tsuchiya et al. 2004), and specially HESS (Aharonian et al. 2004) and MAGIC (Albert et al. 2006) have already carried out detailed observations of the GC and all of them reported a gamma point-like source at the Sag A* location. However, if this signal was interpreted as fully due to DM annihilation, it would correspond to a very massive neutralino very difficult to fit within the WMAP cosmology (Spergel et al. 2007) in the preferred SUSY framework (Bergstrom et al. 2005), although an alternative scenario with multi-TeV neutralinos compatible with WMAP is still possible (see Profumo 2006). Furthermore, an extended emission was also discovered in the GC area, but it correlates very well with already known dense molecular clouds (Aharonian et al. 2006). Recently, new HESS data on the GC have been published and a reanalysis has been carried out by the HESS collaboration (Aharonian et al. 2006b). In this work, they especially explore the possibility that some portion of the detected signal is due to neutralino annihilation. According to their results, at the moment it is not possible to exclude a DM component hidden under a non-DM power-law spectrum due to an astrophysical source.

There are also other possible targets with high dark matter density in relative proximity from us, e.g. the Andromeda galaxy, the dwarf spheroidal (dSph) galaxies - most of them satellites of the Milky Way- or even massive clusters of galaxies (e.g. Virgo). DSph galaxies represent a good option, since they are not plagued by the problems of the GC, they are dark matter dominated systems with very high mass to light ratios, and at least six of them are nearer than 100 kpc from the GC (Draco, LMC, SMC, CMa, UMi and Sagittarius).

Concerning DM detection, there are two unequivocal signatures that make sure that the γ-ray signal is due to neutralino annihilation: the spectrum of the source and

its spatial extension. Certainly, the spectrum shape is crucial to state that the gamma source is due to DM annihilation, not only to discriminate it from the astrophysical backgrounds (e.g. hadronic, electronic and diffuse for IACTs), but also from any other astrophysical sources. The keypoint here is that the spectrum of a DM annihilation source is supposed to be in concordance with that expected from the models of particle physics. Indeed, the exact annihilation spectra of MSSM neutralinos depend on the gaugino/higgsino mixing, but all of them show a continuum curved spectrum up to the mass of the DM particle and possibly faint γ-lines superimposed (Bergstrom 2000). This spectrum will be very different from those measured in the case of an astrophysical source (Aharonian et al. 2006b). As for the spatial extension of the source, in this case the important feature is that it should be extended and diffuse, showing also a characteristic shape of the gamma flux profile. Nevertheless, we must note that if we use an instrument that does not have a spatial resolution good enough compared to the extension of the source, we might see only a point-like source instead of a diffuse or extended one. This means that, although we might reach high enough sensitivity for a successful detection, we would not be completely sure whether our signal is due to DM annihilation or not. Therefore, it is clear that it is really important to resolve the source so we can conclude that it can be interpreted as neutralino annihilation.

In this work, we first calculate the gamma ray flux profiles expected in a typical IACT due to neutralino annihilation in the Draco dSph, which represents in principle a good candidate to search for DM. Draco, located at 80 kpc, is one of the dwarfs with many observational constraints, which has helped to determine better its DM density profile. This fact is very important if we really want to make a realistic prediction of the expected γ-ray flux. These flux predictions have been already done for Draco using different models for the DM density profiles (Bergstrom & Hooper 2006; Evans et al. 2004; Colafrancesco et al. 2007; Mambrini et al. 2006). Nevertheless, in our case, we compute these flux predictions for a cusp and a core DM density profiles built from the latest stellar kinematic observations together with a rigorous method of removal of interloper stars. This computation represents by itself a recommendable update of the best DM model for Draco, but as we will see it will be also useful to extract some important conclusions concerning the possible uncertainties in the absolute γ-ray flux coming from astrophysics.

Once we have obtained the flux profiles, we will use them to stress the role of the Point Spread Function (PSF) of the telescope. Including the PSF, which is directly related to the angular resolution of the IACT, is essential to interpret correctly a possible signal profile due to neutralino annihilation, not only for Draco but also for any other target. In fact, we will show that, depending on the PSF of the IACT, we could distinguish or not between different models of the DM density profile using the observed flux profile. In the case of the cusp and core DM density profiles that we use, it could be impossible to discriminate between them if the PSF is not good enough. It is worth mentioning that most of previous works in the literature (except

Prada et al. 2004) that calculated the expected flux profiles in IACTs due to dark matter annihilation did not take into account this important effect. Because of that, to emphasize the role of the PSF constitutes also one of the goals of this work.

Finally, we present the DM detection prospects of Draco for some current or planned experiments, i.e. MAGIC, Fermi and GAW. We carry out the calculations under two different approaches: detection of the gamma ray flux profile from the cusp and core DM models for Draco, and detection of an excess signal in the direction of the dwarf galaxy. We will show how the first approach could give us a lot of information about the origin of the gamma ray flux profile, but it is slightly harder to have success for this case compared to the second approach, where even the PSF of the instrument is not essential and still we could extract some important conclusions if we reached the required sensitivity.

The paper is organized as follows. In Section 4.2 we first present all the equations necessary to properly calculate the expected γ-ray flux in IACTs due to neutralino annihilation. Both the particle physics and the astrophysics involved are described carefully. For the particle physics we analyze neutralino annihilation in the context of the minimal supersymmetric standard models (MSSM) compatible with the present phenomenological and cosmological constraints. In Section 4.3 we show in detail the model that we use for the DM distribution in Draco. In Section 4.4 we calculate the Draco flux predictions. We also stress the important role of the PSF. In Section 4.5, the prospects to detect signal due to neutralino annihilation in Draco are shown for some current or planned experiments, i.e. MAGIC, Fermi and GAW. Conclusions are finally given in Section 4.6.

4.2 The γ-ray flux in IACTs

The expected total number of continuum γ-ray photons received per unit time and per unit area in a telescope with an energy threshold E_{th} is given by the product of two factors:

$$F(E > E_{\rm th}) = \frac{1}{4\pi} f_{SUSY} \cdot U(\Psi_0). \tag{4.1}$$

where Ψ_0 represents the direction of observation relative to the centre of the dark matter halo. The factor f_{SUSY} includes all the particle physics, whereas the factor $U(\Psi_0)$ involves all the astrophysical properties (such as the dark matter distribution and geometry considerations) and also accounts for the beam smearing of the telescope.

4.2.1 Particle physics: the f_{SUSY} parameter

In R-parity conserving supersymmetric theories, the lightest SUSY particle (LSP) remains stable. The widely studied Minimal Supersymmetric extension of the Standard

Model (MSSM) can predict a neutralino as the LSP with a relic density compatible with the WMAP bounds. In this section we concentrate on the MSSM under the assumption that the neutralino is the main component of the DM present in the universe. We consider its abundance inside the bounds $0.09 < \Omega_\chi h^2 < 0.13$ as derived by fitting the ΛCDM model to the WMAP data (Spergel et al. 2007), although the possibility for other DM candidates is not excluded (see Bertone 2005, Muñoz 2004) and references therein).

The properties of the neutralinos in the MSSM are determined by its gaugino-higgsino composition:

$$\chi \equiv \chi_1^0 = N_{11}\tilde{B} + N_{12}\tilde{W}^3 + N_{13}\tilde{H}_1^0 + N_{13}\tilde{H}_2^0 \tag{4.2}$$

At leading order, neutralinos do not annihilate into two-body final states containing photons. However, at one loop it is possible to get processes such as (Bergstrom & Ullio 1997; Bern et al. 2007; Ullio & Bergstrom 1997):

$$\begin{aligned} \chi + \chi &\rightarrow \gamma\gamma \\ \chi + \chi &\rightarrow Z\gamma \end{aligned}$$

with monochromatic outgoing photos of energies

$$E_\gamma \sim m_\chi, \quad E_\gamma \sim m_\chi - \frac{m_Z^2}{4m_\chi} \tag{4.3}$$

respectively. Also, the neutralino annihilation can produce a continuum γ – ray spectrum from hadronization and subsequent pion decay which can be dominate over the monochromatic γ's.

The lack of experimental evidence of supersymmetric particles leaves us with a number of undetermined parameters in the SUSY models. Therefore, the annihilation cross sections involved in both the computation of $\Omega_\chi h^2$ and γ production can change orders of magnitude with neutralino mass and its gaugino–higgsino composition. To be specific we consider mSUGRA models, where the soft terms of the MSSM are taken to be universal at the gauge unification scale M_{GUT}. Under this assumption, the effective theory at energies below M_{GUT} depends on four parameters: the soft scalar mass m_0, the soft gaugino mass $m_{1/2}$, the soft trilinear coupling A_0, and the ratio of the Higgs vacuum expectation values, $\tan\beta = \langle H_u^0 \rangle / \langle H_d^0 \rangle$. In addition, the minimisation of the Higgs potential leaves undetermined the sign of the Higgs mass parameter μ.

To provide some specific values, we assume $A_0 = 0$, $\mu > 0$ and two values of $\tan\beta$, 10 and 50. With this two cases we can provide a qualitative picture of most relevant space of parameters and the constraints imposed by phenomenology. The impact of the size of A_0 or the sign of μ can be found in several studies of the parameter space of the MSSM (see e.g. Cerdeno et al. 2003; Gomez et al. 2005; Gomez et al. 2003; Stark et al. 2005 and references therein).

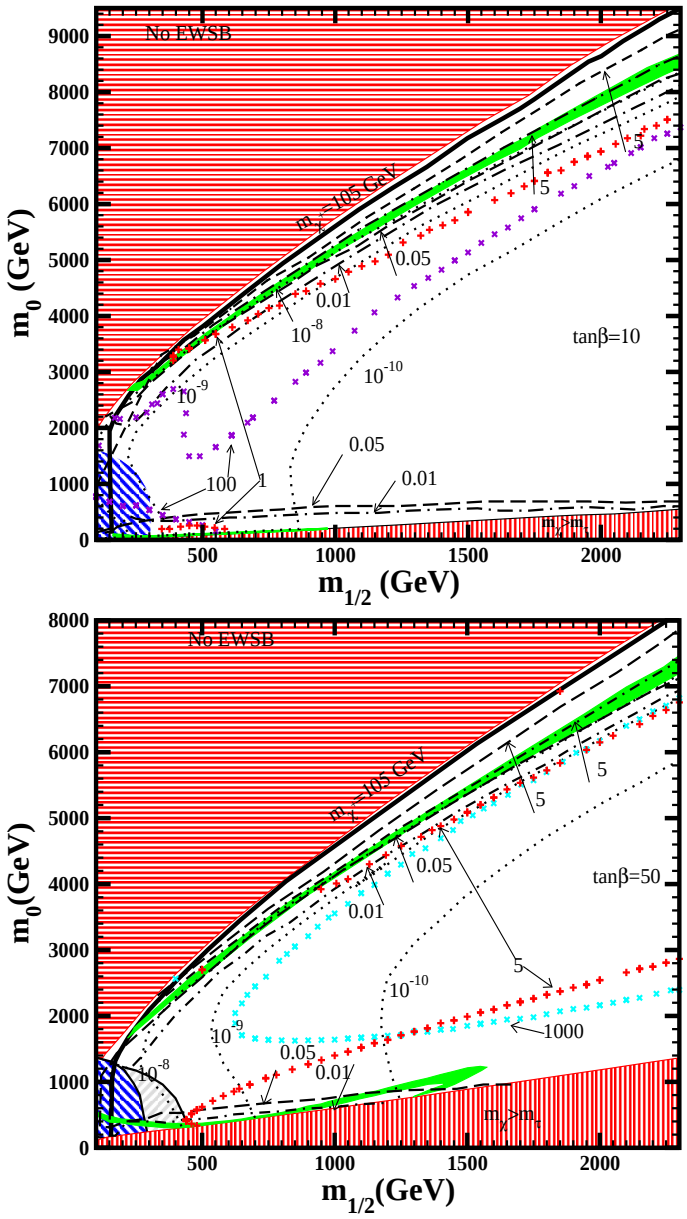

Figure 4.1 Contours on the $m_0 - m_{1/2}$ plane, the up and down ruled areas are excluded by the not satisfaction of the EWSB (up) and because $m_\chi > m_{\tilde{\tau}}$. The area below the upper thick solid line satisfies the experimental bound on the chargino mass, while the green shaded areas indicate the areas that predict neutralino relic density on WMAP bounds. From left to right, the ruled areas are excluded by the bounds on m_h^0 and $BR(b \to s\gamma)$ respectively. The doted lines indicates the values of $\sigma_{\chi p}$ in pb, the dash and dot-dash lines corresponds respectively to $2v\sigma_{\chi\chi\to\gamma\gamma}$ and $v\sigma_{\chi\chi\to Z\gamma}$ in units of $10^{-29} cm^3 s^{-1}$. The line of crosses (plus) correspond to the continuum photon production with $E_\gamma > 1$ GeV ($E_\gamma > 100$ GeV) also in units of $10^{-29} cm^3 s^{-1}$.

In Fig. 4.1 we displayed some lines of constant values of $2\langle v\sigma_{\gamma\gamma}\rangle$, $\langle v\sigma_{\gamma Z}\rangle$ and cross sections for continuum $\gamma-$ray emission on the plane $m_0 - m_{1/2}$ along with the constraints derived from the lower bound on the mass of the lightest neutral Higgs, $m_h^0 = 114.1$ GeV, chargino mass $m_{\tilde{\chi}^+} = 103$ GeV and BR($b \to s\gamma$), and the areas with Ωh^2 on the WMAP bounds. Also we provide the lines with constant values for the elastic scattering χ–proton, relevant for neutralino direct detection. In the computation we used DarkSUSY (Gondolo et al. 2004) combined with isasugra (Paige et al. 2003) implementing the phenomenological constraints as discussed in Gomez et al. 2005); the estimation of BR($b \to s\gamma$) was performed using the works by Belanger et al. 2006 andGomez et al. 2006).

On the lower area consistent with WMAP the neutralino is Bino–like, the relic density is satisfied mostly due to coannihilations $\chi - \tilde{\tau}$ and in the case of $\tan\beta = 50$ because of annihilation $\chi - \chi$ through resonant channels. In this sector $\langle 2v\sigma_{\gamma\gamma}\rangle$ is dominant by a factor of 10 with respect to $\langle v\sigma_{\gamma Z}\rangle$, however its larger values lie in the areas constrained by the bounds on $m_{\tilde{\chi}^+}$, m_{h^0} and BR($b \to s\gamma$).

The higher area consistent with WMAP lies on the hyperbolic branch, the neutralino is gaugino–higgsino mixed. The position of this region is very dependent on the mass of the top; we used $m_t = 175$ GeV.

In Fig. 4.2 we present the values of f_{SUSY} versus the threshold energy of the detector, starting at $E_{th} = 0.4$ GeV, for neutralinos satisfying relic density and phenomenological constraints. f_{SUSY} is calculated as:

$$f_{SUSY} = \frac{\theta(E_{th} > m_\chi)\cdot 2\langle v\sigma_{\gamma\gamma}\rangle}{2m_\chi^2} + \frac{\theta(E_{th} > m_\chi - \frac{m_Z^2}{4m_\chi})\cdot\langle v\sigma_{\gamma Z}\rangle + \ k\langle v\sigma_{cont.}\rangle}{2m_\chi^2}, \quad (4.4)$$

where θ is the step function and k the photon multiplicity for each neutralino annihilation. We display in different panels values of f_{SUSY} corresponding to points on hyperbolic branch ($m_0 > 2$ TeV as we can see in Fig.4.1) and the values corresponding to the $\chi - \tilde{\tau}$ coannihilation and resonant annihilation areas ($m_0 < 2$ TeV). We can appreciate that on the $\chi - \tilde{\tau}$ coannihilation area, m_χ has an upper bound beyond which the relic density constraint is no longer satisfied while on the hyperbolic branch no upper bound for m_χ is reached. The largest values of f_{SUSY} are not present since they correspond to low values of $m_{1/2}$ suppressed by the bounds on $m_{\tilde{\chi}^+}$, m_{h^0} and $b \to s\gamma$. It is interesting to remark that the higher values of f_{SUSY} on the constrained areas lie in which the $\sigma_{\chi-p}$ reaches values in the range of direct detection experiments like Genius (Cerdeno et al. 2003).

To show a more general sampling on the parameter space, we present in Fig. 4.3 the γ-ray production in neutralino annihilation versus m_χ. Each panel contains about 1400 points satisfying the WMAP and phenomenological constraints mentioned above. These points are selected from random scan over 600000 parameter on the ranges:

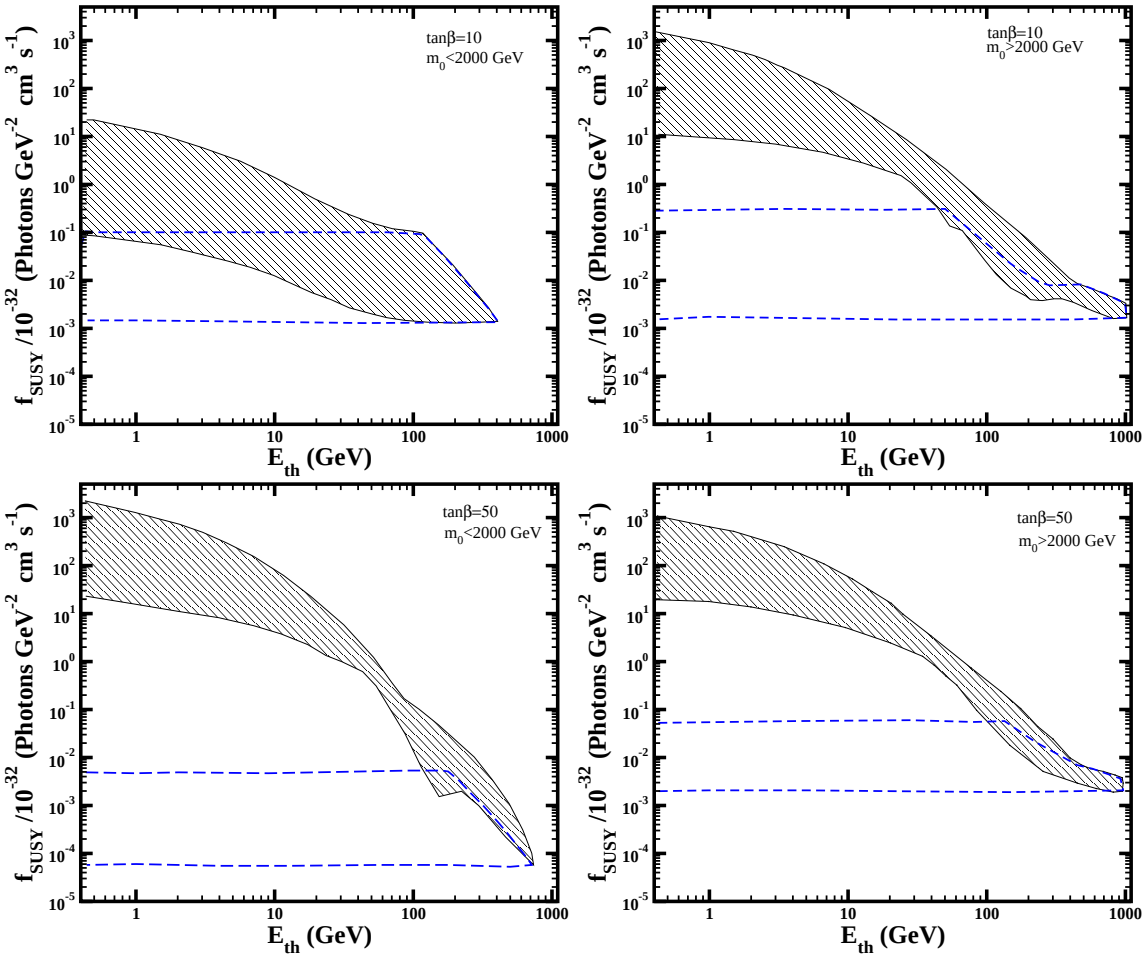

Figure 4.2 Values of f_{SUSY} respect E_{th}, for the points in Fig.4.1 on the WMAP region and satisfying all the phenomenological constraints. The ruled areas include the continuum $\gamma-$ray emission with $E_\gamma > E_{th}$, while the ones limited by thin lines correspond only to monochromatic channels. The left (right) panel corresponds to the upper (lower) allowed WMAP area in Fig. 4.1.

$$\begin{aligned} 3 < &\quad \tan\beta &< 60, \\ 50\ \text{GeV} < &\quad m_{1/2} &< 2300\,\text{GeV}, \\ -3\ m_0 < &\quad A_0 &< 3\ m_0, \\ 50\ \text{GeV} < &\quad m_0 &< 10\ \text{TeV}, \end{aligned} \tag{4.5}$$

and both signs of the μ term.

In the top panel of Fig. 4.3 we include models with $m_0 < 2$ TeV. These points satisfy the relic density constraint due mostly to $\tilde{\tau}-\chi$ coannihilations, and to a minor extend due to resonances in the annihilation channels (for large values of $\tan\beta$);

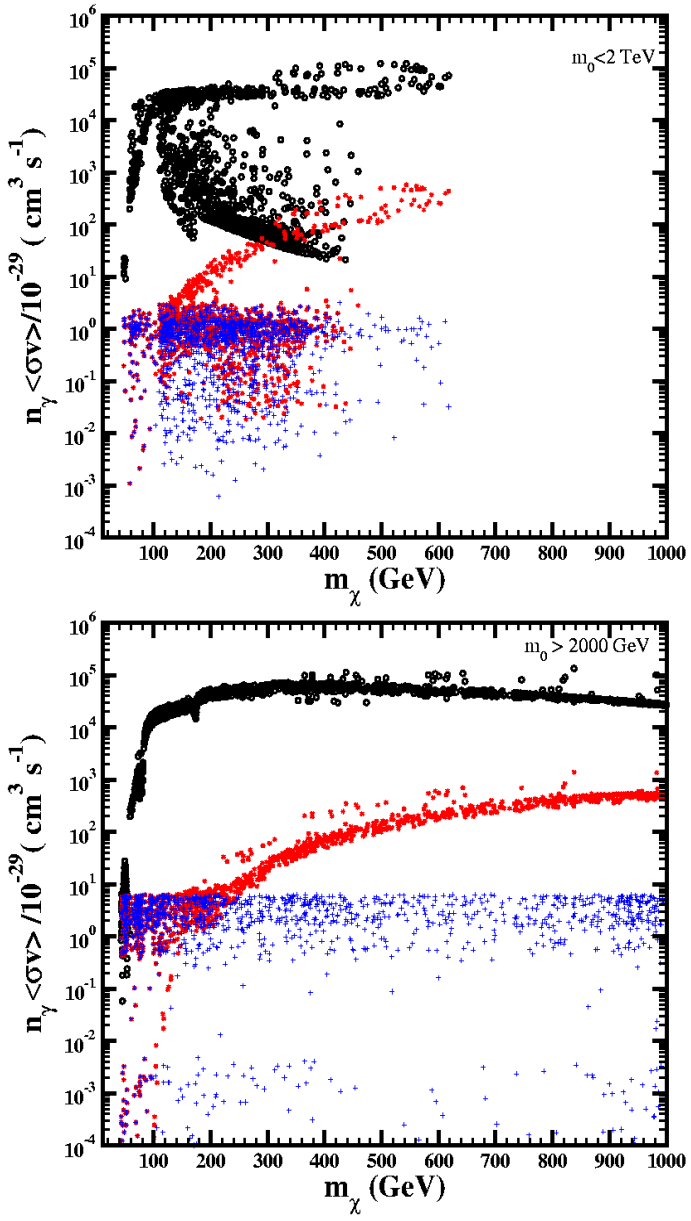

Figure 4.3 Values of $n_\gamma < \sigma_{\chi\chi} v >$ in cm^3/s including continuum emission for $E_\gamma > 1$ GeV (circles), $E_\gamma > 100$ GeV (stars), and considering only the two monochromatic channels (plus).

m_χ remain below 700 GeV in this panel. The continuum emission dominates for $E_\gamma > 1$ GeV, while for $E_\gamma > 100$ GeV we find points where the continuum production is of the same order as the monochromatic γ's. The bottom panel of Fig. 4.3 contains models $m_0 > 2$ TeV. These correspond mostly to the hyperbolic branch region; also we can appreciate that larger values for m_χ are allowed in this area than in the top panel. The points with larger cross sections in both panels corresponds to the

smaller values of the pseudo-scalar Higgs mass m_A and higher higgsino composition of the neutralino. These two factors favour the fermion production in neutralino annihilation channels. On the top panel, the larger cross sections correspond to the larger values of $\tan\beta$ while on the right panel low values for m_A can be reached for any $\tan\beta$.

The mSUGRA results do not differ significantly that the ones obtained in the more general MSSM models obtained by waiving the universality conditions on the soft terms as we will present in section 4.5.2.

4.2.2 Astrophysics: the $U(\Psi_0)$ parameter

All the astrophysical considerations are included in the expression $U(\Psi_0)$ in Eq.(4.1). This factor accounts for the dark matter distribution, the geometry of the problem and also the beam smearing of the IACT, i.e.

$$U(\Psi_0) = \int J(\Psi) B(\Omega) d\Omega \tag{4.6}$$

where $B(\Omega)d\Omega$ represents the beam smearing of the telescope, commonly known as the Point Spread Function (PSF). The PSF can be well approximated by a Gaussian:

$$B(\Omega)d\Omega = \exp\left[-\frac{\theta^2}{2\sigma_t^2}\right] \sin\theta \; d\theta \; d\phi \tag{4.7}$$

with σ_t the angular resolution of the IACT. It is worth mentioning that there is some dependence of σ_t with the energy (see e.g. Aharonian et al. 1997). However, for simplicity, we will suppose this term to be constant. The PSF plays a very important role in the way we will observe a possible DM signal in the telescope. However, most of previous works in the literature did not take into account its effect (except Prada et al. 2004; in Profumo & Kamionkowski 2006 the PSF apparently was also used, although it is not mentioned in the text (S. Profumo, private communication)). In Section 4.4 we will study in detail the importance of the PSF in the determination of the gamma ray flux profile.

The $J(\Psi)$ factor of Eq.(4.6) represents the integral of the line-of-sight of the square of the dark matter density along the direction of observation Ψ:

$$J(\Psi) = \int_{l.o.s.} \rho_{dm}^2(r) \; d\lambda = \int_{\lambda_{min}}^{\lambda_{max}} \rho_{dm}^2[r(\lambda)] \; d\lambda \tag{4.8}$$

Here, r represents the galactocentric distance, related to the distance λ to the Earth by:

$$r = \sqrt{\lambda^2 + R_\odot^2 - 2 \; \lambda \; R_\odot \cos\Psi} \tag{4.9}$$

where $R_\odot$ is the distance from the Earth to the centre of the galactic halo, and Ψ is related to the angles θ and ϕ by the relation $\cos\Psi = \cos\psi_0 \cos\theta + \sin\psi_0 \sin\theta \cos\phi$.

The lower and upper limits λ_{min} and λ_{max} in the l.o.s. integration are given by $R_\odot \cos\psi \pm \sqrt{r_t^2 - R_\odot^2 \sin^2\psi}$, where r_t is the tidal radius of the dSph galaxy in this case.

4.3 Dark matter distribution in Draco

In our modelling of Draco we used the sample of 207 Draco stars with measured line-of-sight velocities originally considered as members by Wilkinson et al. (2004). In selecting these stars these authors relied on a simple prescription going back to Yahil & Vidal (1977) and based on rejection of stars with velocities exceeding $3\sigma_{\rm los}$ where $\sigma_{\rm los}$ is the line-of-sight velocity dispersion of the sample. Lokas et al. (2005) have shown that if all these 207 stars are used to model Draco velocity distribution the resulting velocity moments can be reproduced only by extremely extended mass distribution with total mass of the order of a normal galaxy. Their arguments strongly suggested that some of the stars may in fact be unbound and the simple $3\sigma_{\rm los}$ rejection of stars is insufficient.

Here we apply a rigorous method of removal of such interlopers originally proposed by den Hartog & Katgert (1996) and applied to galaxy clusters. The method relies on calculating the maximum velocity available to the members of the object assuming that they are on circular orbits or infalling into the structure. The method was shown to be the most efficient among many methods of interloper removal recently tested on cluster-size simulated dark matter haloes by Wojtak et al. (2007). Its applicability and efficiency in the case of dSph galaxies was demonstrated by Klimentowski et al. (2007). Fig. 4.4 shows the results of the application of this procedure to Draco. The 207 stars shown in the plot are divided into those iteratively rejected by the procedure (open circles) and those accepted at the final iteration (filled circles).

The final sample with 194 stars is different from any of the three considered by Lokas et al. (2005) therefore we repeat their analysis here for this new selection. Our analysis is exactly the same, except that in the calculation of the velocity moments we use 32-33 stars per bin instead of about 40 and we consider a DM profile with a core in addition to the cusp one. The profiles of the line-of-sight velocity moments, dispersion and kurtosis, obtained for the new sample are shown in Fig. 4.5. The kurtosis was expressed in terms of the variable $k = [\log(3K/2.7)]^{1/10}$ where K is the standard kurtosis estimator. We assumed that the DM distribution in Draco can be approximated by

$$\rho_{\rm d}(r) = Cr^{-\alpha}\exp\left(-\frac{r}{r_{\rm b}}\right) \tag{4.10}$$

proposed by Kazantzidis et al. (2004), which was found to fit the density distribution of a simulated dwarf dark matter halo stripped during its evolution in the potential of a giant galaxy. In the same work it was found that the halo, which initially had a NFW distribution, preserves the cusp in the inner part (so that $\alpha = 1$ fits the final

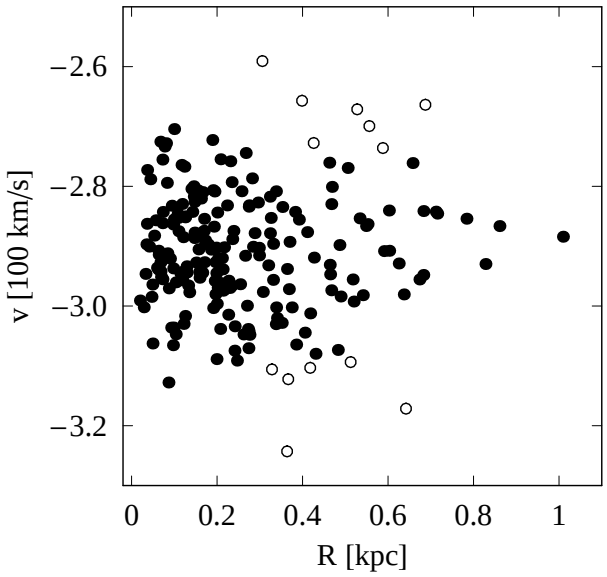

Figure 4.4 The line-of-sight velocities versus projected distances from the galaxy centre for 207 stars from Wilkinson et al. (2004). Open circles mark the 13 stars rejected by our interloper removal procedure, filled circles show the 194 ones accepted.

Table 4.1 Best-fitting parameters of the two-component models for the DM profiles with a cusp ($\alpha = 1$) and a core ($\alpha = 0$) obtained from joint fitting of velocity dispersion and kurtosis profiles shown in Fig. 4.5. The last column gives the goodness of fit measure χ^2/N.

profile	$M_{\rm D}/M_{\rm S}$	$r_{\rm b}/R_{\rm S}$	β	χ^2/N
cusp	830	7.0	-0.1	8.8/9
core	185	1.4	0.06	9.5/9

remnant very well) but develops an exponential cut-off in the outer parts. Here we will consider two cases, the profile with a cusp $\alpha = 1$ and a core $\alpha = 0$. It remains to be investigated which scenarios could lead to such core profiles.

The best-fitting solutions to the Jeans equations (see Lokas et al. 2005) for two component models with dark matter profiles given by (4.10) are plotted in Fig. 4.5 as solid lines in the case of the cusp profile and dashed lines for the core. The best-fitting parameters of the two models are listed in Table 4.1, where $M_{\rm D}/M_{\rm S}$ is the ratio of the total dark matter mass to total stellar mass, $r_{\rm b}/R_{\rm S}$ is the break radius of equation (4.10) in units of the Sérsic radius of the stars and β is the anisotropy parameter of the stellar orbits.

Fig. 4.6 shows the best-fitting dark matter density profiles in the case of the cusp (solid line) and the core (dashed line). As we can see, both density profiles

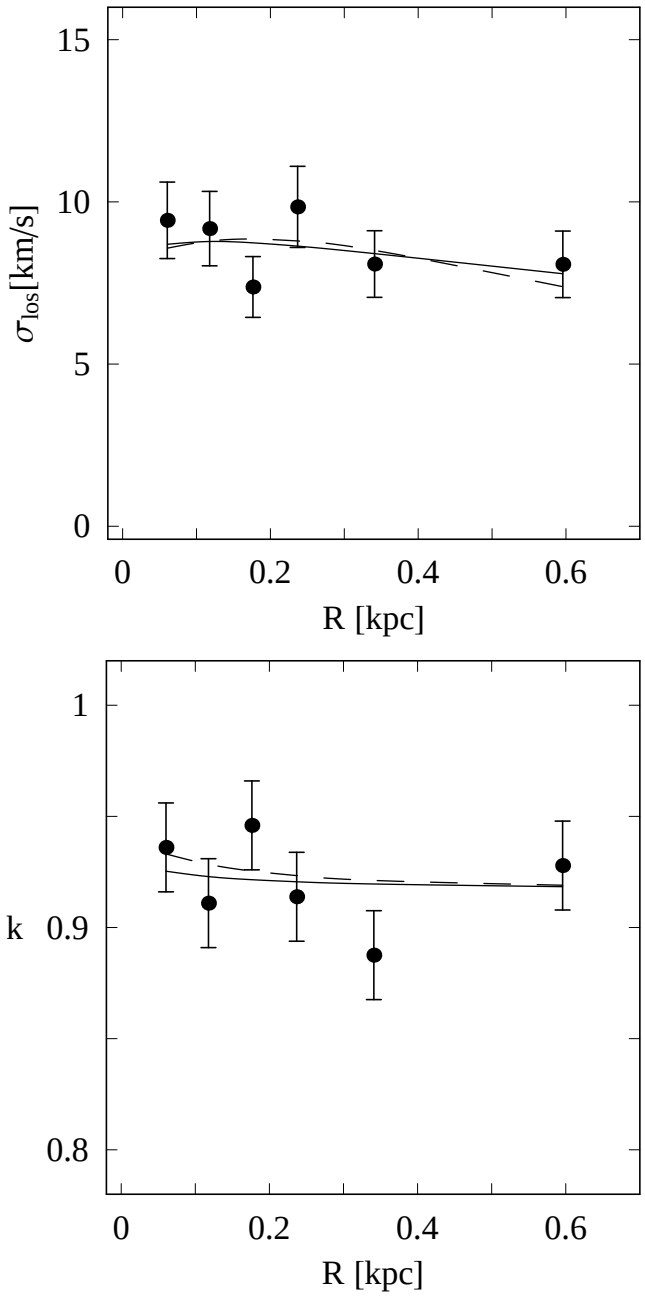

Figure 4.5 The line-of-sight velocity dispersion (upper panel) and kurtosis variable k (lower panel) calculated for the sample of 194 stars with 32-33 stars per bin. The lines show the best-fitting solutions of the Jeans equations for the DM profile with a cusp (solid lines) and a core (dashed lines).

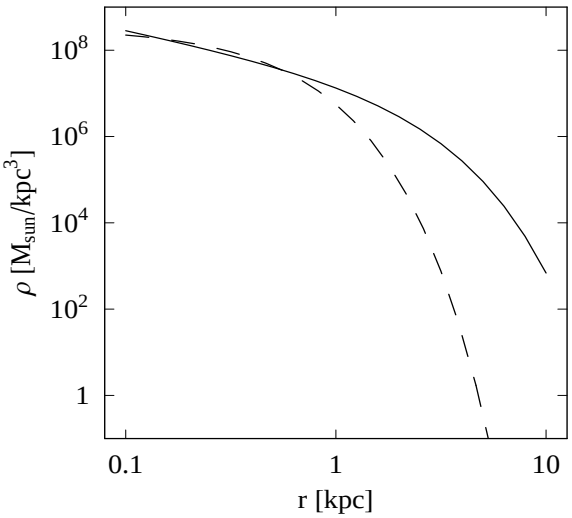

Figure 4.6 The best-fitting DM density profiles for Draco with a cusp (solid line) and a core (dashed line).

are similar up to about 1 kpc, where they are constrained by the data. The reason for very different values of the break radius $r_{\rm b}$ in both cases is the following. The kurtosis is sensitive mainly to anisotropy and it forces β to be close to zero in both cases. However, to reproduce the velocity dispersion profile with $\beta \approx 0$ the density profile has to be steep enough. In the case of the core it means that the exponential cut-off has to occur for rather low radii, which is what we see in the fit. The cusp profile does not need to steepen the profile so much so it is much more extended and its total mass is much larger.

4.4 Draco gamma ray flux profiles

In order to compute the expected gamma flux, we need to calculate the value of the "astrophysical factor", $U(\psi_0)$, given in Eq.(4.1) and presented in detail in Section 4.2.2. We calculated it for the core ($\alpha = 0$) and cusp ($\alpha = 1$) density profiles given by Eq.(4.10) using the parameters listed in Table 4.2 (that were deduced from those given in Table 4.1 and where we used $R_S = 7.3$ arcmin for Draco, following Odenkirchen et al. (2001). $R_\odot$ was set to 80 kpc, as derived from an analysis on the basis of wide-field CCD photometry of resolved stars in Draco (Aparicio et al. 2001). For the tidal radius we used a value of 7 kpc as given by Evans et al. (2004) and derived from the Roche criterion supposing an isothermal profile for the Milky Way. Nevertheless, this value depends strongly on the profile used for the Milky Way and Draco, e.g. a value of 1.6 kpc is found when a NFW DM density profile is used for both galaxies (Evans et al. 2004). It is worth mentioning, however, that we computed $J(\Psi)$ for different values of r_t and we checked that the difference between choosing

Table 4.2 Values of C and r_b for a cusp and a core DM density profile given by Eq.(4.10), as deduced from those parameters listed in Table 4.1.

profile	C	r_b (kpc)
cusp	3.1 x 10^7 $M_\odot$/kpc^2	1.189
core	3.6 x 10^8 $M_\odot$/kpc^3	0.238

$r_t = 1.6$ kpc and $r_t = 7$ kpc is less than 5% for $\Psi = 0.5°$, and still less than 10% for $\Psi = 1°$. Therefore, for the case of Draco, any value $r_t \gtrsim 1.5$ leads to robust and very similar results.

There is another issue that we will have to take into account in order to calculate $U(\psi_0)$. If we integrate the square DM density along the line of sight using a cusp DM density profile, we will obtain divergences at angles $\psi_0 \to 0$ (clearly there will not be any problem for core profiles). This can be solved by introducing a small constant DM core in the very centre of the DM halo. In particular, the radius r_{cut} at which the self annihilation rate $t_l \sim (< \sigma_{ann} v > n_\chi \; r_{cut})^{-1}$ equals the dynamical time of the halo $t_{dyn} \sim (G \; \overline{\rho})^{-1/2}$, where $\overline{\rho}$ is the mean halo density and n_χ is the neutralino number density, is usually taken as the radius of this constant density core (Fornengo et al. 2004). For the NFW DM density profile this value for r_{cut} is of the order of $10^{-13} - 10^{-14}$ kpc. For steeper DM density profiles (such as the compressed NFW or the Moore profile) a value of $r_{cut} \sim 10^{-8}$ kpc is obtained. We used a value of 10^{-8} kpc in all our computations. We must note that r_{cut} represents a lower limit concerning the acceptable values for this parameter, so the obtained fluxes should be taken as upper bounds.

Once we have calculated $U(\psi_0)$, we will need also to take a value for the f_{SUSY} parameter in order to obtain the absolute flux due to neutralino annihilation (see Eq. 4.1). We chose a value of $f_{SUSY} = 10^{-33} \; ph \; GeV^{-2} \; cm^3 \; s^{-1}$ in all our computations for a typical $E_{th} \sim 100$ GeV of the IACT. In the framework of MSSM, this value corresponds to one of the most optimistic values that is possible to adopt for f_{SUSY} according to Fig. 4.2 for the two different values of tan β presented.

The resulting γ-ray flux profiles for Draco are plotted in Figure 4.7, where we used a PSF with $\sigma_t = 0.1°$ (to simplify the notation, hereafter we will use PSF$= 0.1°$ to refer to a PSF with $\sigma_t = 0.1°$). This value of $0.1°$ is the typical value for an IACT like MAGIC or HESS. It is important to note that the core and a cusp density profiles would be distinguishable thanks to a different and characteristic shape of the flux profile in each case.

To illustrate the PSF effect on the shape of the observed flux profile with IACTs, in the top panel of Figure 4.8 we show the same as in Fig. 4.7, but here for a PSF$= 1°$. As we can see, although we have different DM density profiles, a worse telescope resolution makes both resulting flux profiles for a core and a cusp indistinguishable.

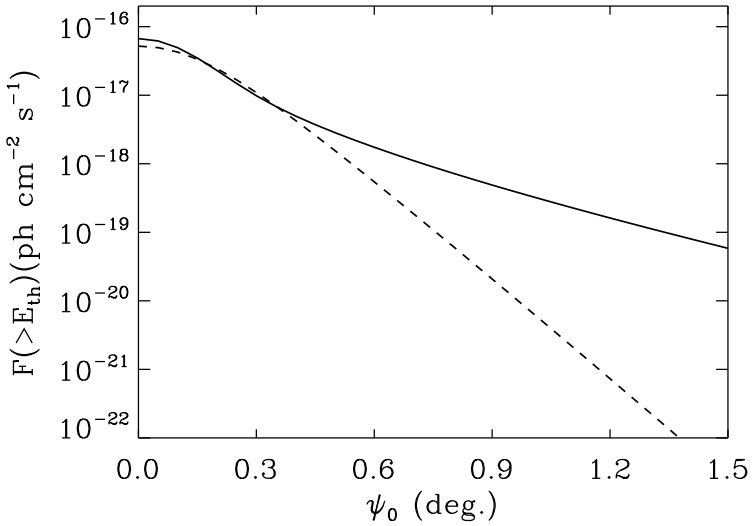

Figure 4.7 Draco flux predictions for the core (dashed line) and cusp (solid line) density profiles, computed for a typical IACT with E_{th} = 100 GeV and a PSF= 0.1°. We used $f_{SUSY} = 10^{-33}$ *ph* GeV^{-2} cm^3 s^{-1} (see text for details).

We may think that we could distinguish them from the value of the absolute flux. However, the difference in the absolute flux between both DM density profiles is very small and in practice the distinction would be impossible. There are many uncertainties in this absolute flux coming from the particle physics. f_{SUSY} may be very different from the most optimistic case assumed here, since it could vary more than three orders of magnitude for this SUSY model (see Fig. 4.2). On the other hand, the uncertainty in flux due to the DM density profile to be core or cusp is negligible at least in the inner 0.5 degrees.

Concerning the effect of the PSF given the same DM density profile, a worse telescope resolution flattens the flux profile as expected. It can be clearly seen in the bottom panel of Figure 4.8, where we plot the Draco γ-ray flux predictions only for the cusp density profile but using two different values of the PSF (0.1° and 1°), and where we plot also the same flux profile computed without PSF for comparison.

A good example to show the real importance of the telescope resolution can be found around the controversy generated in the wake of the Draco γ-ray excess reported by the CACTUS collaboration in 2005 (Marleau 2005). At this moment, it seems clear that this excess was not real and was probably due to instrumental and trigger-related issues. However, concerning our line of work and always just with the intention of clarifying the role of the PSF, we must mention the results shown in Profumo & Kamionkowski (2006). There, the CACTUS data were superimposed on different flux profiles (each of them related to possible models of DM density profiles for Draco) in Figure 2. These flux profiles were computed using an angular resolution of 0.1°, whereas the CACTUS PSF is quite worse than that (around 0.3° for the Crab and

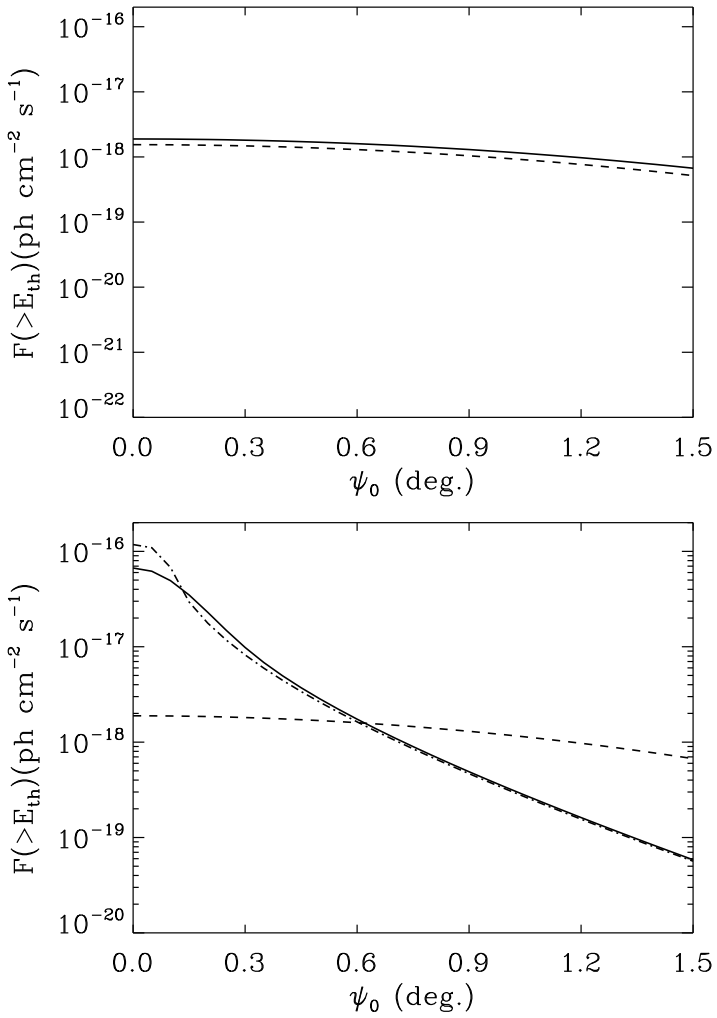

Figure 4.8 Top panel: Draco flux predictions for the core (dashed line) and cusp (solid line) density profiles, computed using a PSF= 1°. Bottom panel: Draco flux predictions for the cusp density profile using two different PSFs. Solid line corresponds to PSF=0.1° and dashed line to PSF=1°. The flux profile computing without PSF is also shown for comparison (dot-dashed line).

probably worse for Draco (Profumo & Kamionkowski 2006; Cactus Collaboration webpage[2]). Looking at that figure (despite the authors' indication to take it with care) one may come to the conclusion that a core profile seems to be the most adequate DM density profile for Draco, as opposed to the cusp profile. However, it would be more appropriate to make this comparison between the CACTUS data and the flux profiles using in both cases the same PSF of the experiment. Doing so and taking

[2]http://ucdcms.ucdavis.edu/solar2/index.php

into account the PSF effect properly, it would be difficult to use the CACTUS data to discriminate between different models for the DM density profile as described in (Profumo & Kamionkowski 2006), since all of the resultant flux profiles would have essentially the same shape. Only the absolute flux could give us a clue to make this distinction possible, but as already mentioned there are too many uncertainties related to an absolute value to be able to extract solid conclusions.

4.5 Detection prospects for some current or planned experiments

4.5.1 Flux profile detection

Would it be possible to detect a signal due to neutralino annihilation in Draco using present or planned IACTs and satellite-based gamma ray experiments? Although there are many uncertainties concerning both particle physics and astrophysical issues, as already pointed out, it is possible (and necessary) to make some calculations. These calculations will allow us to estimate at least the order of magnitude of the flux that we could expect in our telescopes, and will help us learn which instrument is, in principle, the best positioned and optimised to detect a possible signal from Draco.

Draco is located in the northern hemisphere, more precisely at declination 58°. Because of that, and regarding currently operating IACTs, MAGIC (Lorentz et al. 2004) and VERITAS (Weekes et al. 2002) are the best options thanks to their geographical position. Since both experiments have comparable sensitivity and PSF, we will focus only on MAGIC. For this IACT, with an energy threshold around 50 GeV for zenith observations, Draco could be observed 61° above the horizon, so an energy threshold ~ 100 GeV seems to be still possible at that altitude.

Concerning Fermi (Gehrels & Michelson 1999), this satellite-based experiment is designed for making observations of celestial gamma-ray sources in the energy band extending from ~ 10 MeV to 300 GeV, which is complementary to the one for MAGIC. Moreover, it has a PSF $\sim 0.1°$ at 10 GeV, which makes this instrument very competitive also in DM searches. Fermi was successfully launched in June, 2008.

The flux profiles detection prospects for both gamma-ray experiments can be seen in Figure 4.9, where the lines of sensitivity for MAGIC and Fermi are superimposed on the flux profile computed using the cusp DM density profile for Draco as given by Eq.(4.10) together with the parameters listed in Table 4.2. For the case of MAGIC, the sensitivity line represents 250 hours of observation time and a 5σ detection level. As pointed out before, this curve should be comparable and valid for VERITAS experiment as well. Concerning the predicted sensitivity for Fermi, it was calculated by the Fermi team (see the Fermi webpage[3]) for 1 year of observation and a 5σ

[3]http://www-glast.stanford.edu/

detection level. Values of $f_{SUSY} = 10^{-33}$ ph GeV^{-2} cm^3 s^{-1} at 100 GeV (MAGIC) and $f_{SUSY} = 1 \cdot 10^{-29}$ ph GeV^{-2} cm^3 s^{-1} at 1 GeV (Fermi) were chosen to convert the values calculated from the astrophysical factor $U(\Psi_0)$ to flux. These values of f_{SUSY} correspond to the most optimistic values compatible with that shown in Fig. 4.2. We chose $E_{th} = 1$ GeV for Fermi to be sure that we will have a good angular resolution for the arriving photons and also to avoid some uncertainties at low energies in the response of the Fermi LAT detector as pointed out in Bertone et al. (2006).

From Figure 4.9 we can see that the detection of the gamma ray flux profile due to neutralino annihilation in Draco with the MAGIC telescope seems to be impossible (at least for the DM density profiles and the particle physics model used here), since we would need roughly five orders of magnitude more sensitivity than that reached by this instrument in a reasonable time to have at least one opportunity to detect a possible signal coming from DM annihilation. For the case of Fermi we obtain more or less the same, although in this case the expectations are substantially better and we would need three orders of magnitude more sensitivity. We must note that this is the most optimistic scenario, so even leaving space to take into account the large uncertainties coming from the particle physics it seems very hard to have any chance of detection. In fact, in case of adopting a pessimistic value for f_{SUSY}, the γ-ray flux profile shown in Fig. 4.9 could decrease in more than three orders of magnitude easily.

There are some issues concerning a possible detection of DM annihilation not only in Draco but also in any other possible target that should be taken into account at this moment. In the case of a positive detection, this signal would be diffuse (i.e. no point-like source) for an instrument with a PSF good enough. This fact and the characteristic spectrum of the source represent the best clues to distinguish between a γ-ray signal due to neutralino annihilation from other astrophysical sources. In the case of Draco, however, we are very far from obtaining any of these clues, so Draco does not seem a good target for DM searches for current or planned γ-ray experiments (MAGIC-II, for example, will have a factor of 2 more sensitivity than the single MAGIC telescope (Baixeras et al. 2005), still clearly insufficient, and the same improvement in sensitivity is reached in the case of the Fermi satellite if we observe 5 years instead of 1).

4.5.2 Excess signal detection

Although it is strongly recommendable to try to detect the gamma ray flux profile due to neutralino annihilation, we could also search only for a gamma ray excess signal in the direction of Draco with a DM origin. In this case the prospects should be somewhat better, since we are only interested in flux detectability (i.e. no interested in observing an extended emission or not; no discrimination between different flux profiles). Draco is around 2° in the sky (the whole DM halo), and one MAGIC pointing is 4°x 4°, so the whole galaxy is within one of these MAGIC pointings. This

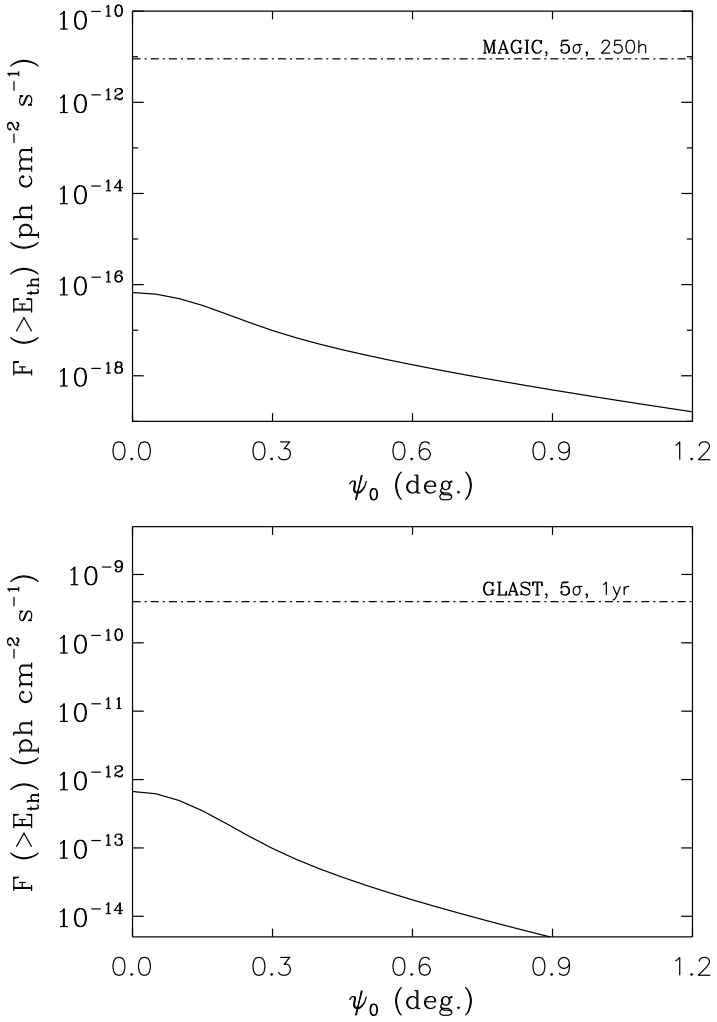

Figure 4.9 Draco flux profile detection prospects for MAGIC (top panel) and Fermi (bottom panel). The flux profile (solid line) corresponds to the cusp density profile given in Table 4.2 and using a PSF=0.1°. The sensitivity lines for both instruments were computed for a 5σ detection level and 250 hours (MAGIC) / 1 year (Fermi) of integration time. These figures should be taken as the most optimistic case, since we used the most optimistic scenario from particle physics in each case. We adopt $E_{th} = 100$ GeV for MAGIC and $E_{th} = 1$ GeV for Fermi. See text for details.

means that, to calculate the prospects of an excess signal detection for MAGIC, we must sum the gamma ray fluxes coming from all the neutralino annihilations that occur in the entire halo of the dSph. The same is valid for the case of Fermi, since one of the main objectives of this mission will be to survey the whole sky, so Draco as a whole will be observed. Nevertheless, most of the γ-ray flux due to DM annihilation comes from the inner regions of the dwarf, so it would be better to integrate the

flux and make all the calculations only for those regions. Otherwise, if we integrate up to very large angles from the center, we would be increasing the noise in a large amount without practically increasing the γ-ray signal, since the gamma ray flux profile decreases very rapidly from the center to the outskirts.

We would like here to take the opportunity to mention GAW (Maccarone et al. 2005), which is a R&D path-finder experiment, still under development, for wide field γ-ray astronomy. GAW will operate above 0.7 TeV and will have a PSF $\sim 0.2^{\circ}$. It will consist of three identical telescopes working in stereoscopic mode (80m side). The main goal of GAW is to test the feasibility of a new generation of IACTs, which join high sensitivity with large field of view (24° x 24°). GAW is planned to be located at Calar Alto Observatory (Spain) and a first part of the array should be completed and start to operate during 2008. It is a collaborative effort of research Institutes in Italy, Portugal, and Spain. We will also present some calculations concerning the possibility to observe a γ-ray signal in the direction of Draco by GAW, just to illustrate the capabilities of the instrument. Nevertheless, the main advantages of GAW will point to other directions, e.g. the possibility to survey a large portion of the sky in a reasonable time above 0.7 TeV.

In Table 4.3 we show the prospects of an excess signal detection (5σ level) for MAGIC, Fermi and GAW and for the case of the cusp DM density profile. Both the integrated absolute fluxes for Draco and the values given for the sensitivities (i.e. the minimum detectable flux, F_{min}) refer to the inner 0.5° of the galaxy (although the total size of Draco in the sky is $\sim 2^{\circ}$), just to improve the signal to noise ratio as explained above. The integrated absolute flux for Draco is not the same for the three experiments, since the f_{SUSY} parameter depends on the energy threshold of each instrument, which is different (we chose 100 GeV for MAGIC, 1 GeV for Fermi and 700 GeV for GAW). We did the calculations for the most optimistic case (i.e. the highest value of f_{SUSY} that we could adopt in the MSSM scenario following Fig. 4.2, and given the energy threshold of each telescope) and the most pessimistic one (the lowest f_{SUSY}).

According to Table 4.3, an excess signal detection would be impossible with any of these three instruments, since even in the most optimistic cases they do not reach the required sensitivity by far. If we compare these numbers with the maximum fluxes shown in Fig.4.9, we can see that the enhancement, although relevant (roughly a factor of 4 in the best case), is still very insufficient for a successful detection.

Moreover, from the results shown in Table 4.3 it becomes really hard to extract any useful results that would help us understand at least a bit better the problem of the dark matter. Indeed, if we observe Draco with MAGIC or Fermi and we do not detect any excess signal, we will not be able to put any useful constraints on the particle physics involved. None of the actual allowed values for f_{SUSY} could be rejected if we find no detection. This makes Draco even less attractive for those current gamma ray experiments that try to find DM traces.

This can be clearly seen in Fig. 4.10, where we show the parts of the SUSY

Table 4.3 Prospects of an excess signal detection for MAGIC, Fermi and GAW. Concerning the integrated flux for Draco, F_{Draco}, the most optimistic and pessimistic values are given in the form $F_{Draco,min}$ - $F_{Draco,max}$. F_{min} represents the minimum detectable flux for each instrument. Both the integrated absolute fluxes for Draco and the values given for the sensitivities (i.e. the minimum detectable flux, F_{min}) refer to the inner 0.5° of the galaxy (although its size is $\sim 2°$), just to improve the signal to noise ratio as explained in the text.

	F_{Draco} (ph cm^{-2} s^{-1})	F_{min} (ph cm^{-2} s^{-1})
MAGIC	4.0 x 10^{-18} - 4.0 x 10^{-16}	2.0 x 10^{-11} (250 h)
Fermi	4.0 x 10^{-16} - 4.0 x 10^{-12}	4.0 x 10^{-10} (1 year)
GAW	2.8 x 10^{-19} - 2.8 x 10^{-17}	2.2 x 10^{-12} (250 h)

parameter space that will be detectable by MAGIC and Fermi for the case of Draco and adopting the cusp DM density profile presented in Section 4.3. The points represent MSSM models, in contrast with Fig. 4.3 the mSUGRA condition of Eq. 4.5 has been waived such that models with random sfermion masses below 10 TeV and gaugino masses below 3 TeV are included (we considered equal soft terms for the first two generations to avoid contradiction with flavor violating observables). In the case of MAGIC we only plot those values of $n_\gamma < \sigma v >$ computed for $E_\gamma > 100$ GeV (which is the MAGIC E_{th}), and for Fermi only those ones computed for $E_\gamma > 1$ GeV (Fermi E_{th}). We must note that for each case we include in the same figure all the points no matter the value of m_0 (a distinction was done in Fig. 4.3). Also, the points related to the monochromatic channels are not shown in both figures, since their values are negligible comparing to those coming from the continuum emission and therefore they are not relevant here.

The limit between the detectable and the non-detectable areas is given by the dashed lines, so that those SUSY points that lie above these lines yield a detectable flux and the points below them are not accessible to observation. As already pointed above, it is clear that the constraints imposed by both experiments to this particular particle physics model (MSSM) are very relaxed and in fact the detection lines do not reach in any case any of the SUSY models by more than two orders of magnitude in the best case. Again, as in Fig. 4.9, the prospects for Fermi are somewhat better than for MAGIC, but they are still clearly insufficient to extract relevant results or conclusions.

4.6 Conclusions

In this work we focused on the possibility to detect a signal coming from neutralino annihilation in the Draco dwarf. This galaxy, a satellite of the Milky Way, represents one of the best suitable candidates to search for dark matter outside our galaxy,

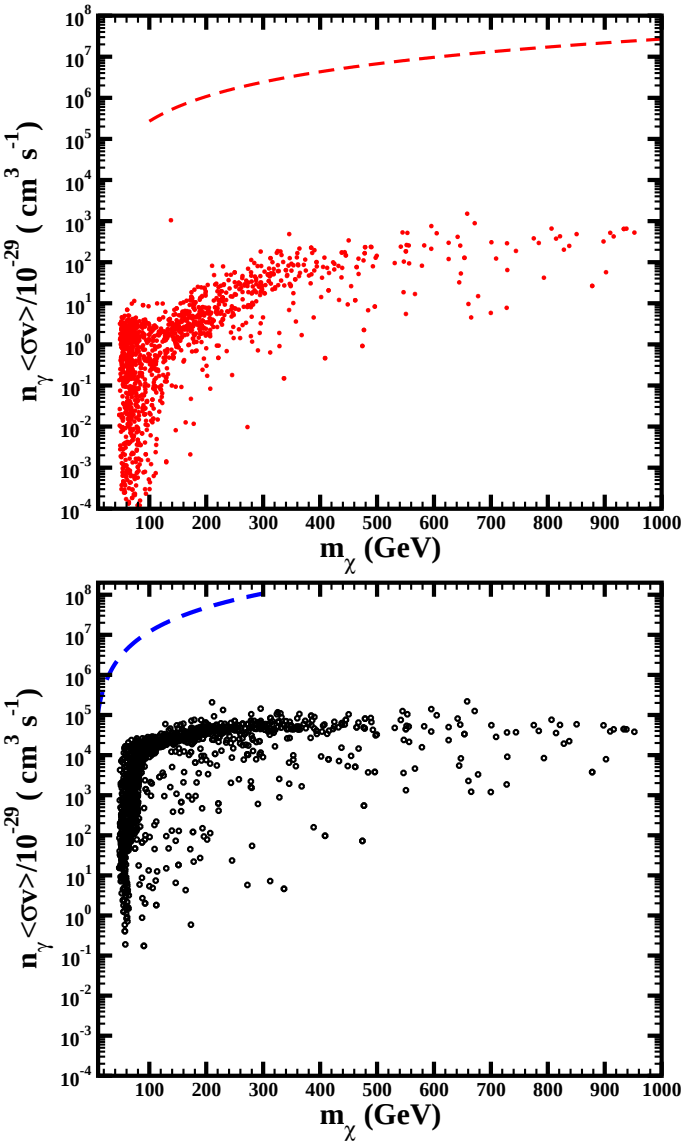

Figure 4.10 Exclusion limits for MAGIC (upper panel) and Fermi (bottom panel), for continuum γ-ray emission above 100 GeV (MAGIC) and 1 GeV (Fermi). The lines represent for each instrument the minimum detectable $n_\gamma < \sigma v >$ adopting the cusp DM density profile given in Table 4.2 for Draco. We used 250 hours (1 year) of integration time for MAGIC (Fermi) and a 5σ detection level. Below the lines, the SUSY models (points) do not yield a flux high enough for a successful detection. According to these plots, neither MAGIC nor Fermi may put any useful constraints at least to this particular particle physics model.

since it is near and it has probably more observational constraints than any other known dark matter dominated system. This fact becomes crucial when we want

to make realistic predictions of the expected observed γ-ray flux due to neutralino annihilation.

Draco is a dwarf galaxy tidally stripped by the Milky Way, so it seems preferable to build a model for the mass distribution that takes into account this important fact. Using this more appropriate model for Draco, we have obtained the γ-ray flux profiles for the case of a cusp and a core DM density profiles (both scenarios are equally valid according to the observations). To do that, we first estimated the best-fitting parameters for each density profile by adjusting the solutions of the Jeans equations to velocity moments obtained for the Draco stellar sample cleaned by a rigorous method of interloper removal. Apart from this recommendable and useful update on the best DM model for Draco, one important conclusion can be extracted concerning the absolute γ-flux: for both cusp and core DM density profiles, the flux values that we obtain are very similar for the inner region of the dwarf, i.e. where we have the largest flux values and signal detection would be easier.

There is, however, a way to distinguish between a core and a cusp DM density profile. The crucial points concerning this issue are the sensitivity and the PSF of the telescope. If the telescope resolution is good enough (and we reach the required sensitivity) a distinction between both cusp and core models may be possible thanks to the shape of the flux profile in each case. However, if the PSF of the instrument is poor, its effect could make it impossible to discriminate between different flux profiles, i.e. different models of the DM density profile. In any case, to be sure that the signal is due to neutralino annihilation, we will need to have a PSF good enough to be able to resolve the source (i.e. we will need to detect with a good resolution at least a portion of the flux profile large enough so we can conclude that it belongs to neutralino annihilation). This fact together with a characteristic spectrum are the unequivocal traces of a DM source. Both issues are of course totally valid not only for Draco but also for any other target, and therefore they should be always taken into account.

We may think that for Draco the effect of the PSF is not especially important, since current experiments do not seem to reach even the required sensitivity to detect a γ-ray signal coming from the center of the dSph. Indeed, the limiting factor here is the expected flux and not the PSF of the telescope. Nevertheless, we should account for the PSF of the instrument in any case, since we do not know a priori the expected gamma flux and we will not have a realistic prediction unless we include it in our calculations. Only then we will know the exact shape of the flux profile as could be observed by the telescope and therefore we can evaluate the real chances of detection. Furthermore, we must note that the inclusion of the PSF corresponds to a more general analysis not only valid for Draco but also for any target (the case the Milky Way for example where the role of the PSF is critical to understand the origin of the gamma emission in its center).

Some estimations concerning flux profile detection prospects for the MAGIC and Fermi experiments have been also shown. According to these calculations, even in

the most optimistic scenario (i.e. with the highest values of f_{SUSY} allowed for the MSSM particle physics model adopted here) a γ-ray signal detection from Draco seems to be really hard at least for the current IACTs and for the Fermi satellite. In addition, it would be really difficult to improve our expectations for Draco, since for example larger integration times will not improve drastically the sensitivity lines of these instruments up to the level allowing successful detection (we need around five and three orders of magnitude more sensitivity for success with MAGIC and Fermi respectively). The uncertainties coming from astrophysics, as already mentioned, are negligible compared to those coming from the particle physics, so either by choosing a cusp or a core DM density profile for Draco (or even modifying this for a steeper one) we will not be able to increase the γ-ray flux up to the level where we can expect a signal detection.

We also explored the prospects of an excess signal detection (i.e. we are not interested in the shape of the gamma ray flux profile, only in detectability) for MAGIC and Fermi, but we reached the same strongly negative conclusions as those obtained for the flux profile detection. Both instruments are very far from the required sensitivity so it seems that they do not have any chance of successful detection. But even more, in the case of an (expected) unsuccessful detection we would not be able to put any useful constraints on the particle physics involved (the uncertainties from different dark matter density profiles and other astrophysical considerations are negligible compared to this). None of the actual allowed values for f_{SUSY} could be rejected if we find no detection. This makes Draco even less attractive for those current gamma ray experiments that try to find DM traces.

From these negative results it seems that, at least for current experiments, Draco does not represent a good target for DM searches (although some important enhancements mechanisms in the γ-ray signal coming from neutralino annihilation in Draco have been proposed in Colafrancesco et al. (2007). If we want to find unequivocal traces of non-barionic dark matter in the Universe, an effort should be done in order to find other more promising DM targets. In this context, it is interesting to note that the number of known dSph galaxies satellites of the Milky Way has increased considerably in the last few years, doing possible that some of them may offer more optimistic detection prospects than Draco itself (Strigari et al. 2007). A quantitative study should be done in this direction. The search of DM subhalos in the solar neighborhood (see e.g. Diemand et al. 2007) or exploring the IMBHs scenario (Bertone et al. 2005b) may represent also other challenging possibilities, although these one more speculative for the moment.

Finally, it is worth mentioning that IACTs that join a large field of view with a high sensitivity will represent the future in this field and will provide a next step in DM searches. In this context, the Cherenkov Telescope Array (CTA) project[4] will be specially important, with a threshold energy well below 100 GeV, a wide spectral

[4]http://www.mpi-hd.mpg.de/hfm/CTA/CTA_home.html/

coverage up to 100 TeV and a factor of 5-10 more sensitivity than present experiments in the mentioned range. Also GAW, a R&D experiment under development, with an energy threshold $\sim$ 700 GeV and a 24° x 24° field of view, will constitute another complementary attempt in the same direction, although under a different approach.

Bibliography

Aharonian F. A., Hofmann F., Konopelko A. K. and Volk H. J., 1997, Astropart. Phys., 6, 343

Aharonian F. et al. , 2004, A&A, 425, L13

Aharonian F. et al. , 2006, Nature, 439, 695

Aharonian F. et al. , 2006b, Phys. Rev. Letters, 97, 221102

Albert J. et al. , 2006, ApJ, 638, L101

Aparicio A., Carrera R. and Martinez-Delgado D., 2001, AJ, 122, 2524

Baixeras C. et al. , 2005, *Proc. of the 29th International Cosmic Ray Conference*, ICRC, 5, 227

Belanger G., Boudjema F., Pukhov A. and Semenov A., 2006, Comput. Phys. Commun., 174, 577; Comput. Phys. Commun., 2002, 149, 103

Bergstrom L. and Ullio P., 1997, Nucl. Phys. B, 504, 27

Bergstrom L., 2000, Rep. Prog. Phys., 63, 793

Bergstrom L. et al. , 2005, Phys. Rev. Letters, 95, 241301

Bergstrom L. and Hooper D., 2006, Phys. Rev. D, 73, 063510

Bern Z., Gondolo P. and Perelstein M., 1997, Phys. Lett. B, 411, 86

Bertone G., Hooper D. and Silk J., 2005, Physics Reports, 405, 279

Bertone G.. Zentner A. R. and Silk J., 2005b, Phys. Rev. D, 72, 103517

Bertone G., Bringmann T., Rando R., Busetto G. and Morselli A., 2006, preprint, astro-ph/0612387

Cerdeno D. G., Gabrielli E., Gomez M. E.and Munoz C., 2003, JHEP, 0306, 030

Colafrancesco S., Profumo S. and Ullio P., 2007, Phys. Rev. D, 75, 023513

den Hartog R. and Katgert P., 1996, MNRAS, 279, 349

Diemand J., Kuhlen M. & Madau P., 2007, ApJ, 657, 262

Evans N. W., Ferrer F. and Sarkar S., 2004, Phys. Rev. D, 69, 123501

Fornengo N., Pieri L. and Scopel S., 2004, Phys. Rev. D, 70, 103529

Gehrels N. and Michelson P., 1999, Astropart. Phys., 11, 277

Gomez M. E., Lazarides G. and Pallis C., 2003, Phys. Rev. D, 67, 097701; Gomez M. E., Lazarides G. and Pallis C., 2002, Nucl. Phys. B, 638, 165

Gomez M. E., Ibrahim T., Nath P. and Skadhauge S., 2005, Phys. Rev. D, 72, 095008

Gomez M. E., Ibrahim T., Nath P. and Skadhauge S., 2006, Phys. Rev. D, 74, 015015

Gondolo P., Edsjo J., Ullio P., Bergstrom L., Schelke M. and Baltz E. A., 2004, JCAP, 0407, 008

Hinton J. A., 2004, New Astron. Rev., 48, 331

Kazantzidis S., Mayer L., Mastropietro C., Diemand J., Stadel J. and Moore B., 2004, ApJ, 608, 663

Klimentowski J., Łokas E. L., Kazantzidis S., Prada F., Mayer L. and Mamon G. A., 2007, MNRAS, 378, 353

Kosack K. et al. , 2004, ApJ, 608, L97

Łokas E. L., Mamon G. A. and Prada F., 2005, MNRAS, 363, 918

Lorentz E. et al. , 2004, New Astron. Rev., 48, 339

Maccarone M. C. et al. , 2005, *Proc. of the 29th International Cosmic Ray Conference*, ICRC, 5, 295

Mambrini Y., Munoz C., Nezri E. and Prada F., 2006, JCAP, 01, 010

Marleau P., *TAUP*, September 2005, Zaragoza (Spain); Tripathi M., *Cosmic Rays to Colliders 2005*, Prague (Czech Republic), September 2005; *TeV Particle Astrophysics Workshop*, Batavia (USA), July 2005; Chertok M., *Proc. of Panic 05*, Santa Fe (USA), October 2005

Munoz C., 2004, Int. J. Mod. Phys. A, 19, 3093

Odenkirchen M., et al. , 2001, AJ, 122, 2538

Paige F. E, Protopopescu S. D., Baer H. and Tata X., 2003, preprint, hep-ph/0312045.

Prada F., Klypin A., Flix J., Martínez M. and Simonneau E., 2004, Phys. Rev. Lett., 93, 241301

Profumo S., 2006, Phys. Rev. D, 72, 103521

Profumo S. and Kamionkowski M., 2006, JCAP, 3, 3

Spergel D. N. et al. , 2007, ApJS, 170, 377

Stark L. S, Hafliger P., Biland A. and Pauss F., 2005, JHEP, 0508, 059

Strigari, L. E., Koushiappas, S. M., Bullock, J. S., Kaplinghat, M., Simon, J. D., Geha, M., & Willman, B. 2008, ApJ, 678, 614

Tsuchiya K. et al. , 2004, ApJ, 606, L115

Ullio P. and Bergstrom L., 1998, Phys. Rev. D, 57, 1962

Weekes T. C. et al. , 2002, Astropart. Phys., 17, 221

Wilkinson M. I., Kleyna J. T., Evans N. W, Gilmore G. F., Irwin M. J. and Grebel E. K., 2004, ApJ, 611, L21

Wojtak R., Łokas E. L., Mamon G. A., Gottlöber S., Prada F. and Moles M., 2007, A&A, 466, 437

Yahil A. and Vidal N. V., 1977, ApJ, 214, 347

5

Hints of the existence of Axion-Like-Particles from the gamma-ray spectra of cosmological sources[1]

Axion Like Particles (ALPs) are predicted to couple with photons in the presence of magnetic fields. This effect may lead to a significant change in the observed spectra of gamma-ray sources such as AGNs. Here we carry out a detailed study that for the first time simultaneously considers in the same framework both the photon/axion mixing that takes place in the gamma-ray source and that one expected to occur in the intergalactic magnetic fields. An efficient photon/axion mixing in the source always means an attenuation in the photon flux, whereas the mixing in the intergalactic medium may result in a decrement and/or enhancement of the photon flux, depending on the distance of the source and the energy considered. Interestingly, we find that decreasing the value of the intergalactic magnetic field strength, which decreases the probability for photon/axion mixing, could result in an increase of the expected photon flux at Earth if the source is far enough. We also find a 30% attenuation in the intensity spectrum of distant sources, which occurs at an energy that only depends on the properties of the ALPs and the intensity of the intergalactic magnetic field, and thus independent of the AGN source being observed. Moreover, we show that this mechanism can easily explain recent puzzles in the spectra of distant gamma-ray sources, like the possible detection of TeV photons from 3C 66A (a source located at z=0.444) by MAGIC and VERITAS, which should not happen according to conventional models of photon propagation over cosmological distances. Another puzzle is the recent published lower limit to the EBL intensity at 3.6 μm (which is almost twice larger as the previous one), which implies very hard spectra for some detected TeV gamma-ray sources located at z=0.1-0.2. The consequences that come from this work are testable with

[1]M. A. Sánchez-Conde, D. Paneque, E. Bloom, F. Prada and A. Domínguez, 2009, Phys. Rev. D, 79, 123511

the current generation of gamma-ray instruments, namely Fermi (formerly known as GLAST) and imaging atmospheric Cherenkov telescopes like CANGAROO, HESS, MAGIC and VERITAS.

5.1 Introduction

The existence of axions is predicted by the Peccei-Quinn mechanism, which is currently the most compelling explanation to solve the CP problem in QCD (Peccei & Quinn 1977). Moreover, amongst all the valid candidates proposed to constitute a portion or the totality of the non-barionic cold dark matter content predicted to exist in the Universe, hypothetical non-thermal axions, or in a more generic way, Axion-Like Particles (ALPs), where the mass and the coupling constant are not related to each other, may represent a good option: they might exist in sufficient quantities to account for the estimated dark matter density and they might interact very weakly with the rest of the particles (Raffelt 2005). There is an additional property of ALPs that makes them even more attractive and that could have important implications for its detectability, i.e. they can oscillate into photons and vice-versa in the presence of an electric or magnetic field (Dicus et al. 1978, Sikivie et al. 1983). This is analogous to that predicted to occur between neutrinos of different flavors, and a similar behavior is expected in the case of the recently proposed chameleons as well (Burrage et al. 2009). This characteristic is the main vehicle used at present to carry out an exhaustive search of ALPs by experiments like CAST (Andriamonje et al. 2007), PVLAS (Zavattini et al. 2006) and ADMX (Duffy et al. 2006).

The oscillation of photons to ALPs (and vice-versa) could have important implications for astronomical observations. This argument was first investigated in the optical band by Csáki et al. (2002), where authors proposed the existence of axions to be the cause of the observed supernova Ia dimming. In this context, the observed dimming might be explained as a result of an efficient photon to axion conversion instead of a cosmic acceleration (albeit this proposal was rejected some time later due to some chromatic problems, pointed out e.g. by Mirizzi et al. (2008). Photon/axion oscillations were also studied by the same authors in Csáki et al. (2003) as an alternative explanation for those photons arriving Earth from very distant sources at energies above the GZK cutoff.

Recently, it has been proposed that, if ALPs exist, they could distort the spectra of gamma-ray sources, such as Active Galactic Nuclei (AGNs) (Hooper & Serpico 2007, De Angelis et al. 2007, Hochmuth & Sigl 2007, Simet et al. 2008) or galactic sources in the TeV range (Mirizzi et al. 2007), and that their effect may be detected by current gamma-ray experiments. In Burrage et al. (2009b), for example, it is stated that also the scatter in AGN luminosity relations could be used to search for ALPs. Other astrophysical environments have been proposed in order to detect ALPs, such as the magnetic field of the Sun (Fairbairn et al. 2007), pulsars (Dupays et al. 2005), the galactic halo (Duffy et al. 2006) or GRBs and QSOs by carefully

studying their polarized gamma-ray emissions (Rubbia & Sakharov 2008, Hutsemekers et al. 2008). In particular, these predictions are very relevant for gamma-ray astronomy, where recent instrumentation developments in the last few years have increased the observational capabilities by more than one order of magnitude. On the ground, we have the new generation of Imaging Atmospheric Cherenkov Telescopes (IACTs) like MAGIC (Lorentz et al. 2004), HESS (Hinton et al. 2004), VERITAS (Weekes et al. 2002) or CANGAROO-III (Enomoto et al. 2002), covering energies in the range 0.1-20 TeV. In space we have Fermi (previously called GLAST) (Gehrels & Michelson 1999), in operation since Summer 2008 and covering energies in the range 0.02-300 GeV[2].

In this work we revisit the photon/axion mixing, for the first time handling under the same consistent framework the mixing that takes place inside or near the gamma-ray sources together with that one expected to occur in intergalactic magnetic field (IGMF). In the literature, both effects have been considered separately. Depending on the source dimension, magnetic field, ALP mass and coupling constant, both effects might produce significant spectral distortions, or one effect could be more important than the other. In any case, we believe that both effects could be relevant and hence need to be considered simultaneously. We neglect, however, the mixing that may happen inside the Milky Way due to galactic magnetic fields. At present, a concise modeling of this effect is still very dependent on the largely unknown morphology of the magnetic field in the galaxy. Furthermore, in the most idealistic/optimistic case, this effect would produce an enhancement of the photon flux arriving at Earth of about 3% of the initial photon flux emitted by the source (Simet et al. 2008). This is in contrast with what we found for the IGMFs: although there is also little information on the strength and morphology of the IGMFs, the derived photon/axion mixing in this case we show to be crucial for a correct interpretation of the observed flux. It is worth mentioning that we will come to this conclusion using a conservative value of B=0.1 nG for the IGMF strength, well below the current upper limits of $\sim$1 nG. We also carry out a detailed analysis of the mixing when varying IGMF strength and source distance. We find results that differ from previously published ones, and we make predictions of effects that have not been noted in the literature so far.

At energies larger than 10 GeV, and especially above 100 GeV, it will be necessary to properly account for the Extragalactic Background Light (EBL) in our IGMF mixing calculations. The EBL introduces an attenuation in the photon flux due to e^-e^+ pair production that comes from the interaction of the gamma-ray source photons with infrared and optical-UV background photons (Hauser & Dwek 2001). Amongst all the EBL models that exist in the literature, in this work we will make use of the Primack (Primack 2005) and Kneiske best-fit Kneiske et al. 2004) EBL models. They represent respectively one of the most transparent and one of the most opaque models for gamma-rays, but still within the limits imposed by the observations. The

[2]In the space we also have a new gamma-ray instrument called AGILE (Tavani et al. 2008), yet the sensitivity is actually similar to that of EGRET

EBL model will play a crucial role in our formalism and results: as we will see, the more attenuating the EBL model considered, the more relevant the effect of photon/axion oscillations in the IGMF.

We also explore in this work the detection prospects for current gamma-ray instruments (Fermi and IACTs). We will show that the signatures of photon/axion oscillations may be observationally detectable provided light ALPs with masses smaller than a given value for typical values of the IGMF. In order to study the detection prospects, we will propose an observational strategy. We can anticipate here that the main challenge for our proposed formalism to be testable comes from the lack of knowledge of the intrinsic source spectrum and EBL density. However, we note that there is the possibility that we could be already detecting the first hints of axions with current experiments. In this context, the potential detection of TeV photons from very distant ($z \sim 0.4$) sources (Acciari 2009, Albert et al. 2008, Nesphor et al. 1998, Stepanyan et al. 2002), or some works claiming energy spectral indices harder than 1.5 for relatively distant (z=0.1-0.2) AGNs (Krennrich et al. 2008), already put in a tight spot the conventional interpretation of the observed gamma-ray data. As we will show, both effects could be explained by oscillations of photon into light ALPs using realistic values for the involved parameters.

The work is organized as follows. In Section 5.2 we describe in detail the photon/axion mixing in both the surroundings of gamma-ray sources and in the intergalactic medium (IGM). Section 5.3 is devoted to present the results obtained when including both mixings under the same framework and after considering realistic parameters for well-known AGNs. In Section 5.4 we present an observational strategy to search for ALPs using the most sensitive gamma-ray instruments, namely Fermi and IACTs like MAGIC or HESS. Finally, we give our conclusions in Section 5.5.

5.2 The formalism

At present, the Peccei-Quinn mechanism remains as the most convincing solution to solve the CP violation of QCD. As early as in 1978, Weinberg (Weinberg 1978) and Wilczek (Wilczek 1978) realized independently that a consequence of this mechanism is the existence of a pseudo-scalar boson, the axion. One generic property of axions is a two-photon interaction of the form:

$$\mathcal{L}_{a\gamma} = -\frac{1}{4\ M}\ F_{\mu\nu}\overline{F}^{\mu\nu} a = \frac{1}{M}\ \mathbf{E}\cdot\mathbf{B}\ a \tag{5.1}$$

where a is the axion field, M is the inverse of the photon/axion coupling strength, F is the electromagnetic field-strength tensor, $\overline{F}$ its dual, $\mathbf{E}$ the electric field, and $\mathbf{B}$ the magnetic field. The axion has the important feature that its mass m_a and coupling constant are inversely related to each other. There are, however, other predicted states where this relation does not hold; such states are known as Axion Like Particles (ALPs). An important and intriguing consequence of Eq. (5.1) is that

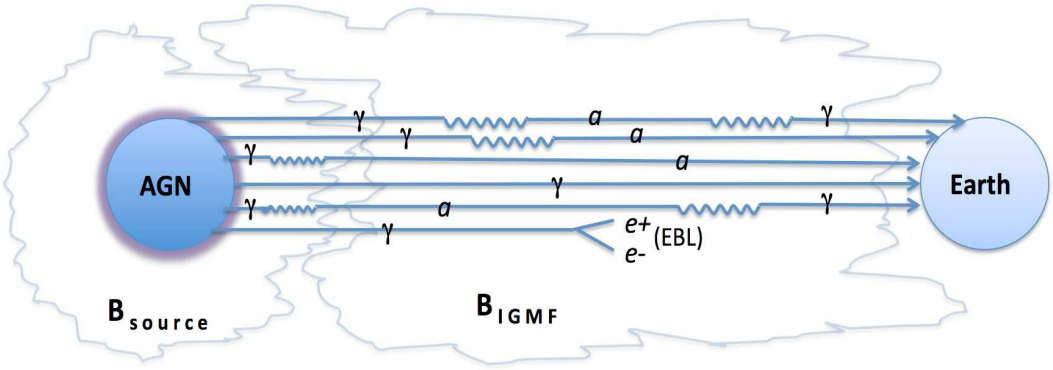

Figure 5.1 Sketch of the formalism used in this work, where both mixing inside the source and mixing in the IGMF are considered under the same consistent framework. Photon to axion oscillations (or vice-versa) are represented by a crooked line, while the symbols γ and a mean gamma-ray photons and axions respectively. This diagram collects the main physical scenarios that we might identify inside our formalism. Each of them are squematically represented by a line that goes from the source to the Earth.

ALPs oscillate into photons and vice-versa in the presence of an electric or magnetic field. In fact this effect represents the keystone in ongoing ALP searches carried out by current experiments.

In this work, we will make use of the photon/axion mixing as well, but this time by means of astrophysical magnetic fields. As already mentioned, we will account for the mixing that takes place inside or near the gamma-ray sources together with that one expected to occur in the IGMFs. We will do it under the same consistent framework. Furthermore, it is important to remark that it will be necessary to include the EBL in our formalism, in particular in the equations that describe the intergalactic mixing. Its main effect we should remember is an attenuation of the photon flux, especially at energies above 100 GeV. We show in Fig. 5.1 a diagram that outlines our formalism. Very squematically, the diagram shows the travel of a photon from the source to the Earth in a scenario with axions. In the same Figure, we show the main physical cases that one could identify inside our formalism: mixing in both the source and the IGMF, mixing in only one of these environments, the effect of the EBL, axion to photon reconversions in the IGMF, etc. A quantitative description of the photon/axion mixing phenomenon in both the source and the IGMFs can be found in the next two subsections.

5.2.1 Mixing inside and near the source

It has been recently proposed that an efficient conversion from photons to ALPs (and vice-versa) could take place in or near some astrophysical objects that should host a strong magnetic field (Hooper & Serpico 2007).

Given a domain of length s, where there is a roughly constant magnetic field and

plasma frequency, the probability of a photon of energy E_γ to be converted into an ALP after traveling through it can be written as (Mirizzi et al. 2007, Hochmuth & Sigl 2007):

$$P_0 = (\Delta_B\ s)^2\ \frac{\sin^2(\Delta_{osc}\ s/2)}{(\Delta_{osc}\ s/2)^2} \tag{5.2}$$

Here Δ_{osc} is the oscillation wave number:

$$\Delta^2_{osc} \simeq (\Delta_{CM} + \Delta_{pl} - \Delta_a)^2 + 4\Delta^2_B, \tag{5.3}$$

Δ_B that gives us an idea of how effective is the mixing, i.e.

$$\Delta_B = \frac{B_t}{2\ M} \simeq 1.7 \times 10^{-21}\ M_{11}\ B_{mG}\ cm^{-1}, \tag{5.4}$$

where B_t the magnetic field component along the polarization vector of the photon and M_{11} the inverse of the coupling constant.

Δ_{CM} is the vacuum Cotton-Mouton term, i.e.

$$\Delta_{CM} = -\frac{\alpha}{45\pi}\ \left(\frac{B_t}{B_{cr}}\right)^2 E_\gamma \simeq -1.3 \times 10^{-21}\ B^2_{mG} \left(\frac{E_\gamma}{TeV}\right)\ cm^{-1}, \tag{5.5}$$

where $B_{cr} = m_e^2/e \simeq 4.41 \times 10^{13}$ G the critical magnetic field strength (e is the electron charge).

Δ_{pl} is the plasma term:

$$\Delta_{pl} = \frac{w^2_{pl}}{2E} \simeq 3.5 \times 10^{-20} \left(\frac{n_e}{10^3 cm^{-3}}\right) \left(\frac{TeV}{E_\gamma}\right)\ cm^{-1}, \tag{5.6}$$

where $w_{pl} = \sqrt{4\pi\alpha n_e/m_e} = 0.37 \times 10^{-4} \mu eV \sqrt{n_e/cm^{-3}}$ the plasma frequency, m_e the electron mass and n_e the electron density.

Finally, Δ_a is the ALP mass term:

$$\Delta_a = \frac{m_a^2}{2E_\gamma} \simeq 2.5 \times 10^{-20} m^2_{a,\mu eV} \left(\frac{TeV}{E_\gamma}\right)\ cm^{-1}. \tag{5.7}$$

Note that in Eqs.(5.4-5.7) we have introduced the dimensionless quantities $B_{mG} = B/10^{-3}$ G, $M_{11} = M/10^{11}$ GeV and $m_{\mu eV} = m/10^{-6}$ eV.

Since we expect to have not only one coherence domain but several domains with magnetic fields different from zero and subsequently with a potential photon/axion mixing in each of them, we can derive a total conversion probability (Mirizzi et al. 2007) as follows:

$$P_{\gamma\to a} \simeq \frac{1}{3}[1 - \exp(-3NP_0/2)] \tag{5.8}$$

where P_0 is given by Eq.(5.2) and N represents the number of domains. Note that in the limit where $N\ P_0 \to \infty$, the total probability saturates to 1/3, i.e. one third of the photons will convert into ALPs.

It is useful here to rewrite Eq. (5.2) following Hooper & Serpico (2007), i.e.

$$P_0 = \frac{1}{1+(E_{crit}/E_\gamma)^2}\ \sin^2\left[\frac{B\ s}{2\ M}\sqrt{1+\left(\frac{E_{crit}}{E_\gamma}\right)^2}\right] \tag{5.9}$$

so that we can define a characteristic energy, E_{crit}, given by:

$$E_{crit} \equiv \frac{m^2\ M}{2\ B} \tag{5.10}$$

or in more convenient units:

$$E_{crit}(GeV) \equiv \frac{m^2_{\mu eV}\ M_{11}}{0.4\ B_G} \tag{5.11}$$

where the subindices refer again to dimensionless quantities: $m_{\mu eV} \equiv m/\mu eV$, $M_{11} \equiv M/10^{11}$ GeV and $B_G \equiv$ B/Gauss; m is the effective ALP mass $m^2 \equiv |m_a^2 - \omega_{pl}^2|$. Recent results from the CAST experiment (Andriamonje et al. 2007) give a value of $M_{11} \geq 0.114$ for axion mass $m_a \leq 0.02$ eV. Although there are other limits derived with other methods or experiments, the CAST bound is the most general and stringent limit in the range 10^{-11} eV $\ll m_a \ll 10^{-2}$ eV.

At energies below E_{crit} the conversion probability is small, which means that the mixing will be small. Therefore we must focus our detection efforts at energies above this E_{crit}, where the mixing is expected to be large (*strong mixing regime*). As pointed out in , in the case of using typical parameters for an AGN in Eq. (5.11), E_{crit} will lie in the GeV range given an ALP mass of the order of $\sim \mu$eV.

To illustrate how the photon/axion mixing inside the source works, we show in Figure 5.2 an example for an AGN modeled by the parameters listed in Table 5.2 (our fiducial model, see Section 5.3). The only difference is the use of an ALP mass of 1 μeV instead of the value that appear in that Table, so that we obtain a critical energy that lie in the GeV energy range; we get $E_{crit} = 0.19$ GeV according to Eq. (5.11). Note that the main effect just above this critical energy is an attenuation in the total expected intensity of the source. However, note also that the attenuation starts to decrease at higher energies (>10 GeV) gradually. The reason for this behavior is the crucial role of the Cotton-Mouton term at those high energies, which makes the efficiency of the source mixing to decrease as the energy increases (see Eq. (5.5) and how it affects to Eq. (5.3)). Indeed, the photon attenuation induced by the mixing in the source completely dissapears at energies above around 200 GeV in this particular example. On the other hand, one can see in Figure 5.2 a sinusoidal behavior just below the critical energy as well as just below the energy at which the source mixing dissapears due to the Cotton-Mouton term. However, it must be noted that a)

the oscillation effects are small; b) these oscillations only occur when using photons polarized in one direction while, in reality, the photon fluxes are expected to be rather non-polarized; and c) the above given expressions are approximations and actually only their asymptotic behavior should be taken as exact and well described by the formulae. Therefore, the chances of observing sinusoidally-varying energy spectra in astrophysical source, due to photon/axion oscillations, are essentially zero.

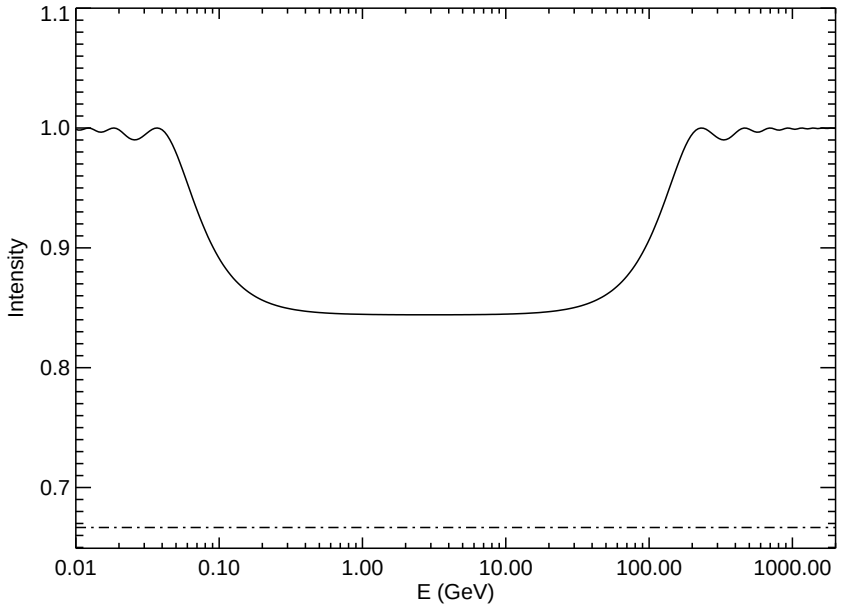

Figure 5.2 Example of photon/axion oscillations inside the source or vicinity, and its effect on the source intensity (solid line), which was normalized to 1 in the Figure. We used the parameters given in Table 5.2 to model the AGN source, but we adopted an ALP mass of 1 μeV. This gives $E_{crit} = 0.19$ GeV. The dot-dashed line represents the maximum (theoretical) attenuation given by Eq. (5.8), and equal to 1/3.

5.2.2 Mixing in the IGMFs

The strength of the Intergalactic Magnetic Fields (IGMFs) is expected to be many orders of magnitude weaker ($\sim$nG) than that of the source and its surroundings ($\sim$G). Consequently, as described by Eq. (5.11), the energy at which photon/axion oscillation occurs in the IGM is many orders of magnitude larger than that at which oscillation can occur in the source and its vicinity. Despite the low magnetic field **B**, the photon/axion oscillation can take place due to the large distances, since the important quantity defining the probability for this conversion is the product B $\times$ s, as described by Eq (5.9). Assuming B $\sim$0.1 nG (see below), and $M_{11} = 0.114$ (coincident with the upper limit reported by CAST), then the effect can be observationally

detectable ($E_{crit} < 1$ TeV) only if the ALP mass is $m_a < 6 \times 10^{-10}$ eV. If the axion mass m_a was larger than this value, then the consequences of this oscillation could not be probed with the current generation of IACTs, that observe up to few tens of TeV [3]. In our fiducial model (see Table 5.2) we used $m_a = 10^{-10}$ eV, which implies $E_{crit} = 28.5$ GeV.

It is important to stress that at energies larger than 10 GeV, and especially larger than 100 GeV, besides the oscillation to ALPs, the photons should also be affected by the diffuse radiation from the Extragalactic Background Light (EBL). The EBL introduces an attenuation in the photon flux due to e^-e^+ pair production that comes from the interaction of the gamma-ray source photons with infrared and optical-UV background photons for the energies under consideration (Hauser & Dwek 2001). Therefore, it will be necessary to modify the above equations to properly account for the EBL in our calculations. These equations can be found in Csáki et al. (2003), where the photon/axion mixing in the IGMF was also studied, although for other purposes and a different energy range. We note that the same equations were also used in De Angelis et al. (2007) to study for the first time the photon/axion mixing in the presence of IGMFs for the same energy range that we are considering in this work.

There is little information on the strength and morphology of the IGMFs. As for the morphology, several authors reported that space should be divided into several domains, each of them with a size for which the magnetic field is coherent. Different domains will have randomly changing directions of **B** field of about the same strength (Kronberg 1994, Furlanetto & Loeb 2001). The IGMF strength is constrained to be smaller than 1 nG (Grasso & Rubinstein 2001), which is somewhat supported by the estimates of ∼0.3-0.9 nG that can be inferred (De Angelis et al. 2008) from recent observations of the Pierre Auger Observatory (Abraham et al. 2008). On the other hand, there is controversy on the possibility of generating such a strong magnetic field. Detailed simulations yield IGMFs of the order of 0.01 nG so that they can later reproduce the measured **B** fields in nearby galaxy clusters (Dolag et al. 2005, Sigl et al. 2004). Given this controversy, we decided to use a mid-value of 0.1nG in our fiducial model (Table 5.2).

In our model, we assume that the photon beam propagates over N domains of a given length, the modulus of the magnetic field **B** roughly constant in each of them. We will take, however, randomly chosen orientations, which in practice will be also equivalent to a variation in the strength of the component of the magnetic field involved in the photon/axion mixing. If the photon beam is propagating along the y axis, the oscillation will occur with magnetic fields in the x and z directions since the polarization of the photon can only be along those axis. Therefore, we can describe the beam state by the vector (γ_x, γ_z, a). The transfer equation will be (Csáki

[3]The next generation of IACTs (namely AGIS and CTA) aim for an order of magnitude of improvement at the highest energies, reaching few hundreds of TeV; but those instruments will not be in operation till 2013 or later.

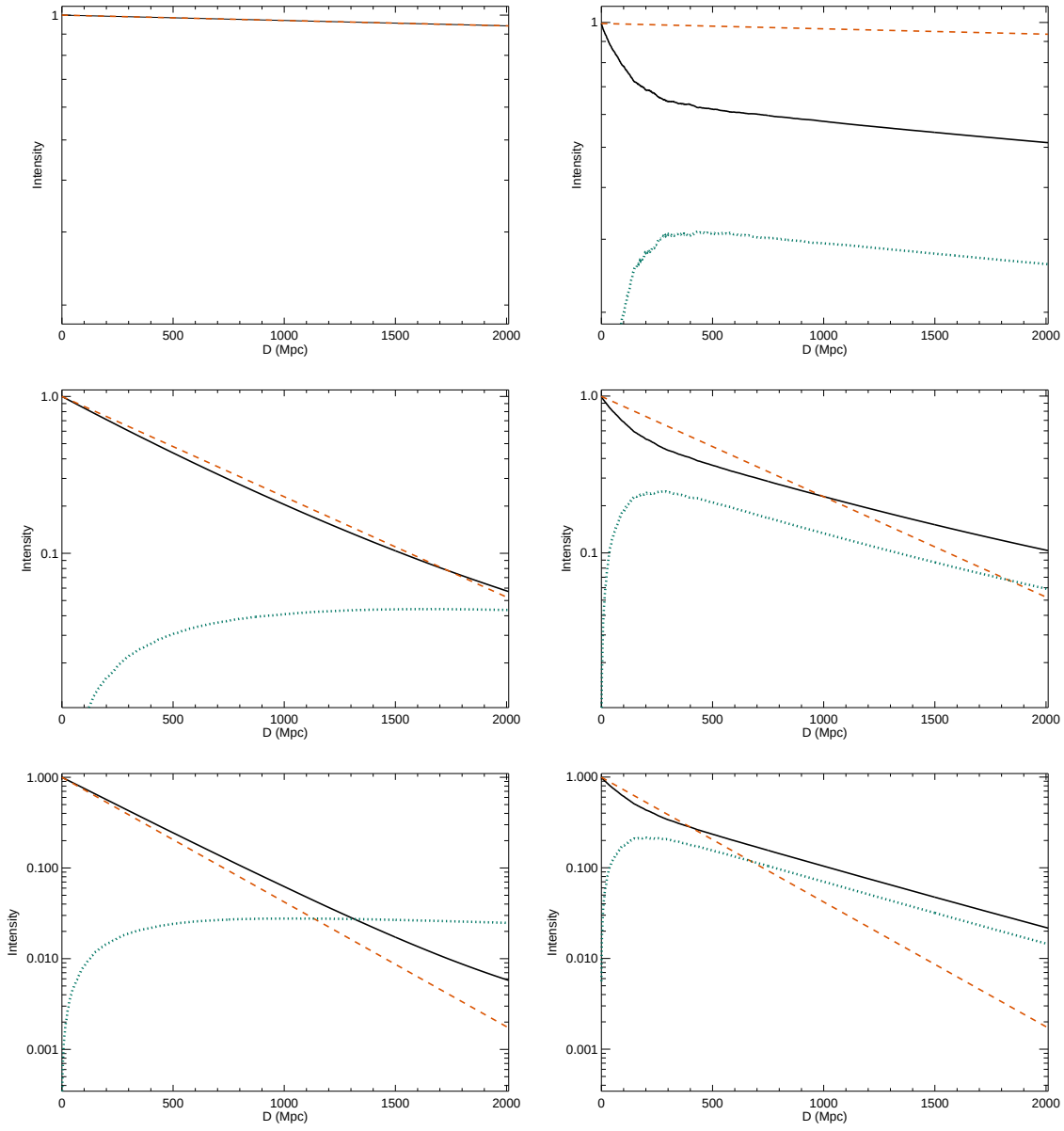

Figure 5.3 Effect of intergalactic photon/axion mixing on photon and ALP intensities versus distance to the source, computed for our fiducial model, i.e. for 3C 279 and those parameters given in Table 5.2 but taking B= 1 nG, and using the Primack EBL model. The black thick solid line represents the total photon intensity, while the blue dotted line is the ALP intensity. The photon intensity as given only by the EBL (i.e. without including photon/axion mixing) is shown as the red dashed line. *Left panels*: mixing computed for $M_{11} = 4$ GeV and an initial photon energy of 50 GeV (top), 500 GeV (middle) and 2 TeV (bottom); *right panels:* $M_{11} = 0.7$ GeV and same energies than left panels.

et al. 2003):

$$\begin{pmatrix} \gamma_x \\ \gamma_z \\ a \end{pmatrix} = \mathrm{e}^{iEy} \left[T_0 \, \mathrm{e}^{\lambda_0 y} + T_1 \, \mathrm{e}^{\lambda_1 y} + T_2 \, \mathrm{e}^{\lambda_2 y} \right] \begin{pmatrix} \gamma_x \\ \gamma_z \\ a \end{pmatrix}_0 \tag{5.12}$$

where:

$$\begin{aligned} \lambda_0 &\equiv -\frac{1}{2\,\lambda_\gamma}, \\ \lambda_1 &\equiv -\frac{1}{4\lambda_\gamma} \left[1 + \sqrt{1 - 4\,\delta^2} \right] \\ \lambda_2 &\equiv -\frac{1}{4\,\lambda_\gamma} \left[1 - \sqrt{1 - 4\,\delta^2} \right] \end{aligned} \tag{5.13}$$

$$\begin{aligned} T_0 &\equiv \begin{pmatrix} \sin^2\theta & -\cos\theta\sin\theta & 0 \\ -\cos\theta\sin\theta & \cos^2\theta & 0 \\ 0 & 0 & 0 \end{pmatrix} \\ T_1 &\equiv \begin{pmatrix} \frac{1+\sqrt{1-4\,\delta^2}}{2\sqrt{1-4\,\delta^2}}\cos^2\theta & \frac{1+\sqrt{1-4\,\delta^2}}{2\sqrt{1-4\,\delta^2}}\cos\theta\sin\theta & -\frac{\delta}{\sqrt{1-4\,\delta^2}}\cos\theta \\ \frac{1+\sqrt{1-4\,\delta^2}}{2\sqrt{1-4\,\delta^2}}\cos\theta\sin\theta & \frac{1+\sqrt{1-4\,\delta^2}}{2\sqrt{1-4\,\delta^2}}\sin^2\theta & -\frac{\delta}{\sqrt{1-4\,\delta^2}}\sin\theta \\ \frac{\delta}{\sqrt{1-4\,\delta^2}}\cos\theta & \frac{\delta}{\sqrt{1-4\,\delta^2}}\sin\theta & -\frac{1-\sqrt{1-4\,\delta^2}}{2\sqrt{1-4\,\delta^2}} \end{pmatrix} \\ T_2 &\equiv \begin{pmatrix} -\frac{1-\sqrt{1-4\,\delta^2}}{2\sqrt{1-4\,\delta^2}}\cos^2\theta & -\frac{1-\sqrt{1-4\,\delta^2}}{2\sqrt{1-4\,\delta^2}}\cos\theta\sin\theta & \frac{\delta}{\sqrt{1-4\,\delta^2}}\cos\theta \\ -\frac{1-\sqrt{1-4\,\delta^2}}{2\sqrt{1-4\,\delta^2}}\cos\theta\sin\theta & -\frac{1-\sqrt{1-4\,\delta^2}}{2\sqrt{1-4\,\delta^2}}\sin^2\theta & \frac{\delta}{\sqrt{1-4\,\delta^2}}\sin\theta \\ -\frac{\delta}{\sqrt{1-4\,\delta^2}}\cos\theta & -\frac{\delta}{\sqrt{1-4\,\delta^2}}\sin\theta & \frac{1+\sqrt{1-4\,\delta^2}}{2\sqrt{1-4\,\delta^2}} \end{pmatrix} \end{aligned} \tag{5.14}$$

θ being the angle between the x-axis and $\mathbf{B}$ in each single domain. δ a dimensionless parameter equal to:

$$\delta \equiv \frac{B\,\lambda_\gamma}{M} \simeq 0.11 \left(\frac{B}{10^{-9}\,\mathrm{G}} \right) \left(\frac{10^{11}\,\mathrm{GeV}}{M} \right) \left(\frac{\lambda_\gamma}{\mathrm{Mpc}} \right) \tag{5.15}$$

that represents the number of photon/axion oscillations within the mean free path of the photon λ_γ. Notice that if there was no EBL, the quanta beam would be equipartitioned between the ALP component and the two photon polarizations after crossing a large number of domains. However, the EBL introduces an energy dependent mean free path λ_γ for the photon.

Amongst all the EBL models that exist in the literature, we chose the Primack (Primack 2005) and Kneiske best-fit (Kneiske et al. 2004) to fix the λ_γ parameter. They represent respectively one of the most transparent and one of the most opaque models for gamma-rays, but still within the limits imposed by the observations (galaxy counts for the lower limit and observations of distant blazars for the

upper one). The model proposed by Kneiske et al. was initially disfavored by some TeV observations of distant AGNs, using the assumption that the intrinsic spectral index needs to be softer than 1.5 (see Aharonian et al. 2006, Mazin & Raue 2007). On the other hand, in the literature we also find work where this assumption is strongly criticized, as reported by Stecker et al. (2006), Stecker et al. (2007) and especially in Krennrich et al. (2008). Therefore, we will consider the Kneiske best-fit EBL model as still valid. In the case of the Primack EBL model, we did not take into account the redshift evolution of the EBL, which effect may be particularly important for sources located at z > 0.3. Although one of the objects we take as the reference, 3C 279, is located at a larger redshift, the difference in the final photon intensity when using the Primack EBL with or without redshift evolution is still small (below 15% for the relevant energies). This is not true for the Kneiske EBL model, for which the differences might be as high as 70% for some of the energies under consideration. Therefore, it became necessary to account for such effect in this case.

From each EBL model, we obtain λ_γ as the distance given by the so-called gamma-ray horizon for the energy considered. Additionally, we have to take into account that the energy of each photon will change continuously for a photon traveling towards us from cosmological distances, due to the cosmological redshift. This effect may have a very important role in the calculations of the photon/axion mixing, since e.g. for a source at a distance of 1000 Mpc (i.e. $z \sim 0.3$) every photon arrives at Earth with 30% less energy. We account here for this effect for the first time by computing at each step (distance) the new energy of the photon due to cosmological redshift, and then using this new energy as the input energy needed for the calculation of λ_γ. We did not include in the formalism, however, those secondary photons that may arise from the interaction of the primary source photons with the EBL.

To illustrate how the mixing in the IGM works, we show in Figure 5.3 various examples of the evolution of the total photon and ALP intensities as a function of the distance to the source when varying some of the critical parameters, using the Primack EBL model in all cases. We use the parameters listed in Table 5.2, that corresponds to our fiducial model, but using an IGMF strength of 1 nG (instead of 0.1 nG), which is still consistent with upper limits. For a photon with an initial energy of 50 GeV (left top panel) and coupling constant $M_{11} = 4$, which yields $E_{crit} \sim 100$ GeV, there is not significant photon/axion oscillations. Since the role of the EBL is almost negligible at these energies, the total photon intensity remains almost constant traveling to the Earth. For 500 GeV photons (middle top panel), the total photon intensity initially decreases as expected due to the EBL absorption, but also an early extra attenuation due to a photon to ALP conversion is clearly observed. At the same time, the ALP intensity, which was initially equal to zero (we neglect here the mixing inside the source for simplicity), grows rapidly. At larger distances the tendency in the total photon intensity is just the opposite; the intensity increases slightly, since an efficient ALP to photon reconversion (although operative since the very beginning) is taking place and becomes relevant specially at these large distances,

where the expected photon intensity is already very low due to the EBL absorption. In the case of photons with higher initial energy (e.g. 2 TeV, right top panel in Fig. 5.3), the expected attenuation due to the EBL becomes very important even for small distances from the source, which makes more relevant the impact of ALP to photon reconversions on the photon intensity. As a result, the photon/axion mixing implies an enhancement in the photon intensity at almost all distances. The situation changes when using a slightly higher coupling constant, but still within the CAST constraints (see bottom panels in Fig. 5.3). In this case, both the attenuation and the enhancement in intensity become more pronounced, as expected. For relatively small distances, the photon/axion mixing produces an attenuation in the photon flux, while for relatively large distances, the mixing produces an enhancement in the photon flux. The same argument is essentially valid for any initial photon energy, the results only changing depending on the relative relevance of the EBL in each case, which will modify the distance at which the photon-intensity enhancement starts occurring.

5.3 Results

Up to now, previous works have focused only in studying the photon/axion mixing either inside the source or in the IGMFs. Instead, for the first time we carried out a detailed study of the mixing in both regimes under the same consistent framework. We neglect for the moment, however, the mixing that may happen inside the Milky Way due to its galactic magnetic fields. We believe that a concise modeling of this effect is still very dependent on the largely unknown morphology of the **B** field in our Galaxy. In the most idealistic/optimistic case, in which 30% of the photons convert to ALPs within the source and 10% of the ALPs convert to photons in the Milky Way, as reported by Simet et al. (2008), this effect would produce an enhancement of the photon flux arriving at Earth of about 3% of the initial photon flux emitted by the source.

As mentioned in the previous section, in order for the photon/axion oscillation to be observationally noticeable by current instruments, that is $E_{crit} < 1$ TeV, we need ALP masses smaller than $6 \cdot 10^{-10} eV$ for typical values of the IGM. Larger ALP mass values translate into higher E_{crit} (e.g. $m_a = 10^{-6}$ eV would yield $E_{crit} \sim$ PeV in the IGM, when using B $\sim$0.1 nG) making the effect of this oscillation undetectable by the current gamma-ray instruments (Fermi and IACTs). In scenarios with heavy ALPs, then the only effect detectable would be an attenuation caused by photon/axion oscillation in the source, which would be of about 30% in the most optimistic case (Hooper & Serpico 2007). It is worth mentioning that the potential photon/axion oscillation in the Milky Way could produce measurable effects only for ALP masses smaller than 10^{-8} eV, as mentioned in Simet et al. (2008).

We use an ALP mass of 10^{-10} eV in our fiducial model (Table 5.2), which implies $E_{crit} \sim 30$ GeV in the IGM (for B$\sim$0.1 nG) and $E_{crit} \sim 1$ eV within the source and its vicinity (B$\sim$1 G). Consequently, both effects need to be taken into account.

5.3.1 Photon/axion oscillation in our framework

In this section we show the results obtained when taking into account the mixing inside the source and in the IGMF simultaneously. Since we expect the intergalactic mixing to be more important for larger distances, due to the more prominent role of the EBL, we chose two distant astrophysical sources (as our benchmark AGNs) that are relatively well characterized at gamma-ray energies; namely the radio quasar 3C 279 (z=0.536), most distant detected gamma-ray source at the VHE range, and the BL Lac PKS 2155-304 at z=0.117. In order to compute the photon/axion oscillation in the source we used the parameters reported in Hartmann et al. (2001) for 3C 279 and Kusunose & Takahara (2008) for PKS 2155-304. As for the size of the region with **B** field (where photons can convert to ALPs) we chose a region 10 times larger than the radius of the gamma-ray emitting blob given in the above mentioned references, the reason being that the blob radius represents only a lower limit for the region where **B** is confined. We note that this parameter, as well as the number of domains where the **B** is coherent, play an important role in the photon attenuations due to the photon/axion mixing in the source. Table 5.1 shows the different attenuations that are obtained when varying the size of the region where **B** is confined (what we called "B region") and the lengths of coherent **B** domains inside that region. One can see that, once the number of domains is fixed, the photon attenuation increases when increasing the size of the "B region". On the other hand, when fixing the size of the "B region" and scanning the size of the domains we find that, as we increase the number of domains, the attenuation increases until the size of the domain is "too small". At this point, the probability of photon/axion conversion is almost zero for the single domains, which reduces the overall photon/axion conversion.

Table 5.1 Maximum attenuations due to photon/axion oscillations in the source obtained for different sizes of the region where the magnetic field is confined ("B region") and different lengths for the coherent domains. Only length domains smaller than the size of the **B** region are possible. The **B** field strength used is 1.5 G (see Table 5.2). The photon flux intensity without ALPs was normalized to 1. In bold face, is the attenuation given by our fiducial model.

B region (pc)	Length domains (pc)			
	3×10^{-4}	3×10^{-3}	0.03	0.3
0.3	0.84	0.67	0.67	0.75
0.03	0.98	**0.84**	0.77	-
3×10^{-3}	0.99	0.98	-	-

We summarize in Table 5.2 the parameters we have considered in order to calculate the total photon/axion conversion in both the source (for the two benchmark AGNs) and in the IGM. As we already mentioned, these values represent our fiducial model.

Table 5.2 Parameters used to calculate the total photon/axion conversion in both the source (for the two AGNs considered, 3c279 and PKS 2155-304) and in the IGM. The values related to 3C 279 were obtained from Hartmann et al. (2001), while those ones for PKS 2155-304 were obtained from Kusunose & Takahara (2008). As for the IGM, $e_{d,int}$ was obtained from Peebles (1993), and B_{int} was chosen to be well below the upper limit typically given in the literature (see discussion in the text). This Table represents our fiducial model.

	Parameter	3C 279	PKS 2155-304
Source parameters	B (G)	1.5	0.1
	e_d (cm^{-3})	25	160
	L domains (pc)	0.003	3×10^{-4}
	B region (pc)	0.03	0.003
Intergalactic parameters	z	0.536	0.117
	$e_{d,int}$ (cm^{-3})	10^{-7}	10^{-7}
	B_{int} (nG)	0.1	0.1
	L domains (Mpc)	1	1
ALP parameters	M (GeV)	1.14×10^{10}	1.14×10^{10}
	ALP mass (eV)	10^{-10}	10^{-10}

The effect of existence of ALPs on the total photon flux coming from 3C 279 and from PKS 2155-304 (using the fiducial model presented in Table 5.2) can be seen in Figure 5.4. We carried out the calculations for the two EBL models cited above: Kneiske best-fit and Primack. The inferred critical energies for the mixing in the source are $E_{crit} = 4.6$ eV for 3C 279 and $E_{crit} = 69$ eV for PKS 2155-304, while for the mixing in the IGM we obtain $E_{crit} = 28.5$ GeV. The photon attenuation due to photon/axion mixing inside the source is 16% for 3C 279 and 1% for PKS 2155-304, as can be seen above their respective critical energies in Figure 5.4. On the other hand, the photon attenuation due to photon/axion oscillation in the IGM is 30% for the distance of both sources, and it occurs at the same critical energy. The role of the EBL is negligible at this low energy (i.e. below ∼100 GeV), which means that the intensity curves for the two EBL models agree to this energy.

The situation changes above ∼100 GeV, where the photon attenuation due to the EBL is noticeable. At this point, the results depend substantially on the source distance and the EBL model used. A stronger photon attenuation is obtained for the Kneiske best-fit model against the Primack EBL model, as expected. Because the strong photon attenuation due to the EBL, the ALPs that later convert to photons imply a further enhancement of the expected photon flux. Therefore, as one can notice from Figure 5.4, the existence of ALPs translates into a relatively small (∼30%) intensity attenuation at low energies and a large intensity enhancement (several orders of magnitude, depending on the energy range, distance of the source and chosen EBL

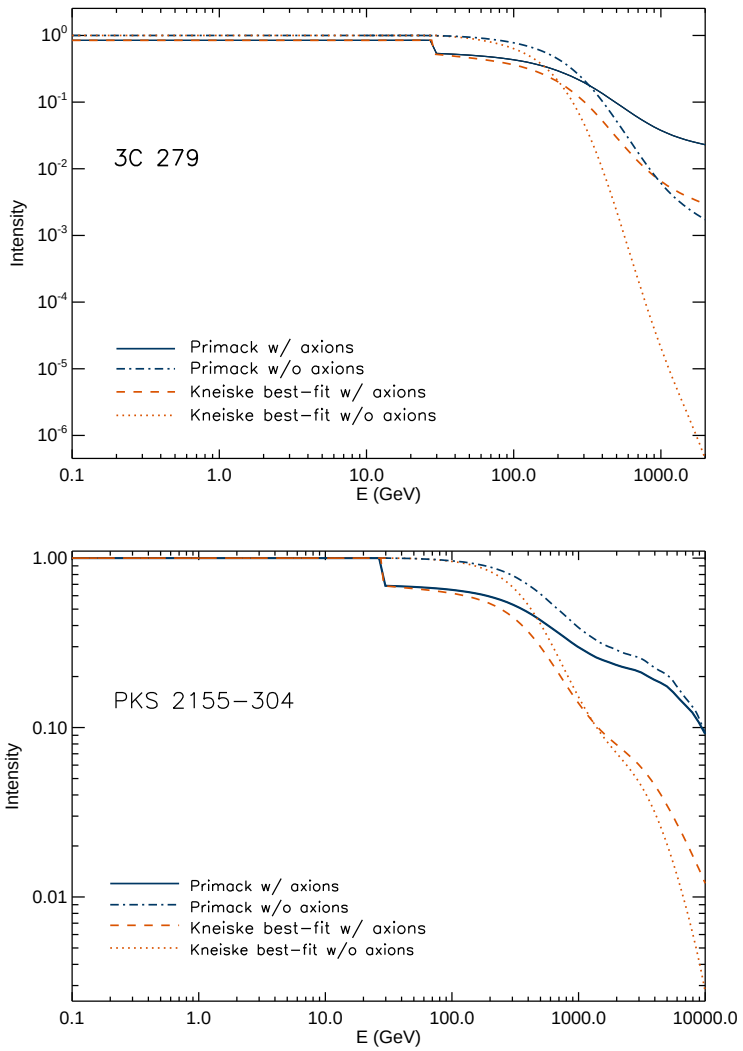

Figure 5.4 Effect of photon/axion conversions both inside the source and in the IGM on the total photon flux coming from 3C 279 (z=0.536) and PKS 2155-304 (z=0.117) for two EBL models: Kneiske best-fit (dashed line) and Primack (solid line). The expected photon flux without including ALPs is also shown for comparison (dotted line for Kneiske best-fit and dot-dashed line for Primack).

model) at high energies.

In order to quantitatively study the effect of ALPs on the total photon intensity, we plot in Figure 5.5 the difference between the predicted arriving photon intensity without including ALPs and that one obtained when including the photon/axion oscillations (called here the *axion boost factor*). Again, this was done for our fiducial model (Table 5.2) and for the two EBL models described above. The plots show differences in the axion boost factors obtained for 3C 279 and PKS 2155-304 due

mostly to the redshift difference.

In the case of 3C 279, the axion boost is an attenuation of about 16% below the critical energy (due to mixing inside the source). Above this critical energy and below 200-300 GeV, where the EBL attenuation is still small, there is an extra attenuation of about 30% (mixing in the IGMF). Above 200-300 GeV the axion boost reaches very high values: at 1 TeV, a factor of ∼7 for the Primack EBL model and ∼340 for the Kneiske best-fit model. As already discussed, the more attenuating the EBL model considered, the more relevant the effect of photon/axion oscillations in the IGMF, since any ALP to photon reconversion might substantially enhance the intensity arriving at Earth. We note that the axion boost factor may vary when changing the parameters we used to model the source (as shown in Table 5.1) and the IGM (see next section). The results we find in this work are in disagreement with those reported by De Angelis et al. (2007). We *always* find that the photon intensity below 200-300 GeV decreases when including the oscillation to ALPs regardless of the ALP and/or IGM parameters, while De Angelis et al. find that the photon intensity increases for a large range of the phase space they tried (see their Fig. 1). At those low energies the photon attenuation due to pair conversion in the EBL is relatively low (see Fig. 5.4) and thus the few ALPs that convert to gamma photons do not imply any substantial relative increase in the photon intensity. On the other hand, 1/3 of the photons oscillate to ALPs, which causes a substantial decrement in the amount of gamma photons with respect to those we would have in the absence of ALPs. Therefore, we think it is very difficult to get a photon enhancement at energies ∼100 GeV. On the other hand, the axion boost factors we find at high energies (>300 GeV) are substantially lower than those obtained in De Angelis et al. (2007). As an example, in the case of a Kneiske best-fit EBL model with B=1 nG, we find a boost ∼4 at 500 GeV, whereas De Angelis et al. obtain ∼20 for the same photon energy and the same redshift (note that, in order to carry out a one-to-one comparison with that work, we also used $M_{11} = 4$, as they do). One of the reasons for the discrepancy in the axion boost factors is the used EBL model. We noted that the EBL model shown in Fig. 1 of De Angelis et al. (2007) is substantially more attenuating than the one from Kneiske best-fit EBL model, which is the one we are using. Consequently, the axion boost factors reported in De Angelis et al. (2007) are larger than the ones they would have obtained if they had used the Kneiske best-fit EBL model. Besides that, it is not clear to us whether the change in photon energy due to cosmological redshift (see Section 5.2.2) was taken into account in De Angelis et al. (2007); this is not explicitely mentioned in their work.

In the case of PKS 2155-304, the situation is different from that of 3C 279 due to the very low photon-attenuation at the source and, mostly, due to the smaller source distance. The low redshift location decreases the impact of the EBL absorption and thus the effect of the relative photon-flux enhancement due to photon/axion oscillation. When using B=0.1 nG, the axion boost factor is larger than 1 only for the Kneiske best-fit model and only above 1.3 TeV. In the case of Primack EBL, the axion

boost factor is always smaller than 1, thus implying no photon-flux enhancement. Note however that the 30% drop in the photon intensity occurs at the same energy as that of 3C 279. This drop in the photon intensity should occur at the same energy for all sources located at relatively medium redshifts (0.1<z<0.3). For very nearby sources (z <0.05), the energy drop should still be the same since it only depends on the ALPs properties and the strength of the IGMF. However, the magnitude of the drop will decrease. This is thus a very distinctive and easily testable prediction of this mechanism. We will discuss this issue again in Section 5.4.

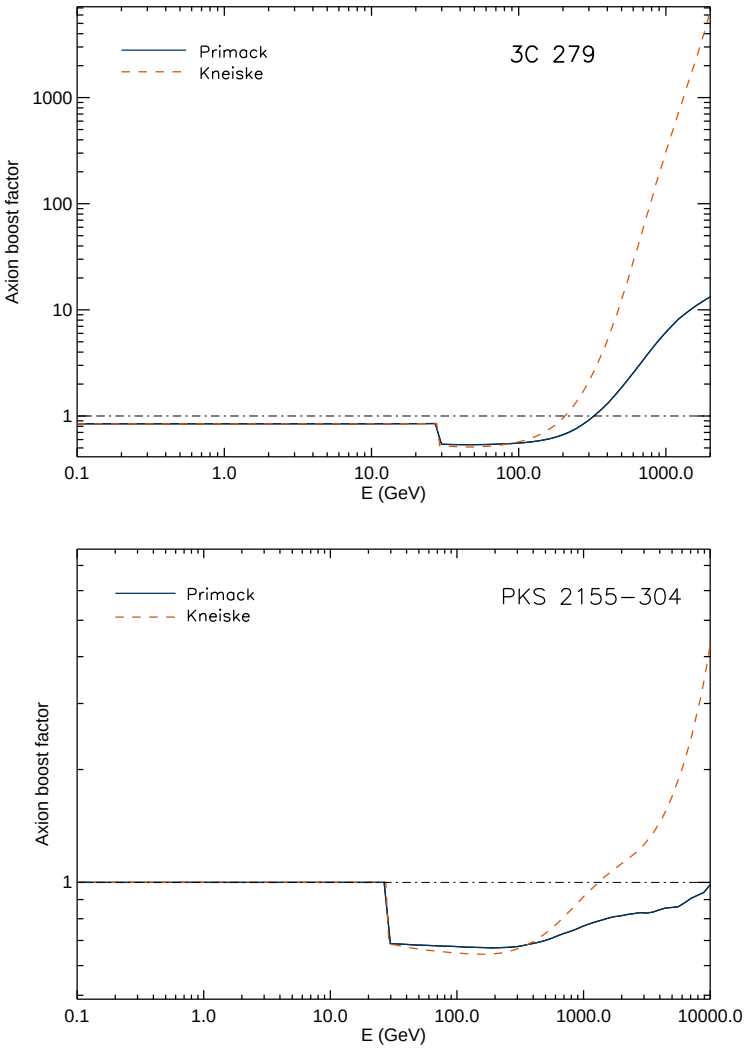

Figure 5.5 Boost in intensity due to ALPs for the Kneiske best-fit (dashed line) and Primack (solid line) EBL models, computed using the fiducial model presented in Table 5.2 for 3C 279 (z=0.536) and PKS 2155-304 (z=0.117).

We want to stress another interesting feature that the photon/axion oscillation

in the IGMF produces in the source spectra at VHE (>100 GeV) of distant sources (z>0.1). As one can notice from Fig. 5.5, the axion boost factor starts increasing at few hundred GeV (when the EBL becomes important), and consequently it will make the source spectra to look harder than they are actually. This happens for both AGNs, yet at slightly different energies: 100 GeV for 3C 279 and 300 GeV for PKS 2155-304. As shown in Figure. 5.5, the hardening of the VHE spectra occurs for both (very different) EBL models that we used, and hence a very robust prediction of this mechanism being at work. Such a hardening of the spectra was already predicted in Simet et al. (2008) for several AGNs located at redshifts 0.1-0.2. While in our work the effect is due mostly to the photon/axion oscillation in the IGMF, in Simet et al. (2008) the effect is due to photon/axion oscillation within the source (up to 30% attenuation of the photon flux) and the one that occurs in the galactic magnetic fields of the Milky Way (up to 10% conversion probability). It is worth mentioning here, however, that when using the parameters (essentially **B** strength and size of the "B region") for the modeling of the gamma-ray emission from AGN sources, we find that the attenuation in the source due to photon/axion conversion is relatively low; 16% for our model of 3C 279 and 1% for that of PKS 2155-304. These low photon-flux attenuation (equivalent to ALP-enhancement) would decrease significantly the effect of the mechanism proposed in Simet et al. (2008).

Finally, it is worth mentioning that we checked that our results are robust against the randomness of the **B** field. We ran 100 different realizations of the same physical scenario, randomly varying the orientation of **B** in each coherent domain and each realization. We did so for the four cases studied along this work, i.e. 3C 279 and PKS 2155-304, Primack and Kneiske best-fit EBL models. Furthermore, we repeated the same exercise using 0.1, 1 and 10 Mpc as the length of the coherent domains in order to explore the dependence of our results on this parameter. In all cases, we chose our fiducial value of 0.1 nG for the **B** field strength. We found that the maximum differences are typically well below 10%, implying that the results obtained are not sensitive to the randomness of the B field. We increased the number of realizations to 1000 for some cases and found no differences with respect to the results obtained with 100 realizations.

A larger effect on the computed axion-boost factors occurs when changing the size of the domains being used. The computed axion-boost factors are sensitive to choice of the size of the coherent domains to be used. Together with the choice of the EBL model (which is also uncertain), the choice of the domain sizes modifies the results obtained by factors of a few.

5.3.2 The impact of changing B

A very interesting result has been found when varying the modulus of the intergalactic magnetic field. In Simet et al. (2008), the intergalactic photon/axion mixing was rejected arguing that its effect on the final intensity at Earth would be negligible

when using a more realistic value for **B**, which should be substantially lower than the value of 1 nG adopted in De Angelis et al. (2007). However, as was shown in the previous section, when using B=0.1 nG we find significant effects even for sources located at redshifts as low as z$\sim$0.1. In order to quantify the impact of changing the IGMF strength, we plot in Fig. 5.6 the result of varying **B** in our fiducial model by one order of magnitude (above and below). We do that for both 3C 279 and PKS 2155-304.

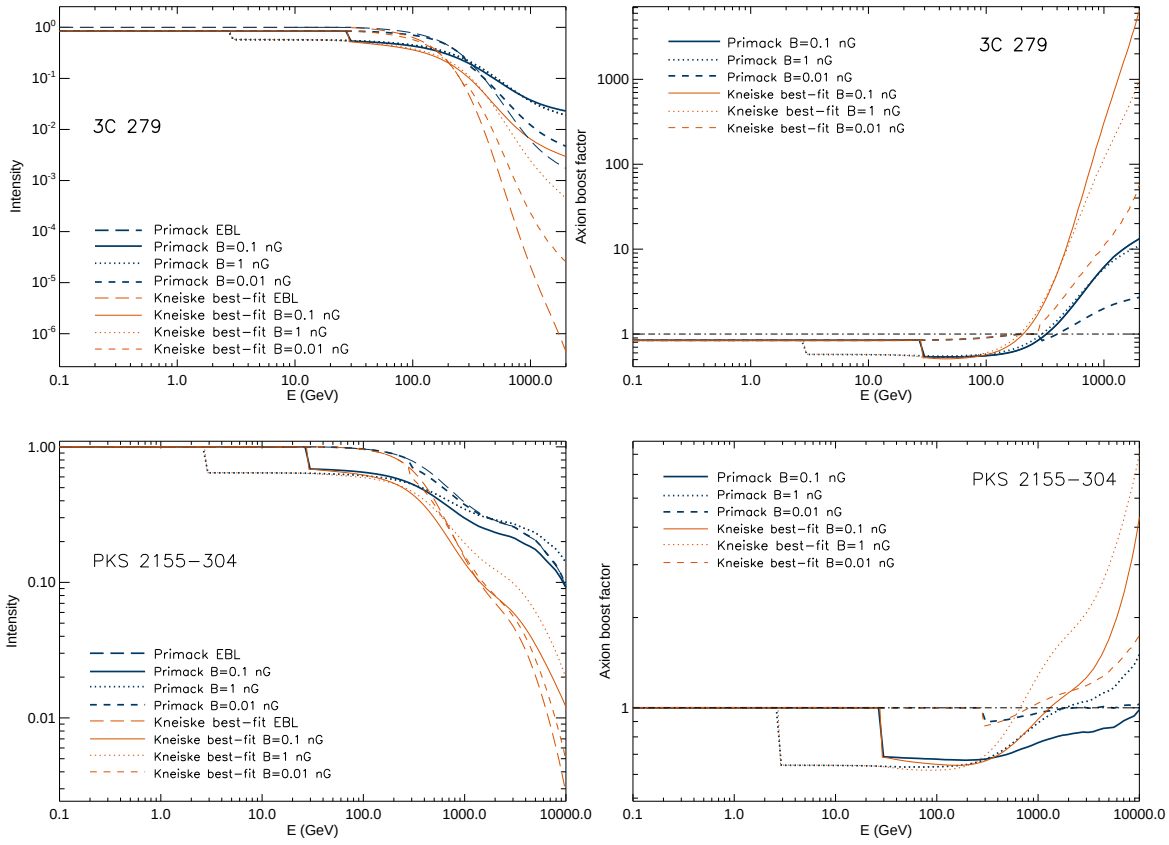

Figure 5.6 Same as in Figures 5.4 and 5.5 but for different values of IGMF. Upper panels: 3C 279 using those parameters listed in Table 5.2, only changing **B**. Lower panels: Same exercise for PKS 2155-304, using the corresponding parameters that can be found in the same Table 5.2.

In the case of 3C 279, we see in the left top panel of Fig. 5.6 that higher intensities (or equivalently, higher axion boost factors in the right top panel), are obtained when using B=0.1 nG instead of taking B=1 nG. This seems to contradict the intuitive idea of getting higher intensities for larger magnetic fields, that make the photon/axion mixing more efficient. The reason for this result is the strong attenuation due to the EBL. If the photon/axion mixing is efficient, then many ALPs convert to photons

which soon disappear due to the EBL absorption. Consequently, if the source distance is large, we end up having a very small number of photons arriving to the Earth. On the other hand, if the photon/axion mixing is not that strong, then we can keep a higher number of ALPs traveling towards the Earth, which act as a potential reservoir of photons. When decreasing **B** to 0.01 nG, then the axion boost factors are lower than for the other two cases. On the other hand, in the case of PKS 2155-304, we see that the highest axion boost factors are obtained with B=1 nG, because the source is not as distant as 3C 279. If we had considered a source located at a much further distance than 3C 279, then we would have found the highest axion boost factors for B=0.01 nG.

In summary, higher **B** values do not necessarily translate into higher photon flux enhancements. There is always a **B** value that maximizes the axion boost factors; this value is sensitive to the source distance, the considered energy and the EBL adopted model.

5.3.3 The impact of using the smallest photon/ALP coupling constant

The most stringent limits on the ALP-photon coupling constant were derived using the non-detection of gamma-rays (by the Solar Maximum Mission Gamma-Ray Spectrometer) from the supernova (SN) 1987A during the ∼10 seconds time window defined by the neutrino burst. This outstanding event allowed several authors in 1996 to set lower limits to the inverse of the coupling constant M_{11} to values larger than 1 (Brockway et al. 1996) and 3 (Griffols et al. 1996). Those limits are only valid for ultralight ALPs. In both works the value $m_a < 10^{-9}$ eV is quoted, although this value holds only for some specific situations. Indeed, a more robust value is $m_a < 10^{-11}$ eV (see Hooper & Serpico 2007, Simet et al. 2008), i.e. the energy below which the exact value of the ALP mass is irrelevant because the "plasma frequency" dominates (see definition of ALP effective mass in Section 5.2.1). Various authors (see Csáki et al. 2003), De Angelis et al. 2007) used $M_{11} = 4$ when dealing with $m_a < 10^{10}$ eV. Since the ALP mass in our fiducial model is 10^{-10} eV, and hence close to this limit, we decided to repeat the calculations using this value for M, which is 35 times larger than the value we used in the previous sections (see Table 5.2).

Before we continue, it is worth pointing out that the limits to the ALP-photon coupling constant given in Brockway et al. (1996) and Griffols et al. (1996) are subject to large uncertainties that are not fully discussed in those papers. Both the flux of ALPs produced in the SN explosion and the back-conversion of ALPs to gamma photons can vary by large factors, and hence the upper limits computed with those numbers have to be taken with caveats.

The calculated flux of ALPs produced and released during the SN explosion depends on the knowledge of the size, temperature and density of the proto-neutron star. Those numbers are subject to large uncertainties because we still do not know how stars explode. Even though there is general agreement that the ultimate energy

source is gravity, the relative roles of neutrinos, fluid instabilities, rotation and magnetic fields continue to be debated. In particular, back in the 90s it was believed that neutrinos would be able to reheat the outgoing shock-wave and produce the explosion. Nowadays, with far more powerful computer simulations, we know that neutrino-driven explosions are only possible when the star has a small iron core and low density in the surrounding shells, as being found in stars near or below 10 solar masses (Janka et al. 2007). The progenitor of SN1987A was a blue supergiant and hence it is expected to be somewhere between 10-50 solar masses. A possibility to explain those explosions might require the proper inclusion of rotation and magnetic fields (see Burrows et al. 2007, Obergaulinger et al. 2008, Dimmelmeier et al. 2008 and references therein). Both B field and rotation are present in stars as well as in pulsars, which are the products of successful SN explosions; thus it is very natural to consider them in SN explosion models. In particular, the rotation of the proto-neutron star can change substantially the temperature and, specially, the density of the inner core; in Dimmelmeier et al. (2008) it is shown that the density can vary by more than one order of magnitude, which would change by a similar factor the flux of ALPs being produced. Brockway et al. (1996) and Griffols et al. (1996) did not consider such level of complexity (and uncertainties) in the parameters used to compute the flux of ALPs, mostly because 15 years ago we lacked that knowledge.

On the other hand, the back-conversion of ALPs to photons relies on the structure of the galactic magnetic field which is, again, not well known. Different models predict B fields that could differ substantially and hence they would predict different values for the amount of gamma photons we would obtain for a given flux of ALPs. This is clearly shown in Fig. 1 from Simet et al. (2008), where the probability of ALP-photon conversion is given for various locations of the sky. Therefore, even if we could accurately predict the number of ALPs from SN1987A, the number of photons would be subject to large uncertainties.

Therefore, we conclude that the limit in the inverse of the ALP-photon coupling constant given in Brockway et al. (1996) and Griffols et al. (1996) is subject to large (orders of magnitude) uncertainties, and thus the limit given by the CAST collaboration remains as the most robust one up to date. However, for the sake of comparison with other works, we computed the axion-boost factors when using $M_{11} = 4$ eV. This is shown in Figure 5.7 for both 3C 279 and PKS 2155-304 for two values of the B field, 0.1 nG and 1 nG. For this low coupling constant, the effect due to the photon/ALP oscillation in the source is negligible. The effect due to photon/ALP oscillation in the IGMF in not negligible, but substantially lower than the one shown in the previous section. Besides, such effect shows up at larger energies now (see Eq. 5.11); 100 GeV and 1000 GeV respectively for 1 nG and 0.1 nG.

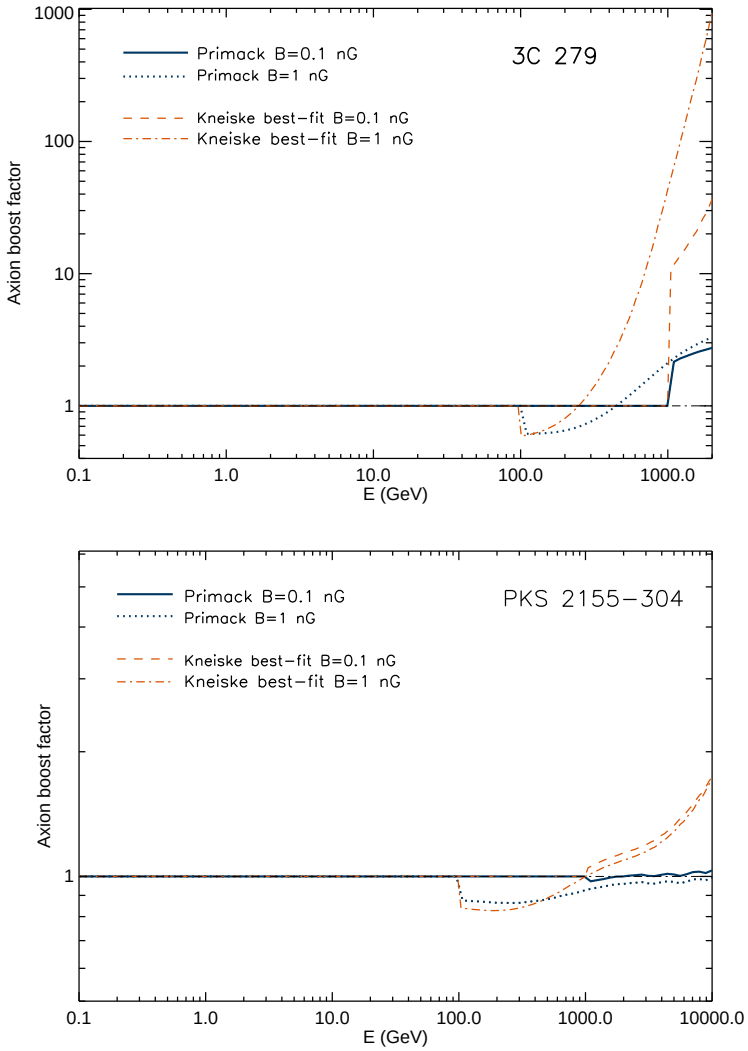

Figure 5.7 Boost in intensity due to ALPs for the Kneiske best-fit and Primack EBL models, computed using the fiducial model presented in Table 5.2 for 3C 279 (z=0.536) and PKS 2155-304 (z=0.117), but with $M_{11} = 4$ GeV and B=0.1 nG (dashed and solid lines for Kneiske best-fit and Primack EBL models respectively) and B=1 nG (dot-dashed and dotted lines).

5.4 Detection prospects for Fermi and IACTs

As mentioned in Section 5.2, for photon/axion coupling constants close to the current published limits, and for realistic ALP mass values, the energy at which the photon/axion oscillation starts to become important is expected to lie in the gamma-ray range. Consequently, the combination of the Fermi/LAT instrument and the IACTs, which cover 6 decades in energy (from 20 MeV to 20 TeV) is very well suited

to study the photon/axion mixing effect. Because of the rapid change in the predicted photon intensity attenuation close to E_{crit}, the energy resolution of the instrument is very relevant in order to detect the ALP signatures. The Fermi/LAT instrument has an energy resolution of about 10%, whereas IACTs, above 150 GeV, have an energy resolution of about 20-25%. The photon intensity attenuation we found in this work goes from 0 to 30% due to the mixing in the source, plus essentially 30% due to the mixing in the IGM. This implies that one needs to be able to determine photon fluxes with a precision better than 10%. Such level of precision might not be achievable for energies >10 GeV with Fermi, or for energies >1 TeV with IACTs due to a low photon counting (which depends obviously on the brightness and hardness of the gamma-ray sources). On the other hand, if the source is emitting at ∼TeV energies and is located at large distances, the photon/axion oscillation in the IGM could translate into an intensity enhancement of more than one order of magnitude (see Figures 5.4, 5.5, 5.6), which should be certainly easy to detect with current IACTs.

Therefore, if we accurately knew the intrinsic spectrum of the sources and/or the density of the EBL, we should be able to observationally detect ALP signatures for a wide range of the parameter space (photon/axion coupling constant and ALP mass). The main problem is that we do neither know accurately the intrinsic spectrum of the sources nor the EBL density. Thus the potential detection of those ALP signatures become quite challenging, but not impossible. In order to study this scenario, we propose the following strategy:

1. Observe several AGNs located at different redshifts, as well as the same AGN undergoing different flaring states (low/high fluxes), at different energy ranges, from radio to TeV. This is important because the modeling of the gamma-ray emission depends critically on the emission at lower energies (specially infrared, optical, UV and X-rays), and also because we do not know *a priori* the energy at which the photon/axion oscillation will start to operate.

2. Try to describe the observational data with "conventional" theoretical models for the broad band emission (Synchrotron Self-Compton, External Compton, Proton synchrotron, etc) and the attenuation of the gamma-rays in the EBL (Primack, Kneiske best-fit or other EBL models). The current models (sometimes very simplistic) will definitely require some modifications to fit the observational data.

3. Look for intensity drops in the residuals ("best-model"-data). We want to stress that the drop in the photon flux due to the attenuation in the IGM only depends on the IGMF and the properties of the ALPs (mass and coupling constant), i.e. it is independent of the gamma-ray sources. Therefore, a detection of such photon flux drops at the same energy in a numerous of different sources would be a clear signature for the existence of photon/axion oscillation, because we do not expect that the intrinsic spectrum from different sources (or same source

at different flux levels) have a rapid drop of ∼30% in the emission at the same energy. The detection (or no-detection) of this photon intensity drop implies a constraint for the product $m_a^2 \cdot M_{11}$. In this specific search, the Fermi-LAT instrument is expected to play a key role since it will detect thousands of AGN sources located at various redshifts (up to z∼5), and at energies where the photon absorption due to the EBL is not important.

4. Look for intensity enhancements in the residuals (i.e. "best-model"-data). This should occur at the highest energies (E>300 GeV) and thus only detectable with IACTs. The origin of the potential photon flux "excess" might be due to a wrong EBL model and/or wrong model for the source emission, the last being very important because it introduces differences between the different sources (or the same source under different activity levels). In this case what we need is to detect distant (z > 0.2) sources at the highest possible energies (>1 TeV). The current EBL models are already very close to the minimum possible photon density limits from galaxy counts; that is, we cannot make them much more transparent. That implies that the detection of TeV photons from a source that is at redshift 0.5 (like 3C 279) could not be explained with conventional physics, regardless of the intrinsic spectrum of the source. This would be a strong hint for the existence of photon/axion oscillation. If the same effect was observed for different sources at different redshifts, we could try to parameterize the effect by varying the ALP parameters (and/or the IGMF strength). If that parameterization could be done successfully, then we would not only have a very strong hint for the existence of ALPs, but also would be able to constrain the available parameter space (coupling constant and ALP mass).

The detection of ALPs is not trivial (and cannot be done with just few sources), but it is certainly possible, as we have shown above. Along these lines, it is worth mentioning that we might be already starting to see hints of the existence of ALPs from the gamma-ray spectra of cosmological sources. Very recent works already pose substantial challenges to the conventional interpretation of the observed source spectra from several distant AGN sources. On the one hand, the VERITAS Collaboration recently claimed a detection of gamma-rays above 0.1 TeV (the highest detected energies are not yet reported) coming from 3C 66A (Acciari 2009), an intermediate-frequency-peaked BL Lac object located at redshift 0.444. This claim coincides with the detection, at GeV energies, of this source in active state by the Fermi-LAT instrument during the same time window (Tosti et al. 2008). In addition, the MAGIC Collaboration reported gamma-rays above 1 TeV coming from a location consistent with the position of 3C 66A (Aliu et al. 2009). Those observations would confirm the earlier claims from the Crimean Astrophysical ObservatoryÕs GT-48 IACT of several detections from this source above 0.9 TeV (Nesphor et al. 1998, Stepaan et al. 2002). Those detections were not confirmed by the HEGRA and Whipple telescopes, which

are more sensitive instruments, but which observed the source at different time windows (Aharonian et al. 2000, Horan et al. 2004). As mentioned above, a detection of TeV photons from a source located at z=0.444 would pose serious problems to conventional models of photon propagation over cosmological distances, where the high energy gammas are expected to disappear due to pair electron-positron production in the EBL. On the other hand, the recent published lower limits to the EBL at 3.6 microns (Levenson & Wright 2008), which is almost twice larger as the previous ones, enhances even further the attenuation of gamma-rays at TeV energies and thus increases even more the magnitude of the mystery. Furthermore, as reported in Krennrich et al. 2008, this fact extends the problems to sources located at medium redshifts (z=0.1-0.2) whose intrinsic energy spectra appear to be harder than previously anticipated. Those observations present blazar emission models with the challenge of producing extremely hard intrinsic spectra (differential spectral index in the spectrum smaller than 1.5) in the sub-TeV to multi-TeV regime. As mentioned in the previous section, the photon/axion oscillation in the IGM would naturally explain these two puzzles; the detection of TeV photons from very distant (z$\sim$0.5) AGNs, and the apparent hardening of the spectra for relatively distant (z>0.1) AGNs.

However, it is worth mentioning that the above reported puzzles might still be explained with conventional physics, as well as uncertainties in the published numbers. The measured redshift of 3C 66A could be wrong (Bramel et al. 2005, Finke et al. 2008), or the TeV photons reported by MAGIC could come from a neighboring source (a radio galaxy), 3C 66B, which has never been detected in gamma-rays (Aliu et al. 2009). As for the blazars with intrinsic spectra harder than 1.5, there is currently quite some controversy. Some authors claim that spectra harder than 1.5 could be possible (see e.g. Katar et al. 2006, Stecker et al. 2007, Aharonian et al. 2008, Boettcher et al. 2008), while others state that spectra should be always softer than 1.5 (see for instance Malkov & Drury 2001, Aharonian et al. 2006, Boettcher et al. 2008, Albert et al. 2008), and use this value to set upper limits to the EBL density at infrared frequencies (Coppi & Aharonian 1999, Aharonian et al. 2006, Mazin & Raue 2007, Albert et al. 2008). An argument in favor of the latter is the fact that EGRET never measured spectra harder than 1.5 at energies below 10 GeV, where the EBL does not distort the gamma-ray spectra, for any of the almost 100 detected AGNs [4].

Finally, we would like to note that the capabilities of detecting the mentioned signatures will increase significantly with the new generation of ground instruments, i.e. MAGIC II or HESS II (with lower energy thresholds, expected to operate in 2009), CTA and AGIS (with even lower energy thresholds and higher sensitivity at multi-TeV energies) and HAWC (higher sensitivity at multi-TeV energies, large duty cycles).

[4] In this matter, the Fermi-LAT instrument, with a sensitivity one order of magnitude better, and scanning the complete sky every 3 hours, is expected to see thousands of AGNs; which will surely shed some light into this mystery.

5.5 Conclusions

If ALPs exist, then we should expect photon to ALP conversions (and vice-versa) in the presence of magnetic fields. This photon/axion mixing will occur in gamma-ray sources as well as in the IGM. We have explored in detail both mixing scenarios together in the same framework. The main conclusions on this work can be summarized as follows:

- If photons oscillate into ALPs in the IGM, then photon/axion mixing in the source is also at work for lower photon energies. In this picture, both effects should be taken into account using the same framework, since they will be governed by the same set of physical parameters (ALP mass and coupling constant). In the case of ALP masses $m_a >> 10^{-10}$ eV, the energies at which the photon/axion oscillation occur in the IGMF are $>>$ 1 TeV and thus not detectable with current gamma-ray instruments. In those cases the photon/axion oscillation in the source would be the only effect that could potentially be detected.

- The photon/axion oscillation in the source (and its vicinity) can produce photon-flux attenuations up to 30%, as previously stated in the literature (Hooper & Serpico 2007, Simet et al. 2008). However, when using available models for gamma-ray emitting blob regions to set values of the **B** field strength and the size of the region where the conversion can take place (we took a radius 10 times the size of the blob), we obtain photon-flux attenuations that are significantly lower.

- The photon/axion oscillation in the IGM produces a photon-flux attenuation up to 30% below the energies at which the EBL is important (but above E_{crit} for the oscillation to be efficient). If the source redshift is larger than $\sim$0.1, this drop in intensity should be about 30% and it shows up in all sources at the same energy. Hence, it presents relatively easy signature of the presence of ALPs. The Fermi-LAT instrument is expected to play a very important role in this search, since it is expected to detect thousands of AGN sources located at various redshifts (up to z=5), and at energies where the EBL is not relevant. The detection of such a photon intensity drop would set the value for the product $m_a^2 \cdot M$, under the assumption of a given IGMF strength. If such an intensity drop is not seen in the spectra, lower limits could be set.

- Above energies at which the absorption of gamma-rays in the EBL become important, the photon/axion oscillation in the IGMF could produce both attenuation and enhancement in the photon flux, depending on the source distance and energy under consideration.

- We find that decreasing the intensity of the IGMF strength does not necessarily decreases the photon-flux enhancements (axion boost factors). For a source located at z=0.5, B=0.1 nG produces higher photon-flux enhancements that B=1 nG. This result is somewhat unexpected since stronger **B** fields allow for a more efficient photon/axion mixing. The reason for this result is the strong attenuation due to the EBL. If the photon/axion mixing is efficient, then many ALPs convert to photons which soon disappear due to the EBL absorption. Consequently, if the source distance is large, it ends up having a very small number of photons arriving at the Earth. On the other hand, if the photon/axion mixing is not that efficient (lower B field), then there is a higher number of ALPs traveling (towards the Earth), which act as a potential reservoir of photons. The net balance between the two processes is sensitive to the source distance, the energy considered and the EBL intensity. Given those parameters, there is always a **B** value that maximizes the photon flux enhancements.

We have shown that the signatures of photon/axion oscillations may be observationally detectable with current gamma-ray instruments (Fermi/LAT and IACTs). Since photon/axion mixings in both the source and the IGM are expected to be at work over several decades in energy, it is clear that a meticulous search for ALPs in the (sub)GeV-(multi)TeV regime will be greatly enhanced by means of a joint effort of Fermi and current IACTs.

The main challenge in such detection comes from the lack of knowledge in conventional physics; namely the intrinsic source spectrum and EBL density and the intensity and configuration of the intergalactic magnetic field. In other words, the effect of the photon/axion oscillations could be attributed to conventional physics in the particular source and/or propagation of the gamma-rays towards the Earth. However, we believe that such photon/axion oscillations could be studied using several distant AGNs located at different redshifts, as well as the same distant AGN detected at distinct activity levels. The signatures of such effect being attenuations (at relatively low energies) and/or enhancements (at the highest energies) in the photon fluxes, that could be visible in the residuals from the "Best-Model-Fit" and the observational data.

Recent work, like the potential detection of TeV photons from very distant ($z \sim 0.4$) sources, or those ones reporting energy spectral indices being harder than 1.5 for relatively distant (z=0.1-0.2) AGNs, already pose substantial challenges to the conventional interpretation of the observed gamma-ray data. Both effects could be explained by oscillations of photons (using $\sim$0.1 nG for the IGMF strength) into light ALPs ($m_a \leq 10^{-10}$ eV) with a photon/axion coupling constant close to current upper limits ($M_{11} \sim 0.114$).

Bibliography

Abraham et al. , 2008, Astropart. Phys., 29, 188

Acciari V. A., 2009, ApJ, accepted, astro-ph/0901.4527

Aharonian F. et al., 2000, A&A, 353, 847

Aharonian F. et al. [H.E.S.S. Collaboration], 2006, Nature, 440, 1018

Aharonian F. A., Khangulyan D. & Costamante L., 2008, MNRAS, 387, 1206

Albert et al., 2008, Science, 320, 1752

Aliu et al. , 2009, ApJ, 692, L29

Andriamonje S. et al. , 2007, JCAP, 0704, 010

Bottcher M., Dermer C. D. & Finke J. D., 2008, ApJ, 679, L9

Bramel et al., 2005, ApJ, 629, 108

Brockway J.W. et al., 1996, Phys. Lett. B, 383, 439

Burrage C., Davis A.-C., & Shaw D. J., 2009, Phys. Rev. D, 79, 044028

Burrage C., Davis A.-C., & Shaw D. J., 2009b, astro-ph/0902.2320

Burrows A. et al. , 2007, ApJ, 664, 416

Coppi P. S., Aharonian F. A., 1999, ApJ, 521, L33

Csáki, C., Kaloper, N. and Terning J., 2002, Phys. Rev. Lett., 88, 161302

Csáki, C., Kaloper, N., Peloso, M. and Terning J., 2003, JCAP, 05, 005

De Angelis A., Roncadelli M. and Mansutti O., 2007, Phys. Rev. D, 76, 121301

De Angelis A., Persic M. and Roncadelli M, 2008, Mod. Phys. Lett. A, 23, 315

Dicus D. A., Kolb E. W., Teplitz V. L. and Wagoner R. V., 1978, Phys. Rev. D, 18, 1829

Dimmelmeier et al. , 2008, Phys. Rev. D, 78, 064056

Dolag K., Grasso D., Springel V. and Tkachev I., 2005, JCAP, 0501, 009

Duffy L. D. et al., 2006, Phys. Rev. D, 74, 012006

Dupays A., Rizzo C., Roncadelli M. and Bignami G. F., 2005, Phys. Rev. Lett., 95, 211302

Enomoto R. et al. , 2002, Astropart. Phys., 16, 235

Fairbairn M., Rashba T. and Troitsky S., 2007, Phys. Rev. Lett., 98, 201801

Finke et al., 2008, A&A, 447, 513

Furlanetto S. R. & Loeb A., 2001, ApJ, 556, 619

Gehrels N. and Michelson P., 1999, Astropart. Phys., 11, 277

Grasso D. and Rubinstein H. R., 2001, Phys.Rept., 348, 16

Griffols J.A. et al. , 1996, Phys. Rev. Lett., 77, 2372

Hartmann R.D. et al. , 2001, ApJ, 553, 683

Hauser M.G., Dwek E., 2001, Annu. Rev. Astron. Astrophys., 39, 249

Hinton J. A., 2004, New Astron. Rev., 48, 331

Hochmuth K. A., Sigl G., 2007, Phys. Rev. D, 76, 123011

Hooper D. and Serpico P., 2007, Phys. Rev. Lett., 99, 231102

Horan et al., 2004, ApJ, 603, 51

Hutsemékers D., Payez A., Cabanac R., Lamy H., Sluse D., Borguet B. and Cudell J.-R., 2008, *To appear in the Proceedings of the Astronomical Polarimetry 2008: Science from Small to Large Telescopes*, July 6-11, 2008, Quebec (Canada), astro-ph/0809.3088

Janka H.-Th. et al. , 2007, Phys. Reports, 442, 38

Katarzynski K., et al. 2006, MNRAS, 368, L52

Kneiske T. M., Bretz T., Mannheim K. and Hartmann D. H., 2004, A&A, 413, 807

Krennrich, Dwek and Imran, 2008, ApJ, 689, L93

Kronberg P. P., 1994, Rep. Prog. Phys., 57, 325

Kusunose M. and Takahara F., 2008, ApJ, 682

Levenson L. R. & Wright E. L., 2008, ApJ, 683, 585

Lorentz E. et al. , 2004, New Astron. Rev., 48, 339

Malkov M. A. & Drury L., 2001, Rep. Prog. Phys., 64, 429

Mazin D. and Raue M., 2007, Astron. Astrophys., 2007, 471, 439

Mirizzi A. Raffelt G. G. and Serpico P. D., 2008, Lect. Notes Phys., 741, 115

Mirizzi A., Raffelt G. G. and Serpico P., 2007, Phys. Rev. D, 76, 023001

Neshpor Y. I., Stepanyan A. A., Kalekin O. P., Fomin V. P., Chalenko N. N. & Shitov V. G., 1998, Astron. Lett., 24, 134

Obergaulinger, M. et al. , 2009, A&A, 498, 241

Peccei R. D. and Quinn H. R., 1977, Phys. Rev. Lett., 38, 1440

Peebles P.J.E., 1993, *Principles of Physical Cosmology*, Princeton University Press, Princeton

Raffelt G. G., 2005, *Contribution to XI International Workshop on Neutrino Telescopes, Venice, Italy*, hep-ph/0504152

Primack J.R., 2005, *Proceedings of the Gamma 2004 Symposium on High Energy Gamma Ray Astronomy*, 26-30 July 2004, Heidelberg, Germany, astro-ph/0502177

Rubbia A. and Sakharov A., 2008, Astropart. Phys., 29, 20

Sigl G., Miniati F. and Ensslin T., 2004, *Proceedings of the Cosmic Ray International Seminar (CRIS), Catania, Italy* astro-ph/0409098

Sikivie P., 1983, Phys. Rev. Lett., 51, 1415 [Erratum ibid., 1984, Phys. Rev. Lett., 52, 695

Simet M., Hooper D. and Serpico P., 2008, Phys. Rev. D, 77, 063001

Stecker W., Malkan M. A. and Scully S.T., ApJ, 2006, 648, 774

Stecker F. W., Baring M. G., Summerlin E. J., 2007, ApJ, 667, L29

Stepanyan A. A., Neshpor Y. I., Andreeva N. A., Kalekin O. P., Zhogolev N. A., Fomin V. P.& Shitov V. G., 2002, Astron. Rep., 46, 634

Tavani M. et al. , 2008, *Nuclear Instruments and Methods in Physics Research Sec. A*, 588, 52

Tosti G. et al., 2008, ATel, 1759, 1

Weekes T. C. et al. , 2002, Astropart. Phys., 17, 221

Weinberg S., 1978, Phys. Rev. Lett., 40, 223

Wilczek F., 1978, Phys. Rev. Lett., 40, 279

Zavattini E. et al. [PVLAS Collaboration], 2006, Phys. Rev. Lett., 96, 110406

6

DM searches with GAW

6.1 GAW: an R&D experiment in Calar Alto

GAW, acronym for Gamma Air Watch, is an R&D experiment to test the feasibility of a new generation of IACT, to reach both, high flux sensitivity and large Field of View (FoV). GAW is conceived as an array of 3 identical imaging telescopes disposed at the vertexes of an equilateral triangle of 80 m side. The specificity of the GAW project resides in the optical system and the detection mode, designed to reach the high sensitivity and large FoV objectives: GAW uses Fresnel refractive lenses (2.13 m each) as light collectors instead of conventional reflective mirrors, providing the system with a clean, aberration free large FoV; and the detectors operate in single photoelectron counting mode instead of the usual charge integration one, lowering the detection limit by a significant factor. GAW will be sensitive in the 1-30 TeV region, with a threshold around 700 GeV. It was born In 2003 as a collaboration effort between our IAA-CSIC group, the DFAMN-University of Sevilla and the GEMDFA-University of Huelva for Spain; IASF/Pa, IASF/Bo, IFSI/To and University of Rome for Italy; and the LIP for Portugal. The GAW telescopes are planned to be installed at the Calar Alto Observatory (CAHA, Almería, Spain) at an altitude of 2,168m.

Two operative phases are foreseen. In Phase I a field of view of $6^\circ \times 6^\circ$ (full angle) will be achieved. During this phase, GAW will monitor the VHE activity of some flaring blazars, and observe SNRs, GRBs and microquasars, among other potential sources. We plan a follow-up of Fermi/LAT detections at high energies as well. In a planned future Phase II, the total focal surface will be covered with detectors, thus providing a huge field of view of 24 deg. (full angle), essential to conduct an all-sky survey above the 700 GeV energy threshold or to look for dark matter.

As for the present status of the experiment, several experts from different European and North American institutions approved the Preliminary Design Review (PDR) of the Project in Spring, 2006. Nowadays, the structure of the first telescope has just arrived and stored at CAHA, the electronics required for Phase I is ready for

operation and most of the rest of components have been already acquired. Also the counting house was already built at CAHA last Summer 2008. Only the Fresnel lens is still under construction, although it is expected that a preliminary commissioning phase can start early this Summer 2009. The IAA-CSIC group plays a crucial role within the GAW collaboration, F. Prada being the Scientific Coordinator of the Collaboration and M. Moles being the Spanish Representative in the Steering Committee. Telescopes design, mechanical mounting and housing, pointing model and accuracy control, site implementation and logistics are the responsibility of the IAA-CSIC group as well, which takes care also of the relationship with CAHA.

In the following we will briefly review the main characteristics of GAW. A more detailed description of the experiment can be found in Cusumano et al. (2007).

6.1.1 Scientific case

To date only a minute fraction of the sky has been scanned beyond 10 GeV. Nevertheless, Very High Energy (VHE) γ-ray astronomy is now a well-established astronomical discipline with galactic and extragalactic sources (both, steady and variable) that, although limited in number, have already implied deep and surprising implications for the theoretical models.

The existing and planned instruments in the VHE domain are firstly intended to extend the coverage towards lower energies, in order to overlap with the energy domain of the forerunner satellite missions. The scientific motivations are obvious after comparing the CGRO/EGRET results with the VHE detections. Thus, whereas the 3^{rd} EGRET catalogue (Hartman et al. 1999) contains a list of more than 250 sources at E $>$ 100 MeV (of which more than half unidentified, with evidence for more than 100 galactic, mostly pulsars and SNRs, and more than 65 extragalactic objects, almost all Blazars), the VHE telescopes have only a few tens of sources (Krennrich et al. 2001, Weekes et al. 2003 and references therein), and only some of them are in the EGRET catalogue. So, the obvious question is about the fate of emission of the EGRET sources above 10 GeV. Technically, the low energy threshold is reached with arrays of heliostats (STACEE, Chantell et al. 1998; Solar-2, Zweerink et al. 1999; CELESTE, Giebels et al. 1998; GRAAL, Arqueros et al. 1999) or with single, large aperture (17 m), Imaging Atmospheric Cherenkov Telescope (IACT) like the European MAGIC (Lorenz et al. 1999), at the La Palma Observatory site. They are also designed to increase the flux sensitivity. This second objective, higher sensitivity in the 0.1 TeV to 10 TeV range, is also achieved by other arrays of IACT, like VERITAS (Weekes at al. 2002), HESS (Bernlhor 2000) and CANGAROO III (Kabuki et al. 2003). All these projects accomplish the high sensitivity capability of the IACTs, increased by the use of stereoscopic techniques.

The NASA mission Fermi is already opening a new scenario on gamma-ray Astronomy in terms of number of sources, accurate positions and counterpart identifications in the energy domain up to 0.3 TeV. Thanks to its large field of view, it will

be used as a guide for VHE astronomy, as EGRET has been till now in its energy domain. With Fermi in operation, the spectral region from 0.1 - 30 TeV is becoming the new frontier to be explored. Nearly simultaneous observations of satellite based gamma-ray experiments and of ground based VHE telescope arrays with a wide field of view such as GAW will give a crucial contribution to the understanding of the source emission in this extreme of the electromagnetic band. Cherenkov observations have demonstrated the existence of stable TeV emitters, which are not bright in the GeV domain of satellite and flaring source at TeV energies. Only a telescope with large FoV capability will have a real chance to discover them. The survey capability is therefore an important objective of the VHE astronomy. However this capability has not yet been taken into account neither in the existing nor in the planned experiments. To date, IACT have useful FoV values ranging between 3 to 5 degrees, but they cannot reach more than 20 degrees FoV. The reasons are technical: the rapid increase of the mirror optical aberrations with off-axis angles, and the vignetting of the focal surface detector. The development of large FoV Cherenkov telescopes with sensitivity and energy threshold comparable to the present VHE experiments would be an important step ahead in this extreme band of the Astronomy.

GAW represents a pathfinder experiment addressed to test and prove the capability of a new generation of Imaging Atmospheric Cherenkov Telescopes with high flux sensitivity and large field of view. It is designed to be very sensitive by using special detection techniques; to have a very large field of view that will make large area surveys feasible; and to be sensitive in the TeV domain. Indeed, a relatively low energy threshold (around 500-700 GeV) will ensure enough spectral overlap with existing and planned experiments, MAGIC in particular.

Even if GAW is a pathfinder project, its unique characteristics prompted us to make a special effort to identify science cases that could be addressed even for Phase I where we will have a field of view of $6^\circ \times 6^\circ$. The main topics we count to address with GAW in its Phase I and in a later Phase II (where the whole focal place will be covered with detectors to yield a field of view of $24^\circ \times 24^\circ$) could be the following:

Phase I

1. Ultra-High Energy Photons from Blazars.
2. Ultra-High Energies from SNRs.
3. Ultra-High Energies from GRBs.
4. Microquasars.
5. Follow-up of EGRET, AGILE and Fermi sources.

Phase II

1. Dark Matter Annihilation in the Milky Way Galaxy.

2. The GAW Search for Nearby Earth-size Dark Matter Micro-Halos.

3. GAW Prospects for Dark Matter detection from Intermediate-Mass Black Holes.

4. The GAW survey.

6.1.2 Main technical characteristics

Optics

GAW light collector is a non-commercial Fresnel lens with a 2.13 m diameter, a focal length of 2.55 m (focal number f/1.2) and a standard thickness of 3.2 mm. The lens is made of UltraViolet transmitting acrylic with a nominal transmittance of about 95% from 300 nm to the near infrared. This material that has a high transmittance and a small refraction index derivative at low wavelength, reduces the chromatic aberrations effects. The lens design is optimized to have a very uniform spatial resolution up to 30 degrees (full angle) at the wavelength of maximum intensity of the Cherenkov light ($\lambda \sim 360$ nm) that fits the requirement of the Cherenkov imaging.

The baseline optics module for the prototype is a single-sided, flat Fresnel lens with the following design parameters:

- Lens Diameter = 2130 mm
- Focal length = 2556 mm
- f/ = 1.2
- Field of view = 24 degrees
- Refraction index, n = 1.5171838 (at λ = 350 nm for acrylic)
- Grooves step size = 3 mm

The lens has a central core of diameter of 50.8 cm, surrounded by an inner circle of petals extending for another 40.6 cm the radius of the lens and an outer circle of petals 40.6 cm wide. The central core will be made with constant depth aspheric grooves. The petals will have constant width aspheric grooves. The assembled lens, as shown schematically in Fig. 6.1, will be constituted by one piece for the central part, 12 pieces for the inner petal ring, and 20 pieces for the outer petal ring. A spider support will maintain the lens pieces together.

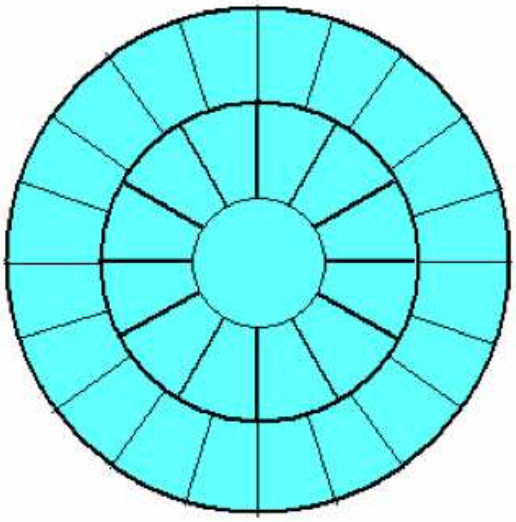

Figure 6.1 Sketch of the GAW Fresnel lens assembly.

Light Guides

The large dead area of the photomultiplier (PMT) used as focal surface detectors induces a low geometrical efficiency factor of around 50% on photon detection. In order to correct that, each PMT pixel is coupled to a Light Guide (LG) such that the ensemble of light guides has a geometrical efficiency factor close to 100%. The design of the light guides has been carried out having in mind current technological limitations. It follows closely that of the detector for the AMS RICH experiment, which proved to be a successful design from the scientific and technological points of view (Delgado 2003). Each LG consists on a UV transparent pyramidal frustum 40 mm tall with squared surfaces at the top and bottom. The smaller area on the bottom matches closely one pixel of the PMT, whereas the large squared area on the top has a size of 3.9mm. The light guides are glued on the top to using a single foil of 1mm thickness and $31\times31\text{mm}^2$ of surface, such that a compact ensemble of 64 light guides is obtained. This ensemble is optically coupled to a single PMT.

Electronics and Trigger System

The GAW electronics has been designed to fully match the specific requirements imposed by the new proposed approach for the detection and measurement of the Cherenkov light produced by high-energy gamma rays traversing the Earth atmosphere. A large number of active channels (of the order of 104) constitute the focal surface of the GAW telescope making it basically a large UV sensitive digital camera with high resolution imaging capability.

The GAW electronics design is based on single photoelectron counting method

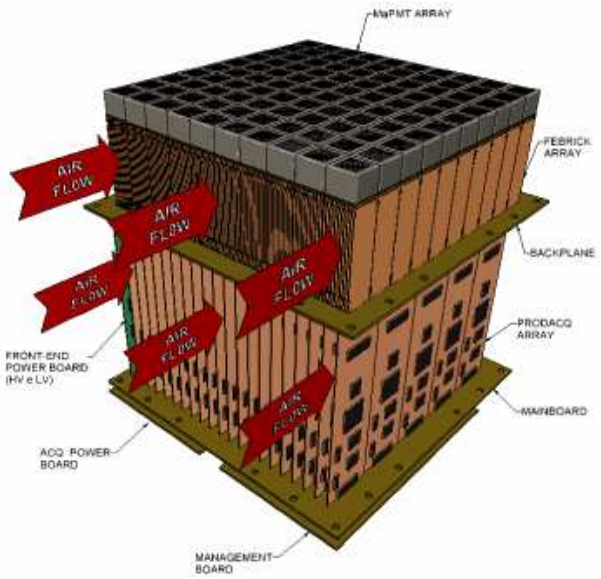

Figure 6.2 Focal Surface Detector Unit: 10×10 MAPMTs array inserted in the UVIScope Instrument.

(front-end) and free running method (data taking and read-out):

- The single photoelectron counting method is a well-established technique and it is used to measure the number of output pulses from the photo-sensors corresponding to incident photons. Small pixel size is required to minimize the probability of photoelectrons pile-up within intervals shorter than the Gate Time Unit (GTU).
- The free running method makes use of cycle memories to continuously store system and ancillary data at a predetermined sampling rate. Once a specialized trigger stops the sampling procedure, data are recovered from the memories and ready to be transferred to a mass memory.

Focal Surface Detector Configuration

GAW Focal Surface Detector is formed by an array of MultiAnode PhotoMultiplier Tubes (MAPMT) inserted in an electronic instrumentation UVIScope (Ultra Violet Imaging Scope) capable for conditioning, acquiring and processing a great number of high speed and high rate pulse signals.

To quickly get a compact detection plane and assure as well a closed tubes assembling, the basic and repeatable parts of the UVIScope instrumentation (like the front-end and the acquisition signals) has been conceived in modular style. For that purpose the following two units was accomplished: a Front-End Brick unit (FEBrick), in order to accommodate just a single tube and a Programmable Data Acquisition unit (ProDAcq) for FEBrick unit signals acquisition.

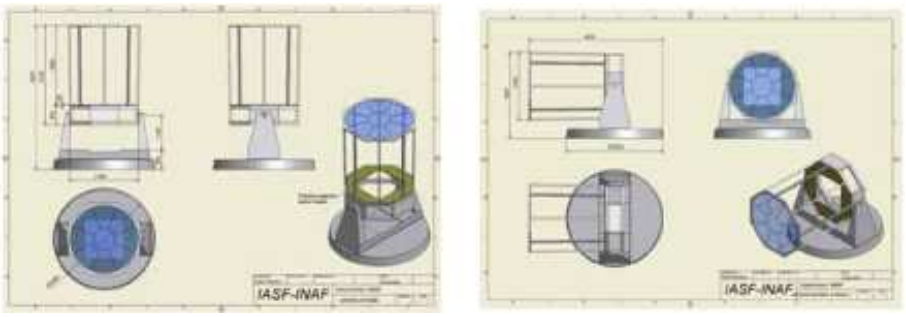

Figure 6.3 Conceptual design of the GAW telescopes.

The whole apparatus gets the major requirements of the GAW Focal Surface Detector:

- Single Photon Sensitivity in the 300-600 nm band, which is the characteristics Cherenkov wavelengths band.
- Fast response (< 10 ns) to follow the very short Cherenkov light time duration.
- Low noise and good signal to noise ratio to detect faint signals.
- Imaging capability with moderate spatial resolution (order of mm).
- Large total Focal Surface area for large FoV application.

Telescopes

In Figure 6.3 we present the telescope tube drawings and dimensions. The three telescopes will be identical with an alt-az mounting. The design and construction solutions of the telescopes do not offer major difficulties given the fact that the required telescope performance is not very demanding in terms of pointing and tracking. This makes for example possible to use commercial encoders and telescope motor drives. The telescopes will be able to work with wind load up to 15 m/s. We plan to use CFK trusses for the focus system, which should be stable within $\pm$ 2 mm. The overall detector weight will be about 500 kg. One detector unit ($6^\circ \times 6^\circ$) will be about 50 kg. The overall dimension of the focal plane (fixed) is 2180 mm $\times$ 2180 mm $\times$ 1100 mm. The idea is to interfacing the focal surface to the fixed focal plane by means of an ad hoc home-made structure, starting from $6^\circ \times 6^\circ$, the initial Focal Surface unit, and changing this structure in case we like to accommodate more units at the focal surface or moving the first one detector unit.

On-Axis Expected Performance

The following figures present the telescope performance obtained from the analysis of the GAW array simulation data using the nominal performance of each telescope

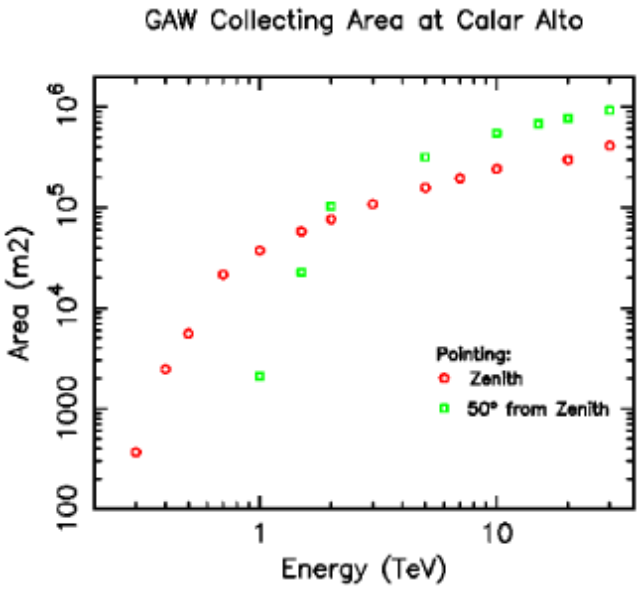

Figure 6.4 Collecting area of the GAW telescope array vs energy for on-axis Gamma Ray events at two different pointing directions.

unit and of the whole array. Figure 6.4 gives the collecting area versus energy for gamma-ray events: values are derived from monoenergetic gamma ray event, in which the source is on axis with respect to the telescope, but at two different pointing directions (θ=0 deg and θ=50 deg from zenith). Each point in the figure is computed multiplying the fiducial area (1520 $\times$ 1520 m^2) by the ratio between triggered events and generated events.

Taking into account the GAW performance for gamma events and having also analyzed the hadronic events file, we also computed: the signal-to-noise ratio reachable in one hour observation for a Crab-like source, the time in which we can reach 5 standard deviations, and the minimum detectable flux. In the sensitivity computation we consider only the hadron contribution because the contribution of the electron component at GAW energy is completely negligible. The results are reported in Table 6.1 while in upper panel of Figure 6.5 the flux limit in 50 h observation in function of the lower energy threshold is shown.

GAW Large Field of View Capability

Highlight of the GAW experiment is its large field of view that is foreseen to reach in Phase II, at the completion of the focal surface, 24° $\times$ 24°. Typical focal detector diameter values for the present and planned IACTs range from 3 deg to 5 deg; by considering that the most external ring ($\sim$1°) is not useful due to the intrinsic size of the Cherenkov image, the actual ratio between GAW and the other IACTs is a factor of 35. This can be used to address GAW to perform high sensitivity survey of

Table 6.1 Summary of GAW performance

Optimum selection cone, OSC [arcminute]	27
Number of Crab gamma events in 1 hour in OSC, S	33
Number of proton events in 1 hour in OSC, N	31
Signal-to-Noise = S/(S+N), in 1 hour observation	4.2
Observation time to reach 5 sigmas [hour]	1.6
Minimum detectable flux in 50 hours, 5 sigma level [milliCrab]	127
Minimum detectable flux in 50 hours, 5 sigma, 700 GeV [ph/(cm^2 s)]	3.5×10^{12}
Number of gamma events in 50 hours at the minimum flux	212

large sky regions.

To evaluate quantitatively this stuff we assumed to point GAW for two years at the zenith position leaving the sky transits. Assuming a reasonable observation duty cycle of 0.15 and a reduced useful FoV of $20^\circ \times 20^\circ$ for the reason discussed before we can survey a sky region of $20^\circ \times 360^\circ$ for a total of 2700 hours (i.e., 150 h for each sky direction). To perform the same survey with IACTs like VERITAS or MAGIC, we need about 1800 independent on-axis pointings, 1.5 h duration each for the same total observation exposure. The comparison between the two surveys is shown in Figure 6.5 bottom panel, in which the sensitivities of the two experiments are derived from upper panel in the same figure, scaling the flux limit for the square root of the exposure time. The exercise demonstrates that GAW has an overall good response and very good performance above the TeV also compared with the best telescopes in construction, despite of the enormous difference in the light collector diameter.

6.2 The GAW strategy to look for DM in the Milky Way

As already discussed in previous chapters, the number of neutralino annihilations in galaxy halos, and therefore the expected gamma signal arriving at the Earth, depends not only on the adopted SUSY model but also on the DM density $\rho_{DM}(\mathrm{r})$. This makes the central region, r ¡ 200 pc, of the Milky Way, where the highest density is, the favorite site to search for that signal. The expected total number of continuum γ-ray photons received per unit time and per unit area, from a circular aperture on the sky of width σ_t (the resolution of the telescope) observing at a given direction Ψ relative to the centre of the Milky Way, can be written as:

$$F(E > E_{\mathrm{th}}) = \frac{1}{4\pi} f_{SUSY} \cdot U(\Psi_0). \tag{6.1}$$

where the factor $f_{SUSY}/4\pi$ represents the isotropic probability of γ-ray production

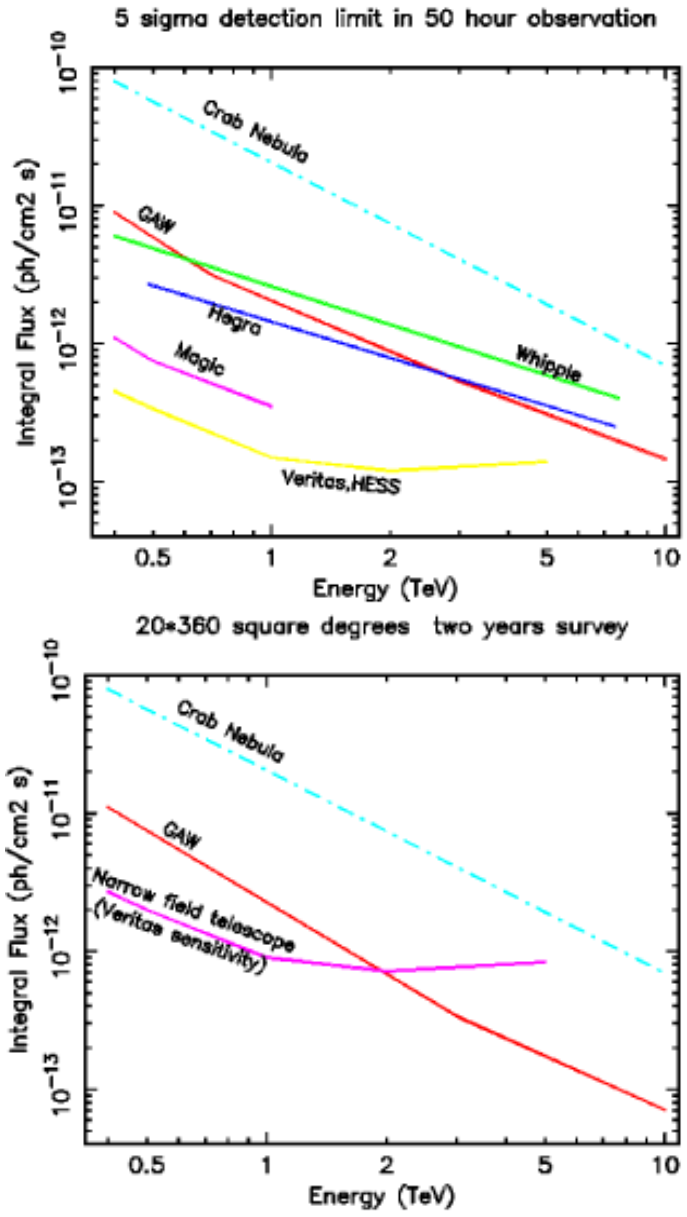

Figure 6.5 Upper panel: GAW sensitivity for known point source. For comparison, the flux of the Crab Nebula and the sensitivity of other TeV experiments are also shown.. Bottom panel: GAW sensitivity limit for a two years survey of a large sky region, 7200 square degrees, compared with a hypothetical survey made by a VERITAS-like Cherenkov telescope in an equivalent overall observation exposure time.

per unit of DM density and depends only on the physics of annihilating neutralino particles. It can be determined for any SUSY scenario given the neutralino properties. The f_{SUSY} parameter decreases with the energy threshold E_{th} and can change by a large factor (up to four orders of magnitude in the minimal supergravity, mSUGRA,

scenario). All the astrophysical properties (such as the DM distribution and geometry considerations) appear only in the factor U(Ψ). This factor also accounts for the telescope beam smearing, and it is the integral of the line-of-sight of the square of the DM density along the direction Ψ. A cuspy DM halo, $\rho \propto r^{-\alpha}$, predicted by ΛCDM simulations is often assumed for the calculations of U(Ψ). The value of α varies from 1 (NFW density profile, Navarro, Frenk & White 1997) to 1.5 (Moore DM profile, Moore et al. 1998), although observational data seems to prefer cored profiles with α <1.

Recent developments in the modelization of the DM distribution in our Galaxy pointed out the necessity to consider some physical processes previously neglected such as the effect of the baryonic compression in the halo, which increases significantly the DM density in the central region of the Milky Way. On the other hand, the non-universality in the scalar and gaugino sectors of supergravity models can also increase significantly the neutralino annihilation cross-section. The combination of both effects results in much higher γ-ray flux prediction from the Galactic Center, that would be detectable by present and future experiments like HESS, MAGIC, VERITAS, CANGAROO, Fermi and our proposed experiment GAW at Calar Alto (Prada et al. 2004; Mambrini et al. 2005 and references therein). In Figure 6.6 we show the expected gamma-ray continuum flux as a function of the angular distance from the Galactic Center, for the compressed DM density profiles provided by our Milky Way models in Prada et al. (2004). The flux is given in units of $f_{SUSY}/10^{-32}$. The flux profiles were determined for a typical IACT of resolution σ_t=0.1°.

A TeV gamma-ray signal in the direction of the Galactic Centre (GC) has already been detected by the HESS experiment in Namibia (Aharonian et al. 2004). The 12σ-detection at TeV energies is consistent with the source being point-like, actually HESS J1745-290 (Aharonian et al. 2005), without further indication for an extended emission. It must be noted that the presence of an extended component in the gamma radiation coming from the central regions of the Milky Way is expected from the SUSY DM annihilation signal as shown in Figure 6.6. The flux and spectrum of this source measured by HESS differ substantially from previous results, in particular those reported by CANGAROO and EGRET (see Mambrini et al. 2005 for a detail comparison). The gamma-ray source reported by HESS exhibits a much harder power-law energy spectrum with spectral index of about -2.2 and extends up to 9 TeV. The interpretation of this signal as being due to the annihilation products of SUSY DM yield a neutralino of mass > 12 TeV. Actually such a heavy LSP neutralino is not natural in the framework of consistent supergravity model when we impose the renormalization group equations and radiative electroweak symmetry breaking (Aharonian et al. 2004; Mambrini et al. 2005). Furthermore, an extended emission was also discovered in the GC area, but it correlates very well with already known dense molecular clouds (Aharonian et al. 2006). Recently, new HESS data on the GC have been published and a reanalysis has been carried out by the HESS collaboration (Aharonian et al. 2006b). In this work, they especially explore the possibility that

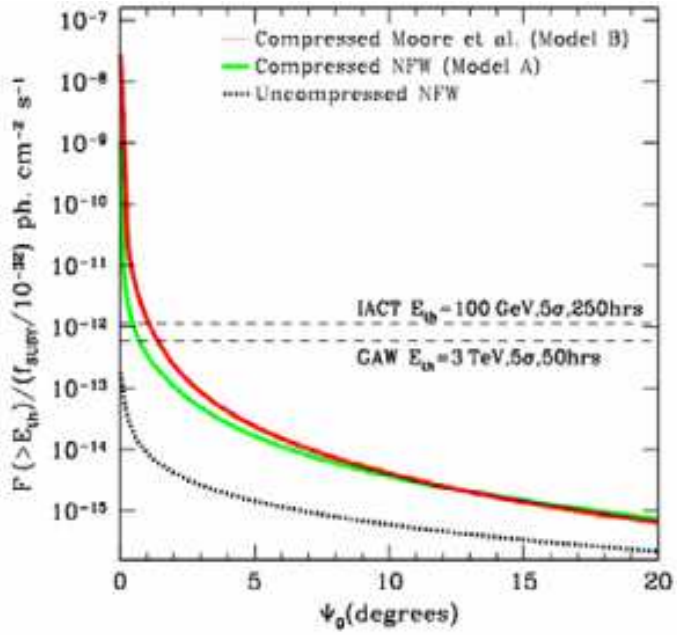

Figure 6.6 Predicted continuum DM annihilation fluxes as a function of distance Φ_0 from the Galactic Centre. The dashed lines give the minimum detectable gamma flux with an IACT such as MAGIC or HESS with E_th=0.1 TeV (see Prada et al. 2004) and GAW with E_th=3 TeV.

some portion of the detected signal is due to neutralino annihilation. According to their results, at the moment it is not possible to exclude a DM component hidden under a non-DM power-law spectrum due to an astrophysical source.

In summary, the current data set of different gamma-rays observations from the GC does not provide a definite conclusion about a DM annihilation origin rather than other source of astrophysics origin. Indeed, the GC is a very crowded region. In particular in the central 10 pc region we have the central compact radio source Sgr A*, the young supernova remnant Sgr A East, dense clouds and cosmic rays in addition to the high background due to diffuse galactic γ-ray emission. All these sources of gamma rays may dominate the signal compare to possible contribution due to the DM annihilation signal that can help to interpret the observed gamma ray spectrum at the GC. This makes any modeling attempt very uncertain (see Aharonian & Neronov 2005).

For all these reasons it would preferable to search for the DM signal away from the central regions of the Milky Way (and also from the galactic plane to avoid the presence of very high energy sources, see Aharonian et al. 2005e). Of course the problem is the fast decrease of the annihilation flux, which falls off three orders of magnitudes when we go up to 20 degrees away from the GC (see Figure 6.6). The only way to compensate for this and have a chance to detect the signal is by using

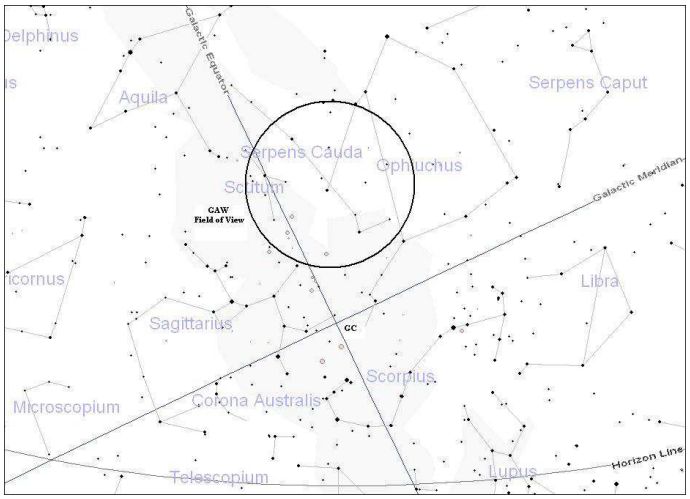

Figure 6.7 Visibility of the Galactic Centre from Calar Alto. The black circle indicates a GAW 24° × 24° field of view, pointing 20° north from the Galactic Centre.

very large FoV Cherenkov telescope which can help to build up the required signal-to-noise needed for the detection. On the contrary this will be very hard with the current generation of IACTs (HESS, MAGIC, VERITAS and CANGAROO) due to their very limited field of view, of only 4° × 4°. In principle the measurements of the extended DM annihilation signal away from the GC might be also reachable by the Fermi satellite. GAW, our proposed wide-field Cherenkov telescope at Calar Alto with a field of view of 24° × 24° will be complementary to the Fermi DM search given our energy sensitivity. Indeed, Fermi will be sensitive up to 300 GeV and GAW, with an energy threshold of 700 GeV and an energy sensitivity up to 30 TeV, will be able to probe more massive neutralinos. We plan to observe a total area of 450 sq. degrees with 1 GAW field 20° north from the Galactic Centre. This will guarantee a visibility of the GC of about 5 hours each night in summer above 60 degrees zenithal distance (see Figure 6.7). Another GAW pointing, located 90° away from the GC, at similar zenithal distance, will be observed in order to determine the background contributions.

A detail study is needed to work out the detectability with GAW of extended sources. This work is under progress where full Monte Carlo simulations will be performed.

6.3 The GAW Search for Nearby Earth-size Dark Matter Micro-Halos

The analysis of the results given by the most recent and very high-resolution N-body cosmological simulations, which try to reproduce the formation and subsequent evolution of DM halos, has shown the possible existence of the so-called DM microhalos.

These microhalos would be the first collapsed structures formed in the Universe and they would have survived until now thanks to its high concentration of matter (see e.g. Moore et al. 2005, Zhao et al. 2005, Pieri et al. 2005, Diemand et al. 2005). These microhalos, with masses similar to the Earth and typical size of the Solar System, would be within a more massive DM halo. In fact, the Milky Way should contain thousands of them, since for example densities of the order of 100 microhalos/parsec3 are considered for the solar galactocentric radius (Pieri et al. 2005). Because of that, microhalos are a suitable target for a search of DM annihilation γ-ray signal using Cherenkov telescopes. Despite of its small size and low content in DM compared to galactic size halos, its extreme proximity (perhaps the nearest one will be less than 0.1 parsec) makes possible to raise its detectability.

GAW constitutes the ideal instrument to search for these DM microhalos, thanks to its large field of view of $24^\circ \times 24^\circ$. Moreover, we plan to survey a large area of the sky in the second phase of the experiment, more specifically $20^\circ \times 360^\circ$ in two years. Studying large areas of the sky is essential if we want to detect these microhalos, because we do not know *a priori* their exact positions, even when they are expected to be isotropically distributed in the Milky Way (except in the very centre, where they can not survive because of the high tidal forces). Furthermore, the GAW survey will be performed keeping the telescope pointing to the zenith at all time (without any kind of sky tracking) so that we can obtain data from different regions of the galaxy.

It becomes possible to make some rough calculations in order to obtain the probability for GAW to be able to detect the γ-ray signal coming from effective DM annihilation inside nearby microhalos. Given the high uncertainties concerning both the DM particle properties and the physical parameters of the microhalo, we can only do some simple assumptions:

1. The microhalos have a constant density core within its scale radius, $\rho_s = 1.29 \times 10^{-22}$ g cm^{-3} (Diemand et al. 2005).

2. We will assume the scale radius r_s for the microhalos to be around 0.0025 parsec (Diemand et al. 2005).

3. Density of microhalos in the solar neighborhood equal to 500 microhalos/parsec^{-3} (Diemand et al. 2005).

4. Neutralino $f_{SUSY} = 10^{-32}$ ph GeV^2 cm^3 s^{-1} (Prada et al. 2004, Sánchez-Conde et al. 2007).

5. GAW flux sensitivity above 1 TeV equal to $F_{GAW} = 3{\times}10^{12}$ ph cm^{-2} s^{-1} (estimated sensitivity for a two years $20^\circ \times 360^\circ$ survey).

Within this scenario we can estimate the number of microhalos that it would be possible to detect in our 7200 square degrees survey. The luminosity of one microhalo,

using the above assumptions, is equal to $L_{MH} = f_{SUSY}\ \rho_s\ r_s\ /\ 3 = 8 \times 10^2 4$ ph s^{-1}. If we use the minimum flux that we can detect with GAW above 1 TeV, we obtain around 0.15 parsec for the maximum distance at which a microhalo could be detected with GAW. With a value of 500 pc^3 for the density of microhalos, we may detect **1**.2 microhalos in our 7200 square degrees survey. According to these calculations the detection of one of these microhalos by GAW may be difficult but still possible, although a more detailed study is necessary.

6.4 GAW Prospects for Dark Matter detection from Intermediate-Mass Black Holes

The detection of γ-rays from DM enhancements around black holes with masses in the interval from 10^0 to 10^6 solar masses has been studied by Bertone et al. (2005). For typical neutralino properties they have shown that these back holes can be bright γ-rays sources, and detectable with a wide field IACT such as Fermi or GAW. The prospects of detection with Fermi are very promising in the energy domain up to 300 GeV. GAW at higher energies will have also a serious chance to detect these intermediate mass black holes, as shown in Figure 6.8 where the number of black holes producing some γ-ray flux as a function of the GAW flux limit for a point source above 400 GeV (blue vertical line) and 2 TeV (black vertical line) is plotted. The yellow shaded region is for a neutralino with a mass of 1 TeV and $< \sigma\ v > = 3 \times 10^{-26}$ cm^3 s^{-1}. The red shaded region is for 5 TeV neutralino mass, with $< \sigma\ v > = 3 \times 10^{-26}$ cm^3 s^{-1}.

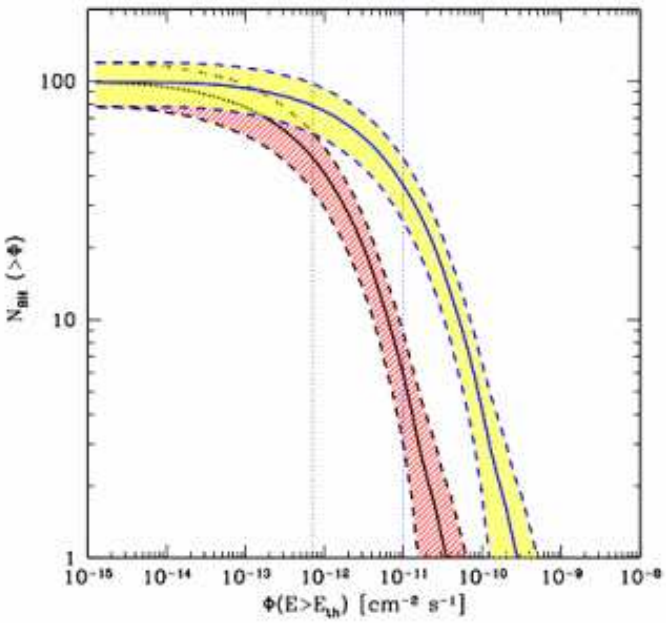

Figure 6.8 Number of intermediate-mass black holes that can be detected with GAW (courtesy of G. Bertone).

Bibliography

Aharonian F.A. et al. , 2004, *A&A*, **425**, L13

Aharonian F.A. et al. , 2005, *Science*, **309**, 746

Aharonian F. et al. , 2006, *Nature*, **439**, 695

Aharonian F. et al. , 2006b, *Phys. Rev. Letters*, **97**, 221102

Aharonian F.A. and Neronov A., 2005, *ApJ*, **619**, 306

Arqueros F. et al. , 1999, Proc. 26th ICRC, **5**, 215

Bernlohr K., 2000, *Astropart. Phys.*, **12**, 255

Bertone G., Zentner A. R. and Silk J., 2005, *Physical Review D*, **72**, 103517

Chantell M.C. et al. , 1998, *Nucl. Instrum. Meth., Phys.Res. A*, **408**, 468

Cusumano G. et al. [GAW Collaboration], Proc. of the 30th ICRC, Merida, Mexico, 3-11 July 2007, **3**, 1313

Delgado C., 2003, PhD Thesis, Universitat Autonoma de Madrid

Diemand J., Moore B., Stadel J., 2005, *Nature*, **433**, 389

Giebels B. et al. , 1998, *Nucl. Instrum. Meth. A*, **412**, 329

Hartman R.C. et al. , 1999, *ApJ Suppl Series*, **123**, 79

Kabuki S., et al. , 2003, *Nucl. Instrum. Meth. A*, **500**, 318

Krennrich F., et al. , 2001, *ApJ*, **560**, L45

Lorenz et al. , 1999, *AIP Conference Proceedings*, **515**, 510

Mambrini Y., Munoz C., Nezri E. and Prada F., 2006, *JCAP*, **01**, 010

Moore B., Diemand J., Stadel J., Quinn T., 2005, astro-ph/0502213

Navarro J. F., Frenk C. S. and White S. D. M., 1997, *ApJ*, **490**, 493

Moore B., Governato F., Quinn T., Stadel J. and Lake G., 1998, *MNRAS*, **499**, L5

Pieri L., Branchini E., and Hofmann S., 2005, *Phys. Rev. Letters*, **95**, 211301

Prada F., Klypin A., Flix J., Martínez M. and Simonneau E., 2004, *Phys. Rev. Letters*, **93**, 241301

Sánchez-Conde M A, Prada F, Lokas E L, Gómez M E, Wojtak R and Moles M, 2007,*Phys. Rev. D.* **76** 123509

Weekes T.C., et al. , 2002, *Astropart. Phys.*, **17**, 221

Weekes T.C., 2003, *Plenary Talk at 28th ICRC*

Zhao H., Taylor J.E., Silk J., Hooper D. 2005, astro-ph/0502049

Zweerink, J., et al. 1999, *Proc. 26th ICRC*, **5**, 223

Part III

DM searches with the MAGIC-I telescope

7

An overview of the MAGIC telescopes

Figure 7.1 The MAGIC telescopes at the Roque de los Muchachos Observatory in La Palma island, as seen in the sunset from the East. Each MAGIC telescope is a single dish mirror of 17 m diameter, the largest collecting mirror in the world to date. They are 85 meters far from each other following sensitivity Montecarlo studies.

The MAGIC telescopes, acronym of *Major Atmospheric Gamma Imaging Cherenkov Telescopes*, are two IACT telescopes located in the island of La Palma (Spain) at the Roque de Los Muchachos Observatory (28.76 N, 17.89 W, 2200 m a.s.l.) and operated by a large European collaboration. The MAGIC experiment was designed in the late 1990s and built in 2001-2003. The first telescope, the MAGIC-I telescope, is a single-dish mirror of 17m diameter, was inaugurated in 2004 and is presently the largest single IACT in the world. It has a sensitivity as impressive as 1.6% of the Crab Nebula emission in 50 hours of observation time, an energy resolution around

25% at 100 GeV and an angular resolution slightly better than 0.1 deg at this same energy. A second MAGIC telescope -located 85 meters away from MAGIC-I and with same dimensions than the telescope currently in operation- was inaugurated last April 2009 and is planned to start data taking this same year 2009. MAGIC-II will surely make possible to improve the excellent marks reached up to now thanks to a factor 2 better sensitivity, a better energy resolution and an even lower energy threshold. The project is funded primarily by the funding agencies BMFB (Germany), MPG (Germany), INFN (Italy), MICINN (Spain), and the ETH Zurich (Switzerland).

Some key points and goals of the MAGIC telescopes are:

- High Cherenkov photon-to-photoelectron conversion efficiency.
- The largest collecting mirror (17 m diameter) in the world to date.
- Lowest energy threshold ever obtained with an IACT. This fact, together with a high sensitivity, makes possible to explore the energy gap between ∼25 GeV and 150 GeV.
- Fast movement of the telescopes to anywhere in the sky (in less than ∼40 seconds), with the clear intention of observing prompt emission from gamma-ray bursts (GRB) following satellite alerts.
- Capability to operate the telescopes even with moonlight (Albert et al. 2007). This makes possible to increase the observation time by roughly a factor 2.
- Steoroscopic system, once the commissioning phase for MAGIC-II is over and this telescope is fully operative. This observation mode is expected to lower even more the energy threshold of the experiment, as well as to increase the sensitivity by a factor 2.

In the following we will briefly review the main characteristics of the MAGIC experiment. This review is only strictly valid for the MAGIC-I telescope. MAGIC-II (recently inaugurated) is essentially a clone of MAGIC-I with some technical improvements, and will be presented separately in section 7.3. A more detailed description of the whole experiment can be found in Baixeras et al. (2003) and Borla et al. (2009).

7.1 MAGIC: the lowest energy threshold of current IACTs

The MAGIC telescope has been built with the clear goal to lower the energy threshold for gamma rays. For many unanswered physics questions, a low energy threshold holds the key. The general argument is the absolute necessity to explore the electromagnetic spectrum at all wavelengths, and the absence, at the present time, of any instrument exploring the energy region between some tens of GeV and several

hundred GeV with adequate sensitivity. At lower energies, satellite experiments, in particular EGRET, have contributed substantial knowledge. Their energy range and sensitivity is being very much improved by the EGRET successor, Fermi, (successfully launched in June, 2008), but even Fermi has the limit of detector size, and will have to be supplemented by complementary terrestrial observations. Pre-MAGIC gamma-ray telescopes, on the other hand, have typically an energy threshold of several hundred GeV.

The interest to this relatively narrow energy band, from 10 to 100 GeV, is motivated not only by the natural desire to enter a new domain which remains a *terra incognita*, but also because it provides a bridge between the high and very high astronomies, and thus may allow key inspections of the current concepts concerning both the GeV and TeV regimes. Moreover, there are good scientific reasons to lower the energy threshold, such as the careful study of the gamma-ray horizon, Cold Dark Matter, quantum gravity, Gamma Ray Bursts, supernova remnants and plerions, pulsars, AGNs, the diffuse photon background, etc. In each of the mentioned fields, a low energy threshold would mean the access to a invaluable and critical information on several physical processes.

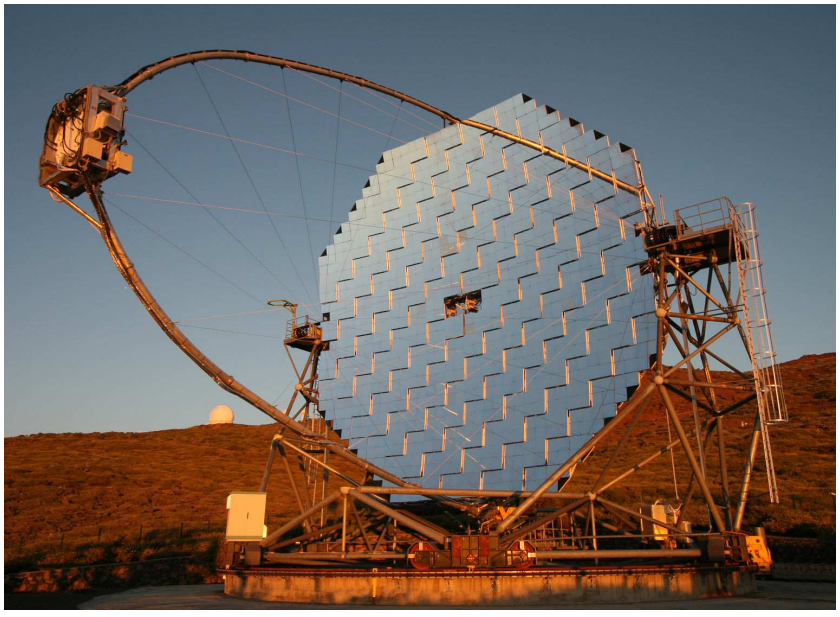

Figure 7.2 The MAGIC-I telescope in the sunset. The camera box is clearly seen 17 meters in front of the 239 m^2 reflecting surface, which consists of 956 square mirrors of 50 cm side. The whole structure wights around 60 tons.

7.2 Main technical characteristics

The most critical technical parameters of MAGIC could be summarized as follows (see Fig. 7.2):

- Active mirror surface 239 sq.m., made of square elements 49.5cm x 49.5cm; $f/D = 1.03$.
- Support frame of carbon fibre made for minimum weight and maximum stiffness.
- Hexagonal camera of 1.05 m diameter, with an inner area of 396 PMTs of 1" diameter each, surrounded by 180 PMTs of 1.5" diameter, arranged in four concentric rings. All tubes have an effective quantum efficiency of 25 to 30%.
- The camera is kept as light as possible, held by an aluminum support stiffened by a web of thin cables.
- Analogue signals are transmitted from the camera to the control house via optical fibers; only the amplifiers and laser diode modulators for transmission are inside the camera housing. Digitization is achieved by new FADCs with a sampling frequency of 2 GHz.
- The threshold for gamma detection is at present as low as ∼50 GeV for low zenith angles. In addition, by means of a recently developed technical configuration, it was possible to reach an energy threshold around 25 GeV for some specific observations (Aliu et al. 2008).
- The average time to reposition the MAGIC telescopes anywhere on the observable sky is less than 40 seconds (despite a moving weight of ∼60 tons).

Frame

The frame of each telescope roughly follows the concept of a large (17 m diameter) solar concentrator with alt/az mount, which was already built and tested a few years ago as part of the German solar power research program. The main mirror support dish consists of a three layer space frame made from carbon fiber-epoxy tubes, which are lighter and more rigid than aluminum. Knots to join the tubes are made from aluminum.

The weight of the frame, including the lower drive ring for azimuthal movement, is about 9 tons (the whole telescope and the undercarriage weights 64 tons). This frame structure keeps the inertia of the telescope low enough for it to be repositioned within 40 s at any position in the sky; this allows, for the first time, the capability of fast repositioning to follow-up GRBs, which is a extremely valuable and unique feature among current IACTs. The frame structure guarantees wind resistance up to < 170

km/h and stability for complete ice coverage up to 3 cm thickness.

Drive
The MAGIC telescope is driven by high precision servo-motors. The azimuth axis of the tele- scope is equipped with two 11 kW motors, while the elevation axis has a single 11 kW motor. In azimuth the movement is limited to a range of 450°, while in zenith to -10°.
The position of the telescope is measured in the mechanical telescope frame by three absolute 14-bit shaft-encoders. With this configuration is possible to monitor the telescope position with an accuracy of 0.02°. By using a high sensitivity CCD camera mounted on the reflector frame, the precision of the tracking system can be verified by monitoring both LEDs installed in the camera frame and stars from the celestial background (Starguider System). With this star-field tracking monitor system it has been measured that the telescope tracks to better than a 1/10 of a pixel size.

Mirrors
The Cherenkov light produced by air showers is collected and focused to the camera by an octagonal shape tessellated mirror reflector of 239 m^2 area. The overall curvature of the reflector is parabolic to minimize the spread in the arrival time of the Cherenkov photons to the camera plane. To assure high optical quality images at the camera, the focal length to diameter ratio (f/D) is set to 1 (to lower astigmatism over 3.6 deg diameter in the focal plane). The 239 m^2 reflecting surface consists of 956 square mirrors of 50 cm side and 34 to 36 m radius of spherical curvature, depending on the position of the mirror in the parabolic dish. Each one is made of an aluminium honeycomb structure; a heating/drying system in case of ice or dew formation; a reflecting 5 mm-thick plate of diamond-milled aluminum and a quartz coating layer. Mirrors are grouped into panels of four; each panel is provided with two motors and a laser pointing to the camera lids, allowing a fine focusing during datataking through the Active Mirror Control. This is necessary in order to correct the residual deformation of the reflector when the telescope is repositioned. The surface global reflectivity is about 85% in the wavelength range 300-650 nm.

Camera
The camera is the most critical element in the performance of a Cherenkov telescope. In the camera, the conversion from Cherenkov photons to photo-electrons takes place and this affects the energy threshold, as it depends directly on this conversion efficiency. In addition, the quality of the shower images which are recorded in the camera is relevant for the posterior gamma/hadron separation. The MAGIC-I camera is composed by an hexagonal board of 1.5 m diameter, placed in the mirror focal plane, which hosts 577 high Quantum Efficiency photomultipliers, of which 397 1" inner pixels and 180 1.5" outer pixels. Light from the reflector is transmitted to each PMT through a Winston cone with an hexagonal end, so that there are no blind

regions in the camera; the total Field Of View (FoV) results equal to 3.5°×3.8°. A special wavelength-shifter coating enhances QE up to an average 20% between 250 and 700 nm wavelength. Since typical duration of Cherenkov flashes is on the order of a few nanoseconds, PMTs are designed to give a fast response with 1 ns FWHM. High Voltage supply is independent for each PMT and remotely controlled by the Camera Control software. Finally, the camera is equipped with heating and cooling systems to prevent the reaching of the dew point and to dissipate the heat from phototubes.

Figure 7.3 *Left*: The MAGIC camera with the lids opened. The hexagonal shape, composed by 577 PMTs, is clearly seen in the picture. *Right*: Pixel scheme of the camera, with 397 1" inner pixels (blue) and 180 1.5" outer pixels (red). The total FoV is 3.5°×3.8°.

In summary, the MAGIC camera has the following features:

- **Fine granularity**: it allows to better deals with low energy shower images and also allows for a more efficient gamma/hadron discrimination. Moreover, the integrated noise per pixel is reduced and trigger threshold at the discriminator level can be lowered. This facilitates the reduction of the energy threshold.
- **Large Field of View**: the 3.5°×3.8° camera FoV makes possible to record most of shower images (showers up to 10 TeV for low zenith angles).
- **Low noise**: the detection of Cherenkov pulses suffers from a strong background of Night Sky Background photons. Therefore, the response of the whole system has to be fast in order to reduce the width of the pulses at trigger level to only a few nanoseconds.
- **Low Gain operation**: it reduces the noise level recorded by the camera. In order to be able to operate the telescope under moonlight, we are forced to operate with a relatively low gain around $\sim 10^4$, in contrast to typical gains around 10^6.

Readout and Trigger

Analogue signals from PMTs are preamplified and then transmitted via optical fibers

to the electronics room located in the Control House, where they will be processed. Only the amplifiers and laser diode modulators for transmission are inside the camera housing. Digitization is achieved by new FADCs with a sampling frequency of 2 GHz.

As for the trigger system, it has the purpose of a first discrimination between signal and background. At this very early stage, however, it is not possible to perform a rejection of hadron-like images with respect to the gamma-like ones: this should be done later in an offline analysis chain. The trigger is segmented in three levels:

Level 0: it acts as a flag for lighted PMTs. A phototube is considered lighted if its current exceeds a fixed threshold; if this happens, a digital signal is generated by L0 and processed by the next trigger stages.

Level 1: this level involves only 325 inner pixels, grouped into 19 overlapping macrocells of 37 pixels each. A temporal coincidence (few ns) among a certain number of neighboring pixels within a macrocell is required: this constraint is motivated with the intention of selecting compact configurations like the elliptic shapes typical from Cherenkov flashes.

Level 2: the last trigger stage performs a fast evaluation of size, shape and orientation of the image, in order to make an effective background rejection and to reduce the trigger rate.

The digitized data which successfully approves all the trigger levels are stored in disks and backed-up into tapes. In addition, every day, data from the last night are copied to the Barcelona and Wurzburg Datacenters, where they are kept and made available to the analyzers.

7.3 The MAGIC-II stereoscopic system

As already commented, a second MAGIC telescope was inaugurated last April 2009 at La Palma. Therefore, now MAGIC is a stereoscopic system of IACTs with the two largest dishes in the world. The second 17m diameter telescope is currently under commissioning and is located 85 meters far from MAGIC-I. The MAGIC experiment, with its large reflector area, high quantum efficiency photomultipliers, optical signal transmission and fast digitization, will benefit from an improved shower reconstruction and increased background rejection thanks to the simultaneous observation by using two telescopes. The stereo observation will result in a better angular resolution, with an improvement of 20%, better energy estimation, with an energy resolution improving from 25% to 15% and higher cosmic-ray background rejection. The flux sensitivity of the 2-telescope system is about 3 times better than that of a single telescope (MAGIC-I) at energies below 200 GeV (see Fig. 7.4).

The structure of the second telescope is almost identical with that of the MAGIC-I telescope. The lightweight reinforced carbon-fiber reflector frame, the drive system

and the active mirror control (AMC) are only marginally improved with respect to the first telescope. New developed components are introduced for improving the performance of the new telescope. Larger 1 m^2 mirrors elements have been developed as well as ultra fast sampling rates, low power consumption readout system and increased quantum efficiency photomultipliers. As for the camera, it is placed in the focus of the reflector at a distance of 17.5 m from the elevation axis of the telescope structure. MAGIC-II has an improved camera equipped uniformly with 1039 pixels of 0.1° diameter each, covering a trigger radius of 1.25° and a FoV of 3.5°. Every seven pixels are grouped in a hexagonal configuration to form one cluster.

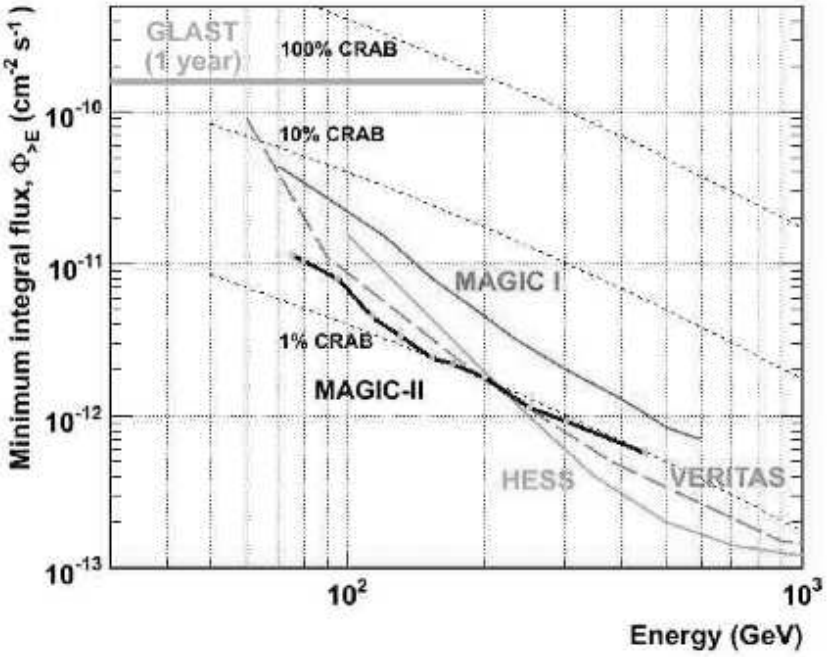

Figure 7.4 Integral sensitivity of the MAGIC-II is compared with MAGIC-I and other experiments. The sensitivity is defined as integral flux of gamma events, exceeding the background fluctuation by factor 5, in 50 hours of observation.

The two telescopes can be operated both in a single mode, by observing two different regions in the sky, and in a stereoscopic mode, with a simultaneous observation of the same region. The stereoscopic observation mode leads to a more precise reconstruction of the shower parameters as well as a stronger suppression of the background.

7.4 Participation of the IAA-CSIC group in MAGIC

The IAA-CSIC group (composed by A. Domínguez, M. Moles, M.A. Pérez-Torres, Francisco Prada (contact person), Fabio Zandanel and myself) is part of the Spanish

participation in MAGIC since November 2006. At present, our group invests a large effort in different scientific and technical aspects inside the MAGIC Collaboration. In particular, and given our experience and research interests, we are deeply involved in the Dark Matter and Exotic Physics Working Group from the very beginning of our membership to the Collaboration. More recently, we crucially contributed to the creation of the Clusters Working Group as part of a new and ambitious observational strategy to look for gamma-ray emissions in galaxy clusters. Finally, we also importantly contribute to the scientific activities carried out inside the Galactic and AGNs Working Groups. In the following, I will summarize my main research activities inside the MAGIC Collaboration:

1. *Dark Matter Working Group (DMWG)*: The IAA-CSIC group has been involved in two internal proposals for the observation of two dwarf satellites of the Milky Way in the context of DM searches: Draco and Willman 1. In the case of Draco, a previous work led by myself (Sánchez-Conde et al. 2007) was the basis for the DMWG to select the most likely DM density profile parameters, needed for a posterior comparison with the MAGIC data. As for Willman 1, I was co-P.I. of the observational proposal and strongly contributed into the astrophysical background. Both objects were finally observed by MAGIC, and both observational campaigns led to two publications (Albert et al. 2008; Aliu et al. 2009). Both works are described in Chapters 8 and 9.

2. *Galaxy Clusters Working Group (GCWG)*. The IAA-CSIC group made a great effort to start a galaxy cluster observation campaign with the MAGIC telescope. This proposal led, as a first result, to the recent observation of a promising galaxy cluster. Although the data analysis shows no gamma signal, this observation represented the first galaxy cluster observation by MAGIC. Furthermore, we will start a similar campaign also during this year 2009, probably for the same object in order to be able to put stringent constraints on fundamental scientific questions concerning the mechanisms of gamma emissions in clusters. I was specially involved in the scientific justification to perform such kind of observations in the context of DM searches in galaxy clusters, making predictions of the expected DM annihilation flux at Earth in a scenario where the neutralino is the DM particle. At present, I am also responsible of the write up of the DM section in the paper to be submitted early.

The participation of the IAA-CSIC group in MAGIC includes important technical tasks as well. In particular, and together with other MAGIC institutions, we have been involved and are responsible of the data daily checks. Daily checks are needed in order to ensure an appropriate quality data to the rest of the Collaboration, as well as to quickly resolve or inform from any eventual technical problems that may appear. As a second and very important technical task, we actively participate in the data taking: periodically, somebody from the IAA-CSIC group has to travel to

the telescope site at La Palma to cover a one-month period of data taking. There, we develop a work as data taking operator, being responsible or helping in the data taking, solving technical problems, etc. In the past, I already carried out this task as shift operator a first time, and as deputy shift leader a second one.

Bibliography

Albert J. et al. [MAGIC collaboration], 2007, ApJL, 664, L87

Albert J. et al. [MAGIC collaboration], 2008, ApJ, 679, 428

Aliu et al. [MAGIC collaboration], 2008b, Science, 322, 1221

Aliu J et al. [MAGIC collaboration], 2009, ApJ, 695, 1

Baixeras C. et al. [MAGIC collaboration], 2003, Nucl.Phys.B (Proc.Suppl.), 114, 247-252

Borla D. et al. [MAGIC collaboration], 2009, Procs. of the 1st International Conference on Technology and Instrumentation in Particle Physics (TIPP09), Tsukuba, Japan, 12 -17 March 2009

Sánchez-Conde M. A., Prada F., Lokas E. L., Gomez M. E., Wojtak, R. & Moles, M., 2007, Phys. Rev. D, 76, 123509

8

Upper limit for γ-ray emission above 140 GeV from the dwarf spheroidal galaxy Draco[1]

The nearby dwarf spheroidal galaxy Draco with its high mass to light ratio is one of the most auspicious targets for indirect dark matter (DM) searches. Annihilation of hypothetical DM particles can result in high-energy γ-rays, e.g. from neutralino annihilation in the supersymmetric framework. With the MAGIC telescope a search for a possible DM signal originating from Draco was performed during 2007. The analysis of the data results in a flux upper limit (2σ) of 1.1×10^{-11} photons cm^{-2} sec^{-1} *for photon energies above* 140 *GeV, assuming a point like source. Furthermore, a comparison with predictions from supersymmetric models is given. While our results do not constrain the mSUGRA phase parameter space, a very high flux enhancement can be ruled out.*

8.1 Introduction

Astronomical observations provide strong evidence for the existence of a new type of non-luminous, non-baryonic matter, contributing to the total energy density of the universe about six times more than baryonic matter (24). This so-called Dark Matter (DM) makes its presence known through gravitational effects, and could be made of so-far undetected relic particles from the Big Bang. Weakly Interacting Massive Particles (WIMP) are candidates for DM, with the lightest supersymmetric particle (neutralino) being one of the most favored candidates in the list of possible WIMPs. Stable neutralinos are predicted in many supersymmetric (SUSY) extensions of the Standard Model of Particle Physics (17). Since the neutralinos are Majorana

[1]Albert et al. [the MAGIC Collaboration] *including M. A. Sánchez-Conde*, 2008, ApJ, 679, 428

particles, pairs of neutralinos can annihilate and produce Standard Model particles. Direct annihilations into $\gamma\gamma$ or $Z\gamma$ produce a sharp line spectrum with a photon energy depending on the neutralino mass. Unfortunately, these processes are loop-suppressed and therefore very rare. Neutralinos can also annihilate to pairs of τ or quarks, leading in subsequent processes to π^0-decays, resulting in a continuous photon spectrum.
Draco is a dwarf spheroidal galaxy accompanying the Milky Way at a galactocentric distance of about 82 kpc. It is characterized by a high mass to light ratio $M/L > 200$, implying a high DM concentration (20; 4) so complying with the trend generally deduced for low-luminosity galaxies (e.g. Persic et al. (21)).

8.2 Expected γ-Ray Flux From Neutralino Self-Annihilation

The expected γ-ray flux depends on details of the supersymmetric (SUSY) model as well as on the density distribution of the DM in the observed source. In general, the DM is assumed to be distributed in an extended halo around spheroidal galaxies. The radial profile of the DM distribution in the halo is modeled by a power law, $\rho_{\rm DM}(r) = Cr^{-\epsilon}$, where the parameter $\epsilon \geq 0$ describes the shape of the DM distribution in the crucial innermost region. $\epsilon = 0$ results in a so-called *core model* with a central flat region, whereas profiles with $0.7 < \epsilon < 1.2$ denote the so-called *cusp profiles*. In addition, we chose an exponential cut-off as proposed by Kazantzidis et al. (18):

$$\rho_{\rm DM} = Cr^{-\epsilon} \exp\left(-\frac{r}{r_b}\right)$$

with the values for r_b, C and ϵ given in Table 8.1 for a cusp and a core profile for Draco. With the present angular resolution of the MAGIC telescope (0.1°), the two models are indistinguishable due to the limited angular resolution of the telescope which smears the determination of the profile (see Figure 8.1). From this figure we can see that the two profiles are discriminated at an angular distance of 0.4°, where the intrinsic flux is already decreased by a factor 20.

Table 8.1 Parameters considered for cusp and core DM density profiles (23).

profile	ϵ	C	r_b(kpc)
cusp	1	$3.1 \times 10^7\, M_\odot\, {\rm kpc}^{-2}$	1.189
core	0	$3.6 \times 10^8\, M_\odot\, {\rm kpc}^{-3}$	0.238

Depending on SUSY model parameters, the annihilation cross section, the average number of photons produced per annihilation and the shape of the γ spectrum

can drastically change. Also a change in the shape of the DM density distribution along the line of sight can significantly change the γ-ray flux. Formula (1) describes the expected γ-ray flux above an energy E_0 from neutralino self-annihilation within Draco.

$$\Phi_\gamma(E > E_0) = \frac{1}{4\pi} f_{\mathrm{SUSY}} < J(\Psi) >_{\Delta\Omega} \tag{8.1}$$

where:

$$f_{\mathrm{SUSY}} = \frac{N_\gamma(E > E_0)\,\langle\sigma v\rangle}{2m_\chi^2}$$

$$< J(\Psi) >_{\Delta\Omega} = \int_\Omega \int_{\mathrm{los}} \rho^2(\Psi, \Omega, s) \cdot B(\Omega)\, ds\, d\Omega$$

$\rho(r)$	DM density profile derived for Draco
N_γ	photon yield per annihilation with $E > E_0$
m_χ	neutralino mass
$\langle\sigma v\rangle$	thermally averaged annihilation cross-section
$B(\Omega)$	Point Spread Function (PSF) of the telescope
Ψ	Pointing angle. ($\Psi = 0$ for the center of Draco)
Ω	solid angle of the telescope's resolution
los	the line of sight

The factor $< J(\Psi) >_\Omega$ is shown for the cusp and the core model in Figure 8.1. Even though this factor converges for both models for small pointing angles Ψ to

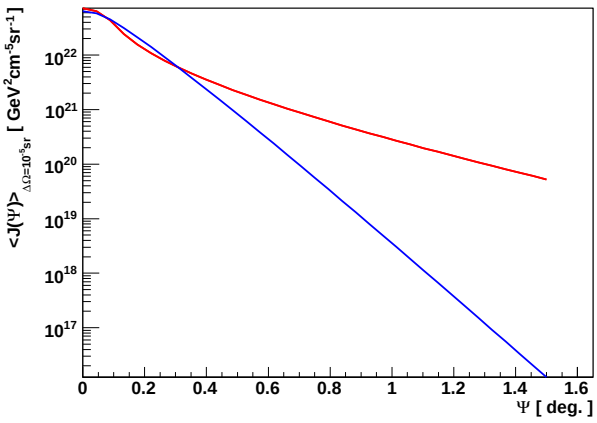

Figure 8.1 The factor $< J(\Psi) >_{\Delta\Omega}$ for the cusp (red) and the core (blue) profile. $\Psi = 0$ corresponds to the center of Draco. At an angular distance of 0.4° of the center of Draco,$< J(\Psi) >_{\Delta\Omega}$ is reduced by a factor of around 20 for both models.

the same value $< J(0) >_\Omega$, there is an uncertainty in the distribution of the DM by the existence of a hypothetical central black hole or a clumpy distribution of the DM (26; 7), which could lead to a significant flux enhancement.
Due to the high predictive power of the mSUGRA framework, where the SUSY breaking effects are transmitted from the high energy scale to the electroweak scale by the graviton, (6; 14; 15; 16) we simulated several million models using the following parameters: $m_0 \leq 6$ TeV, $m_{1/2} \leq 4$ TeV, -4 TeV $\leq A_0 \leq 4$ TeV, $\tan\beta \leq 50$ and $\mu > 0$ (25; 11). Figure 8.2 summarizes the resulting thermally averaged neutralino annihilation cross sections for all models not violating any observational constraints as well as resulting in a total DM relic density $\Omega_{\rm DM}h^2$ in agreement with the 2σ upper limit (u.l.) of 0.113 as derived from combined data from SPSS and WMAP (27). The yellow points correspond to models with $m_0 \leq 2$ TeV (as favored by particle physics), and the blue points represent $m_0 > 2$ TeV. Models resulting in a relic density below the lower WMAP-limit of 0.097 are included, since neutralinos could contribute only a fraction to the total DM in the universe. For these models (shown as dark blue points and dark yellow points in Figure 8.2), a scale factor of $\kappa = \left(\frac{\Omega_\chi h^2}{\Omega_{\rm WMAP}h^2}\right)^2$ is applied to adjust for the DM relic density.

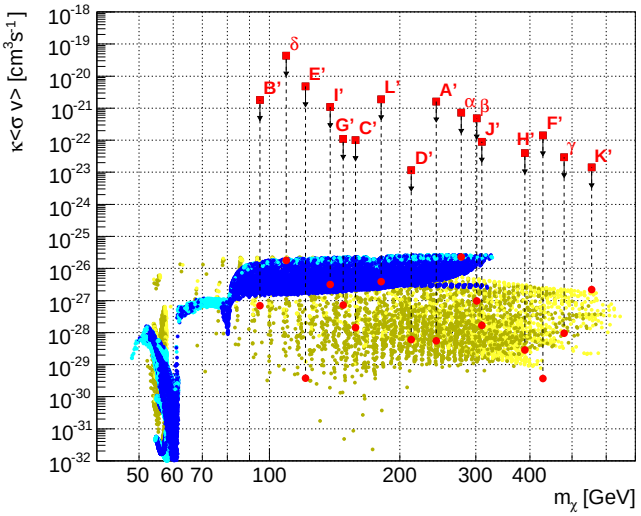

Figure 8.2 Thermally averaged neutralino annihilation cross section as a function of the neutralino mass for mSUGRA models after renormalization to the relic density, as described in the text. The red dots marked with roman letters indicate benchmark models by (3). The ones marked with greek letters are models chosen by the authors. The red boxes indicate the flux upper limit, displayed in units of $< \sigma v >$, assuming a smooth DM halo as given in Table 1. See text for details.

8.3 Observation of Draco and Analysis

Among all Imaging Air Cherenkov Telescopes in operation, MAGIC is the largest single-dish facility (see e.g. (2; 8) for a detailed description) and has the lowest energy threshold. MAGIC is located on the Canary Island La Palma (28.8°N, 17.8°W, 2200 m a.s.l.). The field of view (FOV) of the 576-pixel photomultiplier camera is 3.5°. The angular resolution is $\sim 0.1°$ and the energy resolution above 150 GeV is about 25%. MAGIC has a trigger threshold of ∼60 GeV for small zenith angles (ZA), which increases for larger ZAs.
Data were taken in the false-source tracking (wobble) mode (9) with two pointing directions at 24' distance and opposite sides of the source direction in May 2007 for a total observation time of 7.8 hours. Even though the source is expected to be extended, the wobble mode is justified, as at a distance of 24' of the center of Draco the expected flux from this direction is less than 5% of the flux coming from the center of Draco for both the cusp and the core model (see Figure 8.1). The ZA ranges between 29° and 42°.

Firstly, the calibration of the data (10) was performed. The arrival times of the photons in core pixels (> 6 photoelectrons (phe)) are required to be within a time window of 4.5 ns and for boundary pixels (> 3 phe) within a time window of 1.5 ns of a neighboring core pixel. The next step includes the Hillas parameterization of the shower images (13). Two additional parameters, namely the time gradient along the main shower axis and the time spread of the shower pixels, were computed (28). Hadronic background suppression was achieved using the Random Forest (RF) method (5; 1), where for each event the so-called Hadronness is computed, based on the Hillas and the time parameters. γ/hadron separation is realized by a cut in Hadronness, derived from a γ Monte Carlo (MC) test sample (12; 19), requiring a γ-cut efficiency of 70%. Moreover, the RF method was also used for the energy estimation.

8.4 Results

We searched for a steady γ-ray emission from the direction of the dwarf spheroidal galaxy Draco. The analysis energy threshold defined as the peak of the energy distribution of MC generated γ events after cuts is 140 GeV. Images of air showers initiated by γ-rays coming from the center of Draco are characterized by a small α image parameter, which is the angle between the main axis of the shower image and the connecting line between the center of gravity of the shower and the source position in the camera. The distribution of α is shown in Figure 8.3 for all events after cuts. No significant excess was found. The 2σ u.l. on the number of excess events was calculated using the method of Rolke et al. (22), applying a systematic

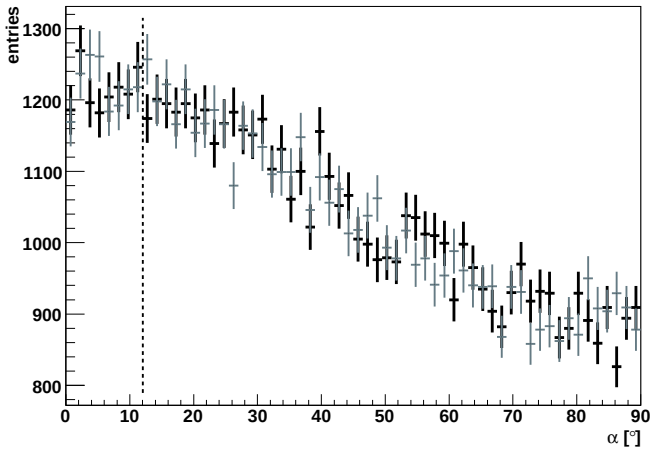

Figure 8.3 Distribution of the α parameter for γ-ray candidates coming from the center of Draco (black marker) and background (grey markers) for data taken between 05/09/2007 - 05/20/2007. The energy threshold is 140 GeV. For the signal region ($\alpha < 12°$), are the number of ON events: 10883 and the number of OFF events: 10996. With the method of (22), the 2σ upper limit on excess events is 231.

error of 30%. The number of excess events were converted into an integral flux u.l., depending on the assumed underlying spectrum. For a power law with spectral index -1.5, typical for a DM annihilation spectrum, and assuming a point like source, the 2σ u.l. is:

$$\Phi_{2\sigma}(E > 140 \text{ GeV}) = 1.1 \times 10^{-11} \,\text{photons}\,\text{cm}^{-2}\,\text{s}^{-1}.$$

For different mSUGRA model parameters using the benchmark points defined in (3) and for other models, we computed the γ-ray spectra expected from neutralino annihilations. Assuming these underlying spectra, the u.l. on the integrated flux above 140 GeV is computed. Using formula (1) and assuming a DM distribution following the profiles according to Table 1, the flux u.l. is displayed in the units of a thermally averaged cross section in Table 2 and in Figure 8.2:

$$F_{2\sigma} = \frac{\Phi_{2\sigma}(E > E_0)}{\Phi_{\gamma}(E > E_0)} < \sigma v > \tag{8.2}$$

As can be seen, the measured flux u.l. is several orders of magnitude larger than predicted for the smooth DM distribution. But a high clumpy structure of the DM distribution or a central black hole could provide a significant flux enhancement (26; 7), which would decrease $F_{2\sigma}$. The analysis presented here can set a limit on the flux enhancement depending on the mSUGRA input parameters. For the benchmark models the values for $\kappa < \sigma v >$ and $F_{2\sigma}$ are displayed in Table 8.2 and in Figure 8.2. For these models, the u.l. on the flux enhancement is around $O(10^3 - 10^9)$.

Table 8.2 Thermally averaged neutralino annihilation cross section $< \sigma v >$, the u.l. on the flux $F_{2\sigma}$, displayed in units of $< \sigma v >$, and the 2σ u.l. on the flux enhancement. Models A' - L' correspond to the benchmark models given by (3). Models α - δ are typical models chosen by the authors with $A_0 \neq 0$.

model:	A'	B'	C'	D'	E'	F'	G'	H'
m_0 [GeV]	107	57	80	101	1532	3440	113	244
A_0 [GeV]	0	0	0	0	0	0	0	0
$m_{1/2}$ [GeV]	600	250	400	525	300	1000	375	935
$\tan\beta$	5	10	10	10	10	10	20	20
m_χ [GeV]	243	95	158	212	121	428	148	389
$\kappa < \sigma v >$ [$\mathrm{cm^3\,s^{-1}}$]	$5.55 \cdot 10^{-29}$	$6.83 \cdot 10^{-28}$	$1.42 \cdot 10^{-28}$	$6.05 \cdot 10^{-29}$	$3.74 \cdot 10^{-30}$	$3.65 \cdot 10^{-30}$	$7.18 \cdot 10^{-28}$	$2.87 \cdot 10^{-29}$
$F_{2\sigma}$ [$\mathrm{cm^3\,s^{-1}}$]	$1.63 \cdot 10^{-21}$	$1.79 \cdot 10^{-21}$	$1.00 \cdot 10^{-22}$	$1.15 \cdot 10^{-23}$	$4.82 \cdot 10^{-21}$	$1.42 \cdot 10^{-22}$	$1.11 \cdot 10^{-22}$	$3.92 \cdot 10^{-23}$
boost factor	$2.9 \cdot 10^7$	$2.6 \cdot 10^6$	$7.0 \cdot 10^5$	$1.9 \cdot 10^5$	$1.3 \cdot 10^9$	$3.9 \cdot 10^7$	$1.5 \cdot 10^5$	$1.4 \cdot 10^6$

model:	I'	J'	K'	L'	α	β	γ	δ
m_0 [GeV]	181	299	1001	303	5980	180	1140	4540
A_0 [GeV]	0	0	0	0	-300	-2800	-1800	300
$m_{1/2}$ [GeV]	350	750	1300	450	680	720	1120	300
$\tan\beta$	35	35	46	47	50	5	50	35
m_χ [GeV]	138	309	554	181	277	301	479	109
$\kappa < \sigma v >$ [$\mathrm{cm^3\,s^{-1}}$]	$3.17 \cdot 10^{-27}$	$1.67 \cdot 10^{-28}$	$2.22 \cdot 10^{-27}$	$3.85 \cdot 10^{-27}$	$2.27 \cdot 10^{-26}$	$9.75 \cdot 10^{-28}$	$9.43 \cdot 10^{-29}$	$1.79 \cdot 10^{-26}$
$F_{2\sigma}$ [$\mathrm{cm^3\,s^{-1}}$]	$1.08 \cdot 10^{-21}$	$9.02 \cdot 10^{-23}$	$1.44 \cdot 10^{-23}$	$1.91 \cdot 10^{-21}$	$7.22 \cdot 10^{-22}$	$4.78 \cdot 10^{-22}$	$2.97 \cdot 10^{-23}$	$4.39 \cdot 10^{-20}$
boost factor	$3.4 \cdot 10^5$	$5.4 \cdot 10^5$	$6.5 \cdot 10^3$	$4.9 \cdot 10^5$	$3.2 \cdot 10^4$	$4.9 \cdot 10^5$	$3.1 \cdot 10^5$	$2.4 \cdot 10^6$

8.5 Conclusions

We present the first search for γ-rays from the direction of Draco using an Imaging Air Cherenkov Telescope (IACT). No signal was detected. The 2σ u.l. on a steady γ-ray emission above 140 GeV originating from Draco does not exceed 1.1×10^{-11} photons cm^{-2} s^{-1} if the underlying spectrum follows a power law with spectral index -1.5.

For the mSUGRA benchmark models defined in (3) and assuming a smooth DM density distribution for Draco as given in (23), our flux upper limits are O(10^3 - 10^9) above the predicted values. It is therefore not possible to constrain the mSUGRA phase space by these results, but a very high flux enhancement can be excluded.

Even though an indirect DM detection by measuring γ-rays from neutralino annihilation within the halo of Draco seems for present IACTs out of reach, future satellite telescopes like GLAST with lower energy thresholds might be sensitive enough to reach the mSUGRA parameter space.

Bibliography

Albert, J. et al. 2007, astro-ph/0709.3719

Baixeras, C. et al. 2004, Nucl. Instrum. Meth., A518, 188

Battaglia, M. et al. 2004, Eur. Phys. J., C33, 273

Bergström, L. & Hooper, D. 2006, Phys. Rev. D, 73, 063510

Breiman, L. 2001, Machine Learning, 45, 5

Chamseddine, A. H., Arnowitt, R., & Nath, P. 1982, Phys. Rev. Lett., 49, 970

Colafrancesco, S., Profumo, S., & Ullio, P. 2007, Phys. Rev. D, 75, 023513

Cortina, J. et al. 2005, 5, 359, proc. of the 29th ICRC, Pune, India

Fomin, V. P., Stepanian, A., A., Lamb, R. C., Lewis, D. A., Punch, M., & Weekes, T. C. 1994, Astroparticle Physics, 2, 137

Gaug, M. 2005, proc. of the 7th Workshop on Towards a Network of Atmospheric Cherenkov Detectors 2005, Palaiseau, France, 27-29 Apr 2005

Gondolo, P., Edsjo, J., Bergstrom, L., Ullio, P., & Baltz, E. A. 2000, astro-ph/0012234

Heck, D., Schatz, G., Thouw, T., Knapp, J., & Capdevielle, J. N. 1998, fZKA-6019

Hillas, A. M. 1985, proc. of the 19th ICRC, La Jolla, 3, 445

Inoue, K., Kakuto, A., Komatsu, H., & Takeshita, S. 1982, Prog. Theor. Phys., 68, 927

—. 1982, Prog. Theor. Phys., 67, 1889

—. 1984, Prog. Theor. Phys., 71, 413

Jungman, G. & Kamionkowski, M. 1995, Phys. Rev. D, 51, 3121

Kazantzidis, S., Mayer, L., Mastropietro, C., Diemand, J., Stadel, J., & Moore, B. 2004, ApJ, 608, 663

Majumdar, P., Moralejo, A., Bigongiari, C., Blanch, O., & Sobczynska, D. 2005, 5, 203, proc. of the 29th International Cosmic Ray Conference (ICRC 2005), Pune, India, 3-11 Aug 2005

Mayer, L., Kazantzidis, S., Mastropietro, C., & Wadsley, J. 2007, Nature, 445, 738

Persic, M., Salucci, P., & Stel, F. 1996, MNRAS, 281, 27

Rolke, W. A., López, A. M., & Conrad, J. 2005, Nucl. Instrum. and Meth., A551, 493

Sánchez-Conde, M. A. et al. 2007, Phys. Rev. D 76, 123509

Spergel, D. N., Bean, R., Doré, O., Nolta, M. R., Bennett, C. L., Dunkley, J., Hinshaw, G., Jarosik, N., Komatsu, E., Page, L., Peiris, H. V., Verde, L., Halpern, M., Hill, R. S., Kogut, A., Limon, M., Meyer, S. S., Odegard, N., Tucker, G. S., Weiland, J. L., Wollack, E., & Wright, E. L. 2007, ApJS, 170, 377

Stark, L. S., Häfliger, P., Biland, A., & Pauss, F. 2005, JHEP, 08, 059

Strigari, L. E., Koushiappas, S. M., Bullock, J. S., & Kaplinghat, M. 2007, Phys. Rev. D, 75, 083526

Tegmark, M. et al. 2006, Phys. Rev. D, 74, 123507

Tescaro, D. et al. 2007, proc. of the 30th ICRC, Merida, Mexico

9

MAGIC upper limits on the VHE gamma–ray emission from the Willman 1 satellite galaxy[1]

We present the result of the observation of the ultra–faint dwarf galaxy Willman 1 performed with the 17 m MAGIC Cherenkov telescope during 15.5 hours between March and May 2008. No significant gamma–ray emission was found above 100 GeV. We derived upper limits of the order of 10^{-12} *ph* cm^{-2} s^{-1} *on the integral flux above 100 GeV, which we compare with predictions from several of the established neutralino benchmark models in the mSUGRA parameter space. The neutralino annihilation spectra are defined after including the recently discovered contribution of internal bremsstrahlung from the virtual sparticles that mediate the annihilation. Flux boost factors of three orders of magnitude are required even in the most optimistic scenario to match our upper limits. However, uncertainties in the DM distribution (e.g., presence of substructure in the halo) may significantly reduce such boost estimates. Future observations will likely allow us to improve the derived upper limits probably by up to one order of magnitude so that — at least in some regions — the mSUGRA parameter space may be constrained.*

9.1 Introduction

Dwarf Spheroidal Galaxies (dSph) are believed to be the smallest (size 1 $\sim$ kpc), faintest (luminosities $10^2 - 10^8$ $L_\odot$) astronomical objects whose dynamics are dominated by dark matter (DM) (Gilmore et al. 2007 and references therein). They are found as satellites orbiting in the gravitational field of a larger host galaxy (e.g., the

[1]Aliu et al. [the MAGIC Collaboration] (*corresponding authors:* M. Doro and M. A. Sánchez-Conde), 2009, ApJ, 697, 1299

Milky Way (MW)). Usually, their member stars show large circular velocities and velocity dispersions that, combined with their modest spatial extent, can be interpreted by the presence of a large DM halo of the order of $10^5 - 10^8$ $M_\odot$. In recent years the Sloan Digital Sky Survey (SDSS) (York et al. 2000) led to the discovery of a new population of MW satellites, comprising about as many (new) objects as were previously known (Willman et al. 2005a; Zucker et al. 2006; Irwin et al. 2007; Walsh et al. 2007; Belokurov et al. 2007). This population of extremely low–luminosity galaxies can be very interesting for DM searches and for investigating galaxy formation at the lowest mass scales. The existence of a new class of ultra–faint MW satellites is also relevant because it provides a partial solution for the so-called "missing satellite problem" (Klypin et al. 1999; Simon & Geha 2007; Strigari et al. 2007; Madau et al. 2008) by partially filling the gap between the predicted and the measured number of galactic sub-halos. In this family is Willman 1, discovered by Willman et al. (2005a) and soon established as potentially the most DM dominated dSph satellite of the MW (Martin et al. 2007; Sánchez-Salcedo & Hernandez 2007; Strigari et al. 2008).

The physics of DM has gathered much interest in recent years, in particular after WMAP (Spergel et al. 2006; Komatsu et al. 2008) measured its relic density with great precision. It is generally believed that DM manifests itself as a general class of weakly–interacting massive particles that includes several candidates which satisfy both experimental constraints and theoretical requirements (see Bertone et al. 2005a and reference therein). Among them, one of the best theoretically motivated, for whom the relic density is calculated without fine–tuning from its nature, is the *neutralino*, arising in Super–Symmetric (SUSY) theories beyond the Standard Model (Wess et al. 1974; Haber & Kane 1984) and in particular the mSUGRA SUSY–extension (Chamseddine et al. 1982). The mSUGRA neutralino annihilations can be observed through the production of $\gamma-$rays. The main emission comes from secondary products of hadronization processes and from final state radiation. In addition, line emissions are found through direct processes such as $\chi\chi \rightarrow \gamma\gamma$, and $\chi\chi \rightarrow Z^0\gamma$, which provide $\gamma-$rays of energies $E = m_\chi$ and $E = m_\chi - m^2_{Z^0}/m^2_\chi$ respectively, even if these lines are normally strongly suppressed compared to broad–band emission.

Recently Bringmann et al. (2008a), following an earlier idea from Bergström (1989), showed that in some regions of the mSUGRA parameter space, a hitherto neglected contribution to $\gamma-$ray emission comes directly from charged sparticles mediating the annihilation into leptons, in processes like $\chi\chi \rightarrow l^+l^-\gamma$. They defined this intermediate state radiation as *internal bremsstrahlung* (IB). The IB mechanism permits to restore the helicity balance in processes that would otherwise be strongly forbidden, and supplies $\gamma-$rays towards high energies ($E > 0.6\ m_\chi$) of up to several orders of magnitude. This boosted emission is particularly interesting for ground–based $\gamma-$ray observation, as performed by Imaging Atmospheric Cherenkov Telescopes (IACTs), which are usually sensitive above $\sim$ 100 GeV where normally the IB boost takes place.

As the $\gamma-$ray flux is proportional to the square of the DM density, IACTs focus on concentrated DM objects. Dwarf galaxy satellites of the MW represent very good candidates, since they are the most DM dominated systems known in the Universe, with very high mass–to–light ratios (M/L), close distance and reduced $\gamma-$ray background from unresolved conventional Galactic sources (i.e. stellar evolutionary remnants). Some dSphs have already been studied in $\gamma-$rays: Draco by MAGIC (Albert et al. 2008a) and Whipple (Wood et al. 2008); UMi by Whipple (Wood et al. 2008) and Sagittarius by HESS (Aharonian et al. 2007) without any significant observation of DM annihilations and only flux upper limits were estimated.

In this article we report results of the observation of the sky region around Willman 1 performed by the MAGIC telescope for a total of 15.5 hours between March and May 2008. After a brief description of Willman 1 in 9.2, in 9.3 we estimate the flux using benchmark models for the neutralino and a typical DM density profile. In 9.4 we briefly describe the MAGIC telescope and the Willman 1 data sample. In 9.5 we present and discuss the results of the observation and we set upper limits for the flux. In 9.6 we report our conclusions.

9.2 Willman 1

In 2004, Willman et al. discovered a new MW companion SDSS J1049+5103 ($10^h40^m22.3^s$, $51°03'03.6''$) (Willman et al. 2005a) as a faint overdensity of red, resolved stars, which was observed again the next year (Willman et al. 2005b) and named Willman 1. At that moment, this object represented the tenth dSph of the MW and, the first one discovered in ten years. Further observations performed with the Keck/DEIMOS telescope confirmed the SDSS results (Martin et al. 2007), while a more recent observation is reported by Siegel et al. (2008).

Willman 1 is located at a distance of 38 ± 7 kpc in the Ursa Major constellation. It is characterized by a very low number of resolved stars, the total luminosity being $L = 855\ L_\odot$, and a very small half–light radius of $r_{1/2} = 21 \pm 7$ pc, almost two orders of magnitude smaller than other known dSphs. The source was defined by previous authors as an "extreme" dwarf galaxy, because some of its characteristics lie between those typical for a globular cluster (GC) and those expected in an extremely faint dSph. The large spread in metallicity of its stars favours the dSph interpretation rather than that of a GC, which would contain stars of a similar age and metallicity (Martin et al. 2007), even if this evidence was recently put under discussion by Siegel et al. (2008). Willman 1 is the least massive satellite galaxy known to date, with a total mass ($M \sim 5 \times 10^5 M_\odot$) about an order of magnitude smaller than those of the least massive satellite galaxies previously known. The corresponding mass–to–light ratio, $M/L \sim 500 - 700\ M_\odot/L_\odot$, is one of the highest in dSph's. This makes Willman 1 one of the most attractive dSph galaxies to look for DM at present (see e.g. Bringmann et al. 2008b), its predicted DM annihilation flux being probably at

least a factor of 3 larger than the second best DM candidate, according to recent work (Strigari et al. 2007).

9.3 Theoretical modeling of the gamma-ray emission from Willman 1

The $\gamma-$ray flux originating from DM particle annihilations can be factorized into a contribution called the *astrophysical factor* $J(\Psi)$ related to the morphology of the emission region and a contribution called the *particle physics factor* Φ^{PP} depending on the candidate particle characteristics:

$$\Phi(> E_0) = J(\Psi) \cdot \Phi^{PP}(> E_0) \ , \tag{9.1}$$

where E_0 is the energy threshold of the detector and Ψ the angle under which the observation is performed.

9.3.1 Astrophysical Factor

At present, a concise and exact characterization of the DM density profile of Willman 1 is a delicate task, since observational data are still scarce. This paper is based on the modeling from Strigari et al. (2008), who modeled the profile by using only 47 stars after removing those with unclear kinematics. Furthermore, to avoid membership problems, only the observational data related to the inner half of the galaxy were taken into account. It is important to note that a null/insignificant tidal–stripping was assumed in order to carry out the modeling of the DM distribution as a system in dynamical equilibrium, a fact which is still under debate. For example, Willman et al. (2006) claim the existence of strong tidal debris, the evolution of the dwarf being strongly affected by tidal interactions with the MW still now, although DM constitutes 90% of its total mass. In the same line, Martin et al. (2007), following deep observations in the r-band, infer that Willman 1 may probably be surrounded by tidal tails. The authors give as a plausible scenario that the dwarf could have been significantly tidally stripped but only in the past, when the object was more luminous and massive. At that age, Willman 1 could have lost most of its outskirts, only the innermost regions surviving intact. This picture would then allow the two contradictory arguments to coexist, since at least a correct modeling for the core of the dwarf may be possible assuming this region to be in dynamical equilibrium.

A very common modeling of the DM distribution, and the only one so far applied to Willman 1 (Strigari et al. 2008), is the NFW DM density profile (Navarro et al. 1996):

$$\rho_{\rm NFW}(r) \ = \ \rho_s \left(\frac{r}{r_s}\right)^{-1} \left(1+\frac{r}{r_s}\right)^{-2} \ , \tag{9.2}$$

where ρ_s and r_s are a typical scale density and radius respectively. The astrophysical factor can be written as:

$$J(\Psi_0) = \frac{1}{4\,\pi} \int_V d\Omega \int_{l.o.s} d\lambda \, [\rho^2(r) * B_{\vartheta_r}(\theta)] \, , \tag{9.3}$$

where Ψ_0 denoted the direction of the target. The first integral is performed over the spatial extension of the source, the second is performed over the line of sight variable λ. The density is convoluted with the Gaussian function $B_{\vartheta_r}(\theta)$ describing the telescope angular resolution where $\theta = \Psi - \Psi_0$ is the angular distance with respect to the center of the object. We remark that the integration of 9.3 involves foreground (MW halo) and extragalactic background whose contributions can be substantial (Elsaesser & Mannheim 2004).

At a distance of 38 kpc, the scale radius corresponds to an extension of 0.54° in the sky, which is well inside the MAGIC field of view ($\sim 3.5°$), but is rather extended if one considers that the telescope angular resolution is around 0.1°. This evidence is mitigated by the fact that the main emission still comes from the very core of the source, due to the very steep NFW profile at the center and the square density dependence. For this reason, we performed an analysis adapted for just slightly extended sources (Sitarek & Mirzoyan 2008). To compute the astrophysical factor for Willman 1, we substitute $r_s = 0.18$ kpc and $\rho_s = 4 \times 10^8$ $M_\odot$/kpc^3 taken from Strigari et al. (2008) into 9.2, and by computing 9.3 we obtain $J(\Psi_0) \sim 3.5 \times 10^{17}$ GeV^2/cm^5. As already commented, this value for the DM annihilation flux probably represents the largest over the rest of dwarfs.

9.3.2 Particle Physics Factor

In many mSUGRA models, the lightest supersymmetric particle is one of four neutralinos ($\tilde{\chi}^0_{1...4}$) which are linear combinations of the Bino $\tilde{B^0}$, the Wino $\tilde{W^0}$ and the two neutral higgsinos $\tilde{H^0_u}$, $\tilde{H^0_d}$. Only five free parameters fully characterize mSUGRA: the scalar mass m_0 and the gaugino mass $m_{1/2}$ defined at the unification scale, the trilinear scalar coupling A_0 and the ratio $\tan\beta$ of the Higgs vacuum expectation values. In addition, one needs to define the sign of the Higgs mass parameter $sign(\mu)$. The typical DM $\gamma-$ray annihilation spectrum is a power–law with a sharp cutoff at the DM candidate's mass, and with a possible bump at energies larger than 0.6 m_χ in case the IB is present, see 9.1. WMAP relic density measurements provide an upper limit in the total neutralino cross section of order of $\langle\sigma v\rangle \sim 10^{-26}$ cm^{3}s^{-1} (Bertone et al. 2005b), which implies that the neutralino is an extremely low–interacting particle and thus the expected $\gamma-$ray flux is correspondingly low today.

The particle physics factor can be written as a product of two terms, the first depending only on the DM candidate's mass and cross section, and a second term, depending on the annihilation $\gamma-$ray spectra, which must be integrated above the

Table 9.1 Definition of benchmark models as in Bringmann et al. (2008b) and computation of the particle physics factor: $m_{1/2}$ and m_0 [GeV] are the gaugino and scalar mass respectively defined at the unification scale; $\tan\beta$ is the ratio of the Higgs expectation values; A_0 [GeV] the trilinear coupling constant and $sign(\mu)$ the sign of the Higgs mass; m_χ [GeV] is the neutralino mass; $\langle\sigma v_{\chi\chi}\rangle$ [cm^3 s^{-1}] is the cross section times the relative velocity of DM particles and $\Phi^{PP}(>100)$ [cm^3 GeV^{-2} s^{-1}] is the particle physics factor above 100 GeV.

BM	$m_{1/2}$	m_0	$\tan\beta$	A_0	$sign(\mu)$	m_χ	$\langle\sigma v_{\chi\chi}\rangle$	$\Phi^{PP}(>100)$
I'	350	181	35	0	+	141	3.62×10^{-27}	7.55×10^{-34}
J'	750	299	35	0	+	316	3.19×10^{-28}	1.23×10^{-34}
K'	1300	1001	46	0	−	565	2.59×10^{-26}	6.33×10^{-33}
F^*	7792	22100	24.1	17.7	+	1926	2.57×10^{-27}	5.98×10^{-34}

energy threshold E_0 of the telescope:

$$\Phi^{PP}(>E_0) = \frac{\langle\sigma v_{\chi\chi}\rangle}{2\,m_\chi^2}\int_{E_0}^{m_\chi} S(E)\,\mathrm{d}E\,, \tag{9.4}$$

where $\langle\sigma v_{\chi\chi}\rangle$ is the total averaged thermal cross section times the relative velocity of particles, m_χ is the DM particle mass, and the factor 2 takes into account that the neutralino annihilates with itself. The $\gamma-$ray annihilation spectrum is composed of different contributions: $S(E) = \sum_i \mathrm{d}N_\gamma^i/\mathrm{d}E$ where $\mathrm{d}N_\gamma^i/\mathrm{d}E$ is the spectrum of the i-th annihilation mode.

The mSUGRA parameter space is conventionally described in a $m_0 \oplus m_{1/2}$ plane, after having fixed the other free parameters. Usually, four zones are identified: the *bulk region*, with low m_0 and $m_{1/2}$ and neutralino masses at around 100 GeV, the *focus point* where m_0 and the neutralino are more massive, the *funnel region* where both m_0 and $m_{1/2}$ take large values, and the *co-annihilation tail* characterized by large $m_{1/2}$. A neutralino shows very different annihilation modes depending on the location in this plane. A representative set of benchmarks was defined by Battaglia et al. (2001) and Battaglia et al. (2003). Hereafter, we use a subset of four slightly modified Battaglia models, as defined by Bringmann et al. (2008b), which include the contribution of IB in the computation of the cross sections and spectra: models *I', J', K', F** for the bulk, co-annihilation, funnel and focus point regions respectively. All the defining parameters of the benchmarks, as well as the derived Φ^{PP} for each of them, are listed in 9.1.

The total estimated flux due to DM annihilation computed according to 9.1 is given in 9.2. There are some sources of uncertainty that may largely affect the values for the predicted flux: *a*) our lack of knowledge of the DM density profile, which may change the astrophysical factor by more than one order of magnitude, *b*) the possible boost due to the presence of substructures in the dwarf, which may enhance the $\gamma-$ray flux at least by a factor of $2-3$ according to $N-$body simulations (Diemand

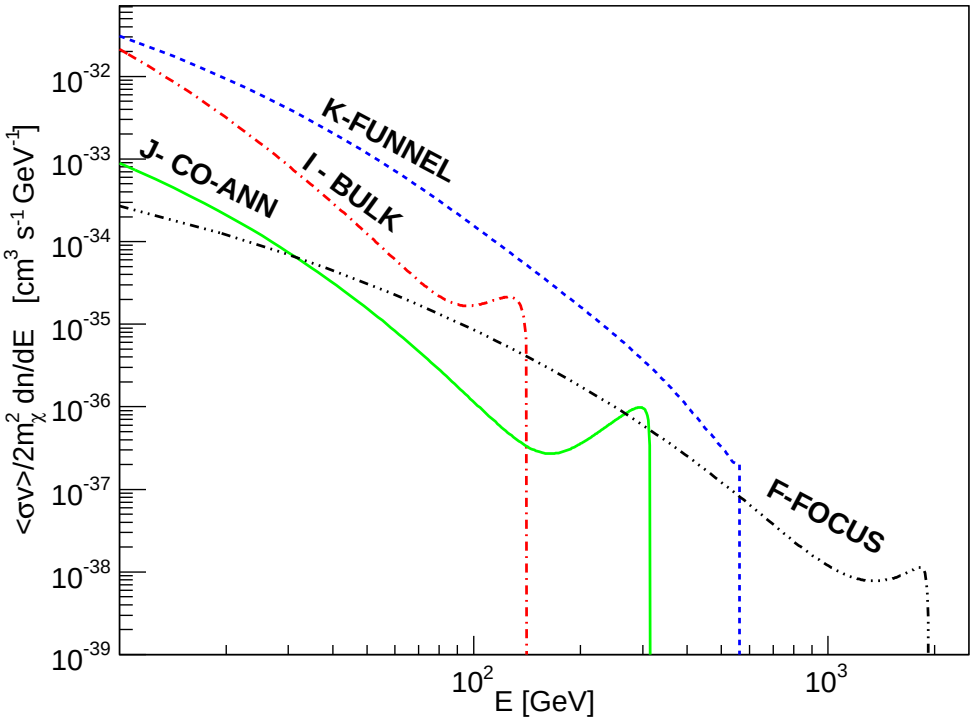

Figure 9.1 Differential particle physics factor for the benchmarks models as in Bringmann et al. (2008b). Line gamma emissions are not included, since their contribution to the flux is negligible.

et al. 2007a, 2007b; Kuhlen et al. 2008). Substructures are in fact expected to be present not only in Willman 1 but also in any other DM halo, since CDM halos are approximately self-similar until a cutoff scale mass (which lies in the range of 10^{-4}–10^{-12} $M_\odot$ (Profumo et al. 2006), *c*) the exclusion of the baryons in the modelization of the total density profile. However, the effect of the adiabatic compression (Prada et al. 2004; Gnedin et al. 2004), although important for larger DM halos, will probably play a marginal role in the case of Willman 1, given its relatively low amount of baryons even in the central regions, where the effect is expected to be more important. Finally, we underline that our choice of benchmarks does not scan the complete parameter space and different neutralinos could have a larger expected flux. A deeper study of the parameter space is therefore very desirable.

9.4 MAGIC data

The MAGIC (Major Atmospheric Gamma Imaging Cherenkov) telescope is located on the Canary Island La Palma (2200 m asl, 28.45°N, 17.54°W). MAGIC is currently the largest IACT, having a 17 m diameter tessellated reflector dish. The faint Cherenkov

light flashes produced by air showers initiated by VHE $\gamma-$rays in the top atmosphere are recorded by the telescope camera, which consists of 577 photomultiplier tubes. More details can be found in Cortina et al. (2005).

MAGIC observed Willman 1 between March and May 2008. The source was surveyed at zenith angles between 22° and 30°, which guarantees the lowest energy threshold. The source was surveyed for 16.8 hours plus another 9.3 hours in OFF observation mode, i.e. pointing to a dark patch in the sky close to Willman 1 where no $\gamma-$ray emission is expected, to estimate the background. The main background Cherenkov telescopes have to deal with is produced by cosmic hadronic particles impinging on the atmosphere and generating electromagnetic sub–showers that can mimic pure $\gamma-$rays showers, and by the night sky background. Background events are partly rejected at the trigger level and in the later off–line analysis event selection following a procedure called gamma/hadron (g/h) separation.

The analysis proceeds as follows (for a detailed description see Albert et al. 2008b): data are calibrated and the number of photoelectrons per pixel extracted (Albert et al. 2008c), then an image cleaning selects pixels with at least 6 photoelectrons (3 photoelectrons for pixels in the boundary of the image). Additional suppression of pixels containing noise is achieved by requesting a narrow time coincidence between adjacent pixels ($\sim$ 7 ns). Based on the Hillas parameterization algorithm (Hillas 1985), the shower parameters are reconstructed. The hadronic background is suppressed with a multivariate method, the Random Forest (Breiman 2001; Albert et al. 2008d), that uses the Hillas parameters to define an estimator called *hadronness* by comparison with Monte Carlo (MC) $\gamma-$ray simulations. The hadronness expresses the likeness of an event to be a hadron and runs from 0 for gammas to 1 for hadrons. The Random Forest method is also used to estimate the energy of a reconstructed shower: the energy threshold is defined by the peak of the distribution of reconstructed MC gamma events. The g/h separation is optimized on a real data sample from the Crab Nebula, a Supernova Remnant and one of the brightest and stable $\gamma-$ray emitters, which is taken as standard candle in very high energy $\gamma-$ray astronomy. The optimization yields a best set of cuts in the Hillas parameters which defines the gamma and hadron acceptance of the analysis. In our case, the optimal set of cuts is obtained for an energy threshold of 100 GeV and a hadronness cut of 0.15. The overall data quality is very high, with only 7% data rejection, resulting in 15.5 hours effective observation time. Independent cross–checks were performed on the data giving compatible results.

9.5 Results and Discussion

No significant $\gamma-$ray excess beyond 100 GeV above the background was observed in 15.5 hours of observation of the sky region around Willman 1. This is also shown in 9.2, where the "α–plot" is reported. The α–parameter is the angular distance between the shower image main axis and the line connecting the image barycenter

and the camera center. Due to their isotropic origin, hadronic events, in case they survive the analysis, are randomly oriented in the camera both in the ON–data and OFF–data sample. This is reflected into a more or less smooth distribution of events in the α–plot, the non–perfect flatness being due to an increased camera acceptance for showers with small α. On the other hand, $\gamma-$rays trace back the source, and thus the orientation of the shower image is toward the center of the camera. Therefore, in case of positive detection, an excess of events in the ON–data above the OFF–data sample is expected at small α. A fiducial region $\alpha < 12^\circ$ is chosen where the signal is assumed with a cut slightly larger than for a point–like source to take into account the moderate source extension. The OFF–data are normalized to the ON–data in the region where clearly no signal is expected, i.e. between $\alpha = 30^\circ$ and $\alpha = 80^\circ$.

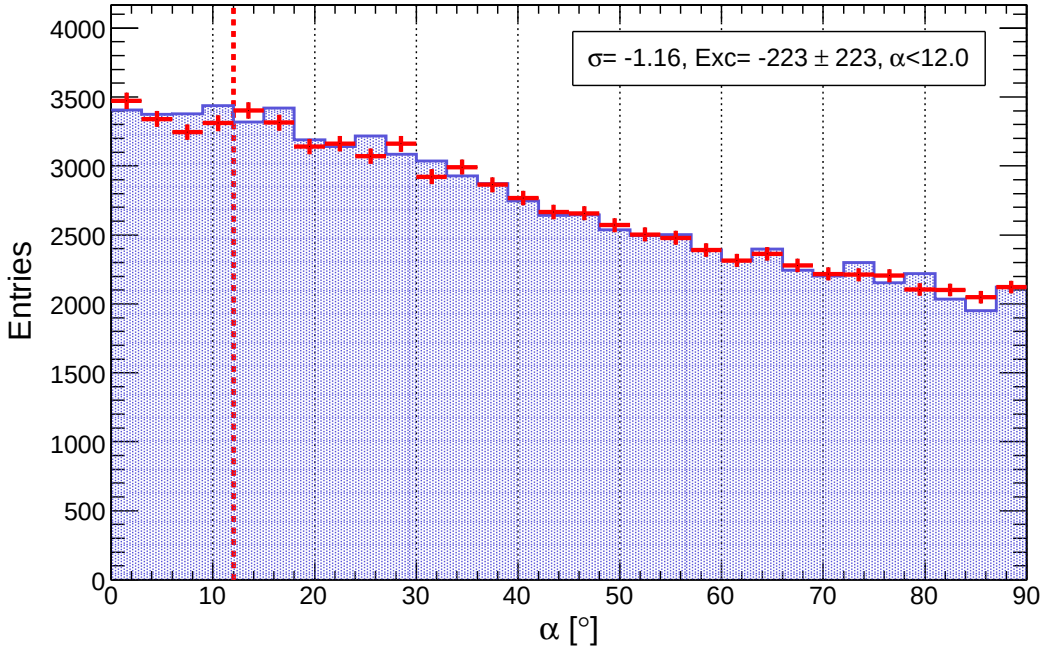

Figure 9.2 Willman 1 α–plot as seen by MAGIC in 15.5 hours above a fiducial energy threshold of 100 GeV and using a hadronness<0.15. The red crosses represent the ON–data sample, the blue shaded region is the OFF–data sample normalized to the ON–data sample between $30^\circ-80^\circ$. The vertical red dotted line represents the fiducial region $\alpha < 12^\circ$ where the signal is expected.

The significance of the detection is calculated using Equation (17) of Li & Ma (1983). The number of excess events $N_{exc}(> 100\ \mathrm{GeV}) = -223 \pm 223$ is calculated as the difference between the number of ON–events and the number of OFF–events in the fiducial $\alpha-$region. We applied the Rolke method (Rolke et al. 2005) to estimate the upper limit in the number of excess events with a 90% confidence level and including 30% of systematic errors, giving as a result $N^{ul}_{exc}(> 100\ \mathrm{GeV}) \sim 191.4$

Table 9.2 Comparison of estimated integral flux above 100 GeV using 9.1 for the benchmarks models defined in Table 9.1 and the upper limit in the integral flux $\Phi^{u.l.}$ above 100 GeV coming from MAGIC data in units of photons cm^{-2} s^{-1}. On the rightmost column, the corresponding upper limit on the boost factor $B^{u.l.}$ required to match the two fluxes is calculated.

BM	$\Phi^{model}(>100$ GeV)	$\Phi^{u.l.}(>100$ GeV)	$B^{u.l.}$
I'	2.64×10^{-16}	9.87×10^{-12}	3.7×10^{4}
J'	4.29×10^{-17}	5.69×10^{-12}	1.3×10^{5}
K'	2.32×10^{-15}	6.83×10^{-12}	2.9×10^{3}
F^{*}	2.09×10^{-16}	7.13×10^{-12}	3.4×10^{4}

events. This value is used to reconstruct the corresponding photon flux for a general $\gamma-$ray spectrum $S(E)$ using:

$$\Phi^{u.l.}_{>E_0} = \frac{N^{u.l.}_{exc}}{\int S(E)\, A^{cuts}_{eff}(E)\, \mathrm{d}E\, \Delta T} \int_{E_0} S(E)\mathrm{d}E\ , \tag{9.5}$$

where E_0 GeV is the energy threshold, $A^{cuts}_{eff}(E)$ is the effective telescope area after analysis and ΔT is the effective observation time.

We applied 9.5 for the four neutralino benchmarks defined. Results are reported in 9.2, where we also compare $\Phi^{u.l.}_{>E_0}$ with the estimated model–dependent flux of 9.1. We also report the upper limits on the *boost factors* that are required to match the two fluxes, calculated again for each neutralino model. The boost factor is defined as the ratio between the upper limit and the theroretical flux, and defines the minimal boost that the theoretical flux should be subject to in order to allow for a positive detection of the source. In order to provide results less dependent of the particular benchmark spectrum, we also calculated flux upper limits in four different energy bins [100–170, 170–350, 350–1000, 1000–20 000] GeV for a generic annihilation spectrum without cutoff and spectral index -1.5. Respectively, the resulting upper limits are $[\,9.94,\ 4.75,\ 0.68,\ 0.35\,]\times10^{-12}$ photons cm^{-2} s^{-1}.

9.2 reveals that although we derived upper limits of the same order of magnitude for the four models considered, there are evident differences in the prospects of detection for different neutralinos. The boost factor largely depends on the benchmarks, but the main differences are connected to the particle physics factor, which varies by orders of magnitude among the different benchmarks, as shown in 9.1. The best prospects are for neutralinos in the $funnel$ region (model K') of the parameter space, for which the mass is large enough to place the cutoff well within the MAGIC energy threshold but still small enough to not reduce the particle physics factor Φ^{PP} of 9.4 too much. Next, with similar boost requirements follow the I' and F^{*} models. In the former case, the effect of the IB plays an important role at energies close to the cutoff even if the neutralino mass is very close to the MAGIC energy threshold. In

the latter case, although the IB effect is negligible, the signal is very extended in the energy region suitable for MAGIC, whereas the large mass makes the flux suppression too large. The worst case scenario is the co–annihilation neutralino. In this case, even if the IB contribution is large, the intrinsic total cross section is very low, which makes the flux very low compared to the others. The IB effect cannot counteract this intrinsic deficit.

Although the results of 9.2 seem to show that we could still be far from DM detection (the most promising scenario being three orders of magnitude below our sensitivity), we should keep in mind that there are important uncertainties in our modeling that may play a crucial role in detectability issues, as already discussed in 9.3.2. In particular our imperfect knowledge of the exact DM density profile as well as the presence of substructure in the dwarf, which is theoretically well–motivated, may increase the astrophysical factor and therefore the flux of more than one order of magnitude. Furthermore, since the parameter space was not fully scanned, it is likely that there are models of neutralino with higher Φ^{PP}. The use of a more advanced detector like MAGIC II, with increased sensitivity and lower energy threshold, favours possible scenarios of DM detection or at least of exclusion of relevant parts of the mSUGRA paparemeter space. Nonetheless, while all other current IACTs can only cover SUSY models with a large IB contribution due to their higher energy threshold, MAGIC II will explore a much larger region of DM annihilation models where the peak of the emission is at lower energy.

9.6 Conclusion

In the context of DM searches, we have observed the Willman 1 dwarf galaxy with the MAGIC telescope for a total of 15.5 hours between March and May 2008. Willman 1 represents one of the best DM dominated systems known in the Universe to search for DM at present, according to its inferred dynamical properties and distance. No $\gamma-$ray signal was detected above an energy threshold of 100 GeV. We have obtained different flux upper limits of the order of 10^{-12} ph cm^{-2} s^{-1} for four benchmark models considered in the framework of mSUGRA.

Using the latest estimations of its structural parameters to build the DM density profile as well as the inclusion of the recently proposed IB mechanism, we calculated the boost factors needed to match the expected flux values from DM annihilation in Willman 1 with the upper limits obtained from the data. We can see that boosts in flux in the order of 10^3 are required in the most optimistic scenario considered. However, uncertainties in the DM distribution, the role of DM substructure or/and a different choice of the neutralino model may reduce this boost significantly. It is expected that deeper observations of the Willman 1 dSph with the upcoming MAGIC II telescope will allow us to improve the flux limits presented here by a factor $2 - 10$.

Bibliography

Aharonian F et al. 2007 *Astrop. Phys.* **29** 55

Albert J et al. 2008a *Astrop. J.* **679** 428

Albert J et al. 2008b *Astrop. J.* **674** 1037

Albert J et al. 2008c Nucl. Instrum. MethodsA **594** 407

Albert J et al. 2008d Nucl. Instrum. MethodsA **588** 424

Battaglia M et al. *Proc. of the APS/DPF/DPB Summer Study on the Future of Particle Physics (Snowmass 2001)* (Snowmass, Colorado) p 347

Battaglia M, De Roeck A, Ellis J R, Gianotti F, Olive K A and Pape L 2004 *Eur. Phys. J. C* **33** 273

Belokurov V et al. 2004 *Astrop. J.* **654** 597

Bergström L 1989 *Phys. Lett. B* **225** 372

Bertone G, Hooper D and Silk J 2005a *Phys. Rept.* **405** 279

Bertone G, Zentner A R and Silk J 2005b *Phys. Rev. D* **72** 103517

Breiman L 2001 *Machine Learning* **45** 5

Bringmann T, Bergström L and Edsjo J 2008a *J. High Energy Phys.* **801** 49

Bringmann T, Doro M and Fornasa M 2008b *(Preprint)* astro-ph/0809.2269v2

Chamseddine A H, Arnowitt R and Nath P 1982 *Phys. Rev. Lett.* **49** 970

Cortina J et al. 2005 *Proc. of 29th International Cosmic Ray Conference (ICRC 2005)* p 359

Diemand J, Kuhlen M and Madau P 2007 *Astrop. J.* **657** 262

Diemand J, Kuhlen M and Madau P 2007 *Astrop. J.* **667** 859

Elsaesser D and Mannheim K 2005 *Phys. Rev. Lett.* **94** 171302

Gilmore G, Wilkinson M I, Wyse R F G, Kleyna J T, Koch A, Evans N W and Grebel E K 2008 *Astrop. J.* **663** 948

Gnedin O Y, Kravtsov A V, Klypin A A and Nagai D 2004 *Astrop. J.* **616** 16

Haber H E and Kane G L 1985 *Phys. Rept.* **117** 75

Hillas A M 1985 *Proc. of the International Cosmic Ray Conference (ICRC) 1985* p 445

Irwin M J et al. 2007 *Astrop. J.* **656** L13

Klypin A A, Kravtsov A V, Valenzuela O and Prada F 1999 *Astrop. J.* **522** 82

Komatsu E et al. 2008 *(Preprint)* arXiv:0803.0547 [astro-ph]

Kuhlen M, Diemand J and Madau P 2008 *(Preprint)* arxiv:0805.4416 [astro-ph]

Li T and Ma Y 1983 *Astrop. J.* **272** 317

Madau P, Diemand J and Kuhlen M 2008 *(Preprint)* arxiv:0802.2265 [astro-ph]

Martin N F, Ibata R A, Chapman S C, Irwin M and Lewis G F 2007 *Monthly Notices of the Royal Astron. Society* **380** p 281

Navarro J F, Frenk C S and White S D M 1997 *Astrop. J.* **490** 493

Prada F, Klypin A, Flix J, Martínez M and Simonneau E 2004 *Phys. Rev. Lett.* **93** 241301

Profumo S, Sigurdson K and Kamionkowski M 2006 *Phys Rev Lett* **97** 031301

Rolke W A, López A M and Conrad J 2005 Nucl. Instrum. MethodsA **551** 493

Sánchez-Salcedo F J and Hernandez X 2007 *Astrop J.* **667** 878

Siegel M H, Shetrone M D and Irwin M 2008 *(Preprint)* arXiv:0803.2489 [astro-ph]

Simon J D and Geha M 2007 *Astrop. J.* **670** 313

Sitarek J and Mirzoyan R 2008 *MAGIC Internal Note TDAS/08-03*

Spergel D N et al. [WMAP Collaboration] 2007 *Astrop J.* **170** 377

Strigari L E et al. 2007 *Astrop. J.* **669** 676

Strigari L E, Koushiappas S M, Bullock J S, Kaplinghat M, Simon J D, Geha M and Willman B 2008 *Astrop. J.* **678** 614

Walsh S M, Jerjen H and Willman B 2007 *Astrop. J.* **662** 83

Willman B et al. 2005a *Astronom. J.* **129** 2692

Willman B et al. 2005b *Astrop. J.* **626** L85

Willman B et al. 2006 *(Preprint)* arXiv:0603486 [astro-ph]

Wess J and Zumino B 1974 *Nucl Phys B* **70** 39

Wood M et al. 2008 *Astrop. J.* **678** 594

York D G et al. 2000 *Astronom. J.* **120** 1579

Zucker D B et al. 2006 *Astrop. J.* **650** L41

Part IV

Conclusions and future work

10

Conclusions

During the last four years, my main research activities have been focused on the understanding of the nature of the Dark Matter. In order to shed some light on this challenging topic, I used different approaches. In the following, I will briefly describe my main contributions to this field.

A large effort was done in the theoretical side to understand how Cold Dark Matter halos form and evolve within the ΛCDM paradigm. In particular, I studied the formation and evolution of CDM halos by means of the spherical infall model with shell-crossing (Chapter 3). In order to take the shell-crossing properly into account, we developed in Sánchez-Conde et al. (2007) a framework based on the numerical follow-up of individual shells of matter with time. Within this framework -which we named Spherical Shell Tracker (SST)- it was possible to study in detail the evolution of the halo. One of the main results we found is that the effect of shell-crossing plays a crucial role in the way the halo evolves and reaches the virial equilibrium and stabilization in radius. Indeed, the values currently adopted in the literature for the actual density contrast at the moment of virialization may not be accurate enough. This fact has important implications e.g. in the definition of a virial mass and a virial radius for the halo.

Also related to these issues, I have been involved in some works (Prada et al. 2006, Betancort-Rijo et al. 2006, Tavío et al. 2008) focused on the understanding and characterization of the outskirts of CDM halos, i.e. well beyond the virial radius. Part of this work was presented in Chapter 2. Using N-body cosmological simulations, we show in Prada et al. (2006) that isolated halos in the mass range 10^{11} to 5×10^{12} solar masses exhibit all properties of virialized objects up to 2-3 virial radii. In Betancort-Rijo et al. (2006) we describe the framework that allows for a comparison of these results with the predictions given by the spherical collapse model (without shell-crossing). A new approximation for the DM density profile up to 10 virial radii is given in Tavío et al. (2008), where we also use it to study the weak gravitational lensing.

During my Thesis, I also paid special attention to DM detectability. My efforts in DM searches were centered on the gamma-ray energy range. Whenever possible, I combined both theory and observations, the latter being possible thanks to my membership in the MAGIC Collaboration:

Theory. Two ingredients are needed in order to make realistic predictions for the expected DM annihilation flux coming from a potential DM candidate: the DM density profile and the selection of a specific Particle Physics model to work with. Although there are indeed large uncertainties concerning both issues, it is worth carrying out predictions on the DM annihilation flux as detailed as possible for the most promising candidates. This was exactly what I did for the Draco dwarf satellite, for which my collaborators and I performed an exhaustive study of the expected DM annihilation flux for the Fermi satellite (formerly GLAST) and for a typical IACT (Sánchez-Conde et al. 2007). The results, that were presented in Chapter 4, helped to understand the real potential of Draco as a good DM candidate and the real capabilities of the current IACTs in the search for DM in this dwarf. In the same work, I also stressed the role of the angular resolution of the instrument in a correct interpretation of the observational data in the context of DM searches. Similar exercise is being carried out for other potential targets as well (Sánchez-Conde et al. 2009, in prep.), in particular for the Coma, Perseus, Virgo and Ophiuchus galaxy clusters. In the same work, we will also compare their DM annihilation fluxes with those expected to come from recently discovered Milky Way dwarf satellites like Willman 1 and Segue 1.

Observations. As a member of the MAGIC Collaboration and an active member of the MAGIC DM Working Group, I was involved in two internal proposals for the observation of two dwarfs in the context of DM searches: Draco (Chapter 8 of this Thesis) and Willman 1 (Chapter 9). In the case of Draco, my previous work (Sánchez-Conde et al. 2007, Chapter 4) was the basis for the DM group to select the most likely DM density profile parameters, needed for a posterior comparison with the MAGIC data. For Willman 1, I was co-P.I. of the observational proposal and substantially contributed into the astrophysical background. Both objects were observed by MAGIC, and both observational campaigns led to two publications (Albert et al. 2008; Aliu et al. 2009). I was one of the two main authors of the work on Willman 1.

My interest in γ-ray astronomy also becomes evident when taking into account my active participation in the GAW R&D experiment (Cusumano et al. 2007), an array of 3 IACTs planned to be located at Calar Alto Observatory, that will operate above $\sim$700 GeV. The main objective of GAW is to test the feasibility of a new generation of IACTs, which combine high sensitivity with a large Field of View. Up to now, I worked on the definition of the science objectives of the instrument as well as in the justification of such an experiment. I have been also in charge of a substantial part of

logistics and bureaucracy. Chapter 6 was devoted to GAW and to describe my main scientific contributions inside the GAW Collaboration.

Recently, in an attempt to find and explore other plausible DM scenarios where the DM particle could be different from the neutralino, I investigated the possible role of axions on the DM problem (Sánchez-Conde et al. 2009) in collaboration with people from KIPAC/SLAC. The obtained results, which are presented in Chapter 5 of the Thesis, are very interesting for current gamma-ray experiments. If axions exist, then photon/axion oscillations should occur in the presence of magnetic fields, such as those expected to be present in AGNs or in the Intergalactic Medium. As a result, the spectra of gamma-ray sources will probably be distorted by an effective photon/axion mixing. We show that this effect could be already observable by means of a joint effort of Fermi and IACTs looking at distant AGNs ($z > 0.1$). Moreover, we find that axions may play a crucial role for a correct interpretation and modeling of the Extragalactic Background Light (EBL).

Bibliography

Albert J. et al. [MAGIC collaboration], 2008, ApJ, 679, 428

Aliu J et al. [MAGIC collaboration], 2009, ApJ, 695, 1

Betancort-Rijo J., Sánchez-Conde M. A., Prada F. and Patiri S. G., 2006, ApJ, 649, 579

Cusumano G. et al. [GAW Collaboration], Proc. of the 30th ICRC, Merida, Mexico, 3-11 July 2007, astro-ph/0707.4541

Prada F., Klypin A. A., Simonneau E., Betancort-Rijo J., Patiri S. G., Gottlöber S. and Sánchez-Conde M. A., 2006, ApJ, 645, 1001

Sánchez-Conde M. A., Prada F., Lokas E. L., Gomez M. E., Wojtak, R. & Moles, M., 2007, Phys. Rev. D, 76, 123509

Sánchez-Conde M. A., Betancort-Rijo J. and Prada F., 2007, MNRAS, 378, 339

Sánchez-Conde, M. A., Paneque D., Bloom E., Prada F. and Domínguez A., 2009, Phys. Rev. D, 79, 123511

Sánchez-Conde M. A. et al., 2009, in preparation

Tavío H., Cuesta A. J., Prada F., Klypin A. A., Sánchez-Conde M. A., 2008, MNRAS submitted, astro-ph/0807.3027

11

Future work

Although our understanding of the nature of Dark Matter (DM) is now much better than it was only a few years ago, there are still a lot of open questions that have to be addressed in the near future. The answers to these questions will allow us to reach a general and consistent picture not only of the dark part of the Universe, but also of the Universe as a whole. Given my background in the DM field of research, I feel capable to contribute to some of the relevant questions.

For a deeper understanding of the DM problem, I believe it is necessary to pay attention to the formation and evolution of Cold Dark Matter (CDM) halos. In this context, it is my intention to continue working in the SST framework that I described in Chapter 3 of this Thesis (which is based on Sánchez-Conde et al. 2007), and that includes the shell-crossing in the spherical infall model. The SST framework has some evident lacks at this moment. In particular, it will be necessary to take into account some physical quantities such as angular momentum and velocity dispersion to make this framework more robust and capable to show more consistent results.

Also related to the SST framework, it would be very important to make a detailed comparison between the SST results and that obtained with N-body cosmological simulations in order to check the model. This should be done for halos of different virial masses and for different shells of matter inside the same halo, with the aim of studying carefully the virialization and the stabilization in radius of different shells. With this kind of studies, for example, we will be able to obtain the real values of the actual and linear density contrasts at the moment of virialization. Furthermore, it may allow us to also use other important tools to improve the SST, such as those concerning the selection of the initial DM density profile. Up to now, an analytical function based on the BBKS formalism (Baarden et al. 1986) has been used as our initial DM density profile in the SST. However, it would be certainly better to start with an initial DM density profile directly given by high resolution N-body cosmological simulations. This issue, together with a more realistic SST model that

includes angular momentum and velocity dispersion, may lead to very good results and hence to a better understanding of how halos form and evolve in the Lambda CDM paradigm.

I am planning to continue my work on DM detection already started in this Thesis as well: exploring the prospects for other potential DM candidates and/or other DM scenarios. I believe that a strong effort in understanding the detectability prospects is absolutely needed, not only as a theoretical exercise but in particular to obtain realistic predictions that could attract the attention of current gamma-ray experiments (like the MAGIC telescopes or the Fermi satellite) in some of the proposed DM targets/scenarios. The inclusion of fundamental problems like the DM searches in the observational proposals of these experiments should certainly be a *must*. It is therefore essential to provide promising DM candidates or new strategies to search for DM as well. For this reason, it becomes rather important to monitor the discovery of new dwarf satellites of the Milky Way, to carry out a detailed modeling of individual galaxy clusters, to give a multiwavelength perspective of the DM detection whenever possible, etc. In this context, the Fermi satellite will also be especially important, since it will surely detect a lot of previously unknown gamma-ray sources. Some of them may represent good DM candidates according to their spectra or other features indicative of DM. Therefore, these objects should be studied in the context of DM as well.

Some ideas that have been merely sketched in this Thesis on DM detection still remain to be explored in detail. In particular, I am very much interested in studying the exact contribution of an effective DM annihilation (as given by the preferred mSUGRA Particle Physics model) to the Extragalactic Gamma-ray Background (EGB). This project will require a wide collaboration between experts working on Particle Physics, Extragalactic Background Light (EBL), N-body cosmological simulations and DM detection. Although there exist some works on this issue (see e.g. Ullio et al. 2002), an update is needed in order to include topics such as the new results in Particle Physics on the way the DM annihilation might occur (e.g. the important contribution of the Internal Breemstrahlung as recently pointed out in Bringmann et al. 2008, which was traditionally discarded), the role of DM substructure (that will enhance the DM annihilation flux), new and more sophisticated EBL models, etc. The detection prospects for the Fermi satellite will also be addressed in such a work. Fermi represents indeed the ideal instrument to study the EGB given its all sky-survey operating mode, in contrast to the small field of view ($\sim$4 degrees) of the current Imaging Atmospheric Cherenkov telescopes (IACTs).

Still related to DM detection issues, I believe it is necessary to clarify the relationship between the different experimental constraints obtained by those experiments that try to find the DM in the laboratory (the so-called direct detection) and those

that use detailed astrophysical observations in their search for DM (indirect detection). Usually, each of these communities work independently from the other, so that very often the obtained results are not fully understood and can not be easily translated from one to the other side. It is worth making an effort in this direction, carrying out a comprehensive comparison between both technics, since it may happen that some of the constraints already obtained by direct detection for the usual parameters (DM particle mass, cross sections, etc) could also translate in a useful and stringent constrain in the region of relevance of the indirect detection experiments. Or vice-versa.

Axions should necessarily be another of my main projects for the near future. In Chapter 5 (which is based on Sánchez-Conde et al. 2009), I have already presented the basis of a formalism to properly deal with the photon/axion mixing expected to occur in the magnetic fields of Very High Energy (VHE) sources as well as in the presence of Intergalactic Magnetic Fields (IGMF). In my opinion, the potential of this work is enormous, with many direct consequences for VHE astronomy being testable. For example, it may represent an alternative explanation to those incongruities given by the most promising EBL models when applied to some distant AGNs recently discovered in gamma-rays (Albert et al. 2008, Aliu et al. 2008). According to the standard Physics based astrophysical models that explain the emission mechanisms in the source as well as the preferred EBL models, one should not expect a photon flux as high as recently measured by some experiments, in particular at higher energies. As already pointed out in Chapter 5, an effective photon/axion oscillation may alleviate this problem. In the future it will be worth carrying out particular predictions for the expected photon flux from those controversial objects, so that they can be probed by Fermi and IACTs. In addition, it may happen that some EBL models previously rejected due to their large opacity to gamma-rays would be plausible after all. This idea will be explored as well.

There are also other possible scenarios that I would like to study in order to detect axions with gamma-ray experiments. One of them, already outlined in Fairbairn et al. (2007), suggests to use the magnetic field of the Sun: if axions exist, then we should see a signal when pointing a detector (not an IACT certainly, but e.g. Fermi) to a gamma-ray source located behind the Sun. This signal will be surely very small, but different from zero. I would like to make realistic predictions of this phenomenon, adopting a model as reliable as possible for the solar magnetic field (with some external help) and choosing the most appropriate VHE gamma-ray source for such a detection.

Bibliography

Albert et al., 2008, Science, 320, 1752

Aliu et al. [MAGIC Collaboration], 2008, ApJL, 692, 29

Bardeen J. M., Bond J. R., Kaiser N. & Szalay A. S. 1986, ApJ, 304, 15

Bringmann T., Bergström L., & Edsjö J., 2008, Journal of High Energy Physics, 1, 49

Fairbairn M., Rashba T. and Troitsky S., 2007, Phys. Rev. Lett., 98, 201801

Navarro J. F., Frenk C. S. & White S. D. M. 1997, ApJ, 490, 493

Ullio P., Bergström L., Edsjö J., & Lacey C., 2002, Phys. Rev. D, 66, 123502

A

Appendix

A.1 The Formalism in the ΛCDM cosmology

If we are in a $\Lambda \neq 0$ cosmology, we need to introduce some changes for the initial conditions and in the expressions for the evolution of the spherical perturbation, although the formalism and the algorithm are essentially the same as presented in Chapter 3, i.e. the SST framework.

The equation for the initial radii of the shells is the same as given by Eq.(3.18), but for the velocities the correct expression, instead of Eq.(3.19), is now:

$$v_i(j) = \left[1 - \frac{1}{3}\frac{1}{1+\delta(\delta_l^i(q(j)))}\frac{a_i\ \dot{D}(a)}{D(a)}\Big|_{a=a_i}\frac{\delta_l^i(q(j))}{\frac{d\delta_l(\delta)}{d\delta}\big|_{\delta=\delta(\delta_l^i(q(j)))}}\right] \times\ r_i(j)\ \frac{2}{3}\ (1+\beta_i)^{\frac{1}{2}}\ ln\left[\beta_i^{-\frac{1}{2}} + \sqrt{1+\beta_i^{-1}}\right] \tag{A.1}$$

where

$$\dot{D}(a) = \frac{dD(a)}{da}$$

$$\beta_i = \frac{\Omega_m}{\Omega_\Lambda}\ (1+z_i)^3 = \beta_0\ (1+z_i)^3$$

and,

$$a(t) = \left[\beta_0^{\frac{1}{2}}\left(\frac{(\beta_i^{-\frac{1}{2}} + \sqrt{1+\beta_i^{-1}})^t - (\beta_i^{-\frac{1}{2}} + \sqrt{1+\beta_i^{-1}})^{-t}}{2}\right)\right]^{\frac{2}{3}}$$

$$a_i = \frac{1}{1+z_i}$$

$$D(a) = \frac{1}{2\ a\ f(a)} \int_0^a f^3(a)\ da$$

$$f(a) = \left[1 + \Omega_m \left(\frac{1}{a} - 1\right) + \Omega_\Lambda (a^2 - 1)\right]^{-\frac{1}{2}} \tag{A.2}$$

Note that β_i is simply the parameter $\beta_0 = \Omega_m/\Omega_\Lambda$ but referred to the initial time.

Concerning to the initial density profile, now the initial linear density contrast is essentially the same as given by Eq.(3.15) but now the rescaling factor, $\frac{1}{1+z_i}$, is here replaced by $\frac{D(a_i)}{D(a=1)}$, which gives:

$$\delta_l^i(q(j)) = \frac{D(a_i)}{D(a=1)}\ \delta_l(q(j)) \tag{A.3}$$

where $\delta_l(q(j))$ is the linear profile given by Eq.(3.12).

For the evolution, equations (3.21) and (3.22) are still valid for the radius and the velocity, but to compute the linear and actual density contrast, now we have to include:

$$\delta_l(j,t) = \frac{D(a(t))}{D(a_i)}\ \delta_l^i(q(j)) \tag{A.4}$$

$$\delta(j,t) = \left[[1 + \delta(\delta_l^i(q(j)))] \left(\frac{r_i(j)}{r(j)}\right)^3 \left(\frac{a(t)}{a_i}\right)^3\right] - 1 \tag{A.5}$$

where $D(a)$ and $a(t)$ are the growing and scale factor respectively, as defined in Eq.(A.2), and a_i denotes the scale factor at initial time, given also in Eq.(A.2).

To recompute the enclosed mass at each time step, it is also necessary to take into account the new cosmology, once we have calculated $M(j,t)$ in first place according to Eq.(3.25), i.e.:

$$M(j,t)(\Lambda \neq 0) = M(j,t)(\Lambda = 0) - \frac{2}{\beta_i} r(j,t)^3 \tag{A.6}$$

A.2 Results obtained for stabilization and virialization

In Tables A.1 to A.4 the linear and actual density contrasts that we obtain concerning to the moments of stabilization and virialization are shown. Tables A.1 and A.2 refer to the stabilization, whereas Tables A.3 and A.4 are related to the virialization. In both cases, the moments of stabilization and virialization were matched following the criteria given in Section 3.6. In these Tables, linear and actual density contrast are shown for different values of virial mass, M_{vir}, fraction of virial mass, M_{frac}, and for Einstein-deSitter and $\Omega_m = 0.3$, $\Omega_\Lambda = 0.7$ cosmologies.

Table A.1 Linear and actual density contrasts at the moment of stabilization, this one defined according to two percentages (5% and 10%), for different values of M_{frac} and two cosmologies. A virial mass of $M_{vir} = 3 \times 10^{12} h^{-1}\ M_\odot$ was used in all the cases. See text for details.

Einstein-deSitter ($\Omega_m = 1$, $\Omega_\Lambda = 0$)

	$M_{frac} = 0.2$		$M_{frac} = 0.5$		$M_{frac} = 0.8$		$M_{frac} = 1.0$	
Percentage	δ_l	δ	δ_l	δ	δ_l	δ	δ_l	δ
5 %	-	-	-	-	-	-	-	-
10 %	1.98	3993	2.00	1789	2.05	1223	1.89	700

$\Omega_m = 0.3$, $\Omega_\Lambda = 0.7$

	$M_{frac} = 0.2$		$M_{frac} = 0.5$		$M_{frac} = 0.8$		$M_{frac} = 1.0$	
Percentage	δ_l	δ	δ_l	δ	δ_l	δ	δ_l	δ
5 %	1.91	3306	1.85	1298	1.86	897	1.86	741
10 %	1.67	1496	1.67	703	1.67	463	1.67	390

Table A.2 Linear and actual density contrasts at the moment of stabilization, this one defined according to two percentages (5% and 10%), for three different virial masses and two cosmologies. A value of $M_{frac} = 0.5$ was used in all the cases. Virial masses in units of $h^{-1}\ M_{\odot}$. See text for details.

Einstein-deSitter ($\Omega_m = 1$, $\Omega_\Lambda = 0$)

	$M_{vir} = 6.5 \times 10^{10}$		$M_{vir} = 3 \times 10^{12}$		$M_{vir} = 5 \times 10^{14}$	
Percentage	δ_l	δ	δ_l	δ	δ_l	δ
5 %	-	-	-	-	-	-
10 %	-	-	2.00	1789	1.87	610

$\Omega_m = 0.3$, $\Omega_\Lambda = 0.7$

	$M_{vir} = 6.5 \times 10^{10}$		$M_{vir} = 3 \times 10^{12}$		$M_{vir} = 5 \times 10^{14}$	
Percentage	δ_l	δ	δ_l	δ	δ_l	δ
5 %	1.93	2727	1.85	1298	1.89	680
10 %	1.67	1105	1.67	703	1.67	352

Table A.3 Linear and actual density contrasts at the moment of virialization, this one defined according to two percentages (25% and 35%), for different values of M_{frac} and two cosmologies. A virial mass of $M_{vir} = 3 \times 10^{12} h^{-1}\ M_{\odot}$ was used in all the cases. See text for details.

Einstein-deSitter ($\Omega_m = 1$, $\Omega_\Lambda = 0$)

	$M_{frac} = 0.2$		$M_{frac} = 0.5$		$M_{frac} = 0.8$		$M_{frac} = 1.0$	
Percentage	δ_l	δ	δ_l	δ	δ_l	δ	δ_l	δ
25 %	2.25	6843	2.09	2080	1.97	903	1.90	731
35 %	2.25	6843	2.09	2080	1.97	903	1.90	731

$\Omega_m = 0.3$, $\Omega_\Lambda = 0.7$

	$M_{frac} = 0.2$		$M_{frac} = 0.5$		$M_{frac} = 0.8$		$M_{frac} = 1.0$	
Percentage	δ_l	δ	δ_l	δ	δ_l	δ	δ_l	δ
25 %	-	-	-	-	-	-	-	-
35 %	2.43	13277	2.26	4374	2.13	2070	2.06	1574

Table A.4 Linear and actual density contrasts at the moment of virialization, this one defined according to two percentages (25% and 35%), for three different virial masses and two cosmologies. A value of $M_{frac} = 0.5$ was used in all the cases. Virial masses in units of $h^{-1}\ M_{\odot}$. See text for details.

Einstein-deSitter ($\Omega_m = 1$, $\Omega_\Lambda = 0$)

	$M_{vir} = 6.5 \times 10^{10}$		$M_{vir} = 3 \times 10^{12}$		$M_{vir} = 5 \times 10^{14}$	
Percentage	δ_l	δ	δ_l	δ	δ_l	δ
25 %	1.89	1971	2.09	2080	- [1]	- [1]
35 %	1.89	1971	2.09	2080	- [1]	- [1]

[1] No virialization was obtained below 45%; for this percentage, $\delta_l = 2.32$ and $\delta = 1429$

$\Omega_m = 0.3$, $\Omega_\Lambda = 0.7$

	$M_{vir} = 6.5 \times 10^{10}$		$M_{vir} = 3 \times 10^{12}$		$M_{vir} = 5 \times 10^{14}$	
Percentage	δ_l	δ	δ_l	δ	δ_l	δ
25 %	2.11	4387	-	-	2.43	3092
35 %	2.03	3509	2.26	4374	2.31	2111

B

Publications

Publications in refereed journals

19 refereed publications. A total of **323** citations in the ADS (7-Jul-09).

1. *How far do they go? The outer structure of dark matter halos*
   F. Prada, A.A. Klypin, E. Simonneau, J. Betancort-Rijo, S. G. Patiri, S. Gottlöber and **M. A. Sánchez-Conde**, 2006, ApJ, 645, 1001

2. *Detailed theoretical predictions of the outskirts of dark matter halos*
   J. E. Betancort-Rijo, **M. A. Sánchez-Conde**, F. Prada and S. G. Patiri, 2006, ApJ, 649, 579

3. *The spherical collapse model with shell crossing*
   M. A. Sánchez-Conde, J. Betancort-Rijo and F. Prada, 2007, MNRAS, 378, 339

4. *Dark Matter Annihilation in Draco: new considerations of the expected gamma flux*
   M. A. Sánchez-Conde, F. Prada, E. W. Łokas, M. E. Gómez, R. Wojtak and M. Moles, 2007, Phys. Rev. D, 76, 123509

5. *Upper limit for gamma-ray emission above 140 GeV from the dwarf spheroidal galaxy Draco*
   Albert et al. (including **M. A. Sánchez-Conde**, 2008, ApJ, 679, 428

6. *The dark outside: the density profile of dark matter haloes beyond the virial radius*
   H. Tavío, A. J. Cuesta, F. Prada, A. A. Klypin, **M. A. Sánchez-Conde**, 2008, MNRAS submitted, astro-ph/0807.3027

7. *Upper limits on the VHE gamma-ray emission from the Willman 1 satellite galaxy with the MAGIC telescope*
   Aliu E. et al. (corresponding author **M. A. Sánchez-Conde**), 2009, ApJ, 697, 1299

8. *Hints of the existence of Axion-Like-Particles from the gamma-ray spectra of cosmological sources*
   M. A. Sánchez-Conde, D. Paneque, E. Bloom, F. Prada and A. Domínguez, 2009, Phys. Rev. D, 79, 123511

11 more refereed publications as a member of the MAGIC collaboration:

1. *Very-High-Energy gamma rays from a Distant Quasar: How Transparent Is the Universe?*
   Albert et al. (including **M. A. Sánchez-Conde**), 2008, Science, 320, 1752

2. *Multiwavelength (Radio, X-Ray, and γ-Ray) Observations of the γ-Ray Binary LS I +61 303*
   Albert et al. (including **M. A. Sánchez-Conde**), 2008, ApJ, 684, 1351

3. *Very High Energy Gamma-Ray Observations of Strong Flaring Activity in M87 in 2008 February*
   Albert et al. (including **M. A. Sánchez-Conde**), 2008, ApJ, 685, L23

4. *First Bounds on the High-Energy Emission from Isolated Wolf-Rayet Binary Systems*
   Aliu et al. (including **M. A. Sánchez-Conde**), 2008, ApJ, 685, L71

5. *Probing quantum gravity using photons from a flare of the active galactic nucleus Markarian 501 observed by the MAGIC telescope*
   Albert et al. (including **M. A. Sánchez-Conde**), 2008, Physics Letters B, 668, 253

6. *Observation of Pulsed γ-Rays Above 25 GeV From the Crab Pulsar with MAGIC*
   Aliu et al. (including **M. A. Sánchez-Conde**), 2008, Science, 322, 1221

7. *Improving the performance of the single-dish Cherenkov telescope MAGIC through the use of signal timing*
   Aliu et al. (including **M. A. Sánchez-Conde**), 2009, Astroparticle Physics, 30, 293

8. *The June 2008 Flare of Markarian 421 from Optical to TeV Energies*
   Donnarumma et al. (including **M. A. Sánchez-Conde**), 2009, ApJL, 691, 13

9. *Discovery of a very high energy gamma-ray signal from the 3C 66A/B region*
   Aliu et al. (including **M. A. Sánchez-Conde**), 2008, ApJL, 692, 29

10. *Periodic Very High Energy γ-Ray Emission from LS I +61 303 Observed with the MAGIC Telescope*
    Albert et al. (including **M. A. Sánchez-Conde**), 2009, ApJ, 693, 303

11. *MAGIC upper limits to the VHE gamma-ray flux of 3C 454.3 in high emission state*
    Anderhub et al. (including **M. A. Sánchez-Conde**), 2009, A&A, 498, 83

Publications in non-refereed journals

1. *Dark Matter in Draco: new considerations of the expected gamma flux in IACTs*
   Sánchez-Conde M. A., Prada F., & Łokas E. L., 2006, The Dark Side of the Universe, AIP Conference Proceedings, 878, 125

2. *Characteristics and Performance of the GAW Experiment for a Large Field of View Cerenkov Gamma-ray Telescope*
   Cusumano, G., et al. (including **M. A. Sánchez-Conde**), 2006, Chinese Journal of Astronomy and Astrophysics, Supplement, 6, S1, 369

3. *Gamma Air Watch (GAW) - An Imaging Atmospheric Cherenkov Telescope Large with Large Field of View*
   Mineo T. et al. (including **M. A. Sánchez-Conde**), Proceedings of the Third Workshop on Science with the New Generation of High Energy Gamma-ray Experiments, May 30 - June 1, 2005, Cividale del Friuli, Italy. World Scientific Publishing Co., Pte. Ltd., Singapore, 2006, p.75

4. *Science with the new generation high energy gamma- ray experiments*
   Alvarez, M., et al. (including **M. A. Sánchez-Conde**), Proceedings of the 5th SCINEGHE Workshop, June 18-20, 2007; Frascati Physics Series vol.45, 2007, astro-ph/0712.1548

5. *GAW - An Imaging Atmospheric Cherenkov Telescope with Large Field of View*
   Cusumano, G., et al. (including **M. A. Sánchez-Conde**), Proceedings of 30th ICRC, International Cosmic Ray Conference 2007, Merida, Yucatan, Mexico, 3-11 July 2007, astro-ph/0707.4541

6. *Indirect Dark Matter Search in Dwarf Galaxies*
   Rissi M., et al. (including **M. A. Sánchez-Conde**), 2007, Astronomische Nachrichten, 328, 683

7. *Dark Matter annihilation in Draco: new considerations of the expected gamma flux*
   Sánchez-Conde M. A., The First GLAST Symposium, AIP Conference Proceedings, 2007, 921, 510

8. *The search for DM in nearby dSph galaxies with MAGIC: candidates, results and prospects*
   Sánchez-Conde M. A., to appear in the 8th UCLA Dark Matter Conference Proceedings, Marina del Rey, CA, USA, February 2008

9. *GAW - An Imaging Atmospheric Cherenkov Telescope with Large Field of View*
   Cusumano G. et al. (including **M. A. Sánchez-Conde**), 2008, International Cosmic Ray Conference, 3, 1317

10. *Study of indirect detection of Axion-Like-Particles with the Fermi-LAT instrument and Imaging Atmospheric Cherenkov Telescopes*
    Paneque, D., Bloom, E., & Sánchez-Conde, M. A., 2009, APS Meeting Abstracts, 12007

11. *Search for Dark Matter signatures with MAGIC-I and prospects for MAGIC Phase-II*
    Lombardi, S., et al., (including **M. A. Sánchez-Conde**), 2009, arXiv:0907.0738